

Study of the effect of phase and morphology on the optical properties of lanthanide ion-doped phosphors and their applications

by

Monika Malik
10CC14A26020

A thesis submitted to the
Academy of Scientific & Innovative Research
for the award of the degree of
DOCTOR OF PHILOSOPHY
in
SCIENCE

Under the supervision of
Dr. Pankaj Poddar



CSIR-National Chemical Laboratory, Pune



Academy of Scientific and Innovative Research
AcSIR Headquarters, CSIR-HRDC campus
Sector 19, Kamla Nehru Nagar,
Ghaziabad, U.P. – 201 002, India

December, 2021

Certificate

This is to certify that the work incorporated in this Ph.D. thesis entitled, “Study of the effect of phase and morphology on the optical properties of lanthanide ion-doped phosphors and their applications”, submitted by Monika Malik to the Academy of Scientific and Innovative Research (AcSIR), in partial fulfillment of the requirements for the award of the Degree of Doctor of Philosophy in Science, embodies original research work carried-out by the student. We further certify that this work has not been submitted to any other University or Institution in part or full for the award of any degree or diploma. Research material(s) obtained from other source(s) and used in this research work has/have been duly acknowledged in the thesis. Image(s), illustration(s), figure(s), table(s) etc., used in the thesis from other source(s), have also been duly cited and acknowledged.



(Signature of Student)

Monika Malik

31.12.2021



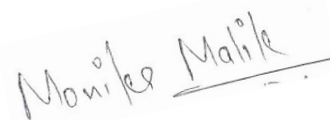
(Signature of Supervisor)

Dr. Pankaj Poddar

31.12.2021

STATEMENTS OF ACADEMIC INTEGRITY

I, Monika Malik, a Ph.D. student of the Academy of Scientific and Innovative Research (AcSIR) with Registration No.10CC14A26020 hereby undertake that the thesis entitled “Study of the effect of phase and morphology on the optical properties of lanthanide ion-doped phosphors and their applications” has been prepared by me and that the document reports original work carried out by me and is free of any plagiarism in compliance with the UGC Regulations on “*Promotion of Academic Integrity and Prevention of Plagiarism in Higher Educational Institutions (2018)*” and the CSIR Guidelines for “*Ethics in Research and in Governance (2020)*”.



Signature of the Student

Date: 31.12.2021

Place: Pune

It is hereby certified that the work done by the student, under my/our supervision, is plagiarism-free in accordance with the UGC Regulations on “*Promotion of Academic Integrity and Prevention of Plagiarism in Higher Educational Institutions (2018)*” and the CSIR Guidelines for “*Ethics in Research and in Governance (2020)*”.



Signature of the Supervisor

Name: Dr. Pankaj Poddar

Date: 31.12.2021

Place: Pune

ACKNOWLEDGEMENTS

The work presented in this thesis would not have been realized without my close association with many people who contributed in numerous ways to the success of this study. Herein, I take this opportunity to acknowledge and extend my heartfelt gratitude and appreciation to all those people who have been involved in making this thesis possible.

Foremost, I would like to express my sincere gratitude and respect to my research supervisor Dr. Pankaj Poddar, for giving me an opportunity to pursue research with him. I like to thank him for his dedicated help, thoughtful advice, constructive comments, and encouragement throughout my PhD tenure. His enthusiasm, integral view on science has inspired me to become an independent researcher. All these years from his interactions, I have learnt about approaching a problem from all possible angles and finding its solution from a basic level. He constantly emphasizes on inculcating the habit of critical thinking and teaches us about dos and don'ts in science and life. Apart from this, I admire his way of teaching, where he starts from a basic level and move towards an advanced level to make any topic crystal clear and simpler. His knowledge in every subject has impressed me a lot. I feel fortunate and privileged to be associated with him and part of his research group.

I would also like to thank my doctoral advisory committee members, Dr. H. V. Thulasiram, Dr. S. Kadhiravan, and Dr. Santosh Kumar Jha, for their time, constructive suggestions, guidance, and support. I owe a great deal of appreciation and gratitude to my external expert Dr. V. G. Anand, IISER Pune, for evaluating my work in my up-gradation meetings. I warmly thank him for his precious time, advice, and discussion on my work.

I extend my sincere thanks to the present Director of CSIR-NCL Dr. Ashish Lele, Dr. Ashwini Kumar Nangia (former Director), and Dr. Sourav Pal (former Director) for giving me an opportunity to work in this prestigious institute and making the facilities available to carry out the research. I am also grateful to the Head of Physical and Materials Chemistry Division, Dr. T. Ajithkumar, Dr. P. A. Joy (former HoD), and Dr. B. L. V. Prasad (former HoD) for their kind help during the course of my PhD. I would also extend my gratitude to former HoD Dr. Anil Kumar for the exciting interactions, for his continuous support and care. Even in the most challenging lockdown times due to COVID-19, he used to keep an update on the health of his beloved students. I again thank Dr. B. L. V. Prasad for allowing me to perform luminescence measurements in his lab. Many thanks to the staff members of

our division, who have helped me with the routine official work. I wish to thank all the administrative and non-teaching staff of CSIR-NCL for their kind support and assistance over the years on various occasions.

I am also grateful to many people in the Center for Materials Characterization division, NCL, who have assisted me during my tenure. My sincere thanks to Mr. S. S. Deo, Mr. R. S. Gholap, Venkatesh, Sheetal, Chetan and Harsha for their timely help in XPS, TEM, and SEM measurements. I would also like to thank Dr. Suresh Gokhale and Rupali Waichal ma'am, for providing access to the Raman instrument. My special thanks to Dr. Rajesh Gonnade for his teaching on the XRD subject in the course work; also, the discussion on TGA/DSC measurements and analysis was very helpful. I want to express my deepest gratitude to Late Dr. Ashutosh Abhyankar, DIAT Pune, for his help with FESEM measurements. He always provided me with the slots whenever I asked him for a favour. Unfortunately, we lost him this year due to COVID-19 complications. May his soul rest in peace.

I am grateful to the Council of Scientific and Industrial Research (CSIR), India, for providing me with the necessary funding and fellowship to pursue research at NCL.

I express my thanks to Suguna Adhyanthaya Ma'am for her continuous cooperation and encouragement. Although she was retired when I joined this group, but her timely help in TGA/DSC measurements is greatly acknowledged. I also take an opportunity to thank my seniors from the lab, Dr. Raja Das, Dr. Chandrasekhar Sharan, Dr. Subha Sadhu, Dr. Puneet Khandelwal, Dr. Preeti Gupta, Dr. Mousumi Sen, Dr. Anupam Biswas, Dr. Sameer Shaikh, and Gayatri Di. I would also like to thank my super seniors Dr. Ramya Jagannathan, Dr. Adhish, Dr. Umesh, Dr. Imran, and Dr. Dheeraj. However, they had moved away from NCL when I joined the lab, but the surprise meetings with them have inspired me to do well in science. I will always remember the experiences they've shared, and I hope to stay in touch with them. It would be incomplete without thanking my lovely senior Dr. Preeti Padhye 😊 with whom I have learnt so much in research. She has helped me familiarized with all the lab facilities and taught me my first chemical reaction of PhD work. She also encouraged and helped me writing my first manuscript. Thank you di, for your support. I also thank postdoc seniors from our lab Dr. Geeta Sharma, Dr. Manorama lakhe, Dr. Subodh Gautam, and Dr. Bhavana Joshi, for the interesting discussions. I would also like to thank my juniors Dinesh and Manisha, for creating a learning and cordial environment in the lab. I thank my closest friends Shubhra, Monika Ghalawat, Supriya, and Tubai for supporting and encouraging me

throughout, whenever the PhD challenges seemed too huge to overcome. I can't forget all the masti and dance we did together in the last five years. I will always remember late night discussions and chitchats with Monika and Supriya ☺. I thank you all for your company, love, and care.

Wholehearted thanks to Ragini di, with whom I spent the most wonderful time in Pune. I can't express my bonding with you in words here. Thank you for understanding and being with me in my tough times. I extend many thanks to my NCL seniors and friends Indrapal bhaiya (my TT partner), Manoj bhaiya, Gunwant, Bhawana di, Sarobjot, Reshma, Arun, Preeti Jain, Indra, Ashish, Amit, Samik, Shibin, Praveen, Govind, Prashant, Abhijit, Amarnath, Pratiksh and Sumana for being a valuable part of my life at NCL. How can I forget my SSBMT table tennis team, Dr. Priyanka Verma (the sweetest person I have ever met), Mohan sir, Deepak bhaiya, and Poorvi Purohit ma'am (person with best smile), with whom I have travelled to different cities for playing TT and enjoyed a lot. I would also like to thank my M.Sc. friends Prachi, Himani, Meenu, Yukti, and Devanshi, who have constantly been in touch with me all these years and asked about my wellbeing. Despite only few meetings past these years, the bond we share is remarkable.

I would like to express my heartfelt gratefulness to my mummy, Mrs. Veena and papa, Mr. Harendra Pal Singh, who provided endless love and unmatched support throughout my life. You both have been a constant source of inspiration in every walk of my life. Thank you for believing and keeping patience with me. I would also like to express my affection to my younger sister and brother, Neha and Siddharth, for their constant moral support. I always remember your teasing "kab kar rahi ho khatam kaam and aisa kya research kar rahi ho☺". But thank you for being with me and trusting me. It gives me immense pleasure to thank everyone who helped me write my thesis successfully.

Last but not least, I thank God for making my life so beautiful and for providing me this opportunity, and granting me the capability to proceed successfully.

Monika Malik

Table of Contents

Chapter 1: Introduction

1.1 Luminescence and its origin.....	2
1.2 Discovery of lanthanides.....	5
1.3 History of lanthanide ion luminescence and its mechanism.....	8
1.3.1 Electronic structure.....	9
1.3.2 Energy levels.....	10
1.3.3 Radiative transitions.....	12
1.4 Different types of lanthanide ion-based materials.....	15
1.4.1 Lanthanide complexes.....	15
1.4.2 Lanthanide ion-doped glasses.....	16
1.4.3 Inorganic crystals/phosphors.....	17
1.4.4 Polymers.....	18
1.5 Energy transfer mechanism.....	19
1.6 Phosphors: concept of host and dopant.....	28
1.6.1 Host lattice.....	28
1.6.2 Activator.....	30
1.6.3 Sensitizer.....	31
1.7 Synthesis methods.....	32
1.7.1 Thermal decomposition.....	32
1.7.2 Co-precipitation.....	33
1.7.3 Hydrothermal/solvothermal.....	34
1.7.4 Sol-gel processing.....	36
1.7.5 Other synthetic procedures.....	37
1.8 Surface modification.....	38
1.8.1 Surface passivation.....	39
1.8.2 Surface functionalization.....	40
1.9 Morphology tuning.....	43
1.9.1 Effect of reaction temperature and time.....	43
1.9.2 Concentration of precursors.....	44
1.9.3 Effect of different dopants and concentration.....	44
1.9.4 Effect of capping agents/ligands.....	45
1.10 Applications.....	45
1.10.1 Optical imaging.....	46
1.10.2 Theranostics.....	48

1.10.3 Sensing applications.....	49
1.10.4 Energy applications.....	51
1.10.5 Security applications.....	53
1.11 Rationale of choosing host and dopants.....	53
1.12 Thesis objective.....	58
1.13 Thesis outline.....	59
1.14 References.....	61

Chapter 2: Analyzing the effect of the ligands on the crystal phase and morphology of NaYF₄ nanophosphors

2.1 Introduction.....	76
2.2 Materials and methods.....	79
2.2.1 Methods.....	79
2.2.2 Synthesis.....	79
2.2.2.1 Synthesis of NaYF ₄ : Gd,Tb phosphors at ambient conditions.....	79
2.2.2.2 Hydrothermal synthesis of NaYF ₄ : Gd,Tb phosphors at 180 °C.....	80
2.2.3 Characterization techniques.....	80
2.3 Results and discussion.....	81
2.3.1 Growth mechanism and evolution of morphology.....	88
2.3.2 Effect of ligands concentration on the phase and morphology.....	94
2.3.3 Photoluminescent properties.....	97
2.4 Conclusions.....	103
2.5 References.....	104

Chapter 3: Graphene quantum dots driven multiform morphologies of β -NaYF₄: Gd³⁺,Tb³⁺ phosphors: the underlying mechanism and their optical properties

3.1 Introduction.....	109
3.2 Materials and Methods.....	113
3.2.1 Materials.....	113
3.2.2 Synthesis.....	113
3.2.2.1 Synthesis of GO.....	113
3.2.2.2 Synthesis of carboxylic and amine co-functionalized GQDs.....	114
3.2.2.3 Synthesis of carboxylic functionalized GQDs.....	114
3.2.2.4 Synthesis of amine functionalized GQDs.....	115
3.2.2.5 Synthesis of reduced GQDs.....	115
3.2.2.6 Synthesis of amine functionalized β -NaYF ₄ : Gd ³⁺ ,Tb ³⁺	115
3.2.2.7 Synthesis of β -NaYF ₄ :Gd ³⁺ ,Tb ³⁺ incorporated with GQDs.....	116
3.2.3 Characterization techniques.....	116

3.3 Results and discussion.....	117
3.3.1 Characterization of GQDs.....	117
3.3.2 Structural and morphological investigations of β -NaYF ₄ : Gd ³⁺ ,Tb ³⁺ -xGQDs.....	119
3.3.3 Growth mechanism of GQDs incorporated NaYF ₄ : Gd ³⁺ ,Tb ³⁺ multiform morphologies.....	122
3.3.3.1 Effect of size of the foreign particles introduced in the reaction.....	127
3.3.3.2 Effect of functionalization of GQDs on the β -NaYF ₄ : Gd ³⁺ ,Tb ³⁺ phosphors growth.....	129
3.3.3 Photoluminescence studies.....	137
3.4 Conclusions.....	142
3.5 References.....	143

Chapter 4: A downconversion luminescence-based nanosensor for label-free detection of explosives

4.1 Introduction.....	151
4.2 Materials and methods.....	154
4.2.1 Materials.....	154
4.2.2 Synthesis.....	155
4.2.2.1 Synthesis of amine functionalized β -NaYF ₄ : 15%Gd ³⁺ ,5%Tb ³⁺	155
4.2.2.2 Preparation of stock solutions.....	155
4.2.3 Characterization techniques.....	155
4.3 Results and discussion.....	156
4.3.1 Detection of explosives.....	164
4.3.2 Interference study.....	166
4.3.3 Mechanism of highly selective detection.....	168
4.3.4 Interference from other analytes.....	172
4.4 Conclusions.....	173
4.5 References.....	174

Chapter 5: Summary and future scope

5.1 Summary.....	179
5.2 Future scope.....	181

Abstract

List of publications

List of abbreviations

1. Lanthanides	Ln
2. Trivalent lanthanides	Ln ³⁺
3. Photoluminescence	PL
4. Ultraviolet	UV
5. Infrared	IR
6. Near-infrared	NIR
7. Electromagnetic radiation	EMR
8. Excited state	ES
9. Ground state	GS
10. Electric dipole	ED
11. Magnetic dipole	MD
12. Electric quadrupole	EQ
13. Judd-Ofelt Theory	JO theory
14. Nanoparticles	NPs
15. Ligand-to-metal charge transfer	LMCT
16. Metal-to-ligand charge transfer	MLCT
17. Fluorescence resonance energy transfer	FRET
18. Polymethylmethacrylate	PMMA
19. Upconversion	UC
20. Downconversion	DC
21. Downshifting	DS
22. Quantum cutting	QC
23. Two-photon absorption	TPA
24. Second-harmonic generation	SHG
25. Excited state absorption	ESA
26. Energy transfer upconversion	ETU
27. Cross-relaxation	CR
28. Photon avalanche	PA
29. Cooperative sensitization upconversion	CSU
30. Energy migration-mediated upconversion	EMU

31. 1-Octadecene	ODE
32. Oleyl amine	OM
33. Oleic acid	OA
34. Ethylenediamine tetraacetic acid	EDTA
35. Upconverting nanoparticles	UCNPs
36. Cetyltrimethylammonium bromide	CTAB
37. X-ray diffraction	XRD
38. Transmission electron microscope	TEM
39. Scanning electron microscope	SEM
40. Field emission scanning electron microscope	FESEM
41. Selected area electron diffraction	SAED
42. X-ray photoelectron spectroscopy	XPS
43. Thermogravimetric analysis	TGA
44. Energy dispersive X-ray analysis	EDXA
45. Doxorubicin	DOX
46. Photodynamic therapy	PDT
47. Quantum-dots	QDs
48. Sodium yttrium fluoride	NaYF ₄
49. Dye-sensitized solar cell	DSSCs
50. Photon conversion efficiency	PCE
51. Trisodium citrate	TSC
52. Ethylene diamine	EDA
53. Phosphate buffer saline	PBS
54. Polyethyleneimine	PEI
55. Joint committee on powder diffraction standards	JCPDS
56. Graphene quantum dots	GQDs
57. Carbon nanotubes	CNTs
58. Multiwalled carbon nanotubes	MWCNTs
59. Graphene oxide	GO
60. Cellulose nanofibers	CNF
61. Deionized water	DI
62. 2,4,6-Trinitrotoluene	TNT

63. Fast Fourier transform	FFT
64. Inverse fast Fourier transform	IFFT
65. Stern-Volmer plot	SV plot
66. Excitation wavelength	λ_{ex}
67. Emission wavelength	λ_{em}
68. Ultraviolet visible spectroscopy	UV-vis
69. Metal-organic frameworks	MOFs
70. Limit of detection	LOD
71. Fluorescence resonance energy transfer	FRET
72. Luminescence resonance energy transfer	LRET
73. Light-emitting diodes	LEDs

Chapter 1



Introduction

Outline

In this chapter, initially, a brief overview of the discovery of lanthanides and their optical properties is provided. Later, the mechanisms of upconversion and downconversion processes in lanthanide ions are summarized. As the present study deals with the lanthanide ion-doped phosphors, an overview of the dependence of their luminescence on the dopant-concentration in the host matrices, temperature, time, particle size, shape, etc., has been given. After a brief review of the different synthetic approaches along with various applications, the rationale behind choosing the fluoride as the host and Gd^{3+} and Tb^{3+} ions as the dopants are discussed. Finally, the thesis outline and the scope of the investigation are presented.

1.1 Luminescence and its origin

Luminescence is the spontaneous emission of electromagnetic radiation (EMR) from electronically or vibrationally excited species not in thermal equilibrium with its environment.¹ This is distinguished from incandescence which is the emission of light because of heating specific objects such as molten iron, burning wood or coal, a light bulb with filament, etc. Luminescence is described by the transitions of electrons from the excited states (ES) of a system; the excitation of these electrons is not associated with the thermal agitation of the atoms. Thus, the thermal energy (K_bT , K_b is Boltzmann constant and T is temperature) is insufficient to populate the ES of the system. Luminescence occurs when a material absorbs energy from a source such as EMR, electron beams, electric field, chemical reactions, etc.² The energy of the primary source lifts the atoms into the ES. The outermost electrons of the atoms are involved in this excitation process. Then, due to the instability of ES, the atoms return to their ground state (GS). This absorbed energy is emitted as light. Matter in any of the states— solids, liquids, and gases, can show luminescence. Nature had admiring examples of luminescence such as luminous animals (jelly fish, fireflies, and glowworms), aurora borealis, the glow of the ocean, stones, lightning, phosphorescent wood, etc.³

The term “luminescence” was coined by German physicist Wiedemann in 1888 to describe the emission of light not conditioned by a rise in temperature. This word originated from the Latin word *lumen*, meaning light.⁴ Luminescent materials have been recognized since approximately the 10th century in Japan and China as well as since the end of the Middle Ages in Europe.⁵ The discovery of the Bolognian stone in 1603 by Cascariolo on Mount Paderno, near Bologna, Italy, and of the element phosphorus in 1669 were milestones that led to the understanding of the phenomenon linked to the emission of light.⁶ The first identified inorganic phosphor to show persistent luminescence, the bologna stone emitted yellow to orange light without any external excitation.⁷ During these times, luminescent

materials were used only for decorative purposes. The first significant breakthrough regarding luminescent materials was the realization of gas discharges in evacuated glass tubes by Geissler and Braun and X-rays discovery by Röntgen at the end of the 19th century. The visualization of gas discharges, X-rays, and cathode rays represented the earliest practical uses of luminescent materials.⁵ Thereafter, the research on finding the luminescent materials to be used in various applications was stimulated.

There are several types of luminescence distinguished which depends on the excitation source—

- Chemiluminescence results from some chemical reactions. The best chemical to show chemiluminescence is luminol which, when oxidized by hydrogen peroxide in the presence of Fe^{2+} present in hemoglobin, can yield strong blue-green luminescence. This reaction is used in forensics to trace blood spots at the crime scene.
- Photoluminescence is a luminescence caused by exciting electrons to higher energy levels via photon absorption. The most common examples include organic molecules such as anthracene, quinolone, naphthalene; semiconductors such as zinc sulfide, barium sulfide; and lanthanide ions based-phosphors such as $\text{Y}_3\text{Al}_5\text{O}_{12}:\text{Nd}^{3+}$, $\text{LaF}_3:\text{Ln}^{3+}$, $\text{LaPO}_4:\text{Ln}^{3+}$, etc.
- Cathodoluminescence occurs when an electron beam impacts a luminescent material such as a phosphor. The practical use includes the viewing screen of oscilloscope tubes, televisions, and electron microscopes.
- Electroluminescence involves the generation of light in response to an electric field applied to a material. Examples include fluorescent lamps, light-emitting diodes (LEDs), etc.
- Thermoluminescence is a phenomenon where certain preirradiated crystalline materials emit light when heated. The electrons and holes are released from the traps by thermal fluctuations and then are radiatively combined. The process is used in geology,

archeology, forensics, etc.

- Radioluminescence occurs when some materials are exposed to ionizing radiation like α , β , or γ rays from a radioactive substance. Self-luminous paints used in dial marking for watches owe their behavior to radioluminescence. The paints comprise of radioactive substances such as tritium and phosphors.
- Mechanoluminescence results from organic or inorganic materials upon any mechanical stimulus such as sound, stress, and pressure. This type of luminescence can be induced by rubbing solids or separating two solids in contact.^{2,3,8}

In this thesis, photoluminescence (PL) is utilized to study the luminescent properties of lanthanide ion-doped nanomaterials. As mentioned above, photoluminescence results from the absorption of photons leading to the emission of light from electronically excited (ES) states of atoms, molecules, and ions.⁸ Photoluminescence is further divided into two phenomena based on their time delay in de-excitation: fluorescence and phosphorescence. Fluorescence is spin-allowed transitions between levels of the same multiplicity in molecules or direct recombination of electrons and holes in crystals. The characteristic emission duration is usually less than nanoseconds, $< 10^{-9}$ s. Talking about phosphorescence, earlier, this term was used in a very loose way to indicate all kinds of luminescence, particularly that of phosphorus. With the modern understanding of luminescence, the term became clear. So, it is a spin-forbidden process; i.e., electronic transitions take place between levels of different multiplicity in organic molecules. The phenomenon exhibits the decay time greater than 10^{-3} s, in some cases lasting for several hours. This is a delayed process because the radiative transitions from the ES are forbidden by the quantum selection rules.³ The situation is far more complicated in inorganic phosphors. The persistent luminescence (afterglow) in phosphors was defined by the term phosphorescence. Thus, in modern usage, if the afterglow is detectable by the human eye even after the cessation of exciting radiation is called phosphorescence, while the light emission from a substance only when it is exposed to

radiation is called fluorescence.⁴ In this thesis, the terms fluorescence and phosphorescence are not used to define photoluminescence. Since the work focuses on lanthanide ion-doped phosphors, thus the broader term “photoluminescence” or “luminescence” is used throughout. In the subsequent sections, the discovery and origin of luminescence in lanthanide ions are discussed in detail.

1.2 Discovery of lanthanides

The lanthanides are electropositive metals that intervene between *s* and *d* block elements. They have electronic configurations of $[\text{Xe}] 4f^n 5d^1 6s^2$ or $[\text{Xe}] 4f^n 6s^2$ where the inner core belongs to the xenon ion configuration. The lanthanides were earlier called rare earth elements as the scientists believed these elements were present in Earth’s crust only in minimal amounts. Thus, the term “lanthanides” was adopted, originating from the first element of this series, lanthanum. Although, most of the lanthanides are not particularly rare in Earth’s crust. Today, except for promethium, the lanthanides have abundances comparable to many other elements in the periodic table. The 15 elements in the lanthanide series, together with their chemical symbols, atomic numbers, and ionic radii, are summarized in **Table 1.1**.⁹

The lanthanides discovery extended more than 150 years of work, which began in the late 18th century. Many lanthanides occurred in the same minerals, and separation of the elements proved a challenge to the scientists due to their similar chemical properties because of similar ionic radii, same dominant oxidation state (+3), and small differences in complex formation and solubility.⁹ Nevertheless, significant efforts from scientists worldwide and the invention of the spectroscope unraveled the lanthanide ions identification.

In 1787, Arrhenius discovered an unusual mineral called ytterite in a quarry in a small village, Ytterby, Sweden. After seven years, Finnish chemist Johan Gadolin studied and concluded that ytterite contained yttria (later called yttrium), an impure form of yttrium oxide. Yttrium was isolated from this ore, although this element was not included in the

lanthanide series. The mineral ytterite was later named gadolinite in honor of Johan Gadolin in 1800. Subsequently, nine new elements were extracted from this ore: ytterbium, erbium, terbium, holmium, thulium, scandium, gadolinium, dysprosium, and lutetium.¹⁰

Talking about the discovery of the elements in the lanthanide series, cerium was the first lanthanide to be discovered in the latter half of the 18th century from the oxide ore called ceria. In 1803, Swedish chemists Wilhelm Hisinger and Jacob Berzelius and independently German chemist Klaproth analyzed the ore and concluded it to be a new element. It was named after Ceres, an asteroid between Jupiter and Mars discovered in 1801. The ore was later shown to contain oxides of lanthanum, samarium, neodymium, praseodymium, and europium. In the 19th century, most of the lanthanides were discovered from the mineral gadolinite and black rock ceria. Swedish chemist Gustav Mosander discovered and extracted various lanthanides between 1839 and 1848.

Table 1.1 The lanthanide elements with their chemical symbol and ionic radii.

Atomic No.	Name	Symbol	Ionic radii of Ln ³⁺ (in pm with 6 coordination)
57	Lanthanum	La	103
58	Cerium	Ce	102
59	Praseodymium	Pr	99
60	Neodymium	Nd	98.3
61	Promethium	Pm	97
62	Samarium	Sm	95.8
63	Europium	Eu	94.7
64	Gadolinium	Gd	93.8
65	Terbium	Tb	92.3
66	Dysprosium	Dy	91.2
67	Holmium	Ho	90.1
68	Erbium	Er	89
69	Thulium	Tm	88
70	Ytterbium	Yb	86.8
71	Lutetium	Lu	86.1

He first succeeded in extracting the element lanthanum from the black rock, which he named lanthana from the Greek word *lanthanein*, which means "to lie hidden." While analyzing an oxide formed from lanthanum in 1879, French chemist Boisbaudran (1838-1912) concluded that it contained more than one element, and one was named samarium after the mineral samarskite.¹¹

Mosander examined gadolinite in 1842 when he identified three "earths" (oxides): yttria, erbia, and terbia. Subsequently, erbium was yielded from erbia. He also identified another element in this ore, terbium; however, Swiss chemist Marignac isolated it in a purer form in 1886. While analyzing erbia in 1879, Swedish chemist Nilson observed that it contained two elements named ytterbium and scandium, Sc (Sc is not part of the lanthanides). Later, Swedish chemist, Cleve concluded that erbia contained two more elements named thulium and holmium. In 1886, Boisbaudran discovered the element in the gadolinite ore and proposed it to be called gadolinium. Then, Dysprosium was also discovered by Boisbaudran, which he isolated after 8 years of repeated separations from the mineral gadolinite; because of this, he named this new element from the Greek word *dysprositos* which means "hard to get".¹¹

Nearly at the same time, the element praseodymium was discovered, whose name was taken from Greek words *prasios* and *didymos*, meaning green twin. The element was isolated from a cerium-containing ore which also contained another element as neodymium (new twin). In 1901, French chemist Demarçay discovered another element, europium, in samarskite mineral. The last element in the series was lutetium, which was discovered by George Urbain in 1907. All the elements of the lanthanides were discovered and isolated, except the one with atomic no. 61 and thus, the search was intense in the 1920s. It was during World War II; the element promethium was found in the fission product of uranium. It was isolated by scientists at the US Atomic Energy Commission's Oak Ridge National Laboratory in Tennessee.

1.3 History of lanthanide ion luminescence and its mechanism

The optical properties of trivalent lanthanide ions (Ln^{3+}) have been studied in various domains of physics and biology. Their spectra are described by sharp emission, whose intensities may vary, but positions do not depend on the surrounding. In 1866, these unusual sharp features were first observed by Robert Bunsen on “didymium sulfate”. Then, in 1906, a detailed study was done by J. Becquerel, where he recorded the spectrum of YPO_4 , which contained traces of Ce, Th, and Er. However, the spectra’s origin remained a puzzle for a considerable time. Around 1930, Kramers, Bethe, and Becquerel proposed that the spectral lines could be because of the electronic transitions within the $4f$ levels rather than from the $4f$ shell to the $5d$ shell. The filled $5s$ and $5p$ orbitals shield the $4f$ electrons, and thus, they do not take part in the chemical bonding and have a negligible effect on the metal-to-ligand distance. Consequently, the influence of the matrix or ligands on the electronic transitions of ions is very small, which results in sharp and narrow spectra which resemble from free ions, whether in solution or in crystals.¹⁰

Although f - f transitions are intraconfigurational and thus are forbidden by the Laporte selection rule, still they occur. This puzzle was addressed by Van Vleck in 1937, who gave the quantum mechanical solution for the strength of emission lines due to f - f transitions.¹² He suggested using the simple model that due to the mixture of configurations of odd-parity, such as $4f^{n-1} 5d^1$ configurations, f - f transitions become partially allowed as electric dipole (ED) transitions. Few f - f transitions are allowed as magnetic dipole (MD) transitions with the same order of magnitude as ED transitions. McCoy provided the first spectroscopic studies of Eu^{3+} samples in solution. The relative intensities of the absorption lines of Eu^{3+} were different in different solvents, which was observed by Freed et al.¹³ Later, Weissman discovered that the Eu^{3+} -complex with specific ligands were highly luminescent under UV light.¹⁴ During those times, the optical spectra and the electronic energy levels of lanthanide ions were qualitatively understood; thus, many efforts were taken by research groups to

calculate and assign the energy levels. In the 1950s, theoretical advancement facilitated quantitative fits of the energy levels throughout the lanthanides. The sharp emission peaks in the visible region were assigned to the intraconfigurational $4f$ transitions, while the more intense and broader peaks at higher energies were ascribed to parity allowed interconfiguration $4f^n \rightarrow 4f^{n-1} 5d^1$ transitions.

In 1961, the German physicist G. H. Dieke provided the overview of the $4f^n$ energy levels of all Ln^{3+} ions in the UV, visible, and near-infrared (NIR) region.¹⁵ This diagram is applied to Ln^{3+} ions in any matrix due to the negligible effect of the host matrix on the energy levels.¹⁰ At the same time, Judd and Ofelt worked independently on the theoretical work for calculating the intensities of the induced ED transitions of the Ln^{3+} ions.^{16,17} Also, at the beginning of the 1960s, more studies on Eu^{3+} and Tb^{3+} based β -diketonate complexes appeared, which explained many concepts still used today for developing lanthanide complexes.

1.3.1 Electronic structure

Moving from La^{3+} to Lu^{3+} , the electrons in $4f$ orbitals are filled. The GS electronic configuration of the lanthanide atom possesses a Xe atom configuration with three outer electrons ($4f^n 6s^2$ or $4f^n 6s^2 5d^1$ where $n \leq 14$), with a change in the f electrons. When lanthanide atoms are ionized, $6s^2 5d^1$ electrons are removed, leaving them to be Ln^{3+} ions, which have the configuration $[\text{Xe}] 4f^n$. The trivalent state is the most stable ionization state of the lanthanides.¹⁸ The $4f$ orbitals are shielded due to the larger radial expansion of the $5s^2 5p^6$ subshells outside $4f$ shells, which act to screen the levels from the influence of the environment. The electronic configurations of Ln and Ln^{3+} ions with their ground state term symbols are mentioned in **Table 1.2**.¹¹

Table 1.2 The electronic configurations of lanthanides and lanthanide ions along with their ground state term symbols.

Atomic No.	Name, Symbol	Electronic configuration	Ln ³⁺ electronic configuration	Ground states term symbol for Ln ³⁺
58	Cerium, Ce	[Xe] 4f ¹ 5d ¹ 6s ²	[Xe] 4f ¹	² F _{5/2}
59	Praseodymium, Pr	[Xe] 4f ³ 6s ²	[Xe] 4f ²	³ H ₄
60	Neodymium, Nd	[Xe] 4f ⁴ 6s ²	[Xe] 4f ³	⁴ I _{9/2}
61	Promethium, Pm	[Xe] 4f ⁵ 6s ²	[Xe] 4f ⁴	⁵ I ₄
62	Samarium, Sm	[Xe] 4f ⁶ 6s ²	[Xe] 4f ⁵	⁶ H _{5/2}
63	Europium, Eu	[Xe] 4f ⁷ 6s ²	[Xe] 4f ⁶	⁷ F ₀
64	Gadolinium, Gd	[Xe] 4f ⁷ 5d ¹ 6s ²	[Xe] 4f ⁷	⁸ S _{7/2}
65	Terbium, Tb	[Xe] 4f ⁹ 6s ²	[Xe] 4f ⁸	⁷ F ₆
66	Dysprosium, Dy	[Xe] 4f ¹⁰ 6s ²	[Xe] 4f ⁹	⁶ H _{15/2}
67	Holmium, Ho	[Xe] 4f ¹¹ 6s ²	[Xe] 4f ¹⁰	⁵ I ₈
68	Erbium, Er	[Xe] 4f ¹² 6s ²	[Xe] 4f ¹¹	⁴ I _{15/2}
69	Thulium, Tm	[Xe] 4f ¹³ 6s ²	[Xe] 4f ¹²	³ H ₆
70	Ytterbium, Yb	[Xe] 4f ¹⁴ 6s ²	[Xe] 4f ¹³	² F _{7/2}
71	Lutetium, Lu	[Xe] 4f ¹⁴ 5d ¹ 6s ²	[Xe] 4f ¹⁴	

1.3.2 Energy levels

Due to the riveting optical properties, Ln³⁺ ions have grabbed the attention of the research world for more than 150 years. As mentioned earlier, the filled 5s² and 5p⁶ shells shield the 4f electrons of the Ln³⁺ ions, resulting in weak surrounding interaction and electron-phonon coupling interactions. As a result, the narrow and sharp 4f-4f transition peaks are exhibited by Ln³⁺ ions. Furthermore, Ln³⁺ ions have the ladder-like structure of the energy levels allowing for emission in the UV, visible, and NIR regions, with relatively long lifetimes (usually from μs to ms) of these levels. These versatile properties of Ln³⁺ ions allow them to be utilized in diverse fields such as lasing, imaging, and so forth.¹⁹

The emission peaks or positions of Ln³⁺ ions are not affected by the external environment; thus, they can be embedded into various matrices. The spectroscopic

properties of Ln^{3+} ions are very similar to their corresponding element as the ligand field of the host has a feeble effect on their electronic cloud. Hence, for a given ion in different host matrices, the $4f$ - $4f$ transition energies are relatively the same. The existence of different energy levels in Ln^{3+} ions result from several interactions within the ion. The degeneracy of the free Ln^{3+} ion levels is removed by Coulombic, spin-orbit, and crystal field interactions when it is doped in a matrix. The resultant splitting of the $4f^n$ configuration of Eu^{3+} ions is shown in **Fig. 1.1**. The electron-electron repulsions represented by Coulombic interactions are the largest among the $4f$ electronic interactions, which yields ^{2S+1}L levels with a separation of typically 10^4 cm^{-1} . Next, the interactions of the electronic spin with the magnetic field created by the electronic motion causes the spin-orbit interactions, which split each ^{2S+1}L term into $(2J+1)$ states, denoted by $^{(2S+1)}L_J$, where $2S+1$ is the total spin multiplicity, L the total orbital angular momentum, and J the total angular momentum of the $4f$ electrons.

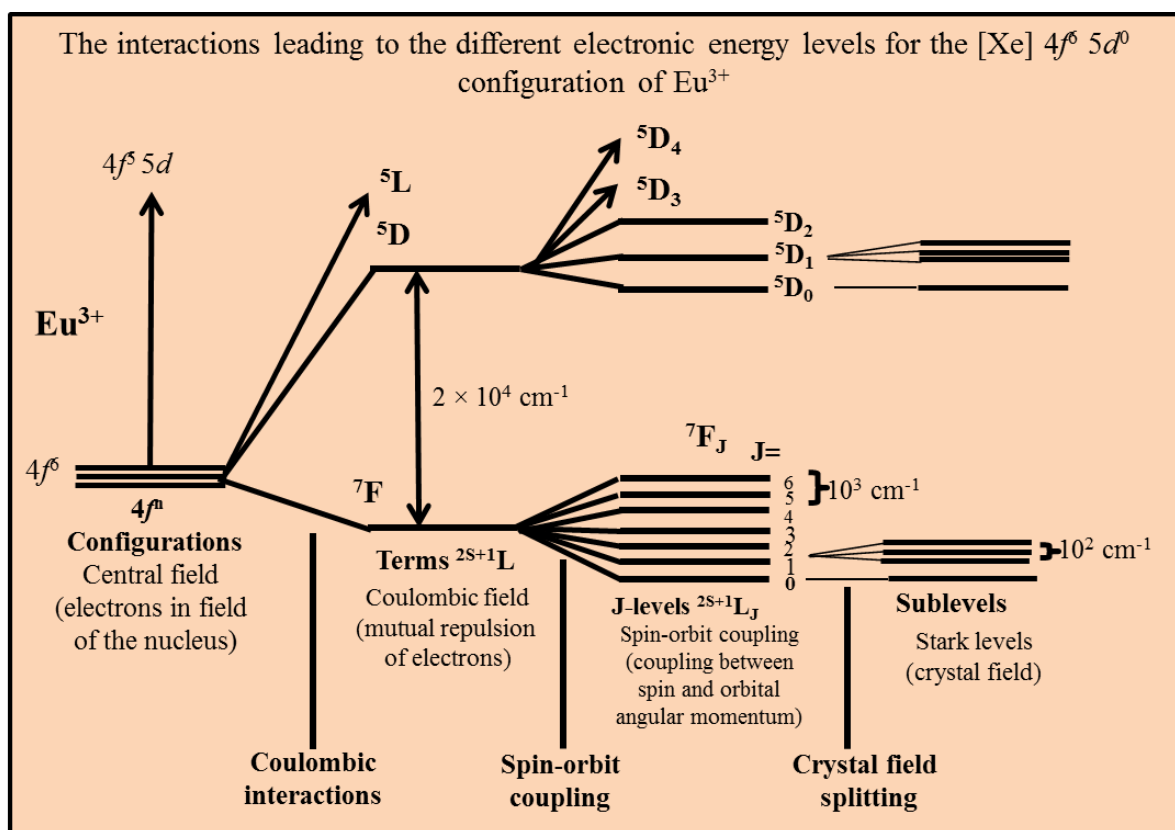


Figure 1.1 The splitting of the $4f^n$ configuration of Eu^{3+} ions.

The splitting of $(^{2S+1})L_J$ levels is in the order of 10^3 cm^{-1} , which is relatively large in Ln^{3+} ions due to their heavy nuclei. Lastly, the $4f$ electrons interactions with the crystal field of the surroundings, such as a ligand or crystal, result in a Stark splitting. The term $(^{2S+1})L_J$ is further split into $(2J+1)$ terms if $4f$ electrons are even or $(J+1/2)$ terms if $4f$ electrons are odd, denoted by $(^{2S+1})L_{J,\mu}$. Thus, the term μ in the expression $(^{2S+1})L_{J,\mu}$ denote the splitting of $(^{2S+1})L_J$ term due to the crystal field of ligands. The Stark splitting is typically in the order of 10^2 cm^{-1} and appears as a fine structure on the individual peaks, which depends on the spectrometer resolution. Many times, the fine structures are ignored, although they may be utilized to understand the symmetry of the coordinating environment.

As mentioned in the section above, the calculation of the energy levels of the $4f^n$ configurations of Ln^{3+} ions was first carried out by Dieke and co-workers, and the data was summarized in his book, which was published posthumously in 1968.²⁰ The “Dieke diagram” is referred to the energy level diagram for Ln^{3+} ions. The results presented became the reference to approximate the energy levels of the $(^{2S+1})L_J$ multiplet. Detailed work by Carnall et al. was the study of the spectra of Ln^{3+} ions in LaF_3 .²¹ In 1989, the report by Carnall et al. provided a thorough study of the energy levels of the entire series of Ln^{3+} in a host lattice, as shown in **Fig. 1.2**.

1.3.3 Radiative transitions

The three types of electronic transitions which involve Ln^{3+} ions are sharp $4f-4f$ transitions, broad $4f-5d$ transitions, and broad charge-transfer transitions.¹⁸

The energy from the incoming photon is transferred to an electron, which then reaches a higher energy state. The excitation is promoted by operators linked to the nature of light by the odd-parity ED operator, the even-parity MD, and electric quadrupole (EQ) operators. Laporte selection rule states that the energy levels with the same parity are not connected by ED transitions; as a result, $f-f$ transitions are not allowed by the ED mechanism. However, as mentioned earlier, when Ln^{3+} ion is surrounded by crystal or ligand, the opposite parity

electronic states mix with $4f$ wavefunctions due to the non-centrosymmetric interactions of the field. This slightly relaxes the selection rules, and the transitions become partially allowed to yield an induced ED transition. In Ln^{3+} ions, even-parity MD transitions are allowed with weak intensities; however, their intensities often are of the same order of magnitude as induced ED transitions. Quadrupolar transitions (EQ) are also parity-allowed transitions with much weaker intensities than MD transitions. So far, the quadrupole transitions have no experimental evidence for their occurrence in Ln^{3+} .

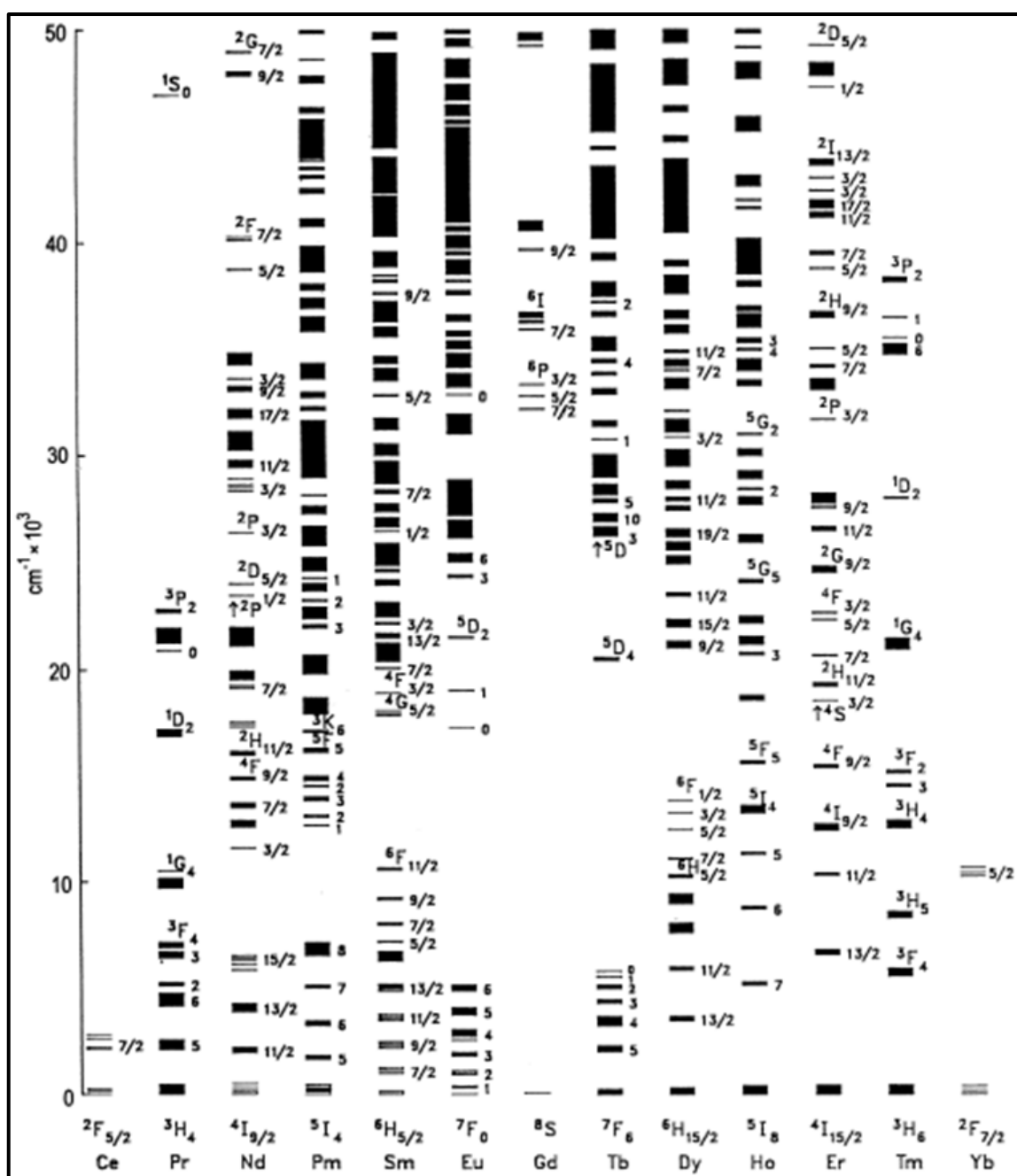


Figure 1.2 The energy levels $4f^n$ configurations of lanthanide ions (Ln^{3+}).²¹

However, some hypersensitive transitions are considered to be induced EQ transitions or pseudo-quadrupolar transitions as they obey the ED selection rules.¹⁸ It should be noted that the terms “forbidden” and “allowed” transitions are not proper as the selection rules are derived under several hypotheses. In other words, an allowed transition has a high probability of occurring, whereas the forbidden transition has a low probability.

- ***Induced ED f-f transitions: Judd-Ofelt theory***

In 1962, Judd and Ofelt independently reported their studies on the theory called Judd-Ofelt (JO) theory for the $4f-4f$ transition intensities for Ln^{3+} ions both in solutions and solids.^{16,17} It only considers intraconfigurational transitions, so, $4f^n \rightarrow 4f^{n-1} 5d^1$ interconfigurational interactions are neglected. The probability of radiative transitions and lifetimes of ES can be calculated using JO analysis.¹⁸ The basic idea in this theory is that $f-f$ transitions are allowed due to the mixture of odd-parity configurations, such as $4f^{n-1} 5d$ or $4f^{n-1} g$ states to $4f^n$ states in the presence of odd-parity crystal field. In general, the JO theory can give good agreement between experimental and calculated oscillator strengths. However, this theory has not been used to give an explanation for the hypersensitive transitions.

- ***f-d transitions and charge-transfer spectra***

The transition of a $4f$ electron into a $5d$ subshell is a parity-allowed transition that is comparatively broader than the $f-f$ transition and occurs at higher energy. Their spectral peak positions depend primarily on the Ln surrounding as their $5d$ orbitals are expanded outwards, interacting directly with the ligand orbitals. The $4f-5d$ transitions are commonly observed in Pr^{3+} , Ce^{3+} , and Tb^{3+} ions.

Ligand-to-metal, LMCT, and metal-to-ligand, MLCT charge-transfer transitions, are allowed transitions with high energies in the case of Ln^{3+} ions. These are intense, broad and generally appear in the UV region at nearly 250 nm. The LMCT transitions are widespread for d -elements, although are commonly observed in Ln^{3+} ions as well. The ions Eu^{3+} , Yb^{3+} ,

Sm^{3+} , and Tm^{3+} show LMCT in ordinary solvents.

1.4 Different types of lanthanide ion-based materials

The compelling interest in lanthanide ion-based materials is stimulated due to the continuous demand for advanced luminescent materials. The research for these materials is constantly and rapidly expanding, connecting diverse research communities with their specific subjects and approaches. Lanthanide ion-activated compounds include lanthanide complexes, glasses, semiconductors, inorganic phosphors, ceramics, polymers, metal-organic frameworks (MOFs), etc.

1.4.1 Lanthanide complexes

For many years, most of the studies of lanthanide ions were limited to molecular lanthanide complexes. The Ln^{3+} ions complexes are formed by coordinating Ln^{3+} ions with organic molecules, as shown in **Fig. 1.3**. The lanthanide complexes were developed to protect the luminescence of Ln^{3+} ions from quenching due to the presence of molecular vibrations, hydroxide ions, water molecules, etc. These complexes also increase the overall light absorption of the Ln^{3+} ions.²² Ln^{3+} ions possess large ionic radii and a large range of coordination numbers (3-12), with 8 and 9 as most frequently observed. Thus, they strongly bind to the ligands, which help minimize the nonradiative decay from Ln^{3+} ions. The lanthanide complexes can be formed with many types of ligands, such as calixarenes, podands, cryptates, β -diketones, terphenyl ligands, heteroaryl ligands, carboxylic acid derivatives, pyridines, etc.

It was S. I. Weissman who discovered the metal-centered luminescence in complexes of europium in 1942 for the first time.¹⁴ He observed that the strong emission from Ln^{3+} ions appeared when the organic ligand was excited in its absorption band. In this process, firstly, the organic ligands absorbed the incident energy, and then this excitation energy was transferred to lanthanide ions by an intramolecular energy transfer mechanism. This phenomenon was described for Eu^{3+} complexes of salicylaldehyde, dibenzoyl methane,

meta-nitrobenzoyl acetone, and benzoyl acetone. However, it was in the 1960s that the Eu^{3+} and Tb^{3+} -based complexes were explored in detail.^{23,24} They possessed long luminescent lifetimes in comparison to conventional organic molecules, which exhibit lifetimes in ns (nanoseconds). These properties of lanthanide complexes make them relevant as imaging agents.²⁵ They also have shown many advantages for the past 30 years in organic light-emitting diodes (OLEDs), optical fibers, lasers, (Fluorescence resonance energy transfer) FRET-based sensing, time-resolved fluoroimmuno assays, etc.

Furthermore, based on the published reports, Eu^{3+} and Tb^{3+} -based complexes are attractive as visible emitters in OLEDs, while Nd^{3+} and Yb^{3+} -based complexes are more promising NIR emitters.²⁷

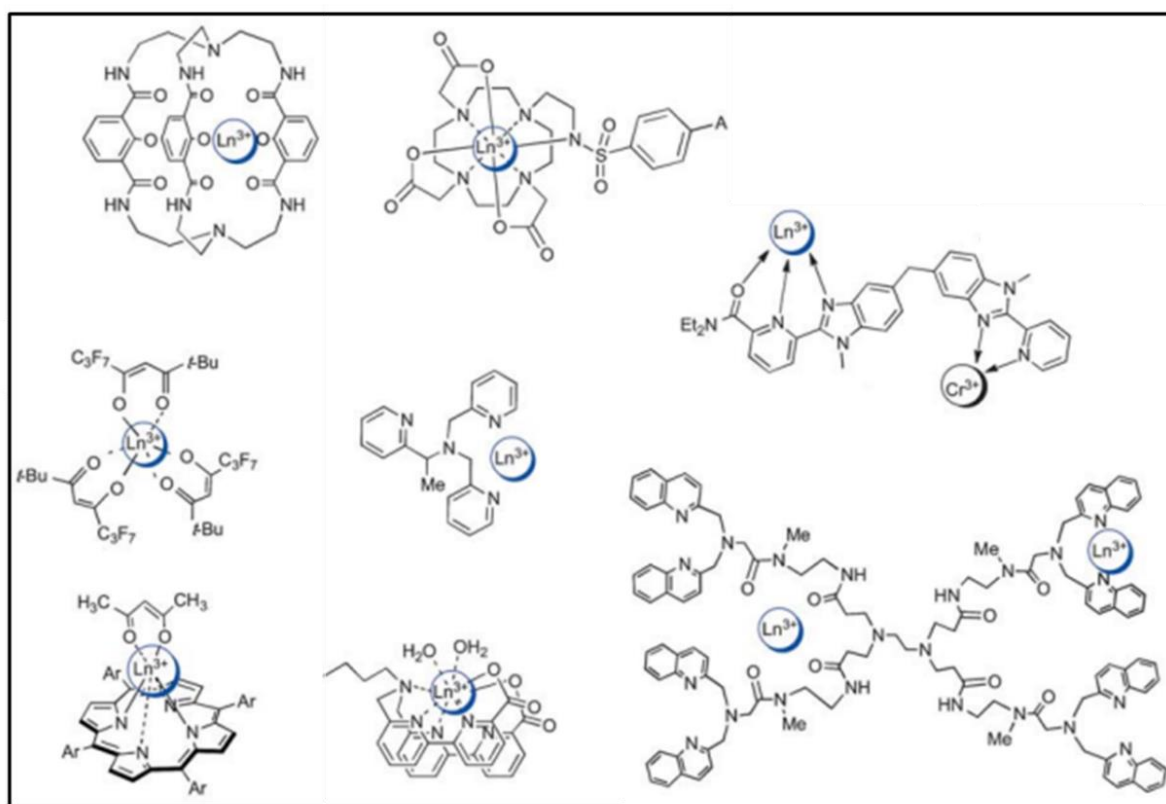


Figure 1.3 The structures of lanthanide complexes formed with various ligands.²⁶

1.4.2 Lanthanide ion-doped glasses

Glasses play a significant role in optoelectronics and photonics as they have transparency in the spectral region required in laser and optical amplifier applications.²⁸

They have applications as both active (switches, amplifiers) and passive devices (fibers, lenses). Lanthanide ions-doped glasses are of extreme importance due to their intriguing optical properties. Nearly all glass lasers use Ln as the active ions because their diverse energy level of $4f$ shells are suitable for laser action. Lanthanide ions-doped glasses offer a variety of applications such as sensor devices, environmental monitoring, fluorescent display devices, and solid-state lighting applications, etc.²⁹ When compared to crystals, more amount of Ln^{3+} can be integrated with glasses either through doping or by being an integral part of their composition. The ES lifetimes of Ln^{3+} ions in glasses can be in the range of milliseconds and can have high luminescence efficiencies. The host glass material should have a high refractive index with good thermal and chemical stability to be useful in industries. It was observed quite early that the sharpness of the optical lines of Ln^{3+} vanishes in glasses, and the peaks are inhomogeneously broadened. Due to this lower symmetry, induced ED transitions become feasible, and thus, luminescence is observed in Ln^{3+} -doped glasses. The oxide glasses are the most preferred host materials for Ln^{3+} ions as they are chemically and thermally stable and optically transparent at the lasing wavelengths. Various lanthanide ions like Eu^{3+} , Yb^{3+} , Tb^{3+} , Pr^{3+} , Tm^{3+} , Nd^{3+} , Sm^{3+} etc. have been doped in glass matrices such as in oxides, fluorides, phosphates, fluorophosphates, zinc tellurites, zinc borates, aluminates,³⁰⁻³³ and so forth; some of the examples include $\text{Eu}^{3+}, \text{Dy}^{3+}$: SrAl_2O_4 glass,³⁴ Tb^{3+} : oxynitride glass,³⁵ Eu^{3+} and Tb^{3+} co-doped metaphosphate glass,³⁶ Tb^{3+} and Dy^{3+} doped borosilicate glass,³⁷ Tb^{3+} and Dy^{3+} co-doped borate glass,³⁸ $\text{Er}^{3+}, \text{Yb}^{3+}$: TeO_2 - WO_3 glasses,³⁹ etc.

1.4.3 Inorganic crystals/phosphors

Historically, solid materials which emit light upon the exposure of radiation or an electron beam were termed “**phosphors**”. Ln^{3+} -doped phosphors comprise an inorganic host and Ln^{3+} ions as emitters incorporated in the host lattice. Intensive studies on the luminescence characteristics of phosphors have been started since 1950. Barium sulfide was

probably the first phosphor synthesized with very low luminescence efficiency. It was observed that the sulfide phosphors do not emit in a chemically pure state; instead, they emit when small quantities of an activator ion are present. The localized energy levels are generated in the forbidden band when an activator ion is incorporated into a crystalline material. Thus, characteristic and non-characteristic luminescence are differentiated depending on the involved energy levels in the process. In the former process, the energy levels of activator atoms are involved. In this type, the activator atom absorbs the incident energy, and then electronic transition occurs from one level to another. While in the latter case, a charge-transfer process takes place through the lattice involving the host energy levels modified because of activator atoms. Since the activator ions are embedded in the host, which forms luminescent centers, thus, their luminescent properties are strongly dependent on the symmetry of neighboring ions present. This is proved by the shift in peak positions in some phosphors activated with Ln^{3+} ions.

Earlier, phosphors were only used for display and lasers applications. During the last two decades, the introduction of lanthanide ions-doped phosphors in fluorescent lamps has improved the color rendering index and light output drastically.⁴⁰ Till 1990, bulk or single crystals of phosphor material were explored; however, with the advancement in nanotechnology after 1990, nanophosphors were explored, forming different shapes and sizes. Later, applications of lanthanide ions-based nanoparticles (NPs) were primarily investigated in the medical sciences, such as bioimaging, biosensing, biomedical diagnostics, etc.² A variety of host matrices with different combinations of Ln^{3+} ions have been presented by different research groups, such as $\text{NaYF}_4: \text{Gd}, \text{Tb}$,⁴¹ $\text{NaGdF}_4: \text{Yb}, \text{Er}$,⁴² $\text{LaF}_3: \text{Yb}, \text{Ho}$,⁴³ $\text{GdPO}_4: \text{Nd}$,⁴⁴ $\text{Y}_3\text{Al}_5\text{O}_{12}: \text{Ce}$,⁴⁵ etc.

1.4.4 Polymers

Integration of inorganic and organic constituents into the same material can lead to a range of advanced materials with superior properties. The incorporation of polymers makes

the flexible matrix for Ln^{3+} ion-doped fibers and films. The ease of polymer processing and film-forming with Ln^{3+} ions was demonstrated in various reports.⁴⁶ In a study by Wong et al., Er^{3+} and Yb^{3+} co-doped in epoxy Novolak resin polymer was studied for applications in an optical amplifier.⁴⁷ To enhance the optical properties, lanthanide complexes are also incorporated into organic polymers such as polymethylmethacrylate (PMMA).^{48,49} In one approach, narrow bandwidth emitting lanthanide ion-doped OLED was fabricated using the poly(N-vinylcarbazole) host matrix doped with Eu^{3+} -based β -diketonate complex.⁵⁰ In another study, PMMA-based thin films of Eu^{3+} and Tb^{3+} β -diketonate complexes were fabricated, and their photoluminescence studies were done. The system was shown to have improved photostability.⁵¹

Lanthanide ion-doped phosphors were also incorporated in the polymer matrix for various applications. In a study by Wang and group,⁵² oleic acid capped LaF_3 : Yb,Er NPs were prepared, which were dispersed in PMMA matrix to be utilized as a promising material for optical waveguide amplifiers. In another work by Tan et al., upconverting nanoparticles (UCNPs) and polyvinyl alcohol composite films were fabricated using an aqueous solution casting method. The as-prepared films were utilized for anti-counterfeiting applications.⁵³ A range of other materials with polymer for different applications have been reported by various research groups, for e.g., LiYF_4 : Eu,Ce,Tb nanophosphors with poly(dimethylsiloxane) for display devices,⁵⁴ NaYF_4 : Yb,Er with PMMA,⁵⁵ $\text{BaGd}_2\text{ZnO}_5$: Er with PMMA,⁵⁶ and so forth.

1.5 Energy transfer mechanism

Energy levels of lanthanide ions provide various energy transfer potentials to the materials. Mainly, three energy transfer mechanisms are downshifting (DS); quantum cutting (QC), also known as downconversion (DC), and quantum splitting (QS); and upconversion (UC) emissions, as shown in **Fig 1.4**. When one photon is emitted per absorbed photon, the process is known as downshifting emission, restricting the quantum

efficiency to less than 100 %.^{57,58} There are numerous studies reported for lanthanide ions to show DS mechanism for applications in bioimaging,⁵⁹ temperature sensing,⁶⁰ anticounterfeiting,⁶¹ etc.

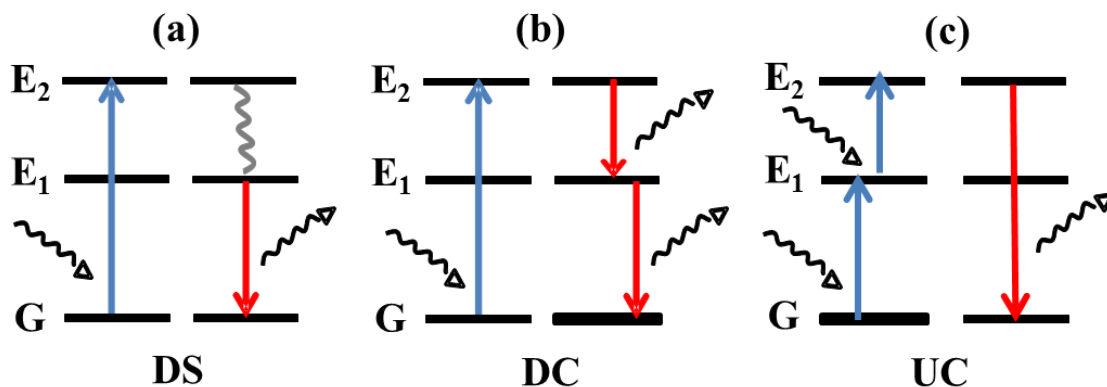


Figure 1.4 The schematic representation of the mechanism in lanthanide ion-doped phosphors showing (a) downshifting (DS), (b) downconversion (DC), and (c) upconversion (UC) luminescence.

- **Downconversion process**

Luminescent materials whose quantum efficiency is greater than unity demonstrate a downconversion (DC) or quantum cutting (QC) mechanism and offer the prospect of providing improved energy efficiency in many applications. DC or QC phosphors generate two or more lower energy photons for every higher energy photon, with quantum efficiency well over 100 %.⁶² DC was first theoretically suggested by Dexter⁶³ in 1953 and experimentally reported in $\text{YF}_3: \text{Pr}^{3+}$ in which two visible photons were generated from one UV photon.⁶⁴ In this case, a quantum yield of 140 % was achieved at 185 nm excitation. Lanthanide ions such as Pr^{3+} , Gd^{3+} , Tm^{3+} , Ho^{3+} , and Er^{3+} are capable of cascade emission; therefore, they can show DC even when they are singly doped.

Recent progress has been made to the dual ion showing DC mechanism, for e.g., Gd^{3+} - Eu^{3+} , and Gd^{3+} - Tb^{3+} , Pr^{3+} - Er^{3+} , Pr^{3+} - Eu^{3+} , Pr^{3+} - Cr^{3+} , Pr^{3+} - Mn^{2+} dual ion combination. Eu^{3+} doped LiGdF_4 was employed by Meijerink et al. using two Ln^{3+} ions to cut vacuum UV photon into two visible photons.⁶⁵ An efficient two-step energy transfer from Gd^{3+} to Eu^{3+} took place with nearly 200 % quantum efficiency. In another study, BaF_2 with a very high

band gap of 10.9 eV, doped with Gd^{3+} and Eu^{3+} ions, showed DC mechanism with quantum efficiency up to 194 %.⁶⁶ The experimental evidence for the cooperative energy transfer from Tb^{3+} ion to two Yb^{3+} ions in $(\text{Y},\text{Yb})\text{PO}_4$: Tb^{3+} phosphor was reported by Vergeer et al.⁶⁷ A quantum efficiency of 188 % was observed in this report. There have been many reports in the literature using Ln^{3+} ions as spectral converters for applications in solar cells.⁶⁸⁻⁷⁰

The concept of DC is depicted in **Fig 1.5**, with two types of ions exhibiting hypothetical energy levels. Ion 1 is a type of ion in which the emission can take place from a high energy level, while in the case of ion 2 energy transfer process takes place from ion 1. Evaluation of the energy levels from the Dieke diagram reveals that possible type 1 ions are Pr^{3+} , Tb^{3+} , Nd^{3+} , Er^{3+} , Ho^{3+} , and Tm^{3+} . As shown in **Fig. 1.5a** for a single ion, the DC process occurs by the sequential emission of two visible photons. When the ion is excited to the higher metastable level with only one photon, in this case, level E_2 , then two visible photons are emitted sequentially from levels E_2 and E_1 . In the schematic, the solid blue line shows the excitation while the solid red lines depict the emission in the visible region.

In the second mechanism demonstrated in **Fig 1.5b**, a two-step energy transfer process occurs between two types of ions to yield emission. Firstly, when the excitation energy from the source is matched with the energy of the transition from level G to the excited energy level E_2 , then the energy is absorbed, and the transition takes place to E_2 level. Then, in the first step of the energy transfer process, a part of the energy is transferred to ion 2 by cross-relaxation, as depicted in the purple dashed line. Ion 2 then comes back to the G state by emitting one photon of visible light, while ion 1 is still at E_1 level; and thus, can transfer its remaining energy to the second ion of the type 2 ion as shown in the green dashed line. Consequently, this ion also emits a photon in the visible region of the spectrum, as shown in solid red lines. In the remaining two mechanisms (**Fig. 1.5c,d**), only one energy transfer step is involved, as depicted in dotted green line, which is sufficient to obtain DC mechanism.⁶⁵

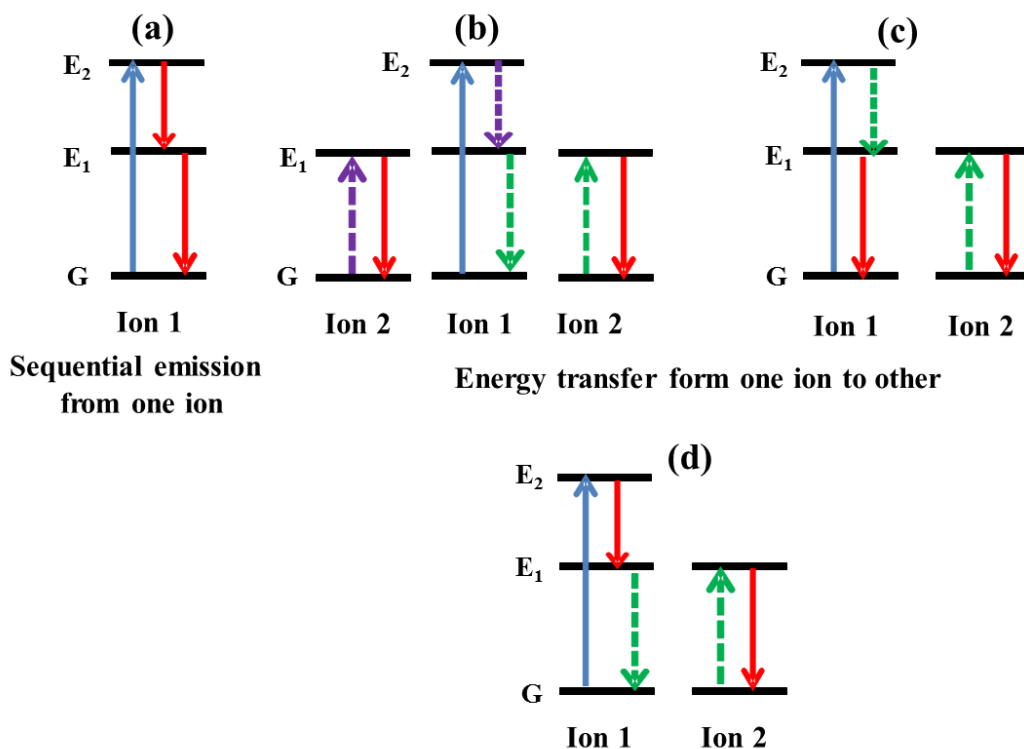


Figure 1.5 The schematic representation related to the energy transfer mechanism in the downconversion process; (a) emission involving only one ion, (b-d) emission process involving two ions where energy transfer from one to another takes place.

- **Upconversion process**

Upconversion is a process where one photon with higher energy is converted from two photons. Generally, a combination of two ions such as $\text{Yb}^{3+}\text{-Tm}^{3+}/\text{Er}^{3+}/\text{Ho}^{3+}$ shows an upconversion mechanism and has been studied extensively.⁷¹ The upconversion mechanism has been discussed in detail in the following section.

Low energy light can be converted into higher energy photons via different mechanisms. Second-harmonic generation (SHG) and two-photon absorption (TPA) are well-known mechanisms to perform anti-Stokes emission, as shown in **Fig 1.6**. The major constraints associated with these two methods are the use of expensive pulsed lasers (usually a femtosecond laser). Only high-density photon flux can be converted into higher energy photons in these processes, as they involve the non-stationary quantum states. At the same time, photon upconversion (UC) is the conversion of NIR light to visible light, which is a promising alternative method performed by incoherent low power excitation sources, such

as continuous-wave lasers. Moreover, the UC process takes place through physically existing intermediary ES, so it allows efficient conversion without the need for coherent light sources.^{72,73}

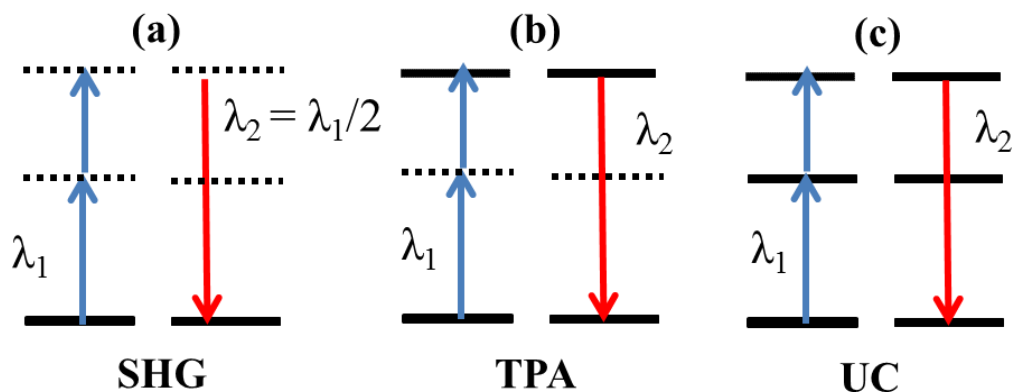


Figure 1.6 The schematic representation showing (a) second harmonic generation (SHG), (b) two-photon absorption (TPA), and (c) upconversion (UC) processes.

To date, two processes are explained for achieving UC emission, namely triplet-triplet annihilation (TTA)-based UC, which relies on the triplet states of organic chromophores and UC luminescence from Ln^{3+} ions such as Er^{3+} , Tm^{3+} , Ho^{3+} , etc., having abundant energy levels required for excitation/emission studies. The photon UC on Ln^{3+} ions was first reported by Auzel and co-workers in 1966 from Er^{3+} , Yb^{3+} in a glass matrix. The detailed UC mechanism in the lanthanide ions is discussed below.

As already explained, the UC mechanism is a nonlinear optical process that converts two or more lower-energy photons to a higher-energy photon. It is an anti-Stokes process, which was first predicted by Bloembergen in 1959⁷⁴ and noticed independently by Auzel, Feofilov and Ovsyankin in 1966.⁷⁵ Several mechanisms have been identified in the UC process, including excited-state absorption (ESA), energy transfer upconversion (ETU), photon avalanche (PA), and energy migration-mediated upconversion (EMU). UC emissions are generated by Ln^{3+} ions, which have long-lived and metastable intermediate energy levels giving the possibility for various energy transfer pathways. To facilitate the sequential photon adsorption and energy transfer process, the energy differences between three or more

subsequent energy levels should be close enough. For this purpose, Er^{3+} , Ho^{3+} , and Tm^{3+} ions are the most commonly used activators, exhibiting ladder-like energy levels facilitating the successive absorption of photon and energy transfer in the process. In order to generate enhanced UC emission efficiency, Yb^{3+} ions exhibiting sufficient absorption cross-section at 980 nm compared to other lanthanide ions are used along with activators. Also, the energy separation between the GS and the ES of Yb^{3+} is resonant with the energy differences in $\text{Er}^{3+}/\text{Ho}^{3+}/\text{Tm}^{3+}$ ions, allowing efficient resonant energy transfer from Yb^{3+} to these activator ions. All the mechanisms of the UC process are discussed thoroughly in the section below.

Excited-state absorption (ESA) is for singly-doped phosphors involving successive absorption of two photons. When the incident energy is matched with the transition from G level to the metastable E_1 level, as shown in **Fig. 1.7a**, then the system absorbs another photon in E_1 level with an energy matched with the transition from this state to E_2 . Consequently, the emission will take place from the E_2 level to the G level. A large absorption cross-section of the Ln^{3+} ion and high pump power density facilitates ESA processes. In order to get high efficiency, a low active concentration of the ions is required to avoid cross-relaxation energy losses between the luminescent centers.^{62,73}

Energy transfer processes (ETU) involve two ions, sensitizer and activator. It employs sequential absorption of two photons to populate the ES of the ions; the emission is realized via energy transfer between two neighboring ions rather than sequential absorption in a single ion. In the first step, the two ions are excited to their respective metastable levels via the absorption of photons. This step is followed by a nonradiative energy transfer to the activator from the sensitizer so that the activator ion is promoted to E_2 level. The sensitizer ion simultaneously relaxes to GS, which is then followed by the emission of light from the E_2 level of the activator. The ETU process takes advantage of the large absorption cross-section of a sensitizer.

Four types of ETU processes are discussed schematically in **Fig. 1.7(b-e)**, including energy transfer (ET) followed by ESA, successive energy transfer, cross-relaxation, and cooperative sensitization upconversion.^{73,76} In energy transfer followed by ESA, firstly sensitizer absorbs one photon and goes from G level to E_1 level, it then successively transfers its energy to the activator, promoting the activator to the metastable E_1 level. The sensitizer returns to G level, and finally, ESA takes place to generate the E_2 state from which the emission takes place. If only the sensitizer ion absorbs photons, then a successive energy-transfer process occurs. The activator is promoted to its E_1 and E_2 levels by two processes of energy transfer giving rise to UC emission (**Fig. 1.7c**).⁶²

Cross-relaxation (CR) upconversion takes place from ion-ion interactions due to the similar nature of sensitizer and activator ion. Here, in the first step, both the sensitizer and the activator absorb the incoming energy. Then, an energy transfer process excites the activator to its E_2 level while the sensitizer comes back to G level. CR is the main reason for the “concentration quenching mechanism” of emission. The last ETU process, **cooperative sensitization (CSU) (Fig. 1.7e)**, involves a cooperative effect as more than one center takes part in the process. In this process, one photon each is absorbed by ions 1 and 2 to generate their respective excited levels. The contained energy is then cooperatively transferred to ion 3, which is elevated to the higher ES. The excited ion 3 can relax back to its GS by emitting a photon of higher energy. The CSU efficiency is generally lower than ETU and ESA process, as it involves the quasi-virtual energy levels during the transitions, since the activator ions do not have sufficient long-lived intermediate energy levels compatible with the sensitizers.

Cooperative sensitization-based studies have focused mainly on bulk materials, glasses, and polymers. A few reports have proven the feasibility of this process in nanomaterials, for e.g., $\text{Yb}^{3+}/\text{Pr}^{3+}$, $\text{Yb}^{3+}/\text{Tb}^{3+}$, and $\text{Yb}^{3+}/\text{Eu}^{3+}$ ion pairs.⁶²

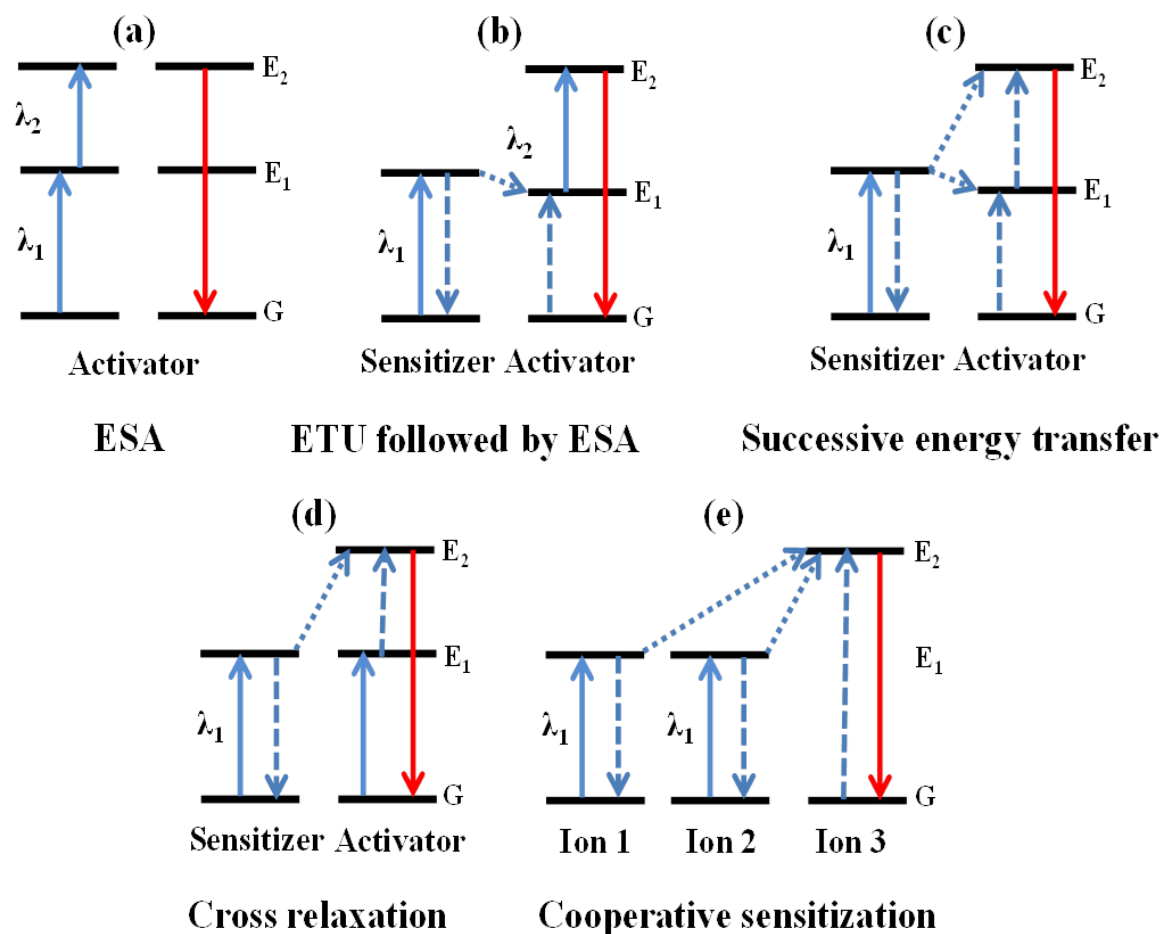


Figure 1.7 The schematic representation related to the energy transfer mechanism in the upconversion process; (a) excited state absorption, ESA, (b) energy transfer followed by ESA, (c) successive energy transfer, (d) cross-relaxation upconversion, (CR), and (e) cooperative sensitization, (CSU).

In conclusion, the average distance between the neighboring sensitizer-activator ions decides the UC efficiency of an ETU process, which is determined by the concentrations of dopant ions. Generally, Yb^{3+} ions are co-doped into the host lattice in high concentrations (below 30 mol%) without evoking deleterious cross-relaxations. Also, the content of activators is kept below 10 mol% to avoid a quenching effect.⁷³

Photon avalanche (PA) generates the UC process above a certain threshold of excitation power, increasing the photoluminescence intensity by orders of magnitude. This mechanism was explained in Pr^{3+} -based IR quantum counter by Chivian et al. in 1979 for the first time.⁷⁷ The energy of the incoming photon does not match with the energy gap (**Fig. 1.8a**) between the GS and intermediate levels. Initially, the ion 2 is excited to populate

its E_1 level by non-resonant weak absorption, and then the ESA process excites ion 2 to the emitting E_2 level to start the looping process. Thereafter, cross-relaxation process of E_2 (ion2) + G (ion 1) \rightarrow E_1 (ion 2) + E_1 (ion 1) between ion 1 and ion 2 occurs. Lastly, ion 2 populates its E_1 level after getting energy from ion 1, which then completes the loop. The net effect is that one ion at the E_1 level generates two ions at this state. The repetitions of such processes exponentially populate the metastable levels above the excitation threshold. In this way, two ions at the E_1 state will generate four; four will generate eight, evoking an avalanche effect for the PA process.⁷¹ This process relies on the power density of the pump photons and cross-relaxation within the doped ions. Due to the certain number of required cycles of cross-relaxation and ESA processes, the looping process produces feedback that delays the response to pumps limiting their extensive applications.⁷⁸

Liu and his group suggested an energy transfer pathway, **energy migration-mediated upconversion (EMU)**, as shown in **Fig. 1.8b**, to enhance the efficiency of UC emissions. This process was first suggested in NaGdF₄: Yb,Tm@NaGdF₄: Ln (Ln = Sm, Tb, Eu, and Dy) core-shell nanostructures. In this process, four types of luminescent centers (sensitizer (type I), an accumulator (type II), a migrator (type III), and an activator (type IV)) are added into different layers with defined concentrations. In the first step of the process, the sensitizer extracts incident energy promoting the neighboring accumulator ion to its ES via an ETU process. This absorbed energy migrates from the accumulator ion to the migrator, followed by random energy transfer through the interface of the core-shell. Finally, the energy is trapped by the neighboring activator ion.⁷⁹ To minimize the cross-relaxation between the ions, the sensitizer/accumulator and the activator are confined in different layers of the core-shell structure, while a migrator is needed at the interface of the core-shell to bridge the energy transfer from the accumulator to the activator ion. The core-shell layout allows us to modulate the composition and concentration of activator ions, minimizing luminescence quenching. Therefore, multicolor UC luminescence from the activators

without long-lived intermediate energy levels can be realized. This widens the applications of Ln^{3+} ion-doped UCNPs. The UC process is fascinating as low-energy NIR can penetrate tissues and is non-phototoxic and non-cytotoxic, which gives the opportunity to be used in biomedical sciences. It should be mentioned that the commonly used excitation wavelength is 980 nm due to the high absorption coefficient of transitions of Yb^{3+} in this region.¹⁹

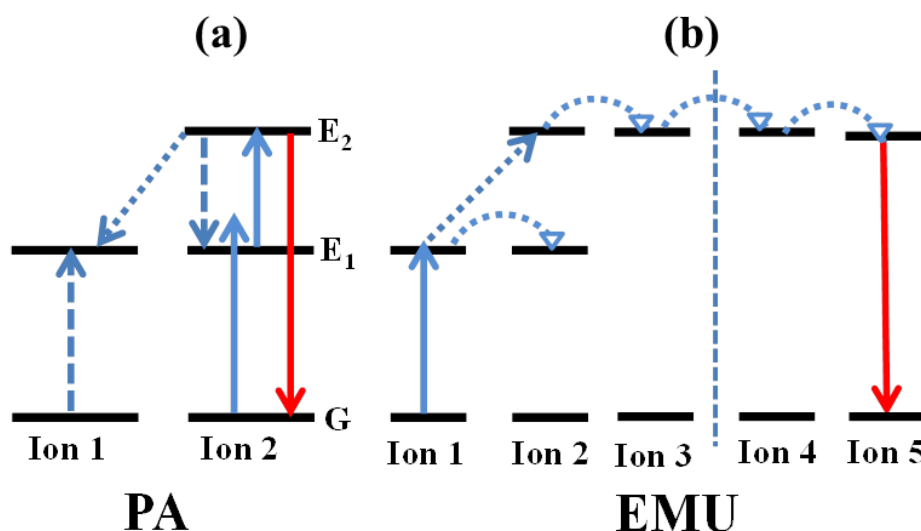


Figure 1.8 The schematic demonstrates (a) photon avalanche (PA) and (b) energy migration-mediated upconversion (EMU) processes.

1.6 Phosphors: concept of host and dopant

A crystalline host and a dopant make an inorganic phosphor. The dopant provides luminescent centers, while the host matrix provides a lattice to bring these centers into optimal positions. Lanthanide ion-doped phosphors can be prepared by doping Ln^{3+} ions into numerous host matrices, such as metal oxides, aluminates, vanadates, fluorides, nitrides, sulfides, phosphates, etc. To obtain efficient luminescence, the selection of the right dopant combination and host material is crucial. The section below contains a discussion on the criteria to choose suitable hosts and dopants for superior properties.

1.6.1 Host lattice

The selection of the host decides their relative spatial position, the distance between them, coordination numbers, and coordinating ion's type. Thus, the appropriate host lattice

selection is important in the synthesis of Ln^{3+} ion-doped phosphors to obtain favorable optical properties. The ES dynamics of the Ln^{3+} ions and their interactions with the host lattice determine the luminescence efficiency of phosphors.⁷¹ The ideal host matrices should exhibit low phonon energies as they suppress the multiphonon relaxation process of the emissive states, thereby minimizing nonradiative loss and maximizing radiative emission. Additionally, the host material should be chemically stable and should require a lattice match with the dopant ions. Since Ln^{3+} ions exhibit similar ionic radii and chemical properties, thus compound containing them are best suited as host matrices. In addition, metals like Ca^{2+} , Ba^{2+} , Sr^{2+} , and Na^+ and some transition metals such as Ti^{4+} and Zr^{4+} also show close ionic sizes to Ln^{3+} ions. Thus, host materials containing these ions are also utilized.⁸⁰

The fluoride compounds seem to be an ideal host to prepare highly luminescent materials as they have low lattice phonon energy, typically $\sim 350 \text{ cm}^{-1}$. Although heavy halides exhibit lattice phonon energy usually less than 300 cm^{-1} , but they are moisture sensitive, thus, are of less use. However, oxides overcome this problem as they are chemically stable, but they possess high lattice phonon energy ($>500 \text{ cm}^{-1}$) due to stretching vibrations of the host lattice. The low phonon energies of the fluoride host minimize potential phonon-mediated, nonradiative de-activation process, thus are commonly used lattices. Moreover, the fluoride compounds can be reliably synthesized by various approaches to yield NPs with a narrow size distribution, well-defined morphology, and crystal phase¹⁹ Among the fluorides, NaYF_4 is the most efficient host matrix known to date, which exists in two phases, viz. cubic and hexagonal. The UC efficiency in a hexagonal phase of NaYF_4 is greater than that of the cubic phase of NaYF_4 . For instance, the hexagonal phase of NaYF_4 : Er, Yb exhibit about an order of magnitude enhancement of luminescence efficiency as compared to cubic phase counterparts as reported by Heer et al.⁸¹ The variation of the crystal structure in the host also influences the optical properties, which is ascribed to

the change in the crystal field around the Ln^{3+} ions in the matrix of various symmetries.^{71,76}

1.6.2 Activator

The multiple long-lived metastable ES required for DC/UC makes the Ln^{3+} ions well-suited for these processes. As mentioned earlier, the lanthanide ions essentially exist as trivalent ions (Ln^{3+}) as their most stable oxidation state. The luminescent centers doped in the host matrix are called activators or emitters. The activator creates a center that absorbs excitation energy and converts it into visible radiation. With the exception of Lu^{3+} , Yb^{3+} , Ce^{3+} , and La^{3+} , all other lanthanide ions have more than one excited $4f$ energy level; hence can be used as activators. Lanthanide ions such as Ho^{3+} , Tm^{3+} , and Er^{3+} possess ladder-like energy levels, thus are mostly used as activators for the UC process, while ions such as Tb^{3+} , Eu^{3+} , Pr^{3+} are frequently used as activators for the DC process.

The energy difference between the excited level and its next lower-lying level should be close enough for the ease of absorption of photons and the energy transfer process.⁷¹ The population of intermediate and emitting levels is decided by the nonradiative multiphonon relaxation rate between these energy levels, which ultimately determines the overall efficiency. The multiphonon relaxation rate constant K_{nr} for $4f$ levels is defined by the equation:

$$K_{nr} \propto \exp\left(-\beta \frac{\Delta E}{\hbar\omega_{max}}\right)$$

where, β is an empirical constant of the host matrix, $\hbar\omega_{max}$ is the highest energy vibrational mode of the host matrix, and ΔE is the energy gap between the populated level and next lower-lying energy level of Ln^{3+} ion. This energy gap law signifies that K_{nr} decreases exponentially with increasing energy gap between levels;⁷¹ thus, if the gap is large, then there are low probabilities of nonradiative transitions. Keeping with the above-mentioned law, ions Er^{3+} and Tm^{3+} are the most efficient activators for the UC mechanism.

1.6.3 Sensitizer

In singly doped NPs, the distance between two neighboring activator ions and the absorption cross-section of the ions affects the emission process. Higher doping concentration can cause deleterious cross-relaxation, which results in quenching; therefore, to avoid the quenching process, activator ion concentration should be kept low and precisely adjusted. Moreover, most Ln^{3+} activator ions exhibit low absorption cross-sections, which leads to low emission efficiency. Hence, to effectively increase the luminescence efficiency, a sensitizer is chosen doped along with the activator ion. The process schematically depicted in **Fig. 1.9** shows direct and indirect excitation from activator and sensitizer ion.

The sensitizer is a dopant ion that can transfer its energy to the neighboring activator ion. Typically, Yb^{3+} possesses a simple energy level with only one ES $4f$ level $^2\text{F}_{5/2}$. At 980 nm, Yb^{3+} ions have large absorption cross-section (10^{-20} cm^2) than other Ln^{3+} ions.⁸² Additionally, this transition of Yb^{3+} ion is well resonant with many $f-f$ transitions of activator ions like Ho^{3+} , Tm^{3+} , and Er^{3+} , hence facilitate efficient energy transfer. Apart from Yb^{3+} , Ce^{3+} and Gd^{3+} are commonly used UV sensitizers. Generally, the sensitizer content is kept high ($> 20 \text{ mol } \%$) while the activator concentration is kept relatively low ($< 3 \text{ mol } \%$) to minimize the cross-relaxation energy loss in the system.⁸³

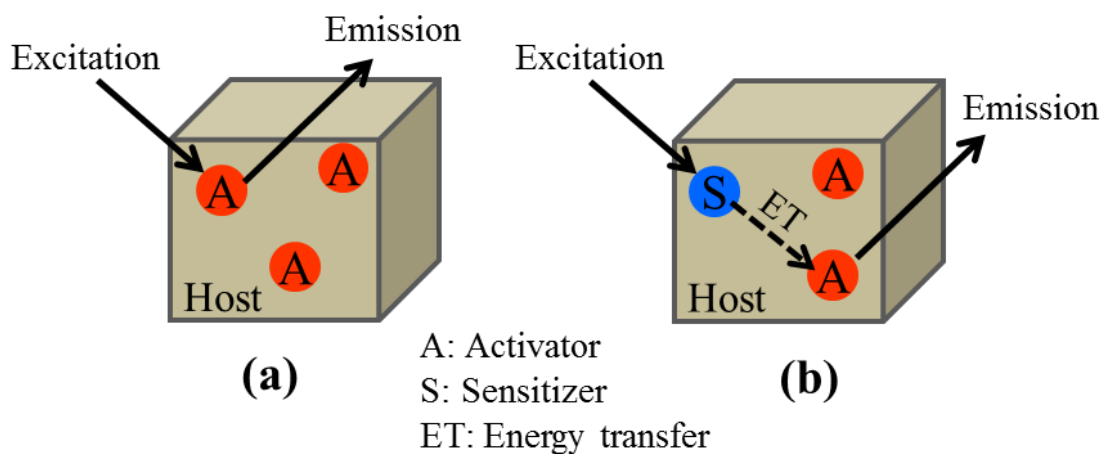


Figure 1.9 The schematic diagram showing (a) direct excitation of the activator ion and (b) indirect excitation followed by energy transfer from the sensitizer to the activator.

1.7 Synthesis methods

The development of a simple, efficient synthesis process for NPs with well-controlled size, shape, phase, and chemical composition is essential to explore the relationship between their structure and properties. For this, the optimization of the synthesis is very critical, as this tailor the optical properties of the phosphors. A variety of chemical techniques have been mentioned in the literature to prepare Ln³⁺ ion-doped DC/UC nanocrystals which include thermal decomposition, co-precipitation, hydro/solvothermal synthesis, sol-gel processing, flame synthesis, and combustion synthesis, etc. This section introduces various reported synthesis techniques to prepare well dispersed, pure phase nanocrystals.

1.7.1 Thermal decomposition

This method involves the decomposition of the organometallic precursors in a high-boiling organic solvent like 1-octadecene (ODE, boiling point ~ 315 °C) under thermal treatment into desired compounds in an inert atmosphere. Organometallic precursors such as acetates, trifluoroacetates are used as lanthanide ion-based organic salts, which at high temperature break down, initializing the nucleation process to form nanoparticles. Generally, oleyl amine (OM), oleic acid (OA), and trioctylphosphine are used as the capping agent to control the size and shape of the crystals by selectively binding to specific facets. Here, OA acts as a solvent as well as a passivating ligand that prevents the agglomeration of NPs. Size and morphology can be tuned by altering the synthesis parameters such as temperature, heating rate, time, concentration of precursors, etc. Nanoparticles synthesized through the thermal decomposition method are highly monodispersed and possess uniform morphology⁸⁴.

This method was developed by Yan et al. to prepare monodispersed LaF₃ nanocrystals (**Fig. 1.10a**).⁸⁵ This approach was extended by many groups to synthesize UC nanocrystals,^{73,86} such as NaYF₄: Yb, Tm/Er NPs. This group further extended the method to prepare oxides, oxyfluorides (**Fig. 1.10b**), oxychlorides (**Fig. 1.10c**), fluorides like NaLnF₄,

Li(K)LnF₄, NaMF₃ (M = Mg, Ni, Co, Mn), and LiMAIF₆ (M = Sr, Ca). Uniform CeO₂ NPs were also obtained using this method with cubic and star-like morphology from the decomposition of (NH₄)₂Ce(NO₃)₆ (**Fig. 1.10(k-l)**). Various studies are reported in literature using the thermal decomposition approach such as BaGdF₄,⁸⁷ NaGdF₄,⁸⁸ GdOF,⁸⁹ LiYF₄,⁹⁰ etc.

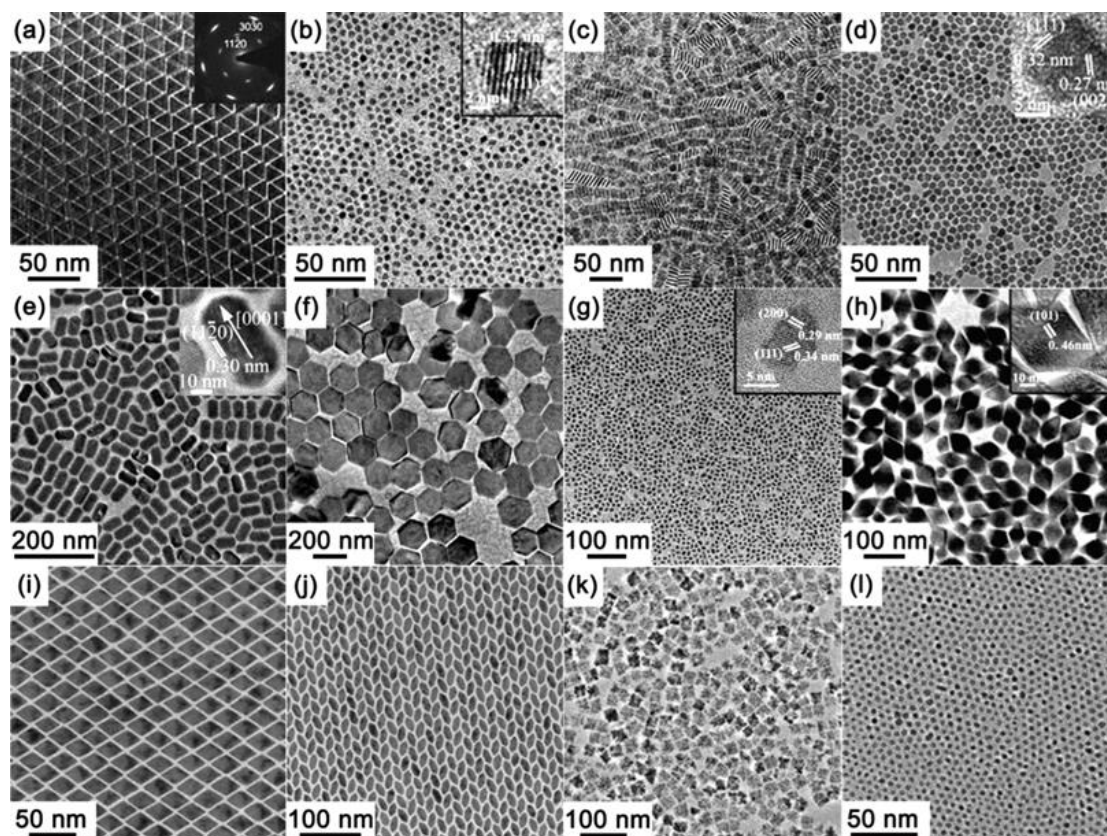


Figure 1.10 TEM images of (a) LaF₃, (b) LaOF: Eu³⁺, (c) LaOCl, (d) α -NaYF₄, (e) β -NaYF₄, (f) β -NaYF₄: Yb³⁺, Er³⁺, (g) KPrF₄, (h) LiErF₄, (i) DyF₃, (j) TbF₃, (k-l) CeO₂ nanoparticles synthesized by the thermal decomposition method.⁸⁴

1.7.2 Co-precipitation

Co-precipitation is used for preparing Ln³⁺ ion-doped NPs with narrow size distribution. In comparison with other methods, there is no need for costly equipment and stringent reaction conditions, subsequently saving time. However, the crystallinity of the NPs synthesized by the above method is relatively low, and therefore post-synthesis heat treatment is required to improve the crystallinity of the as-prepared NPs.⁷¹

In some rare cases, NPs having good crystallinity were prepared directly by the co-

precipitation method, eliminating the need for a calcination step. In general, lanthanide ion-based oleates, nitrates, acetates, and chlorides are used as a precursor for Ln^{3+} ions, whereas NH_4F , NaOH , and NaF are used to provide F^- ions to synthesize fluorophosphor NPs. One of the earliest works was done by van Veggel et al. to produce lanthanide (Ln^{3+}) doped LaF_3 NPs with Ln^{3+} ($\text{Ln} = \text{Nd}, \text{Er}, \text{Eu}, \text{and Ho}$) with co-precipitation method in a mixed solvent (ethanol and water) using NaF and $\text{Ln}(\text{NO}_3)_3$ as the precursors.⁹¹ In another study, Yi et al. synthesized the LaF_3 nanoparticles using the same procedure, taking LnCl_3 and NaF as precursors. Ammonium di-n-octadecyldithiophosphate was added during the synthesis to control the growth of NPs and adjusted the precipitation rate of different Ln^{3+} ions⁴³. During the same period, Haase et al. synthesized lanthanide ion-doped NaYF_4 nanoparticles using LnCl_3 , NH_4F , and sodium alkoxide as precursors and N-(2-hydroxyethyl)ethylenediamine as a high boiling organic solvent.^{81,92} In 2009, $\text{LaF}_3:\text{Eu}^{3+}$ and $\text{GdF}_3:\text{Eu}^{3+}$ NPs were synthesized by Lis and co-workers using the same method⁹³. In another study, Ln^{3+} -based oleates and NaF in ODE and OA were used to synthesize NaGdF_4 -based NPs. Higher temperature favored the formation of hexagonal phase while lower temperature tended to make cubic phase⁹⁴. In further studies, ethylenediamine tetraacetic acid (EDTA) was used as a chelating agent and prevented the agglomeration of the particles by shielding the Ln^{3+} ions, and particles size were tuned by adjusting the molar ratio of Ln^{3+} ions to EDTA.⁹⁵

1.7.3 Hydrothermal/solvothermal

The hydro/solvothermal method uses a solvent above its critical point to increase the solubility of the solid and to speed up the reaction between the solids in autoclaves. The autoclaves usually are steel containers for carrying out the chemical reactions under high pressure and temperature for prolonged periods of time⁸³. In this method, the solvent allows modulating the growth dynamics and prevents agglomeration. Parameters such as temperature, time, and concentration of precursors can be tuned to maintain a high nucleation rate and good crystallization. The crystallinity of the prepared NPs using this

method is usually very good; however, the disadvantages include the need for autoclaves and the impossibility of observing the growth of nanocrystal.

The synthesis of NPs using the hydrothermal method was demonstrated by Su et al.⁹⁶, who prepared hexagonal $\text{NaYF}_4: \text{Yb, Ln}$ ($\text{Ln} = \text{Tm}$ or Er). Later, Li and group developed a method to synthesize UCNPs of varied shapes, sizes, and crystal phases.⁹⁷ Lin et al. demonstrated the synthesis of $\text{Y}_2\text{O}_3: \text{Eu}^{3+}$ microspheres (**Fig. 1.11a**) through the solvothermal route.⁹⁸ Ln^{3+} -doped YF_3 nanospindles (**Fig. 1.11b**) were synthesized as reported by Qian and group, where EDTA was used to control the growth of the nanospindles.⁹⁹ $\text{LaF}_3: \text{Yb}^{3+}/\text{Er}^{3+}$ (Tm^{3+} , Ho^{3+}) nanoplates (**Fig. 1.11c**) with multicolor UC luminescence were prepared via thermal decomposition/solvothermal method.¹⁰⁰ Zhao et al. utilized an OA-mediated method to prepare UC NaYF_4 nanorods, nanotubes, and flower-like nanodisks (**Fig. 1.11d**).¹⁰¹ They further reported the synthesis of carboxyl-functionalized UCNPs (**Fig. 1.11(f-g)**) using binary acid, such as oxalic acid, succinic acid, malonic acid, and tartaric acid, as the capping

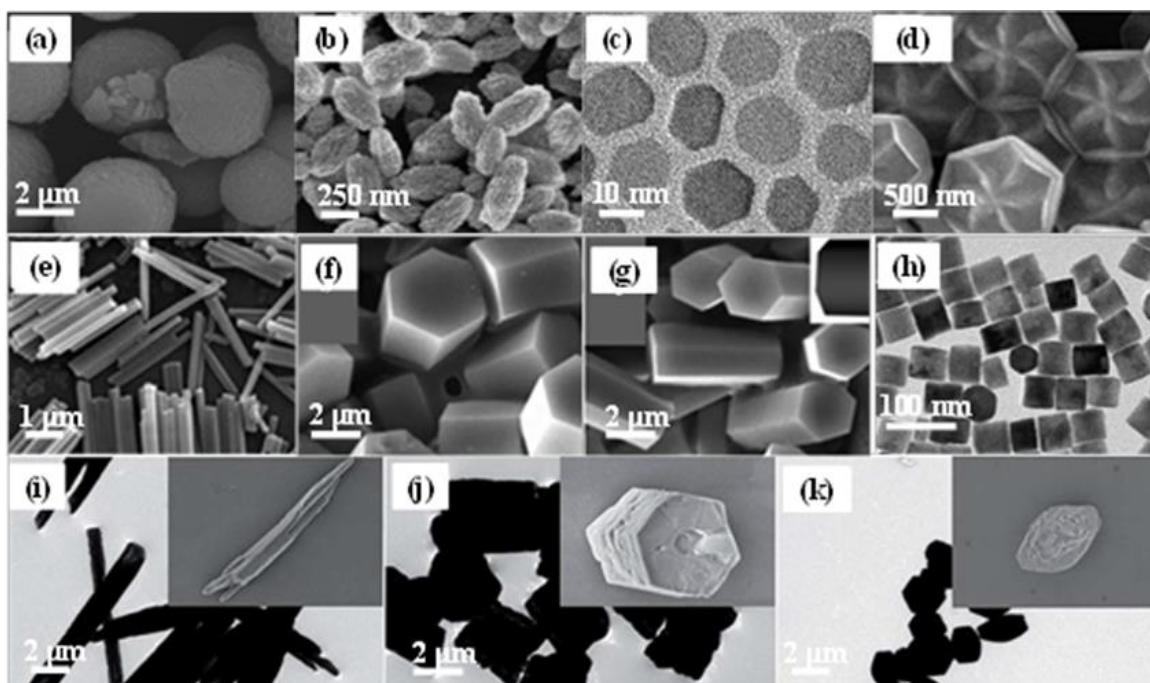


Figure 1.11 Electron microscopy images of (a) $\text{Y}_2\text{O}_3: \text{Eu}^{3+}$, (b) $\text{YF}_3: \text{Eu}^{3+}$, (c) $\text{LaF}_3: \text{Yb}^{3+}/\text{Er}^{3+}$, (d) β - NaYF_4 nanodisks, (e) β - NaYF_4 rods, (f-g) carboxylic acid capped $\text{NaYF}_4: \text{Yb}/\text{Er}$, (h) $\text{LaF}_3: \text{Yb}/\text{Er}$ using oleic acid and 6-aminohexanoic acid as binary coordinating ligands, (i-k) $\text{NaYF}_4: \text{Tb}$ nanoparticles at pH = 3, 7, and 11 respectively, synthesized by the hydrothermal method.

agents.¹⁰² In 2011, Li and group prepared water-dispersible surface-functionalized UCNPs using binary cooperative ligands, (**Fig. 1.11h**) hydrophilic 6-aminohexanoic acid and hydrophobic OA to control nuclei and growth of small NPs.¹⁰³ In 2014, our group also demonstrated the use of binary capping agent trisodium citrate (TSC) and cetyltrimethylammonium bromide (CTAB) on the crystal growth of NaYF₄: 5 % Tb through hydrothermal route at different reaction temperatures and pH of the solution.¹⁰⁴ The resultant morphologies are shown in **Fig. 1.11(i-k)**.

1.7.4 Sol-gel processing

The sol-gel technique is a wet chemical method to prepare NPs without requiring complicated synthetic procedures or instruments. This process involves the inorganic precursor, usually metal salts and alkoxides, which upon reaction with water, undergo hydrolysis and polycondensation, which lead to the formation of 3D network followed by annealing at a high temperature for a few hours.¹⁰⁵ Annealing removes the solvent from the gel and increases the crystallinity of the NPs, which is directly associated with the luminescence efficiency. The quality of the synthesized material using this method is significantly dependent on the annealing temperature and time of the reaction. The most well-known example is the fabrication of colloidal silica spheres using the Stöber method in 1968.¹⁰⁶ Advantages of using silica are that it is easily functionalized with several groups such as carboxyl, thiols or amines, which enables the connection of other molecules. In an interesting work, Hu et al. demonstrated that UCNPs coated with silica integrated with other functionalities such as Au and CuS NPs used for the applications in CT imaging¹⁰⁷ and photothermal therapy, respectively.¹⁰⁸ Furthermore, the Stöber process was utilized to coat the NPs with mesoporous silica giving them high porosity, good compatibility, and controllability of the release of restricted NPs. Apart from this, the sol-gel method was also used to prepare various nanocrystals with metal oxides as host materials which include BaTiO₃,¹⁰⁹ TiO₂: Er,¹¹⁰ BaTiO₃: Er,¹¹¹ BaTiO₃: Eu,¹¹² Lu₃Ga₅O₁₂: Er garnets,¹¹³

SiO₂@YVO₄: Eu,¹¹⁴ and YVO₄: Nd.¹¹⁵

Despite intensive work in this area, the derived particles from this method are of irregular shapes and sizes; also, considerable aggregation and water insolubility limit their use as luminescent probes for biological assays. Yet, this method is still applied for the synthesis of NPs on a large scale.

1.7.5 Other synthetic procedures

In contrast to hydrothermal, sol-gel methods, and thermal decomposition, **combustion synthesis** provides high throughput of producing NPs within a very short period. A mixture of oxidizers (metal nitrates) and a reducing agent (fuel) is selected to release maximum energy during the reaction time. A series of explosions occur in the process, raising the temperature typically from 500 to 3000 °C in the form of a combustion wave that propagates through the reaction precursors in a self-sufficient condition without requiring any extra heat for the total reaction. Generally, this method is one of the attractive techniques for the synthesis of oxide and oxysulfide nanocrystals. Reports have been found on the synthesis of Ln-doped Y₂O₃,^{116,117} La₂O₂S,¹¹⁸ Gd₂O₃,^{119,120} and CeTbMgAl₁₁O₁₉¹²¹ as reported by various groups. This process is a relatively milder, scalable, time and energy-saving process which can be extended for industrial uses.

Another time-saving technique is **flame synthesis**, which proceeds in a single step and is easily scalable. Synthesis of Y₂O₃: Yb,Er nanocrystals was reported by Ju et al. in 2010.¹²² There are some other synthetic strategies that have been attempted by other groups such as cation exchange,^{123,124} microwave-assisted synthesis^{125–127} and ionic-liquid based synthesis¹²⁸ to fabricate lanthanide doped luminescent nanoparticles with different shapes and sizes.

It should be noted here that in some cases, more than one method can be used to synthesize NPs to obtain narrow size distribution and high aqueous stability. The advantages and disadvantages of the methods adopted are listed in **Table 1.3**. Among these approaches,

hydro/solvothermal and thermal decomposition are the most popular and effective in preparing high-quality NPs. In this thesis, the hydrothermal method has been used to synthesize Ln^{3+} -doped NaYF_4 crystals— the resulting NPs exhibit good crystallinity, beneficial for efficient luminescence.

Table 1.3 A list of advantages and disadvantages of typical synthetic methods used for Ln^{3+} ion-doped phosphors.

Method	Examples	Advantages	Disadvantages
Thermal decomposition	LaF_3 , NaYF_4 , GdOF , CeO_2	High quality and monodispersed nanoparticles, smaller size particles can be obtained	High working reaction temperature, exceeding $300\text{ }^\circ\text{C}$, use of expensive and air sensitive precursors, toxic by-products, need of inert atmosphere, need of surface modification after synthesis
Co-precipitation	LaF_3 , GdF_3 , NaYF_4 , NaGdF_4 , LuPO_4 , YbPO_4	Fast synthesis, low cost, does not require costly setup or severe reaction conditions	Require post heat treatment, require high temperature calcination, lack of particle size control, not applicable for large-scale synthesis
Hydro/solvothermal	LaF_3 , NaYF_4 , YVO_4 , Y_2O_3	High quality crystals with controllable particle size, shape and phase, reaction temperature is much lower	Not able to observe the nanocrystal growth process, require specialized autoclaves to carry out the reaction
Sol-gel	ZrO_2 , TiO_2 , BaTiO_3 , YVO_4	Cheap precursor, can be used for large-scale synthesis	Post heat treatment is required, considerable particle agglomeration, broad particle size distribution, irregular morphologies
Combustion	Y_2O_3 , Gd_2O_3 , $\text{La}_2\text{O}_2\text{S}$	Scalable process	Considerable particle aggregation, lack of shape control

1.8 Surface modification

Surface modification of the NPs is one of the extensive areas of research in the field of material and biomedical sciences. The surface modification of Ln^{3+} ion-doped NPs not only improves photostability but also provides a potential platform for linking macromolecules for numerous biomedical applications. It also endows hydrophilicity to the NPs, which is a crucial step for their biological applications. Surface modification preserves the original photophysical properties of the NPs, and they retain their size as well. Several methods have

been developed to produce water-soluble NPs, which are discussed in the subsequent section.

1.8.1 Surface passivation

The luminescent efficiency of the lanthanide ion-doped NPs is usually less than the bulk counterparts, owing to their larger surface-to-volume ratio. Also, these NPs have less quantum efficiency than other luminescent materials like organic fluorophores and quantum dots (QDs) due to their less molar absorption coefficient. The presence of ligands on the surface with high-energy vibrational modes such as hydroxyl (OH) and amine (NH₂) can lead to the quenching of the ES of the Ln³⁺ ions present in the host lattice due to multiphonon relaxation processes.^{129,130} Increasing the dopant ion concentrations also do not solve the problem. Furthermore, high-quality NPs prepared by the techniques described above, especially thermal decomposition, are in organic solvents giving rise to hydrophobic capping, which is not suitable for biological applications. To reduce the losses, the general strategy adopted is to coat the surface of the NPs with appropriate shell material to get the **core-shell** structures. In such structures, all the dopant ions are confined in the interior of the NPs, which suppresses the energy transfer to the surface of the crystal, thereby increasing the UC intensity. The interface between the core and shell of the NPs should be of high quality and with similar lattice constants to avoid defect formation to decrease the quenching. The shell should not allow any kind of energy transfer from the core to the outer environment.⁷⁸ Recently, many groups have adopted this synthetic route to design lanthanide ion-doped nanoparticles for upconversion luminescence. In most of the cases, the shell is inert, whose main role is to increase the emission intensity of the core particle. The shell mostly has the same composition as the NPs host. The formation of passivating shells on phosphors such as LaF₃, NaYF₄, KYF₄, and NaGdF₄ and their undoped counterparts have been published by several authors. An enhancement of 30 times was observed by 1.5 nm thick shell of undoped β -NaYF₄:Yb/Er NPs as demonstrated by Chow et al. in 2007.¹³¹

Some other examples include $\text{LaF}_3:\text{Eu}^{3+}@\text{LaF}_3$,¹³² $\text{CeF}_3:\text{Tb}^{3+}@\text{LaF}_3$,¹³³ $\text{NaYbF}_4:\text{Tm}@\text{CaF}_2$,¹³⁴ and $\text{NaYF}_4:\text{Yb,Er}@\text{NaYF}_4$,^{135,129} etc.

Years after 2008, different groups reported the fabrication of core-shell NPs in which shell also contained luminescent centers, laying an effort to achieve multicolor tunability and enhancement of the UC luminescence. The active shell protects the Ln^{3+} ions luminescence from the nonradiative transitions and transfers NIR-absorbed energy to the luminescent core. Different core-shell type structures were fabricated such as $\text{NaGdF}_4:\text{Yb,Er}@\text{NaGdF}_4$: Ag,¹³⁶ $\text{NaGdF}_4:\text{Yb,Er}@\text{NaGdF}_4$: Yb@ NaGdF_4 : Nd,¹³⁷ $\text{LaPO}_4:\text{Er}@\text{LaPO}_4$: Yb,¹³⁸ $\text{NaGdF}_4:\text{Yb}^{3+},\text{Er}^{3+}@\text{NaGdF}_4$: Nd³⁺@sodium gluconate,¹³⁹ etc. The formation of core-shell architectures can be inferred from X-ray diffraction (XRD), transmission electron microscopy (TEM), and energy-dispersive X-ray spectroscopy (EDS) directly. The quality of the NPs can also be investigated by X-ray photoelectron spectroscopy (XPS) measurements that provide the evidence of the core-shell structures.

UCNPs were also coated with amorphous silica shells to obtain high luminescence efficiency by minimizing the surface defects. There is a report by Lu et al., who showed the synthesis of $\text{Y}_2\text{O}_3:\text{Yb,Tm}$ NPs by coating them with SiO_2 or TiO_2 shell.¹⁴⁰ The upconversion intensity was varied by adjusting the thickness of the coated shell. In the core-shell consisting of NPs and SiO_2 , image contrast was seen in the TEM, thereby showing the thickness of the shell directly. Their quality was also investigated by XPS measurements.

1.8.2 Surface functionalization

Most phosphors NPs synthesized using routes, as described in *Section 1.7* have no or less aqueous solubility. Moreover, they lack functional moieties in their structures, resulting in the insolubility of the nanoparticles, which limits their applications in biological sciences. Therefore, surface functionalization with hydrophilic ligands is required prior to the chemical attachment of biomolecules so that they can be homogeneously dispersed and stable in the aqueous environment and biological buffers, showing a high affinity to

biological targets.⁷⁶ To this end, a variety of strategies such as ligand attraction, ligand oxidation, ligand exchange, layer-by-layer assembly, and surface silanization⁸⁶ as illustrated in **Fig. 1.12**, have been currently investigated by several research groups to provide the NPs both solubility and functionality for better alternatives in biological applications and will be briefly discussed in the following section.

1.8.2.1 Ligand exchange involves the displacement of hydrophobic ligands anchored on the surface like OM, OA by bifunctional molecules, which can provide a hydrophilic surface to the nanoparticles. Such bifunctionality provides a hydrophilic functional group at one end to disperse the NPs in aqueous media and other functional groups which is capable of binding to the nanoparticle surface. The hydrophilic end to the NP can be further functionalized. In this regard, various ligands such as polyethylene glycol-phosphate,^{141,142} 6-aminohexanoic acid,¹⁴³ polyacrylic acid,¹³¹ and polylysine,¹⁰³ 3-mercaptopropionic acid,¹⁴⁴ etc., have been used.

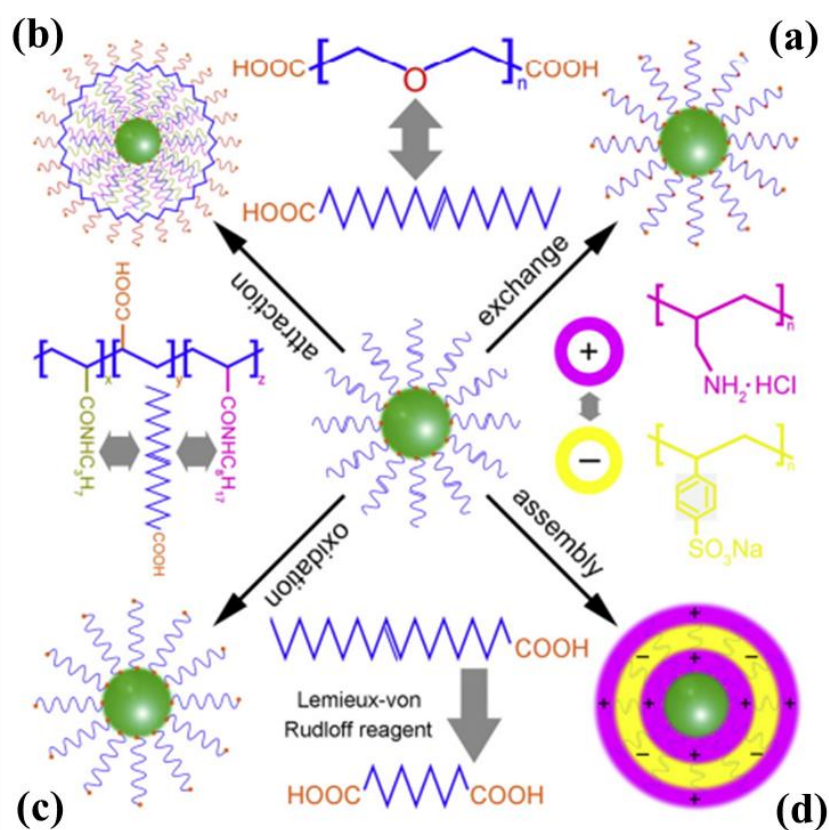


Figure 1.12 The mechanism of surface modification of nanoparticles involving (a) ligand exchange, (b) ligand attraction, (c) ligand oxidation and (d) ligand assembly.

This approach can be applied to metals, metal oxides, dielectrics, semiconductors regardless of their composition. This method modifies the hydrophobic NPs surface without affecting their shape and composition.

1.8.2.2 Ligand oxidation involves oxidation of the unsaturated carbon-carbon bond of the ligand like OA to generate carboxylic acid groups for providing them the dispersibility by Lemieux-von Rudloff reagent. Using this, Li et al. studied the conversion of OA-capped hydrophobic NaYF₄: Yb,Er nanocrystals¹⁴⁵ into water-dispersible NPs, preserving their morphology and luminescence properties. Yan and group¹⁴⁶ reported the OA oxidation into an azelaic aldehyde or azelaic acid through ozonolysis on the NaYF₄: Yb,Er NPs surface. Although the method is simple for the modification of hydrophobic NPs, but it is only applicable to a few ligands having a carbon-carbon double bond.

1.8.2.3 Ligand attraction involves the absorption of an amphiphilic block copolymer onto the NP surface. The original ligand and the hydrocarbon chain of the polymer are connected through the hydrophobic-hydrophobic van der Waals interactions. The hydrophilic portion of the polymer faces outwards, and this outer block permits aqueous dispersion and further bioconjugation to the NPs. The most commonly used polymers are poly(L-lysine),¹⁴⁷ polyacrylic acid,¹⁴⁸ 6-aminohexanoic acid,¹⁰³ poly(ethyleneglycol)-block-poly(caprolactone),¹⁴⁹ etc.

1.8.2.4 Layer-by-layer assembly takes advantage of the electrostatic attraction between the oppositely charged species to achieve surface modification. The layer thickness can be controlled precisely. In one of the earliest reports, Li et al. successfully modified NaYF₄: Yb,Er NPs with positively charged poly(allylamine hydrochloride) and negatively charged poly(sodium 4-styrenesulfonate) which were sequentially adsorbed onto the NP surface.¹⁵⁰ Although this method allows preparing water-soluble NPs with uniform layers with controllable thickness, but the significant increase in the size and time-consuming procedure limits the use.

1.8.2.5 Surface silanization (silica coating) involves the coating of amorphous silica on the NPs. It is the only inorganic surface treatment to fabricate NPs with the silica surface.¹⁵¹ van Veggel and group have prepared $\text{LaF}_3: \text{Ln}^{3+}$ UCNPs via Stöber process.¹⁵² Further amino or carboxylic group can be functionalized for bioconjugation with diverse biomolecules by reacting it with 3-aminopropyltrimethoxysilane as discussed by Shan and Ju.¹⁵³ The presence of these groups ensures the solubility of the NPs in an aqueous solvent.

1.9 Morphology tuning

The arrangement of atoms in NP and bulk crystal has a vital role as it changes the physical and chemical properties by changing the surface-to-volume ratio. It has been realized over the last two decades that the design and synthesis of inorganic crystals with well-defined shapes and tunable size are of high interest as the precise control over morphology and size allows manipulation of the properties of the nanocrystals as desired.^{104,154,155} To examine the relationship between shapes, sizes, and properties, control over the synthesis, thus over morphology is essential, which is usually governed by reaction conditions. During the synthesis process, size, morphology, and crystal phase of the NPs can be controlled by tuning various parameters as reaction time, temperature, concentration of precursor, different dopants, capping agents, etc.

1.9.1 Effect of reaction temperature and time

The temperature and time of the reaction play a crucial role in controlling the crystal phase and morphology of the products. Wang et al. prepared monodispersed NaYF_4 nanorods, nanoplates, and NPs, where they showed that the aspect ratio of the as-synthesized nanorods decreased at higher temperature and less reaction time resulted in only small NPs instead of nanorods.⁹⁷ In contrast to this, there are also some reports indicating an increase in size with increasing temperature. Hu et al. reported that the edge and thickness of hexagonal nanoplates increased with an increase in the hydrothermal temperature.¹⁰⁰ Temperature and time also have a notable effect on the phase of the crystal. At low reaction

temperature, NaYF₄ exist in the cubic (α) phase, and as the temperature increases, the α -phase transforms to the hexagonal (β) phase.^{156,157} Even at the higher temperature, in short reaction time, NaYF₄ existed in α -phase and a longer time duration α -phase transformed to β -phase NaYF₄ crystal.¹⁵⁸ Ma et al. also reported a change in the morphology with change in the temperature;¹⁵⁷ they demonstrated that the NaYF₄ sample consisted of a large number of cubes with an average size of 150 nm at 160 °C. When the reaction temperature increased to 180 °C, nanowire bundles with a small amount of NPs were observed. With further increase in temperature till 190 °C, the ratio of NPs to nanowire bundles decreased, while at 195 °C, the NPs disappeared completely, and a single nanowire appeared from nanowire bundles.

1.9.2 Concentration of precursors

Multiple kinds of precursors have been used by different groups. The commonly used precursors are lanthanide nitrates, chlorides, vanadates, etc. The lower the Ln³⁺ ion precursor concentration, the smaller the average size of the products. Lanthanide concentration affects not only the morphology but also the luminescence intensity of the samples.¹⁵⁹ Nunez et al. reported the variation in morphology with change in the type of precursor.¹⁶⁰ They compared and observed changes in the shape and size using different precursors as lanthanide nitrate, acetate, acetylacetonate. The increase in the particle size with a decrease in reactant concentration was also observed.

1.9.3 Effect of different dopants and concentration

Doping is a widely used process involving the incorporation of appropriate ions into host matrices to yield materials with desirable properties. Wang et al. prepared NaYF₄ nanocrystals where doping affected the growth process controlling the size, crystal phase, and optical properties of the NPs.¹⁶¹ They showed that NPs could be tuned in size (down to 10 nm), phase (hexagonal or cubic), and emission color (green to blue) using Ln³⁺ ions introduced at defined concentrations. Li et al. reported the effect of Eu³⁺ dopant concentration on NaYF₄: Eu³⁺ crystals. They demonstrated that with the increase in the Eu³⁺

concentration⁹⁷, the size of the as-synthesized nanorods decreased. Also, the length of the nanorods rapidly elongated with the decrease in Eu^{3+} concentration. It was also demonstrated in the study that upon reaching the Eu^{3+} concentration at 71.4%, $\beta\text{-NaYF}_4$ changed to $\beta\text{-NaEuF}_4$.

1.9.4 Effect of capping agents/ligands

The nanocrystals growth can also be controlled through the addition of a ligand that binds to the surface of the growing NPs. The addition of a ligand often makes the NPs soluble in either polar or nonpolar solvents. The commonly used organic ligands for the fabrication of Ln^{3+} ion-doped phosphors are OA,^{162,163} EDTA,^{164,165} CTAB,^{164,166} citric acid,¹⁶⁷ and sodium citrate.¹⁰⁰ The fundamental role of capping agent/ surfactant molecules is that it selectively adsorbed on certain crystalline surfaces or facets, which significantly decrease their growth rates and allow preferential growth leading to a highly anisotropic shape. The crystal growth is related to the relative growth rate of different crystal facets, and these differences in the growth rates of facets result in a different outlook of the crystallites. Sodium citrate and EDTA are considered to be strong chelating agents. The importance of the presence of the strong chelating/coordinating ligand can be explained by the LaMer model. According to the LaMer model, definite separation of nucleation and growth stages is the primary requisite for uniform particles formation. The controlled release of Ln^{3+} ions from an Ln-ligand complex helps separate the nucleation and growth stages. Further, the capping on the surface of nanoparticles prevents aggregation as well.

1.10 Applications

In recent times, Ln^{3+} ions have found widespread use in nanomaterials as lanthanide ion-doped NPs. These NPs are the most useful luminescent probes because of their riveting optical properties, including long luminescent lifetime, large Stokes or anti-Stokes shift, sharp emission, and good chemical stability. The successful synthesis of high-quality Ln^{3+} ion-doped NPs has broadened their applications. They have been widely used in solid-state

lasers,^{82,168,169} light-emitting devices,^{170–172} solar cells,^{173,174} and waveguide amplifiers.^{175,176}

These materials do not exhibit photobleaching or photoblinking, thus have the edge over other luminescent materials. The use of luminescent Ln^{3+} ion-based materials has become an area of interest for various applications in biological and material sciences due to their range of non-overlapping absorption and emission lines from the visible to NIR region. The utilization of these materials in various applications has been schematically shown in **Fig. 1.13** and briefly discussed below.

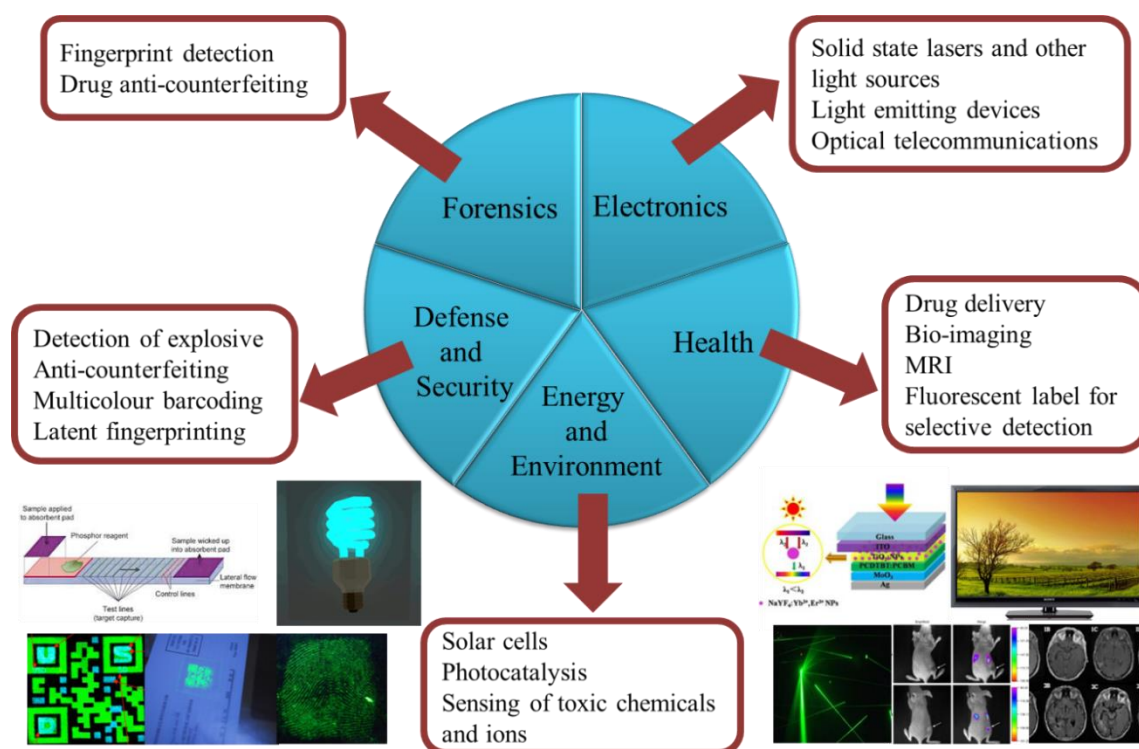


Figure 1.13 Various applications of lanthanide ion-doped phosphors.

1.10.1 Optical imaging

Optical imaging has become an important tool in biomedical applications because it gives detailed images of tissues and organs. Conventional tools for optical imaging possess some drawbacks, such as short penetration depth, significant auto-fluorescence from biological tissues, and DNA damage or cell death. Also, the spectral interpretation during multicolor imaging becomes a problem due to significant spectral overlapping resulting from their broad emission bands. Therefore, an alternative with low background signal and

having deep penetration ability was required.

For this purpose, Ln^{3+} ion-doped nanocrystals become better alternatives to quantum dots and organic molecules for bioimaging. In 1999, they were first used by Zijlman et al. for tissue imaging, where a low autofluorescence signal from the tissues was observed.¹⁷⁷ Even after the continuous high excitation energy source exposure, no bleaching was observed. Since the size of the utilized particles was in micron size, thus they are of limited use. With the advancement in the synthesis techniques over these years, smaller size and high-quality UCNPs were prepared. Wu et al. showed that the UCNPs could be used for single-molecule imaging with enough brightness.¹⁷⁸ The as-prepared UCNPs were observed to be photostable even after continuous 1 h laser illumination. Zhang and group first studied *in vivo* imaging using $\text{NaYF}_4: \text{Yb,Er}$ UCNPs with a penetration depth of 1 cm in small mammals showing much high luminescence as compared to quantum dots.¹⁷⁹ In the same year, Nyk et al. developed an approach for imaging *in vitro* and *in vivo* utilizing NIR-to-NIR UC in $\text{NaYF}_4: \text{Tm,Yb}$ phosphors.¹⁸⁰ Balb-c mice were injected intravenously with UCNPs used for animal imaging studies, demonstrating the high contrast PL imaging *in vivo*.

Later, Xiong et al. developed an imaging tool for targeted imaging of tumors both in *in vivo* and *in vitro* based on UCNPs.¹⁸¹ No autofluorescence signal was observed even at high penetration depth, and a high signal-to-noise ratio was obtained. Wang et al. utilized polymer-modified $\text{KMnF}_3: \text{Yb,Er}$ and $\text{NaYF}_4: \text{Yb,Er}$ NPs for imaging with a depth of 0.5 cm and 1 cm, respectively.¹⁸²

Lanthanide ion-doped based probes in combined optical and magnetic resonance (MR) imaging were utilized by Rajiv¹⁴⁴ et al. NaYF_4 crystals co-doped with the lanthanide ions Gd^{3+} and $\text{Eu}^{3+}/\text{Yb}^{3+}/\text{Er}^{3+}$ having sizes 20-30 nm were prepared and dispersed in water. An efficient UC and DC emission from the ions doped into fluoride matrix allowed optical imaging modality for the nanoprobe. Various other nanocrystals have been used as imaging probes, such as $\text{Dy}_2\text{O}_3: \text{Tb}$,¹⁸³ $\text{KGdF}_4: \text{Ln}$ (Ln= Dy, Tb, Eu),¹⁸⁴ $\text{NaLuF}_4: \text{Gd,Yb,Tm}$,¹⁸⁵ etc.

1.10.2 Theranostics

The nanoprobe based on lanthanide ion-doped NPs provide great imaging functionality, tumor-targeting ability, and therapy efficiency; thus, these materials have been applied to theranostics applications. Tian et al. represented a facile approach for the rational manipulation of green and red UC emission to red emission (650–670nm) of NaYF₄: Yb,Er UCNPs. This has been achieved by doping Mn²⁺ ions.¹⁸⁶ The emission color can be tuned from green to red by controlling the Mn²⁺-doping level. PEG-phospholipid (Polyethylene glycol-phospholipid) layer was coated on the surface of the NPs, which was employed for *in vivo* imaging and drug delivery applications. Our group in 2014,⁴¹ also developed a multifunctional nanoprobe based on polyethylenimine (PEI) capped NaYF₄: Gd,Tb nanorods for optical/magnetic imaging and pH-triggered drug delivery applications.

The UCNPs are often combined with a range of other materials for effective theranostics applications. In this regard, Deng et al. reported a metal-organic framework-based aptamer-conjugated core-shell NaYF₄: Yb,Er@Fe-MIL100 composite for the targeted delivery of doxorubicin (DOX) and for cell imaging.¹⁸⁷ Here, UCNPs emitted intense green light under 980 nm excitation, while the MOF based on the iron carboxylate MOF, Fe-MIL-100 possessed high porosity and low cytotoxicity, which was beneficial for the drug delivery. The anticancer aptamer, 26-mer guanine-rich oligonucleotide, was conjugated covalently on the surface of the UCNP@MOF, which helped in targeting the cancer cell and enhanced the intracellular uptake. In another work, UCNPs@MIL-53/FA dual-function system (FA = Folic acid) was developed that integrated bioimaging and drug delivery. For this purpose, Cong and group prepared core-shell NaYF₄: Yb,Er@NaYF₄: Nd@MIL-53 microsphere system via layer-by-layer self-assembly method.¹⁸⁸ MIL-53 acted as a drug carrier for delivery of DOX, and further FA was functionalized as a targeting agent, which was encapsulated to the core-shell structure to yield UCNPs@MIL-53/FA. In an interesting attempt, a multifunctional Fe₃O₄@Y₂O₃: Eu core-shell structure was synthesized by Gowd

et al. via a facile wet-chemical route followed by annealing.¹⁸⁹ The NPs were expected to possess a prospect for drug delivery and multimodal bio-imaging applications. In another study, a multicomponent sandwich structured $\text{Fe}_3\text{O}_4@\text{nSiO}_2@\text{mSiO}_2 @\text{YVO}_4:\text{Eu}$ hybrid microspheres were developed with mesoporosity, luminescence, and magnetic properties by Yang et al.¹⁹⁰ The storage and release properties were studied for this drug-carrier multifunctional system, wherein ibuprofen was used as a drug. This system was reported to be utilized as a targeted drug delivery system, where the amount of drug release can be observed with the change in the luminescence intensity of Eu^{3+} ions since the Eu^{3+} luminescence intensity increased with the released amount of drug.

Recently, one concept for the fabrication of histidine and octadecylamine-functionalized graphene quantum dots (GQDs) and $\text{NaYF}_4:\text{Yb,Er}$ UCNPs hybrid nanocage was proposed, which was adequate for the controlled drug delivery and cancer theranostics.¹⁹¹ This system exhibited the DOX loading capacity of 461.2 % at nearly 100 % of encapsulation efficiency. This study opens a pathway to develop and synthesize ideal nanocarriers for cancer theranostics. Chen et al. reported UCNPs@mHTiO₂ nanoplatfom for chemo/photodynamic therapy and imaging based on the UCNPs, $\text{NaYF}_4:\text{Yb,Tm}@ \text{NaYF}_4$ as core, coated with hollow, mesoporous-TiO₂.¹⁹² The hollow structure helped to store the antitumor drug DOX and thus promoted chemotherapy efficiency. The results showed that the cooperative effect of chemotherapy and photodynamic therapy (PDT) enhanced the cytotoxicity to the cancer cells. These studies offer ample scope in designing and developing novel materials to show promising applications in biological sciences.

1.10.3 Sensing applications

UC nanocrystals have been used as luminescent sensors to detect various molecules such as RNA, DNA, glucose, explosives, pesticides, metal ions like Cu^{2+} , Hg^{2+} , and Pb^{2+} , etc. In one study, GQDs and single-stranded DNA (ssDNA) linked UCNP@SiO₂ based

sensor was designed for the detection of specific microRNA sequences.¹⁹³ The developed sensor deliberated the interactions between the sp^2 carbon atoms of GQDs and DNA nucleobases linked to the UCNPs, which brought GQDs near to the surface of ssDNAUCNP@SiO₂. The UCNPs capacity to interact with GQDs through π - π stacking was hindered by ssDNA in the presence of a complementary microRNA sequence, which resulted in the reduction of the fluorescent intensity-dependent of miRNA sequence. Using biotinylated NaYF₄: Yb,Er UCNPs as energy donors, and biotinylated Au NPs as energy acceptors, Li et al. have developed a highly sensitive sensor for avidin detection.¹⁵⁰ Similarly, the UCNP-to-QD FRET system using biotin-streptavidin interaction as a prototype was demonstrated by Mattsson et al., which can be used for rapid homogeneous optical biosensing.¹⁹⁴ NaYF₄: Yb,Er-streptavidin (sAv) acted as a donor and biotinylated CdSe/ZnS core-shell (biot) QDs acted as an acceptor to form UCNP-sAv-biot-QD system. Ju et al. prepared amine-functionalized KGdF₄ nanocrystals via a one-step solvothermal approach, which employed PEI capping ligand.¹⁸⁴ The system was demonstrated to be a sensitive time-resolved FRET (fluorescence resonant energy transfer) bioprobe to detect trace amounts of avidin at a concentration of 5.5 nM. A biosensing platform was demonstrated by Liu et al. for the detection of various target molecules utilizing UCNPs and graphene oxide as FRET-based pairs.¹⁹⁵

The UCNPs based sensors are not only used in the biomedical field but also in chemical sciences. An ammonia sensor was developed by Mader et al. using UCNPs and phenol red, which were immobilized in a polystyrene matrix.¹⁹⁶ The green emission at 560 nm of the UCNPs was screened off in the presence of ammonia, while the red emission remained unaffected. In another interesting work by Kannan et al.¹⁹⁷, Au-nanorods were decorated on ‘polyamidoamine generation 1 dendrimer’-functionalized NaYF₄: Yb,Tm UCNPs by seed-mediated growth of Au-nanorods. This system was further modified with 2-thiouracil for uric acid detection with a detection limit of 1 pM. Recently, the plasmonic Au-

nanohole-nanoplate bilayer arrays (PABAs) were designed by Zhan et al. to generate the local field. This generated local field then coupled with excitation and emission field of NaGdF₄: Yb,Er@NaYF₄ core-shell UCNPs.¹⁹⁸ The as-prepared PABA-supported core-shell UCNPs were utilized as a sensor to detect acetic acid with much higher sensitivity and a detection limit of 81 nmol mL⁻¹. Cui et al. designed NaYF₄: Yb,Er/CdTe UCNPs/QDs composite as a probe for the detection of the Hg²⁺ ion in serum.¹⁹⁹ The PEI-capped NaYF₄: Yb,Er UCNPs were prepared via solvothermal procedure. The CdTe QDs were then grafted on the NaYF₄: Yb,Er UCNPs surface. The system was irradiated by 980 nm NIR light, which was able to overcome the interfering autofluorescence from the serum. A FRET-based biosensor was able to detect Hg²⁺ ions effectively with a limit of detection of 15 nM. Reports also showed that these UCNPs can be utilized for the detection of organophosphorus pesticides.^{200,201} The sensor using the lanthanide ion-based nanoparticles were also developed for the detection of various explosive molecules.^{202–204} Apart from chemical sensing, lanthanide ion-based phosphors are used in optical temperature sensing as well. A few of the works include Er³⁺,Tm³⁺,Yb³⁺,Li⁺: NaZnPO₄ phosphors,²⁰⁵ Er³⁺,Yb³⁺: Ba₃Y₄O₉ phosphors,²⁰⁶ Er³⁺,Yb³⁺,Na⁺: ZnWO₄ phosphors,²⁰⁷ etc.

1.10.4 Energy applications

Ln³⁺-doped materials are the leading applicants for efficient spectral conversion owing to their electronic structures that permit facile photon management.⁷¹ The composites of TiO₂ with UC phosphors are popular, where UC phosphors absorb NIR, which is converted visible and UV light via anti-Stokes emission. These photons are absorbed by UV-vis photoactive materials such as dyes or semiconductors, consequently harvest the complete solar region and enhance dye-sensitized solar cell (DSSC) efficiency. Thus, the utilization of UC phosphors is the simplest approach to enhance the performance of solar cells. In this regard, Shan et al. tried to enhance the photovoltaic efficiency by using the NaYF₄: Yb,Er phosphors by developing a DSSC configuration, wherein they applied a layer of NaYF₄:

Yb,Er hexagonal nanoplatelets as an external layer, and a single internal transparent TiO₂ layer.²⁰⁸ In this arrangement, the photocurrent and overall DSSC efficiency were improved by approximately 10 %, which were attained by adding the UC external layer. Zhao and co-workers fabricated double-shell β -NaYF₄: Yb,Er@SiO₂@TiO₂ microplates, which were sandwiched between a transparent TiO₂ layer and a counter electrode, and the system achieved nearly 29.4 % increment in DSSCs efficiency.²⁰⁹

In 2016, our group also attempted to develop a multifunctional platform based on β -NaGdF₄: Yb,Er UCNPs, and mesoporous anatase TiO₂ (*m*TiO₂) composite for biomedical and energy applications.⁴² β -NaGdF₄: Yb,Er/*m*TiO₂ nanocomposites were developed to improve the absorption of photons in a broader region of the solar spectrum. The as-synthesized nanocomposites exhibited an enhancement in the photocurrent density and solar cell efficiency by ~24 % and ~17 %, respectively, in comparison to pristine *m*TiO₂. A similar notable study was reported by Ramasamy et al., wherein a rear reflector structure was utilized that combined β -NaGdF₄: Yb,Er,Fe UCNPs for harvesting of NIR light, and silver (Ag) particles for light reflection to improve the DSSC performance.²¹⁰ The photon conversion efficiency (PCE) of DSSC with a rear reflector increased by ~ 21.3 % when compared with the cell without a rear reflector. M. Luoshan and group developed multi-shell-coated β -NaYF₄: Yb,Er— NFYE@SiO₂@Au@TiO₂ hexagonal submicropisms decorated by Au-NPs, which were incorporated into the DSSCs as photoanodes²¹¹. In this case, the overall efficiency was enhanced by 28.1% in comparison to the DSSC with pure TiO₂.

A variety of other materials based on Ln³⁺-doped phosphors for photovoltaic applications have been presented by different research groups, such as Y₂O₃: Yb,Er UCNPs and TiO₂ composite with PCE of 6.68 %, ²¹² NaYF₄: Yb,Er@NaYF₄ core-shell and TiO₂ composite with PCE of 12.5 %, ²¹³ Y₂CaZnO₅: Yb,Er and TiO₂ composite with maximum PCE of 7.21 %, ²¹⁴ β -NaYF₄: Yb,Er and TiO₂ composite with PCE of 7.17 %, ¹⁷³ Y₂O₃:

Yb, Ho and TiO₂ composite with PCE of 10.33 %, ²¹⁵ etc.

1.10.5 Security applications

The development of advanced luminescent materials for constructing a secure and unclonable encryption is required. The majority of features currently utilized in security applications are based on downshifting luminescence, which are easily mimicked by counterfeiters. The UCNPs are promising alternatives for traditional inks for anti-counterfeiting and security applications. Prasad et al. reported an approach to fabricate predefined photo patterns of UCNPs using a chemical amplification reaction, which can produce color-coded multilayer patterns for security applications.²¹⁶ The as-prepared NPs possessed the desired colloidal stability in an organic solvent and the ability to be modified for photopatterning on solid-state film. Blumenthal et al. in 2012, developed a composite ink to produce highly resolved printed features that were invisible under ambient light,²¹⁷ but produce luminescent images when excited with 980 nm laser. Keller and co-workers reported the synthesis of NaYF₄: Yb, Tm, and NaYF₄: Yb, Er emitting blue and green color, respectively.²¹⁸ The security ink combining these UCNPs were prepared to print both the color in the single QR code, thus providing a higher level of security to the ink. Various other UCNPs are reported by researchers for security applications which include, YMoO₄: Yb³⁺, Ho³⁺ core-shell NPs,²¹⁹ PAA-NaYF₄: Yb, Er,²²⁰ UCNPs@Carbon dots@meso-SiO₂,²²¹ UCNPs and azopolymer composite,²²² etc.

Apart from the above application, lanthanide ion-doped materials have also been widely used in LEDs,^{223,224} display devices,^{225,226} and solid-state lasers.²²⁷

1.11 Rationale of choosing host and dopants

• Fluorides as host

Up to now, a variety of host lattices have been utilized for different Ln³⁺ ions, which include oxides, aluminates, nitrides, vanadates, borates, phosphates, tungstates, sulfides, halides, etc. As mentioned in *Section 1.6.1*, host lattices should exhibit low phonon energy,

high bandgap, and good chemical stability. Among these lattices, oxides, phosphates, aluminates show relevant chemical stabilities, but the systems exhibit high phonon energies, typically greater than 500 cm^{-1} because of the strong Ln-O stretching vibration. Furthermore, heavy halides like chlorides, bromides, and iodides possess low phonon energies in the range $(250\text{-}300)\text{ cm}^{-1}$, but they are hygroscopic, hence are of less use. In comparison, only fluorides fulfill the criteria for an ideal host as they exhibit low phonon energies ($\sim 350\text{ cm}^{-1}$), wide bandgap, and have good chemical stability. The comparison of advantages and disadvantages of these host lattices is summarized in **Table 1.4**, while the comparison of phonon energy and bandgap of various host matrices are listed in **Table 1.5**.

Among various fluoride matrices, binary LnF_3 and complex ALnF_4 ($A=\text{Alkali}$) are recognized as outstanding host lattices for various Ln^{3+} ions. The ternary metal fluoride, NaYF_4 has been identified as the most efficient host lattice for UC and DC phosphors, therefore, has grabbed immense attention in the field of material sciences. NaYF_4 possesses a wide bandgap ($\sim 8\text{ eV}$) which is required for enhanced luminescence of Ln^{3+} ions so that the host energy levels do not interfere in the emission process.

Table 1.4 The comparison of advantages and disadvantages of oxides and halides as a host lattice for doping.

Host matrix	Advantages	Limitation
Oxides	High chemical stability	Relatively high phonon energy (larger than 500 cm^{-1})
Heavy halides	Low phonon energies ($\sim 300\text{ cm}^{-1}$)	Hygroscopic and thus are less stable
Fluorides	<ul style="list-style-type: none"> • Low phonon energies ($\sim 350\text{ cm}^{-1}$) • High chemical stability • Wide band gap 	Comparatively less stable than oxides

Table 1.5 The selected lattice phonon energies and bandgap of commonly used matrices for Ln³⁺ doping.^{83,229–231}

Host matrix	Highest phonon energy (cm ⁻¹)	Band gap (eV)
Phosphate glasses	1200	2-6
LaPO ₄	1050	6.15
Y ₃ Al ₅ O ₁₂	860	6.5
YVO ₄	600	4.1
NaYF ₄	350	8.5
NaGdF ₄	360	9.1
LiYF ₄	470	11.1
LaCl ₃	240	7.0
LaF ₃	400	7.8
LaBr ₃	250	5.6

It is well demonstrated that NaYF₄ exists in two forms, viz. cubic (α -NaYF₄) and hexagonal (β -NaYF₄). The cubic is the high-temperature metastable phase, while the hexagonal is the thermodynamically stable phase.²²⁸ The α -NaYF₄ is transformed to β -NaYF₄ under high temperature and longer reaction time. Among them, β -NaYF₄ is recognized as an efficient host lattice for luminescence of Ln³⁺ ions.

- **Crystal structure of NaYF₄**

The cubic phase NaYF₄ crystal structure has a space group *Fm3m*. The structure contains one type of high-symmetry cationic site (4a), which is randomly occupied by Y³⁺ or Na⁺ ions in the lattice, as depicted in **Fig 1.14**. The crystallographic symmetry on site (4a) is O_h. In contrast, the crystal structure of β -NaYF₄ is little understood and is under debate. In literature, three space groups of β -phase are proposed— *P6₃/m*, *P6̄*, and *P6̄2m*,²³² and still theoretical studies are going on to understand the crystal structure.²³³ However, the majority of studies have reported *P6₃/m* as the space group of hexagonal phase. Space group *P6₃/m*

consists of two types of cationic sites: one nine-fold coordinated site (2c) occupied by Na^+ and Y^{3+} ions randomly and another six-fold coordinated site (2b) occupied by Na^+ and vacancies as shown in **Fig 1.14**. The crystallographic symmetries on sites (2c) and (2b) are C_{3h} and C_s , respectively. Upon doping with Ln^{3+} ions, the site symmetry of O_h and C_{3h} in cubic and hexagonal phase, respectively, are reduced to C_s , C_n or C_1 .²³⁴

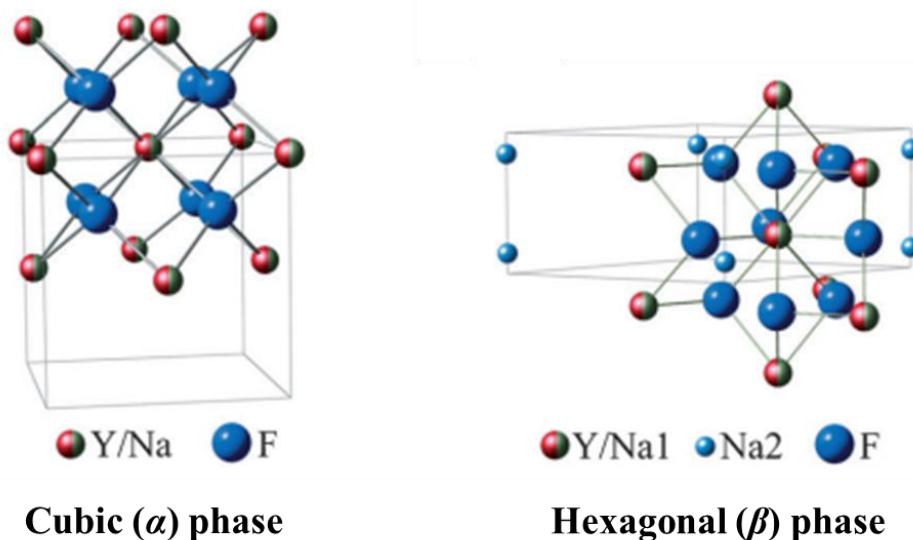


Figure 1.14 The illustration showing two types of the crystal structure of NaYF_4 : Cubic (α) and hexagonal (β) with space groups $Fm\bar{3}m$ and $P6_3/m$, respectively.²³⁴

The electronic transitions of Ln^{3+} ions are hypersensitive to their local structure, and thus luminescence of Ln^{3+} -based materials strongly depends on the crystal field environment around Ln^{3+} . The β - NaYF_4 structure is regarded more efficient than the α - NaYF_4 , because of following reasons: (i) the low symmetry cationic sites are selectively occupied by Y^{3+} and Na^+ ions, which cause their electron cloud distortion to accommodate the structural variation, and thus increase the probability of ED transitions which enhance the emission efficiency, (ii) also the low symmetry of sites in β - NaYF_4 helps Ln^{3+} to accommodate easily with small lattice variations to provide the opportunity for multidoping, (iii) the random occupation of Y^{3+} and Na^+ in the lattice of α - NaYF_4 accounts for reduced emission efficiency. While, in a hexagonal lattice, a highly ordered cation distribution minimizes energy loss due to the strong coupling of distorted electron cloud at low symmetry sites. For

this reason, the UC efficiency in β -NaYF₄ is approximately 10 times greater than α -NaYF₄. Thus, the phase-dependent luminescence study of the phosphors is ascribed to the crystal field around the Ln³⁺ ions in the matrix of various symmetries. In conclusion, a more uneven crystal field is exerted around dopant ions in the presence of low symmetry hosts as compared to the high symmetry counterparts. The asymmetrical component enhances the mixing of 4*f* energy levels and higher energy levels which consequently increases *f-f* transitions probabilities of the dopants.^{71,76}

- ***Gd³⁺ and Tb³⁺ ions as dopants***

In this thesis, lanthanide ions Gd³⁺ and Tb³⁺ are chosen as the dopants ion to study the optical properties of phosphors. In this pair, Gd³⁺ ion acts as a sensitizer, while Tb³⁺ acts as an activator. The emission spectra of Tb³⁺ can be obtained at $\lambda_{\text{ex}} = 375$ nm; however, efficient emission is difficult to realize under direct excitation at 375 nm due to intraconfigurational transitions in Tb³⁺ ions. Hence, Gd³⁺ ions act as a light-harvesting antenna to enhance the emission from Tb³⁺ ions. Gd³⁺ ions exhibit a strong absorption band at 273 nm because of their $^8\text{S}_{7/2} \rightarrow ^6\text{I}_{11/2}$ transitions.²³⁵ Thus, phosphors containing Gd³⁺ and Tb³⁺ ions together exhibit a very intense excitation band at 273 nm, and then the nonradiative energy transfer process takes place from Gd³⁺ ion to Tb³⁺ ion. Therefore, the emission spectra of these phosphors obtained at $\lambda_{\text{ex}} = 273$ nm yield peaks in the range of 480-680 nm because of Tb³⁺ ion. Four emission peaks centered at ~489, ~544, ~583, and ~620 nm arise from the transitions of $^5\text{D}_4 \rightarrow ^7\text{F}_6$, $^5\text{D}_4 \rightarrow ^7\text{F}_5$, $^5\text{D}_4 \rightarrow ^7\text{F}_4$, and $^5\text{D}_4 \rightarrow ^7\text{F}_3$, respectively.¹⁰⁴ Among these transitions, $^5\text{D}_4 \rightarrow ^7\text{F}_5$ at ~544 nm corresponding to green color is the most intense emission.

Although the studies in this thesis deal with DC mechanism of luminescence in lanthanide ions, but the findings can be applied to upconverting phosphors and other nanomaterials in the future.

1.12 Thesis objective

This thesis focuses on fluoride-based phosphors as they possess a wide bandgap, high chemical stability compared to other halide-based phosphors. Sodium yttrium fluoride (NaYF_4) has been chosen as the host, which fulfills the criteria of being the ideal host and is considered the most efficient matrix for the upconversion and downconversion process. As explained in the above section, NaYF_4 exists in two phases, namely cubic (α) and hexagonal (β). The α -phase is a high-temperature metastable phase, whereas β -phase is a thermodynamically stable phase, and thus, α -phase transforms to β -phase under high temperature and longer time. Among them, the hexagonal phase is reported to show higher luminescence efficiency.²³⁶ However, the synthesis of the hexagonal phase requires high temperature and prolonged time. Thus, preparing the hexagonal phase at lower temperatures with a high yield is essential, which can be further used in existing applications. Apart from these concerns, applications of Ln^{3+} ion-doped phosphors in explosives detection are rarely explored. Few reports have employed upconverting phosphors for the sensing applications, but they involved time-consuming and multistep synthetic processes.^{203,237} Moreover, the sensors worked in a relatively high pH range limiting their applicability. Hence, the as-prepared $\text{NaYF}_4: \text{Gd}^{3+}, \text{Tb}^{3+}$ phosphors using a simple synthetic approach are utilized to detect nitro-based explosives in a wide pH range with an acceptable detection limit.

Thus, this thesis investigates the effect of crystal structure, different surface capping, ligand functionalization, temperature, and time on the optical properties of the $\text{NaYF}_4: \text{Gd}^{3+}, \text{Tb}^{3+}$ system. The synthesis of the hexagonal phase of NaYF_4 at ambient temperature with amine-functionalized ligands has also been described in this thesis. A variety of ligands such as trisodium citrate, ethylenediaminetetraacetic acid, ethylenediamine, polyethylenimine, graphene quantum dots were used during the present investigation to alter the phase and morphology of $\text{NaYF}_4: \text{Gd}^{3+}, \text{Tb}^{3+}$ crystals. Furthermore, the thesis shows the sensing application of as-synthesized nanophosphors to detect nitro compounds.

So, the aim of the work presented in this thesis is as follows:

1. Investigating the phase transformation and growth mechanism of NaYF₄: Gd³⁺, Tb³⁺ nanophosphors in the presence of various ligands.
2. Studying the optical dependence on the size, shape and phase, shape as-synthesized nanoparticles.
3. Probing the mechanism of formation of multiform morphologies of NaYF₄: Gd³⁺, Tb³⁺ crystals when graphene quantum dots were *in situ* incorporated during the synthesis.
4. Developing the nanoprobe based on PEI-capped NaYF₄: Gd³⁺, Tb³⁺ phosphors for the selective explosives detection.

1.13 Thesis outline

This thesis emphasizes the synthesis of lanthanide ion-doped nano/microcrystals, NaYF₄, with the doping of Gd³⁺ and Tb³⁺ ions in the host matrix via a hydrothermal route. All the results incorporated in the thesis are summarized in five different chapters, and a brief introduction to each chapter is provided below:

Chapter 1 will provide a brief history of luminescence and its types, along with an overview of the discovery of lanthanides and their luminescence. Different lanthanide ion-based materials such as lanthanide complexes, inorganic phosphors, polymers, etc., will be described. As this thesis deals with the lanthanide ions-doped phosphors, an overview of the dependence of their luminescence on the dopant-concentration in the host, particle size, shape, temperature, time, capping agent, etc., will be given. Later, the mechanisms of upconversion and downconversion processes in lanthanide ions will be summarized. A brief review of the different synthetic approaches along with various applications will be given. Towards the end, the justification of choosing fluoride as the host and Gd³⁺ and Tb³⁺ ions as the dopants will be discussed. Finally, the objective and outline of this thesis will be presented.

Chapter 2 will discuss the fundamental studies on the synthesis, structural and luminescent properties of $\text{NaYF}_4: \text{Gd}^{3+}, \text{Tb}^{3+}$ crystals prepared via hydrothermal route. The prepared nanoparticles exhibit green luminescence when excited at 273 nm, where Gd^{3+} ion acts as a sensitizer and Tb^{3+} is an activator ion. It will be shown that the phases, shapes, and sizes of the NPs can be controlled through the appropriate addition of the ligands during the synthesis. The effect of different functionalized ligands such as trisodium citrate, ethylenediaminetetraacetic acid, ethylenediamine, and polyethylenimine (PEI) on the formation of NaYF_4 phases will be discussed. The formation of cubic phase at ambient temperature with carboxylic-functionalized ligands and hexagonal phase with the amine-functionalized ligands will be described. The results in the investigation will also show the change in their morphology in the presence of different ligands. Then, the possible mechanisms and impact of phase, size, and morphology on the optical properties will be presented.

Chapter 3 will focus on the synthesis of $\beta\text{-NaYF}_4: \text{Gd}^{3+}, \text{Tb}^{3+}$ nanocrystals via *in situ* incorporation of graphene quantum dots (GQDs) and the effect of the same on the growth and optical properties. The plausible mechanism of the formation of NaYF_4 crystals, which transformed from rod to disk-like structures with a change in concentration of GQDs will be described. Then, the effect of the functionalization of GQDs and other carbon-based materials on the growth of the nanocrystals will be presented. Finally, the correlation of the luminescent properties of $\beta\text{-NaYF}_4: \text{Gd}^{3+}, \text{Tb}^{3+}$ phosphors with their multiform morphologies and sizes will be shown.

Ln^{3+} -doped phosphors have been developed for a broad range of applications in the last two decades. Thus, the objective of **chapter 4** is to develop a probe for the detection of nitro-based explosives using PEI-capped $\beta\text{-NaYF}_4: \text{Gd}^{3+}, \text{Tb}^{3+}$ nanorods. The potentiality of the probe for detecting various nitro compounds and the selectivity towards the particular trinitrotoluene (TNT) based on the fluorimetric sensing technique will be explored in this

chapter. The mechanisms of the reduction in the luminescence intensity of Tb^{3+} ions observed in the presence of TNT will be discussed. This excellent selectivity is due to the interactions of PEI with TNT to form the Meisenheimer complex, which decreased the intensity due to luminescence resonance energy transfer (LRET) between nanophosphors and complex formed. It will be shown that the system is efficient for the detection of TNT with a detection limit of 119.9 nM. This work promises to pave the way for many applications in the detection of ultra-trace analytes.

Lastly, **chapter 5** will outline the summary of the studies described in the thesis. Also, the scope of this work will be given in this chapter.

1.14 References

- 1 J. W. Verhoeven, *Pure Appl. Chem.*, 1996, **68**, 2223–2286.
- 2 G. Blasse and B. C. Grabmaier, *Luminescent Materials*, Springer-Verlag, Berlin, Heidelberg, 1994, vol. 1.
- 3 I. Obodovskiy, in *Radiation*, Elsevier, 2019, vol. 63, pp. 207–220.
- 4 W. M. Yen, S. Shionoya and H. Yamamoto, Eds., *Handbook of Phosphors*, CRC Press, 2006, vol. 23.
- 5 C. Feldmann, T. Jüstel, C. R. Ronda and P. J. Schmidt, *Adv. Funct. Mater.*, 2003, **13**, 511–516.
- 6 J.-C. G. Bünzli and C. Piguet, *Chem. Soc. Rev.*, 2005, **34**, 1048.
- 7 M. Lastusaari, T. Laamanen, M. Malkamäki, K. O. Eskola, A. Kotlov, S. Carlson, E. Welter, H. F. Brito, M. Bettinelli, H. Jungner and J. Hölsä, *Eur. J. Mineral.*, 2012, **24**, 885–890.
- 8 W. H. Melhuish and M. Zander, *Pure Appl. Chem.*, 1981, **53**, 1953–1966.
- 9 S. Cotton, *Lanthanide and Actinide Chemistry*, John Wiley & Sons, Ltd, Chichester, UK, 2006.
- 10 M. H. V. Werts, *Sci. Prog.*, 2005, **88**, 101–131.
- 11 D. R. Lide, G. Baysinger, L. I. Berger, R. N. Goldberg, H. V Kehiaian, K. Kuchitsu, D. L. Roth and D. Zwillinger, *Handbook of Chemistry and Physics*, CRC Press, 2003.
- 12 J. H. Van Vleck, *J. Phys. Chem.*, 1937, **41**, 67–80.

- 13 S. Freed, S. I. Weissman, F. E. Fortess and H. F. Jacobson, *J. Chem. Phys.*, 1939, **7**, 824–828.
- 14 S. I. Weissman, *J. Chem. Phys.*, 1942, **10**, 214–217.
- 15 G. H. Dieke, H. M. Crosswhite and B. Dunn, *J. Opt. Soc. Am.*, 1961, **51**, 820.
- 16 B. R. Judd, *Phys. Rev.*, 1962, **127**, 750–761.
- 17 G. S. Ofelt, *J. Chem. Phys.*, 1962, **37**, 511–520.
- 18 J.-C. G. Bünzli and S. V. Eliseeva, in *Lanthanide Luminescence: Photophysical, Analytical and Biological Aspects*, Springer-Verlag Berlin Heidelberg, 2010, vol. 2, pp. 1–45.
- 19 G. A. Mandl, D. R. Cooper, T. Hirsch, J. Seuntjens and J. A. Capobianco, *Methods Appl. Fluoresc.*, 2019, **7**, 012004.
- 20 G. H. Dieke, *Spectra and Energy Levels of Rare Earth Ions in Crystals*, Interscience, 1968.
- 21 W. T. Carnall, G. L. Goodman, K. Rajnak and R. S. Rana, *J. Chem. Phys.*, 1989, **90**, 3443–3457.
- 22 K. Binnemans, *Chem. Rev.*, 2009, **109**, 4283–4374.
- 23 G. A. Crosby, R. E. Whan and R. M. Alire, *J. Chem. Phys.*, 1961, **34**, 743–748.
- 24 G. A. Crosby, R. E. Whan and J. J. Freeman, *J. Phys. Chem.*, 1962, **66**, 2493–2499.
- 25 S. Faulkner, S. J. A. Pope and B. P. Burton-Pye, *Appl. Spectrosc. Rev.*, 2005, **40**, 1–31.
- 26 S. Shinoda and H. Tsukube, *Analyst*, 2011, **136**, 431–435.
- 27 L. Wang, Z. Zhao, C. Wei, H. Wei, Z. Liu, Z. Bian and C. Huang, *Adv. Opt. Mater.*, 2019, **7**, 1801256.
- 28 S. Tanabe, *Comptes Rendus Chim.*, 2002, **5**, 815–824.
- 29 S. Schweizer, a. C. Rimbach, M. Mungra, B. Ahrens, F. Steudel and P. W. Nolte, *Opt. Mater. (Amst)*, 2019, **88**, 74–79.
- 30 K. Binnemans, R. Van Deun, C. Görrler-Walrand and J. L. Adam, *J. Non. Cryst. Solids*, 1998, **238**, 11–29.
- 31 R. Rolli, K. Gatterer, M. Wachtler, M. Bettinelli, A. Speghini and D. Ajò, *Spectrochim. Acta Part A Mol. Biomol. Spectrosc.*, 2001, **57**, 2009–2017.
- 32 J. Adam, *Chem. Rev.*, 2002, **102**, 2461–2476.
- 33 A. Speghini, M. Peruffo, M. Casarin, D. Ajò and M. Bettinelli, *J. Alloys Compd.*, 2000,

300-301, 174–179.

34 T. Nakanishi, K. Watanabe, J. Ueda, K. Fushimi, S. Tanabe and Y. Hasegawa, *J. Am. Ceram. Soc.*, 2015, **98**, 423–429.

35 D. de Graaf, S. J. Stelwagen, H. T. Hintzen and G. de With, *J. Non. Cryst. Solids*, 2003, **325**, 29–33.

36 H. Said, R. O. Omrani, L. R. Arana, D. El Bahri, S. Boussen, C. Bouzidi, H. Terraschke, A. H. Hamzaoui and A. M'nif, *J. Mol. Struct.*, 2019, **1192**, 42–48.

37 K. A. Bashar, W. L. Fong, K. A. Haider, S. O. Baki, M. H. M. Zaid and M. A. Mahdi, *J. Non. Cryst. Solids*, 2020, **534**, 119943.

38 G. Lakshminarayana, K. M. Kaky, S. O. Baki, A. Lira, U. Caldiño, I. V. Kityk and M. A. Mahdi, *Opt. Mater. (Amst.)*, 2017, **72**, 380–391.

39 M. Azam and V. K. Rai, *ACS Omega*, 2019, **4**, 16280–16291.

40 B. C. Feldmann, T. Jüstel, C. R. Ronda and P. J. Schmidt, 2003, 511–516.

41 P. Padhye, A. Alam, S. Ghorai, S. Chattopadhyay and P. Poddar, *Nanoscale*, 2015, **7**, 19501–19518.

42 P. Padhye, S. Sadhu, M. Malik and P. Poddar, *RSC Adv.*, 2016, **6**, 53504–53518.

43 G. Yi and G. Chow, *J. Mater. Chem.*, 2005, **15**, 4460.

44 M. Watanabe, N. Yamamoto, T. Matsuo, R. Oka, S. Ida and T. Masui, *J. Asian Ceram. Soc.*, 2019, **7**, 509–517.

45 Y. Pan, M. Wu and Q. Su, *J. Phys. Chem. Solids*, 2004, **65**, 845–850.

46 R. Shunmugam and G. N. Tew, *J. Am. Chem. Soc.*, 2005, **127**, 13567–13572.

47 W. H. Wong, E. Y. B. Pun and K. S. Chan, *Appl. Phys. Lett.*, 2004, **84**, 176–178.

48 C. Yu, Z. Zhang, L. Liu, W. Feng, X. Lü, W.-K. Wong and R. A. Jones, *Inorg. Chem. Commun.*, 2014, **49**, 30–33.

49 Z. Zhang, C. Yu, L. Liu, H. Li, Y. He, X. Lü, W.-K. Wong and R. A. Jones, *J. Photochem. Photobiol. A Chem.*, 2016, **314**, 104–113.

50 A. O’Riordan, E. O’Connor, S. Moynihan, X. Llinares, R. Van Deun, P. Fias, P. Nockemann, K. Binnemans and G. Redmond, *Thin Solid Films*, 2005, **491**, 264–269.

51 J. Kai, M. C. F. C. Felinto, L. A. O. Nunes, O. L. Malta and H. F. Brito, *J. Mater. Chem.*, 2011, **21**, 3796.

52 J. Wang, J. Hu, D. Tang, X. Liu and Z. Zhen, *J. Mater. Chem.*, 2007, **17**, 1597–1601.

- 53 H. Tan, S. Xie, N. Li, C. Tong, L. Xu, J. Xu and C. Zhang, *Mater. Express*, 2018, **8**, 141–148.
- 54 S. Y. Kim, Y.-H. Won and H. S. Jang, *Sci. Rep.*, 2015, **5**, 7866.
- 55 J. C. Boyer, N. J. J. Johnson and F. C. J. M. van Veggel, *Chem. Mater.*, 2009, **21**, 2010–2012.
- 56 F. Hu, X. Liu, R. Chen, Y. Liu, Y. Mai, R. Maalej and Y. Yang, *J. Rare Earths*, 2017, **35**, 964–969.
- 57 D. Xu, C. Liu, J. Yan, S. Yang and Y. Zhang, *J. Phys. Chem. C*, 2015, **119**, 2–10.
- 58 A. Dwivedi, K. Mishra and S. B. Rai, *J. Appl. Phys.*, 2016, **120**, 1–13.
- 59 C. Cao, Q. Liu, M. Shi, W. Feng and F. Li, *Inorg. Chem.*, 2019, **58**, 9351–9357.
- 60 M. D. Dramićanin, *Methods Appl. Fluoresc.*, 2016, **4**, 042001.
- 61 J. Liu, H. Rijckaert, M. Zeng, K. Haustraete, B. Laforce, L. Vincze, I. Van Driessche, A. M. Kaczmarek and R. Van Deun, *Adv. Funct. Mater.*, 2018, **28**, 1707365.
- 62 H. Dong, L. Sun and C. Yan, *Chem. Soc. Rev.*, 2015, **44**, 1608–1634.
- 63 D. L. Dexter, *J. Chem. Phys.*, 1953, **21**, 836–850.
- 64 J. L. Sommerdijk, A. Bril and A. W. de Jager, *J. Lumin.*, 1974, **8**, 341–343.
- 65 R. T. Wegh, H. Donker, K. D. Oskam and A. Meijerink, *Science*, 1999, **283**, 663–666.
- 66 B. Liu, Y. Chen, C. Shi, H. Tang and Y. Tao, *J. Lumin.*, 2003, **101**, 155–159.
- 67 P. Vergeer, T. J. H. Vlugt, M. H. F. Kox, M. I. den Hertog, J. P. J. M. van der Eerden and A. Meijerink, *Phys. Rev. B*, 2005, **71**, 014119.
- 68 B. M. van der Ende, L. Aarts and A. Meijerink, *Phys. Chem. Chem. Phys.*, 2009, **11**, 11081.
- 69 Q. Y. Zhang and X. Y. Huang, *Prog. Mater. Sci.*, 2010, **55**, 353–427.
- 70 Q. Zhang, A. Meijerink, F. T. Rabouw, D. Yu and R. Marti, *Light Sci. Appl.*, 2015, **4**, 1–8.
- 71 F. Wang and X. Liu, *Chem. Soc. Rev.*, 2009, **38**, 976.
- 72 X. Chen, *Chem. Soc. Rev.*, 2015, **44**, 1318–1330.
- 73 J. Zhou, Q. Liu, W. Feng, Y. Sun and F. Li, *Chem. Rev.*, 2015, **115**, 395–465.
- 74 N. Bloembergen, *Phys. Rev. Lett.*, 1959, **2**, 84–85.

- 75 P. P. Feofilov and V. V. Ovsyankin, *Appl. Opt.*, 1967, **6**, 1828.
- 76 S. Gai, C. Li, P. Yang and J. Lin, *Chem. Rev.*, 2014, **114**, 2343–2389.
- 77 J. S. Chivian, W. E. Case and D. D. Eden, *Appl. Phys. Lett.*, 1979, **35**, 124–125.
- 78 G. Chen, H. Qiu, P. N. Prasad and X. Chen, *Chem. Rev.*, 2014, **114**, 5161–5214.
- 79 W. Zheng, P. Huang, D. Tu, E. Ma and X. Chen, *Chem. Soc. Rev.*, 2015, **44**, 1379–1415.
- 80 P. Qiu, N. Zhou, H. Chen, C. Zhang, G. Gao and D. Cui, *Nanoscale*, 2013, **5**, 11512.
- 81 B. S. Heer, K. Kömpe, H. Güdel and M. Haase, *Adv. Mater.*, 2004, **16**, 2102–2105.
- 82 L. R. P. Kassab, M. E. Fukumoto, V. D. D. Cacho, N. U. Wetter and N. I. Morimoto, *Opt. Mater. (Amst.)*, 2005, **27**, 1576–1582.
- 83 M. Haase and H. Schäfer, *Angew. Chem. Int. Ed.*, 2011, **50**, 5808–5829.
- 84 H. Dong, S. Du, X. Zheng, G. Lyu, L. Sun, L. Li, P. Zhang, C. Zhang and C. Yan, *Chem. Rev.*, 2015, **115**, 10725–10815.
- 85 Y.-W. Zhang, X. Sun, R. Si, L.-P. You and C.-H. Yan, *J. Am. Chem. Soc.*, 2005, **127**, 3260–3261.
- 86 Y. Liu, D. Tu, H. Zhu and X. Chen, *Chem. Soc. Rev.*, 2013, **42**, 6924.
- 87 D. Yang, C. Li, G. Li, M. Shang, X. Kang and J. Lin, *J. Mater. Chem.*, 2011, **21**, 5923.
- 88 N. Bogdan, F. Vetrone, R. Roy and J. a. Capobianco, *J. Mater. Chem.*, 2010, **20**, 7543.
- 89 Y.-P. Du, Y.-W. Zhang, L.-D. Sun and C.-H. Yan, *J. Phys. Chem. C*, 2008, **112**, 405–415.
- 90 V. Mahalingam, F. Vetrone, R. Naccache, A. Speghini and J. A. Capobianco, *Adv. Mater.*, 2009, **21**, 4025–4028.
- 91 V. Sudarsan, S. Sivakumar and F. C. J. M. Van Veggel, *Chem. Mater.*, 2005, **17**, 4736–4742.
- 92 P. Ptacek, K. Ko and M. Haase, *Chem. Mater.*, 2007, **19**, 1396–1400.
- 93 T. Grzyb and S. Lis, *J. rare earths*, 2009, **27**, 588–592.
- 94 C. Liu, H. Wang, X. Zhang and D. Chen, *J. Mater. Chem*, 2009, **19**, 489–496.
- 95 G. Yi, H. Lu, S. Zhao, Y. Ge and W. Yang, *Nano Lett.*, 2004, **4**, 2191–2196.
- 96 L. Liang, H. Wu, H. Hu, M. Wu and Q. Su, *J. Alloys Compd.*, 2004, **368**, 94–100.

- 97 Y. L. L. Wang, *Chem. Mater.*, 2007, **19**, 727–734.
- 98 J. L. J. Yang, Z. Quan, D. Kong, X. Liu, *Cryst. Growth Des.*, 2007, **7**, 3–8.
- 99 M. Zhang, H. Fan, B. Xi, X. Wang, C. Dong and Y. Qian, *J. Phys. Chem. C*, 2007, **111**, 6652–6657.
- 100 H. Hu, Z. Chen, T. Cao, Q. Zhang, M. Yu, F. Li, T. Yi and C. Huang, *Nanotechnology*, 2008, **19**, 375702.
- 101 F. Zhang, J. Li, J. Shan, L. Xu and D. Zhao, *Chem. Eur. J*, 2009, **15**, 11010–11019.
- 102 J. Yang, D. Shen, X. Li, W. Li, Y. Fang, Y. Wei, C. Yao and B. Tu, *Chem. Eur. J*, 2012, **18**, 13642–13650.
- 103 T. Cao, Y. Yang, Y. Gao, J. Zhou, Z. Li and F. Li, *Biomaterials*, 2011, **32**, 2959–2968.
- 104 P. Padhye and P. Poddar, *J. Mater. Chem. A*, 2014, **2**, 19189–19200.
- 105 M. K. Mahata, H. C. Hofsäss, and U. Vetter, *Photon-Upconverting Materials : Advances and Prospects for Various Emerging Applications*, J. Thirumalai (ed.) Luminescence- An Outlook on the Phenomena and their Applications, IntechOpen, 2016.
- 106 A. F. W. Stober, *J. Colloid Interface Sci.*, 1968, **69**, 62–69.
- 107 J. Feng, D. Chang, Z. Wang, B. Shen, J. Yang and Y. Jiang, *RSC Adv.*, 2014, **4**, 51950–51959.
- 108 X. Liu, Q. Ren, F. Fu, R. Zou, Q. Wang, G. Xin, Z. Xiao, X. Huang, Q. Liu and J. Hu, *Dalt. Trans.*, 2015, **44**, 10343–10351.
- 109 A. Kareiva, S. Tautkus and R. Rapalaviciute, *J. Mater. Sci.*, 2006, **4**, 4853–4857.
- 110 R. Palomino-merino, P. Trejo-garcia, O. Portillo-moreno, S. Jiménez-sandoval and S. A. Tomás, *Opt. Mater. (Amst.)*, 2015, **46**, 345–349.
- 111 H. X. Zhang, C. H. Kam, Y. Zhou, X. Q. Han, Q. Xiang, S. Buddhudu, Y. L. Lam and Y. C. Chan, *J. Alloys Compd.*, 2000, **308**, 134–138.
- 112 M. García-hernández, A. García-murillo and F. D. J. Carrillo-romo, *Int. J. Mol. Sci*, 2009, **10**, 4088–4101.
- 113 V. Venkatramu, M. Giarola, G. Mariotto, S. Enzo and S. Polizzi, *Nanotechnology*, 2010, **21**, 175703.
- 114 M. Yu, J. Lin and J. Fang, *Chem. Mater.*, 2005, **17**, 1783–1791.
- 115 H. K. S. Hirano, T. Yogo, K. Kikuta, W. Sakamoto, *J. Am. Ceram. Soc.*, 1996, **79**, 3041–3044.

- 116 I. Kero, R. V Mangalaraja, J. Mouzon and C. P. Camurri, *J. Mater. Process. Technol.*, 2008, **8**, 415–422.
- 117 L. G. Jacobsohn, M. W. Blair, S. C. Tornga, L. O. Brown, B. L. Bennett, R. E. Muenchausen, L. G. Jacobsohn, M. W. Blair, S. C. Tornga, L. O. Brown and B. L. Bennett, *J. Appl. Phys.*, 2008, **104**, 1–7.
- 118 N. Hakmeh, C. Chlique, O. Merdrignac-conanec, B. Fan, F. Chevirié, X. Zhang, X. Fan and X. Qiao, *J. Solid State Chem.*, 2015, **226**, 255–261.
- 119 R. Kumar, D. Prasad and N. Brahme, *J. Radiat. Res. Appl. Sci.*, 2014, **7**, 550–559.
- 120 Y. Li and G. Hong, *J. Lumin.*, 2007, **124**, 297–301.
- 121 D. Ravichandran, R. Roy, P. Ravindranathan and W. B. White, *J. Am. Ceram. Soc.*, 1999, **84**, 1082–1084.
- 122 W. Kong, J. Shan and Y. Ju, *Mater. Lett.*, 2010, **64**, 688–691.
- 123 C. Shell, U. Shell, C. Dong, A. Korinek, B. Blasiak, B. Tomanek, F. C. J. M. Van Veggel and C. Ls, *Chem. Mater.*, 2012, **24**, 1297–1305.
- 124 M. Deng and L. Wang, *Nano Res.*, , DOI:10.1007/s12274-014-0439-6.
- 125 H. Wang and T. Nann, *ACS Nano*, 2009, **3**, 3804–3808.
- 126 H. Wang and T. Nann, *Nanoscale Res. Lett.*, 2011, **6**, 3–7.
- 127 Y. Tm, U. P. Rodrigues-filho and S. J. L. Ribeiro, *CrystEngComm*, 2017, **19**, 3465–3475.
- 128 M. He, P. Huang, C. Zhang, F. Chen, C. Wang, J. Ma and R. He, *Chem. Commun.*, 2011, **47**, 9510–9512.
- 129 L. M. Jin, X. Chen, C. K. Siu, F. Wang and S. F. Yu, *ACS Nano*, 2017, **11**, 843–849.
- 130 X. Liu, S. Han, R. Deng, X. Xie and X. Liu, *Angew. Chem. Int. Ed*, 2014, **53**, 11702–11715.
- 131 G. Yi and G. Chow, *Chem. Mater.*, 2007, **298**, 341–343.
- 132 E. Bovero and F. C. J. M. Van Veggel, *J. Phys. Chem. C*, 2007, **111**, 4529–4534.
- 133 J. M. Chem, S. Gai, P. Yang, X. Li, C. Li, D. Wang and J. Lin, *J. Mater. Chem*, 2011, **21**, 14610–14615.
- 134 G. Chen, J. Shen, T. Y. Ohulchanskyy, N. J. Patel, A. Kutikov, Z. Li and C. E. T. Al, *ACS Nano*, 2012, **6**, 8280–8287.
- 135 Y. Wang, L. Tu, J. Zhao, Y. Sun, X. Kong and H. Zhang, *J. Phys. Chem. C*, 2009, **113**, 7164–7169.

- 136 H. M. X. Zhang, B. Li, M. Jiang, L. Zhang, *RSC Adv.*, 2012, 1–3.
- 137 M. Xia, D. Zhou, Y. Yang, Z. Yang and J. Qiu, *Solid state Sci. Technol.*, 2017, **6**, 41–46.
- 138 P. Ghosh, J. Oliva, E. De Rosa, K. K. Haldar, D. Solis and A. Patra, *J. Phys. Chem. C*, 2008, **112**, 9650–9658.
- 139 D. Ma, L. Meng, Y. Chen, M. Hu, Y. Chen, C. Huang, J. Shang, R. Wang, Y. Guo and J. Yang, *Appl. Mater. Interfaces*, 2015, **7**, 16257–16265.
- 140 Q. Lü, F. Guo, L. Sun, A. Li and L. Zhao, *J. Appl. Phys.*, 2008, **103**, 123533.
- 141 J. M. Chem, H. Wong, F. Vetrone, R. Naccache, L. Wa and J. A. Capobianco, *J. Mater. Chem*, 2011, **4**, 16589–16596.
- 142 J. Boyer, M. Manseau, J. I. Murray, F. C. J. M. Van Veggel, P. O. Box and B. Columbia, *Langmuir*, 2010, **26**, 1157–1164.
- 143 D. Lanthanum and P. Colloidal, *Angew. Chem. Int. Ed*, 2004, **43**, 5954–5957.
- 144 B. R. Kumar, M. Nyk, T. Y. Ohulchanskyy, C. A. Flask and P. N. Prasad, *Adv. Funct. Mater.*, 2009, **19**, 853–859.
- 145 Z. Chen, H. Chen, H. Hu, M. Yu, F. Li, Q. Zhang, Z. Zhou, T. Yi and C. Huang, *J. Am. Chem. Soc.*, 2008, **130**, 3023–3029.
- 146 H.-P. Zhou, C.-H. Xu, W. Sun and C.-H. Yan, *Adv. Funct. Mater.*, 2009, **19**, 3892–3900.
- 147 M. Nichkova, D. Dosev, S. J. Gee, B. D. Hammock and I. M. Kennedy, *Anal. Chem.*, 2005, **77**, 6864–6873.
- 148 G. Yi and G. Chow, *Chem. Mater.*, 2007, **19**, 341–343.
- 149 S. J. Budijono, J. Shan, N. Yao, Y. Miura, T. Hoye, R. H. Austin, Y. Ju and R. K. Prud, *Chem. Mater.*, 2010, **22**, 1244–1251.
- 150 L. Wang, R. Yan, Z. Huo, L. Wang, J. Zeng, J. Bao, X. Wang, Q. Peng and Y. Li, *Angew. Chem. Int. Ed.*, 2005, **44**, 6054–6057.
- 151 Y. Liu, D. Tu, H. Zhu and X. Chen, *Chem. Soc. Rev.*, 2013, **42**, 6924.
- 152 S. Sivakumar, P. R. Diamente and F. C. J. M. Van Veggel, *Chem. - A Eur. J.*, 2006, **12**, 5878–5884.
- 153 J. Shan, J. Chen, J. Meng, J. Collins, W. Soboyejo, J. S. Friedberg, Y. Ju, J. Shan, J. Chen, J. Meng, J. Collins, W. Soboyejo, J. S. Friedberg and Y. Ju, *J. Appl. Phys.*, 2008, **094308**, 1–7.
- 154 C. Li and J. Lin, *J. Mater. Chem.*, 2010, **20**, 6831.

- 155 M. Ghalawat and P. Poddar, *J. Phys. Chem. C*, 2021, **125**, 7932–7943.
- 156 C. Li, C. Zhang, Z. Hou, L. Wang, Z. Quan, H. Lian and J. Lin, *J. Phys. Chem. C*, 2009, **113**, 2332–2339.
- 157 D. Ma, D. Yang, J. Jiang, P. Cai and S. Huang, *CrystEngComm*, 2010, **12**, 1650–1658.
- 158 C. Li, Z. Quan, J. Yang, P. Yang and J. Lin, *Inorg. Chem.*, 2007, **46**, 6329–6337.
- 159 S. Wu, Y. Ning and S. Zhang, *J. Nanomater.*, 2012, **2012**, 1–8.
- 160 M. Oca, *Nanotechnology*, 2007, **18**, 455606.
- 161 F. Wang, Y. Han, C. S. Lim, Y. Lu, J. Wang, J. Xu, H. Chen, C. Zhang, M. Hong and X. Liu, *Nature*, 2010, **463**, 1061–1065.
- 162 S. Zeng, G. Ren, C. Xu and Q. Yang, *CrystEngComm*, 2011, **13**, 1384–1390.
- 163 X. Wang, J. Zhuang, Q. Peng and Y. Li, *Nat. Lett.*, 2005, **437**, 121–124.
- 164 J. Boyer, L. A. Cuccia and J. A. Capobianco, *Nano Lett.*, 2007, **7**, 847–852.
- 165 L. Li, W. Jiang, H. Pan, X. Xu, Y. Tang and J. Ming, *J. Mater. Chem. C*, 2007, **111**, 4111–4115.
- 166 X. Liang, X. Wang, J. Zhuang, Q. Peng, Y. Li and T. U. V., *Inorg. Chem.*, 2007, **46**, 6050–6055.
- 167 T. Jiang, W. Qin, W. Di, R. Yang, D. Liu, X. Zhai and G. Qin, *CrystEngComm*, 2012, **14**, 2302–2307.
- 168 B. M. Walsh, N. P. Barnes, M. Petros, J. Yu and U. N. Singh, *J. Appl. Phys.*, 2004, **95**, 3255–3271.
- 169 O. Hellmig, S. Salewski, A. Stark, J. Schwenke, P. E. Toschek, K. Sengstock and V. M. Baev, *Opt. Lett.*, 2010, **35**, 2263–2265.
- 170 Y. Zhang, L. Li, X. Zhang and Q. Xi, *J. Rare Earths*, 2008, **26**, 446–449.
- 171 C.-H. Huang and T.-M. Chen, *Inorg. Chem.*, 2011, **50**, 5725–5730.
- 172 Y. Zhou, W. Zhuang, Y. Hu, R. Liu, H. Xu, M. Chen, Y. Liu, Y. Li, Y. Zheng and G. Chen, *Inorg. Chem.*, 2019, **58**, 1492–1500.
- 173 X. Mao, J. Yu, J. Xu, L. Wan, Y. Yang, H. Lin, J. Xu and R. Zhou, *Phys. status solidi*, 2019, **216**, 1900382.
- 174 X. Chen, W. Xu, H. Song, C. Chen, H. Xia, Y. Zhu, D. Zhou, S. Cui, Q. Dai and J. Zhang, *ACS Appl. Mater. Interfaces*, 2016, **8**, 9071–9079.
- 175 C. Strohhöfer and A. Polman, *J. Appl. Phys.*, 2001, **90**, 4314–4320.

- 176 P. G. Kik and A. Polman, *J. Appl. Phys.*, 2003, **93**, 5008–5012.
- 177 H. J. M. A. A. Zijlmans, J. Bonnet, J. Burton, K. Kardos, T. Vail, R. S. Niedbala and H. J. Tanke, *Anal. Biochem.*, 1999, **267**, 30–36.
- 178 S. Wu, G. Han, D. J. Milliron, S. Aloni, V. Altoe, D. V. Talapin, B. E. Cohen and P. J. Schuck, *Proc. Natl. Acad. Sci. U. S. A.*, 2009, **106**, 10917–10921.
- 179 D. Chatterjee, A. Rufaihah and Y. Zhang, *Biomaterials*, 2008, **29**, 937–943.
- 180 M. Nyk, R. Kumar, T. Y. Ohulchanskyy, E. J. Bergey and P. N. Prasad, *Nano Lett.*, 2008, **8**, 3834–3838.
- 181 L. Xiong, Z. Chen, Q. Tian, T. Cao, C. Xu and F. Li, *Anal. Chem.*, 2009, **81**, 8687–8694.
- 182 J. Wang, F. Wang, C. Wang, Z. Liu and X. Liu, *Angew. Chem. Int. Ed.*, 2011, **50**, 10369–10372.
- 183 G. K. Das, Y. Zhang, L. D’Silva, P. Padmanabhan, B. C. Heng, J. S. Chye Loo, S. T. Selvan, K. K. Bhakoo and T. T. Yang Tan, *Chem. Mater.*, 2011, **23**, 2439–2446.
- 184 Q. Ju, D. Tu, Y. Liu, R. Li, H. Zhu, J. Chen, Z. Chen, M. Huang and X. Chen, *J. Am. Chem. Soc.*, 2012, **134**, 1323–1330.
- 185 Q. Liu, Y. Sun, T. Yang, W. Feng, C. Li and F. Li, *J. Am. Chem. Soc.*, 2011, **133**, 17122–17125.
- 186 G. Tian, Z. Gu, L. Zhou, W. Yin, X. Liu, L. Yan and S. Jin, *Adv. Mater.*, 2012, **24**, 1226–1231.
- 187 K. Deng, Z. Hou, X. Li, C. Li, Y. Zhang, X. Deng, Z. Cheng and J. Lin, *Sci. Rep.*, 2015, **5**, 7851.
- 188 H.-L. Cong, F.-F. Jia, S. Wang, M.-T. Yu, Y.-Q. Shen and B. Yu, *Integr. Ferroelectr.*, 2020, **206**, 66–78.
- 189 G. S. Gowd, M. K. Patra, M. Mathew, A. Shukla, S. Songara, S. R. Vadera and N. Kumar, *Opt. Mater. (Amst.)*, 2013, **35**, 1685–1692.
- 190 P. Yang, Z. Quan, Z. Hou, C. Li, X. Kang, Z. Cheng and J. Lin, *Biomaterials*, 2009, **30**, 4786–4795.
- 191 L. Ruiyi, L. Zaijun, S. Xiulan, J. Jan, L. Lin, G. Zhiguo and W. Guangli, *Chem. Eng. J.*, 2020, **382**, 122992.
- 192 Y. Chen, H. Lin, R. Tong, N. An and F. Qu, *Colloids Surfaces B Biointerfaces*, 2017, **154**, 429–437.

- 193 M. Laurenti, M. Paez-Perez, M. Algarra, P. Alonso-Cristobal, E. Lopez-Cabarcos, D. Mendez-Gonzalez and J. Rubio-Retama, *ACS Appl. Mater. Interfaces*, 2016, **8**, 12644–12651.
- 194 L. Mattsson, K. D. Wegner, N. Hildebrandt and T. Soukka, *RSC Adv.*, 2015, **5**, 13270–13277.
- 195 C. Liu, Z. Wang, H. Jia and Z. Li, *Chem. Commun.*, 2011, **47**, 4661.
- 196 H. S. Mader and O. S. Wolfbeis, *Anal. Chem.*, 2010, **82**, 5002–5004.
- 197 P. Kannan, F. Abdul Rahim, R. Chen, X. Teng, L. Huang, H. Sun and D.-H. Kim, *ACS Appl. Mater. Interfaces*, 2013, **5**, 3508–3513.
- 198 S. Zhan, J. Xiong, G. Nie, S. Wu, J. Hu, X. Wu, S. Hu, J. Zhang, Y. Gao and Y. Liu, *Adv. Mater. Interfaces*, 2019, **6**, 1802089.
- 199 S. Cui, S. Xu, H. Song, W. Xu, X. Chen, D. Zhou, Z. Yin and W. Han, *RSC Adv.*, 2015, **5**, 99099–99106.
- 200 S. Wang, X. Wang, X. Chen, X. Cao, J. Cao, X. Xiong and W. Zeng, *RSC Adv.*, 2016, **6**, 46317–46324.
- 201 R. Zou, Y. Chang, T. Zhang, F. Si, Y. Liu, Y. Zhao, Y. Liu, M. Zhang, X. Yu, X. Qiao, G. Zhu and Y. Guo, *Front. Chem.*, 2019, **7**, 1–10.
- 202 Y. Ma, S. Huang, M. Deng and L. Wang, *ACS Appl. Mater. Interfaces*, 2014, **6**, 7790–7796.
- 203 Y. Ma and L. Wang, *Talanta*, 2014, **120**, 100–105.
- 204 R. Singhaal, L. Tashi, Z. U. Nisa, N. A. Ashashi, C. Sen, S. Devi and H. N. Sheikh, *RSC Adv.*, 2021, **11**, 19333–19350.
- 205 L. Mukhopadhyay and V. K. Rai, *New J. Chem.*, 2017, **41**, 7650–7661.
- 206 S. Liu, H. Ming, J. Cui, S. Liu, W. You, X. Ye, Y. Yang, H. Nie and R. Wang, *J. Phys. Chem. C*, 2018, **122**, 16289–16303.
- 207 S. Biswas, L. Mukhopadhyay, M. Mondal and V. K. Rai, *J. Rare Earths*, 2021, **39**, 291–296.
- 208 G.-B. Shan, H. Assaoudi and G. P. Demopoulos, *ACS Appl. Mater. Interfaces*, 2011, **3**, 3239–3243.
- 209 L. Liang, Y. Liu and X.-Z. Zhao, *Chem. Commun.*, 2013, **49**, 3958.
- 210 P. Ramasamy and J. Kim, *Chem. Commun.*, 2014, **50**, 879–881.
- 211 M. Luoshan, L. Bai, C. Bu, X. Liu, Y. Zhu, K. Guo, R. Jiang, M. Li and X. Zhao, *J. Power Sources*, 2016, **307**, 468–473.

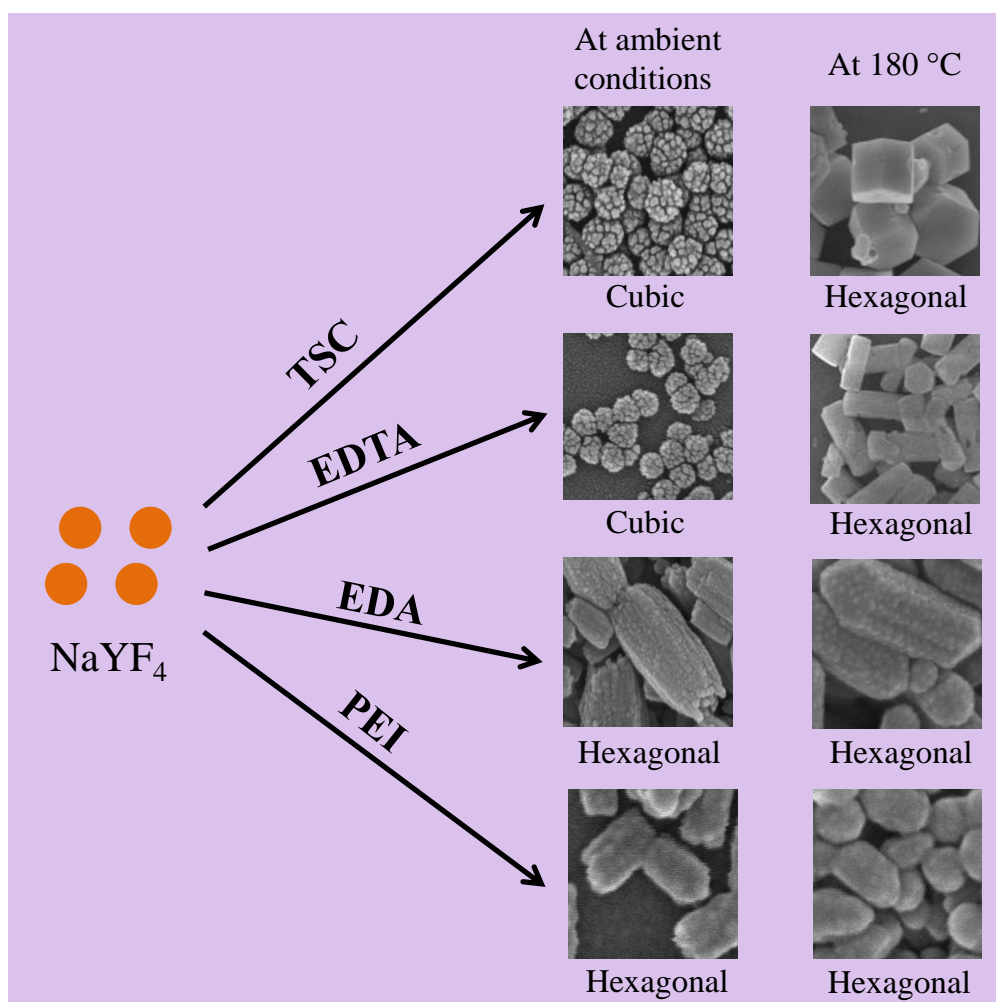
- 212 P. Du, J. H. Lim, J. W. Leem, S. M. Cha and J. S. Yu, *Nanoscale Res. Lett.*, 2015, **10**, 321.
- 213 N. Chander, A. F. Khan, V. K. Komarala, S. Chawla and V. Dutta, *Prog. Photovoltaics Res. Appl.*, 2016, **24**, 692–703.
- 214 R. Rajeswari, K. Susmitha, C. K. Jayasankar, M. Raghavender and L. Giribabu, *Sol. Energy*, 2017, **157**, 956–965.
- 215 P. Tadge, R. S. Yadav, P. K. Vishwakarma, S. B. Rai, T.-M. Chen, S. Sapra and S. Ray, *J. Alloys Compd.*, 2020, **821**, 153230.
- 216 W. J. Kim, M. Nyk and P. N. Prasad, *Nanotechnology*, 2009, **20**, 185301.
- 217 T. Blumenthal, J. Meruga, P. Stanley May, J. Kellar, W. Cross, K. Ankireddy, S. Vunnam and Q. N. Luu, *Nanotechnology*, 2012, **23**, 185305.
- 218 J. M. Meruga, W. M. Cross, P. Stanley May, Q. Luu, G. a. Crawford and J. J. Kellar, *Nanotechnology*, 2012, **23**, 395201.
- 219 M. Mondal and V. K. Rai, *J. Alloys Compd.*, 2018, **750**, 304–311.
- 220 M. You, J. Zhong, Y. Hong, Z. Duan, M. Lin and F. Xu, *Nanoscale*, 2015, **7**, 4423–4431.
- 221 H. Tan, G. Gong, S. Xie, Y. Song, C. Zhang, N. Li, D. Zhang, L. Xu, J. Xu and J. Zheng, *Langmuir*, 2019, **35**, 11503–11511.
- 222 Y. Liu, S. Liang, C. Yuan, A. Best, M. Kappl, K. Koynov, H. Butt and S. Wu, *Adv. Funct. Mater.*, 2021, **31**, 2103908.
- 223 N. Dhananjaya, C. Shivakumara, R. Saraf and H. Nagabhushana, *Mater. Res. Bull.*, 2016, **75**, 100–109.
- 224 M. Rajendran and S. Vaidyanathan, *J. Alloys Compd.*, 2019, **789**, 919–931.
- 225 R. Dey and V. K. Rai, *Dalt. Trans.*, 2014, **43**, 111–118.
- 226 Y. Xu, J. Chen, H. Zhang, H. Wei, L. Zhou, Z. Wang, Y. Pan, X. Su, A. Zhang and J. Fu, *J. Mater. Chem. C*, 2020, **8**, 247–252.
- 227 H. R. V., S. P. P., M. B. M., V. R. P., S. T., S. Luís F. and V. N., *Spectrochim. Acta Part A Mol. Biomol. Spectrosc.*, 2018, **188**, 516–524.
- 228 B. X. Liang, X. Wang, J. Zhuang, Q. Peng and Y. Li, *Adv. Funct. Mater.*, 2007, 2757–2765.
- 229 B. Huang, H. Dong, K.-L. Wong, L.-D. Sun and C.-H. Yan, *J. Phys. Chem. C*, 2016, **120**, 18858–18870.

- 230 S. K. Gupta, P. S. Ghosh, M. Sahu, K. Bhattacharyya, R. Tewari and V. Natarajan, *RSC Adv.*, 2015, **5**, 58832–58842.
- 231 I. V. Khodyuk, F. G. A. Quarati, M. S. Alekhin and P. Dorenbos, *J. Appl. Phys.*, 2013, **114**, 123510.
- 232 S. S. Perera, D. K. Amarasinghe, K. T. Dissanayake and F. a. Rabuffetti, *Chem. Mater.*, 2017, **29**, 6289–6297.
- 233 B. Szefczyk, R. Roszak and S. Roszak, *RSC Adv.*, 2014, **4**, 22526.
- 234 X. C. D. Tu, Y. Liu, H. Zhu, R. Li, L. Liu, *Angew. Chem. Int. Ed.*, 2013, **52**, 1128–1133.
- 235 B. Szpikowska-Sroka, N. Pawlik, T. Goryczka and W. A. Pisarski, *RSC Adv.*, 2015, **5**, 98773–98782.
- 236 L. Wang and Y. Li, *Chem. Mater.*, 2007, **19**, 727–734.
- 237 X. Hu, T. Wei, J. Wang, Z.-E. Liu, X. Li, B. Zhang, Z. Li, L. Li and Q. Yuan, *Anal. Chem.*, 2014, **86**, 10484–10491.

Chapter 2



Analyzing the effect of the ligands on the crystal phase and morphology of NaYF₄ nanophosphors



Outline

In this chapter, the synthesis of NaYF₄: Gd³⁺, Tb³⁺ crystals is reported using various functional molecules at different temperatures. The factors governing the evolution of phase and shape of NaYF₄ crystals are studied and discussed. It was observed that the cubic phase was formed using carboxylic-functionalized ligands at ambient conditions. In contrast, the hexagonal phase of NaYF₄ was formed utilizing amine-functionalized ligands at the same temperature. Since an easy protocol for synthesizing the hexagonal phase NaYF₄ at a lower temperature is still lacking; thus, this work provides an opportunity for the researchers to prepare the phase with precisely controlled morphology and size. The effect of the various functional ligands on the morphology of NaYF₄ is systematically investigated and discussed. Furthermore, the plausible mechanism of influence of ligands on the phase, morphology, and growth process of NaYF₄: Gd³⁺, Tb³⁺ is proposed. The effect of these parameters on optical properties is also studied, which suggests that the emission intensity of the NPs prepared at laboratory temperature is comparable with the intensity of the samples prepared hydrothermally. The work in the chapter suggests that this simple approach can be used and extended further for the synthesis of different phases of NPs.

2.1 Introduction

Lanthanide ion-doped phosphors with luminescence properties are currently utilized in areas ranging from displays, optoelectronics, lasers to being an effective fluorophore in biolabeling and imaging techniques.^{1,2,3} In recent years, due to the size- and shape-dependent physicochemical properties of inorganic materials, morphology control of nano- and micro-materials has taken the spotlight.^{4,5,6} As mentioned in *Chapter 1, Section 1.8*, there are different ways in which morphology can be controlled by altering the reaction conditions during the synthesis. In this work, we selected NaYF₄ as a model system to demonstrate the effect of diffusion flux of monomers on the phase, morphology, and size control. It is reported as the best luminescent matrix owing to its low lattice phonon energy and high chemical stability. Moreover, due to its wide bandgap, it is transparent in the visible and UV regions, which expands its utility in various applications.^{7,8} Up to now, the NaYF₄ with a variety of sizes and shapes can be synthesized via numerous chemical methods such as co-precipitation, thermal decomposition, solvothermal process, and so on.^{9,10} Even attempts have been made to synthesize NaYF₄ crystals under different reaction conditions with various morphologies.^{11,12,13} Besides, the study of the effect of different reaction conditions on crystal growth is important to investigate the controlled synthesis and formation mechanism of NaYF₄ crystals.

The crystal structure is one of the most critical factors affecting the growth behavior of crystals and, thus, their optical properties. The crystalline seed phases induce different growth kinetics (isotropic or anisotropic) during the growth of NPs, thus resulting in various outlooks at the nanoscale.¹⁴ As discussed in *Chapter 1*, NaYF₄ crystallizes in two phases, viz. cubic (α) and hexagonal (β), which are high temperature metastable and low temperature thermodynamically stable phases, respectively.¹⁵ The cubic NaYF₄ has an isotropic unit cell structure, which generally induces isotropic growth of crystals, and therefore quasi-spherical

NaYF₄ NPs are realized. While, the hexagonal NaYF₄ has an anisotropic unit cell structure, which induces anisotropic growth along different directions, and thus rods, wires, plates, or disks are obtained.¹¹ In the non-equilibrium solution reactions, the cubic NaYF₄ NPs are usually formed preferentially. In most cases, the cubic phase is formed under facile conditions, such as low temperature (even at room temperature) and short reaction time. Due to the thermodynamical instability of α -NaYF₄, they inevitably transform into hexagonal ones beyond a certain particle size.^{16–18} The phase transition of NaYF₄ has been obtained by controlling the synthesis conditions, such as increasing the temperature, prolonging the reaction time, and doping with Ln³⁺ or transition metal ions, which are studied by various research groups.^{19,20} Apart from the crystal phase, shapes of the particles (or morphologies) also affect the luminescent properties of the NPs. Among various factors such as increasing temperature and time, the introduction of ligands plays various roles in synthesis by directing the outcome via manipulation of the rate of precursor reduction and particle aggregation, providing colloidal and facet stabilization. Organic ligands can selectively bind to different crystal planes of NPs during the growth, giving them different architectures.^{21,22}

In this work, we introduced the concept of the ligand effect in the preparation of NaYF₄ crystals at ambient temperature as well as at high temperatures using the hydrothermal method. The ligand effect was used to prepare NaYF₄ crystals with certain phases and controllable morphology. A few carboxylic- and amine-functionalized ligands were selected to study the effect of the ligand on the crystal phase and morphology. Investigated by XRD, FESEM, and TEM, the dynamic nature of ligands strongly influenced the crystal phase and their transition from cubic to hexagonal phase and morphology. Furthermore, possible crystal growth mechanisms with various ligands are proposed. The ligands we chose included trisodium citrate (TSC), ethylenediaminetetraacetic acid (EDTA), ethylenediamine (EDA), and

polyethyleneimine (PEI), whose chemical structures are shown in **Fig. 2.1**. The complexing agents/ligands are used to control the nucleation rate and the growth of particles during the synthesis, control the growth rate of different crystalline facets by interacting through adsorption and desorption.²³ In order to examine the possible growth mechanism, the influence of the concentration of ligands was also investigated. It was also observed that amine-functionalized ligands were able to synthesize hexagonal phase (β -NaYF₄) even at low temperatures of about (27 ± 3) °C. It is widely reported that β -NaYF₄ exhibits approximately an order of magnitude higher UC/DC emission than the cubic one.

To obtain a pure hexagonal phase, typically, thermal treatment is applied to provide the activation energy required to convert α to β -phase. This phase transformation also often requires prolonged synthesis time leading to particle growth and agglomeration. So, it remains a

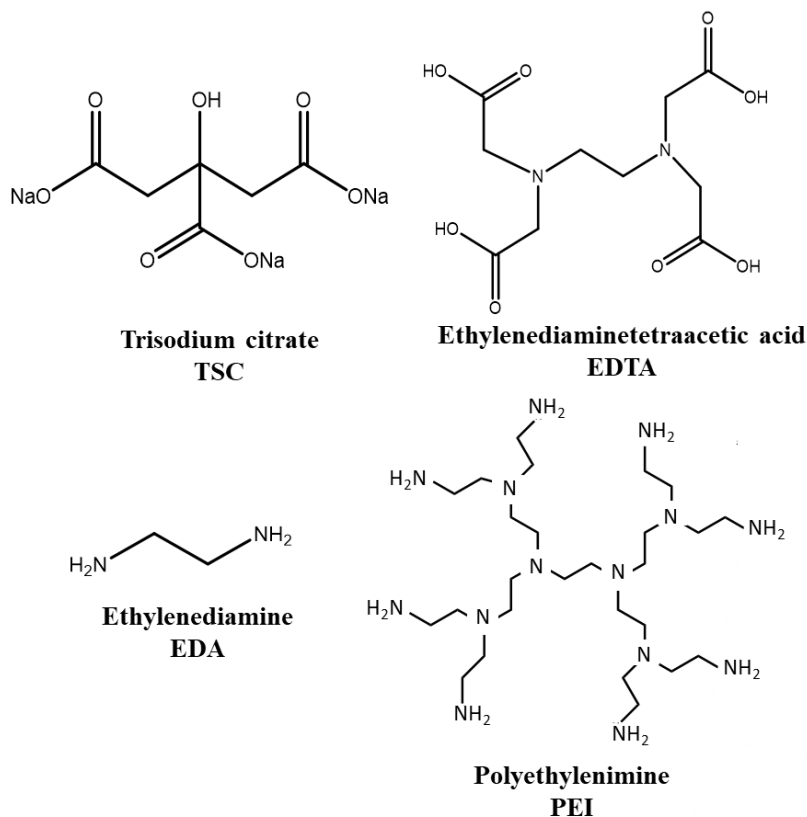


Figure 2.1 The chemical structures of the carboxylic- and amine-functionalized ligands used in this work.

challenge to prepare uniform β -NaYF₄ NPs bypassing the phase transformation process via a facile synthetic approach. There are few methods developed so far for obtaining β -NaYF₄ nanocrystals at low temperatures. In one of the earliest works, Schäfer et al. synthesized β -NaYF₄: Yb, Er using the solid-state method at room temperature; however, the process took more than 200 h to complete.²⁴ Although the reaction completed forming hexagonal phase within 120 min when the temperature was slightly increased to 55 °C. In another attempt by Tang et al. in 2014, pure β -NaYF₄ was prepared using sparingly soluble lanthanide salts and ethanol-water solvent.²⁵ They were able to control the phase by altering the water content in the reaction system. However, for the effective luminescence intensity, samples were treated solvothermally. Thus, a more benign and facile method is required to synthesize hexagonal phase with tunable sizes and shapes.

2.2 Materials and methods

2.2.1 Materials: All the chemicals were of analytical grade and used without further purification. Yttrium nitrate hexahydrate (Y(NO₃)₃·6H₂O, 99.89%), gadolinium nitrate hexahydrate (Gd(NO₃)₃·6H₂O, 99.89%), terbium nitrate hexahydrate (Tb(NO₃)₃·6H₂O, 99.89%) and branched PEI (M_w = 25 000 and M_n = 10 000) were purchased from Sigma Aldrich Inc. Sodium fluoride (NaF), TSC, EDTA, and EDA were received from Thomas Baker chemicals Pvt. Ltd. Ethanol was purchased from Hayman Ltd. Deionized (DI) water was used throughout the experiments.

2.2.2 Synthesis

2.2.2.1 Synthesis of NaYF₄: Gd³⁺, Tb³⁺ phosphors at ambient conditions: For the synthesis of NaYF₄: 15% Gd³⁺, 5% Tb³⁺ phosphors, Y(NO₃)₃, Gd(NO₃)₃, Tb(NO₃)₃ (0.2 M) were added into an aqueous solution containing 0.2 M of TSC as a ligand. The amounts of Gd(NO₃)₃ and Tb(NO₃)₃ were calculated according to 15% and 5% of the total concentration i.e., 0.2 M. After

vigorous stirring for 30 min, NaF solution (2 M) was introduced dropwise into the resultant mixture. The whole solution was continuously stirred for 1.5 h, and the resulting solution was centrifuged and washed with ethanol and DI water. Then, the product was vacuum dried for 8 h. Similarly, other NaYF₄: Gd³⁺, Tb³⁺ samples were prepared at laboratory temperature using different ligands instead of trisodium citrate. It should be noted here that the ratio of Y³⁺/TSC is 1:1 in all of these reactions.

2.2.2.2 Hydrothermal synthesis of NaYF₄: Gd³⁺, Tb³⁺ phosphors at 180 °C: For the hydrothermal synthesis²⁶ of NaYF₄: Gd³⁺, Tb³⁺ phosphors, Y(NO₃)₃, Tb(NO₃)₃, Gd(NO₃)₃ (0.2 M) were added into an aqueous solution containing 0.2 M of TSC as a ligand. After vigorous stirring for 30 min, NaF solution (2 M) was introduced dropwise into the resultant mixture. The whole solution was stirred for 0.5 h and finally was transferred into Teflon liner containing autoclave and heated hydrothermally at 180 °C for 24 h. Thereafter, the autoclave was cooled down to normal temperature; the sample was centrifuged and washed with ethanol and DI water. Finally, the product was dried under vacuum at 60 °C for 8 h. Similarly, other samples of NaYF₄: Gd³⁺, Tb³⁺ were prepared following the procedure as mentioned above using different ligands instead of TSC.

Furthermore, control experiments were done by changing the amount of ligand to study the evolutionary process of the phase and morphology and to understand the coordinating capability of complexing ligands.

2.2.3 Characterization techniques

The purity and crystallinity of the as-synthesized samples were characterized by XRD using a PANalytical X'PERT PRO instrument and iron-filtered Cu-K α radiation ($\lambda = 1.54 \text{ \AA}$) in the 2θ range of 10-80°. To analyze the size and shape of the samples, field emission scanning electron microscopy (FESEM: Hitachi S-4200) was used. The specific structure details,

morphology, and size were obtained by using FEI Tecnai F20 TEM operated at a 200 keV accelerating voltage. The powder samples were dispersed in ethanol and then drop-casted on carbon-coated Cu-TEM grids with 200 mesh and loaded onto a single-tilt sample holder. Photoluminescence spectra were acquired using a Cary Eclipse fluorescence spectrophotometer, equipped with a 400 W Xe-lamp as an excitation source and a Hamamatsu R928 photomultiplier tube as a detector.

2.3 Results and discussion

To investigate the effect of various ligands on the morphology of NaYF₄: Gd³⁺, Tb³⁺ crystals, the structural, morphological, and optical properties of NaYF₄: Gd³⁺, Tb³⁺ phosphors were studied.

- ***Carboxylic-functionalized NaYF₄: Gd³⁺, Tb³⁺ phosphors at ambient conditions***

A series of experiments were carefully designed using different ligands, keeping reaction temperature, time, and concentration of other precursors fixed. The crystallinity and purity of NaYF₄: Gd³⁺, Tb³⁺ crystals prepared using carboxylic-functionalized ligands were first examined by XRD, as shown in **Fig. 2.2**. In this section, the as-prepared samples were synthesized at a laboratory temperature of (27 ± 3) °C. The figure shows that all the peaks in XRD patterns of each product prepared using TSC and EDTA at low temperatures can be indexed to α -NaYF₄, which was in good agreement with the reported (JCPDS no. 77-2042) data. Even though the reactions were performed at low temperature the sharp diffraction peaks in the XRD patterns showed that the samples were formed with good crystallinity. Furthermore, it was observed that the relative intensities of XRD peaks of the as-prepared products were same as compared to the JCPDS data, which confirmed that the NPs did not possess any anisotropic shapes. To validate this observation, the size and shape of the samples were characterized by FESEM and TEM. The FESEM images as shown in **Fig. 2.3a,b** revealed that

the NaYF₄ crystals prepared using both the ligands, TSC and EDTA, have quasi-spherical morphology with an average size of ~100 and ~90 nm, respectively. The average particle sizes in all the samples were calculated by considering nearly 50 nanoparticles. Interestingly, by looking at the images, it appeared that each particle seemed to be formed due to the aggregation of various smaller particles. Thus, to clarify this, the TEM image was taken (**Fig. 2.3c**) for the TSC capped NaYF₄ crystals, which showed that the quasi-spherical particle is not a cluster of smaller particles, but it is just an illusion purely due to morphological features. The average lattice spacing calculated from the image in **Fig. 2.3d** was ~0.31 nm, which matched well with the d-spacing of ~0.32 nm corresponding to (111) plane estimated from the XRD data mentioned above.

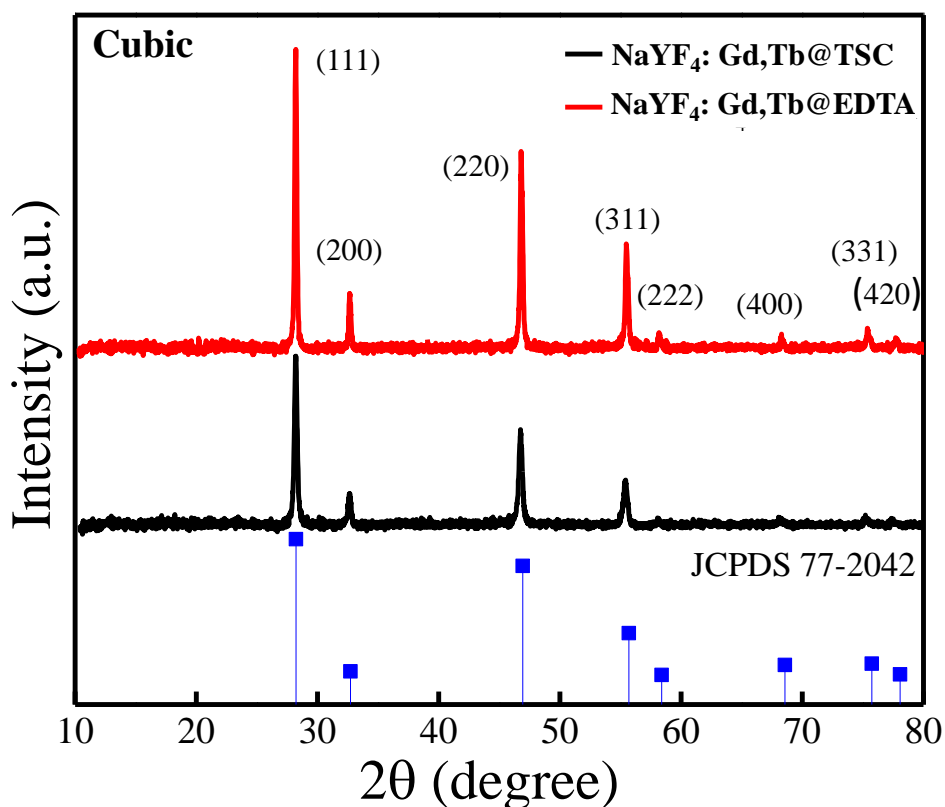


Figure 2.2 The XRD pattern of NaYF₄ capped with carboxylic-functionalized ligands, trisodium citrate (TSC), and ethylenediaminetetraacetic acid (EDTA), synthesized at laboratory temperature of 27 °C ± 3 °C. The XRD data have been compared with standard data of cubic NaYF₄, 77-2042 JCPDS as the reference.

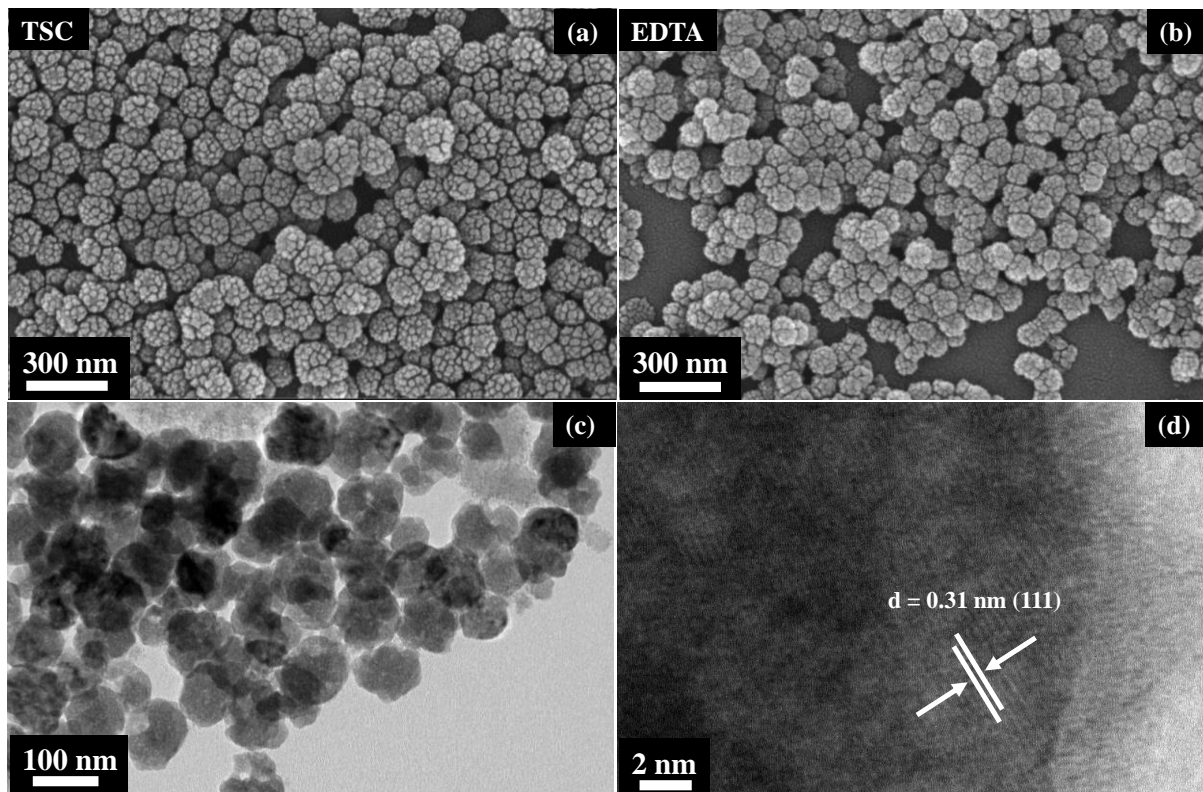


Figure 2.3 The FESEM images showing the morphology of the α -NaYF₄ phosphors capped with (a) TSC and (b) EDTA, synthesized at laboratory temperature of $27\text{ }^{\circ}\text{C} \pm 3\text{ }^{\circ}\text{C}$. The figure (c) shows the TEM image of TSC capped NaYF₄: Gd³⁺, Tb³⁺ crystals with its (d) corresponding lattice fringes with d-spacing of 0.31 nm corresponding to (111) plane.

- **Carboxylic-functionalized NaYF₄: Gd³⁺, Tb³⁺ phosphors at 180 °C**

In this section, the experiments were performed hydrothermally at 180 °C using the carboxylic-functionalized ligands, keeping other controlled parameters fixed. **Fig. 2.4** shows that the peaks in XRD patterns can be indexed to β -NaYF₄ prepared hydrothermally at 180 °C for 24 h using TSC and EDTA as ligands. The data matched well with the reported (JCPDS no. 16-0334) data. The absence of other peaks indicated the purity of as-synthesized crystals with no presence of secondary phase. It is worth mentioning that the relative intensities of (100), (110), (101), and (002) peaks in both the samples were different, indicating the preferentially oriented growth in the presence of different ligands, which was confirmed by the FESEM images. Thus, it can be seen in **Fig. 2.5** that the hexagonal prismatic structures were formed

with TSC, while hexagonal rods were formed in the presence of EDTA with an average length/diameter of $\sim 1.5 \mu\text{m}/1 \mu\text{m}$ and $\sim 1 \mu\text{m}/200 \text{ nm}$, respectively.

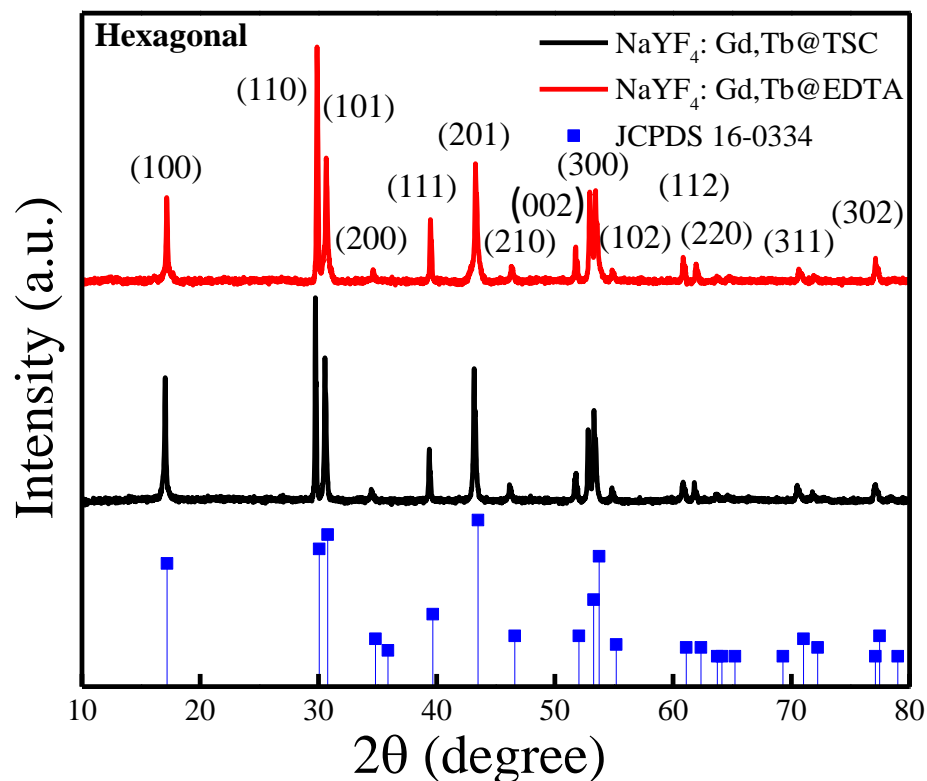


Figure 2.4 The XRD pattern of NaYF₄ capped with carboxylic-functionalized ligands, TSC and EDTA, synthesized hydrothermally at 180 °C for 24 h. The XRD data have been compared with standard data of hexagonal NaYF₄, 16-0334 JCPDS as the reference.

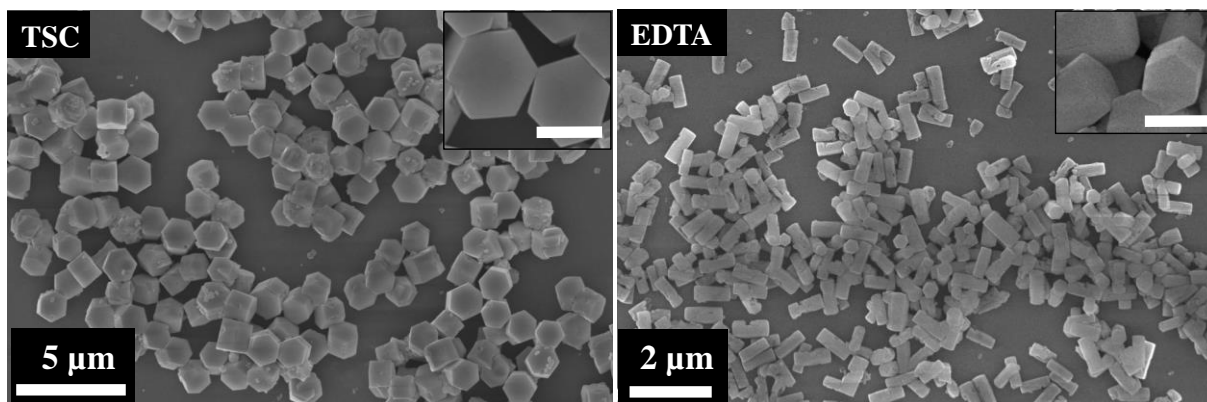


Figure 2.5 The FESEM images showing the morphology of the β -NaYF₄ phosphors capped with TSC and EDTA, synthesized hydrothermally at 180 °C for 24 h. Insets show the zoomed image of the particles with a scale bar of 1 μm and 200 nm, respectively.

Since all the parameters of the reaction were kept constant, the variation in morphology can be ascribed to the pH values and the ligands properties. It should be noted that there was no change in the pH of the system after adding NaF solution during the course of our experiments. Thus, these results strongly suggest that the morphology of the NaYF₄ crystals exhibited remarkable dependence on the type of ligands used in the reaction.

- **Amine-functionalized NaYF₄: Gd³⁺, Tb³⁺ phosphors at ambient conditions**

In this series of experiments, amine-functionalized ligands were used to prepare NaYF₄ crystals at ambient conditions keeping other parameters fixed. The crystallinity and phase purity of NaYF₄: Gd³⁺, Tb³⁺ phosphors prepared using amine-functionalized ligands were examined by XRD, as shown in **Fig. 2.6**. The figure showed that all the peaks in XRD patterns synthesized using EDA and PEI at low temperatures can be indexed to β -NaYF₄. The data matched with the reported (JCPDS no. 16-0334) data in the literature.

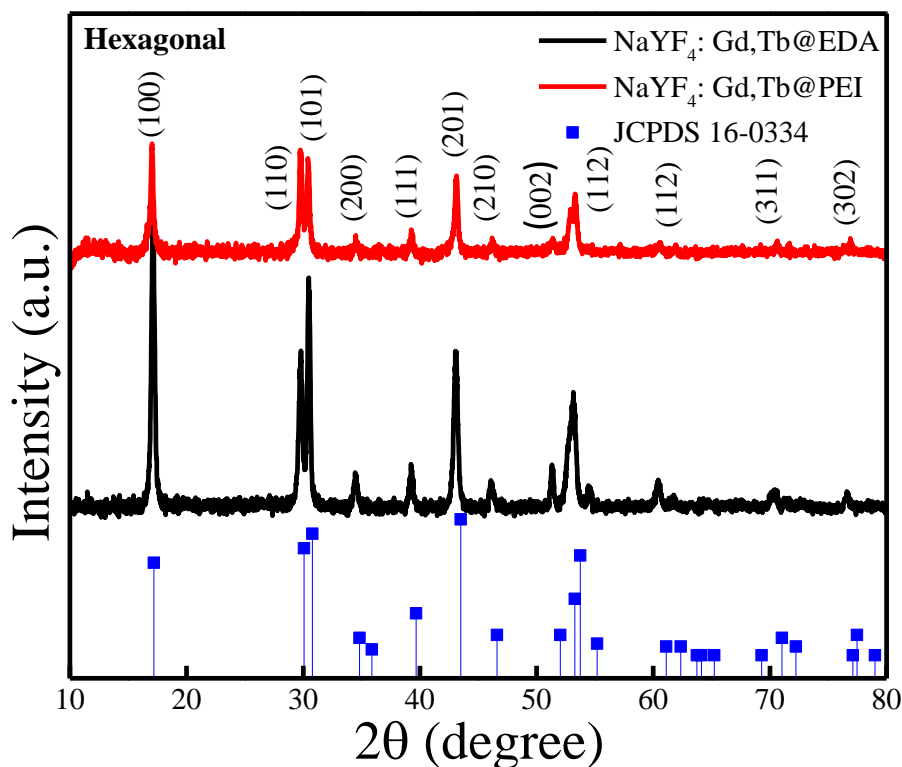


Figure 2.6 The XRD pattern of NaYF₄ capped with amine-functionalized ligands, ethylenediamine (EDA), and polyethylenimine (PEI), synthesized at laboratory temperature of 27 °C ± 3 °C.

In this case also, it was observed that the diffraction peaks were sharp, confirming the good crystallinity of the as-prepared samples even at low temperatures. Furthermore, the relative intensities of (100), (110), (101), and (002) peaks of NaYF₄: Gd³⁺, Tb³⁺ crystals prepared using EDA and PEI as ligands were different when compared to the JCPDS data, which again indicated their preferentially oriented growth. For this, the particle size and shape of various samples were characterized by FESEM and TEM. The FESEM images, as shown in **Fig. 2.7a,b** revealed that the NaYF₄ crystals prepared using EDA and PEI have rods-like morphology with an average length/diameter of ~300 nm/110 nm and ~110 nm/55 nm, respectively. Similar to particles formed in the case of carboxylic-functionalized ligands, the TEM image (**Fig. 2.7c**) confirmed that the rod particle is one single particle and not a cluster or

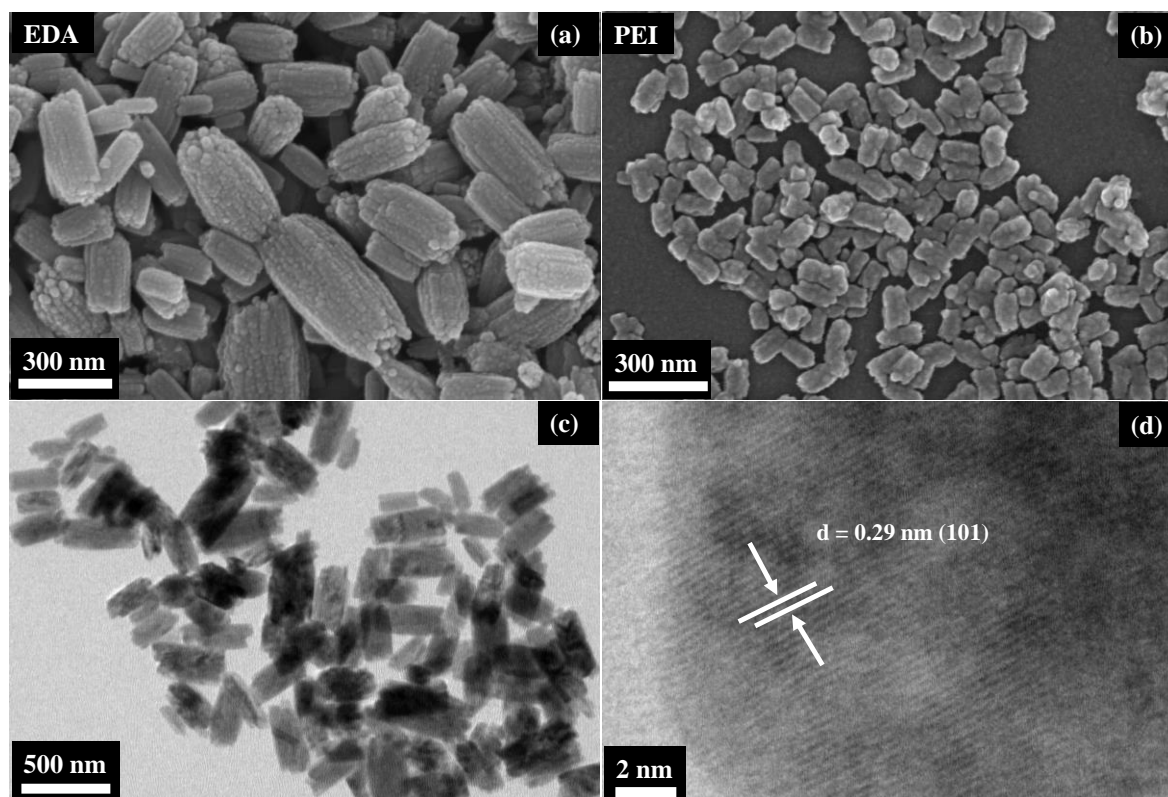


Figure 2.7 The FESEM images showing the morphology of the β -NaYF₄ phosphor nanoparticles capped with (a) EDA and (b) PEI, synthesized at laboratory temperature $27\text{ }^{\circ}\text{C} \pm 3\text{ }^{\circ}\text{C}$. The figure (c) shows the TEM image of EDA capped NaYF₄: Gd³⁺, Tb³⁺ crystals with its (d) corresponding lattice fringes with d-spacing of 0.29 nm.

aggregation of smaller particles. Also, the lattice spacing calculated from the image (**Fig. 2.7d**) was ~0.29 nm, which matched well with the d-spacing of ~0.30 nm, corresponding to (101) plane estimated from the XRD data mentioned above.

- **Amine-functionalized NaYF₄: Gd³⁺, Tb³⁺ phosphors at 180 °C**

In this section, the experiments performed hydrothermally at 180 °C using the amine-functionalized ligands are reported. **Fig. 2.8** showed that all the peaks in XRD patterns prepared hydrothermally using EDA and PEI at 180 °C for 24 h are characteristic of a pure β -NaYF₄. The XRD data matched very well with the reported (JCPDS no. 16-0334) data. The absence of other peaks indicated the purity of as-synthesized products with no secondary phase. The diffraction peaks intensities increased significantly with temperature compared to the samples prepared at ambient conditions, implying that the crystallinity of the sample increased with

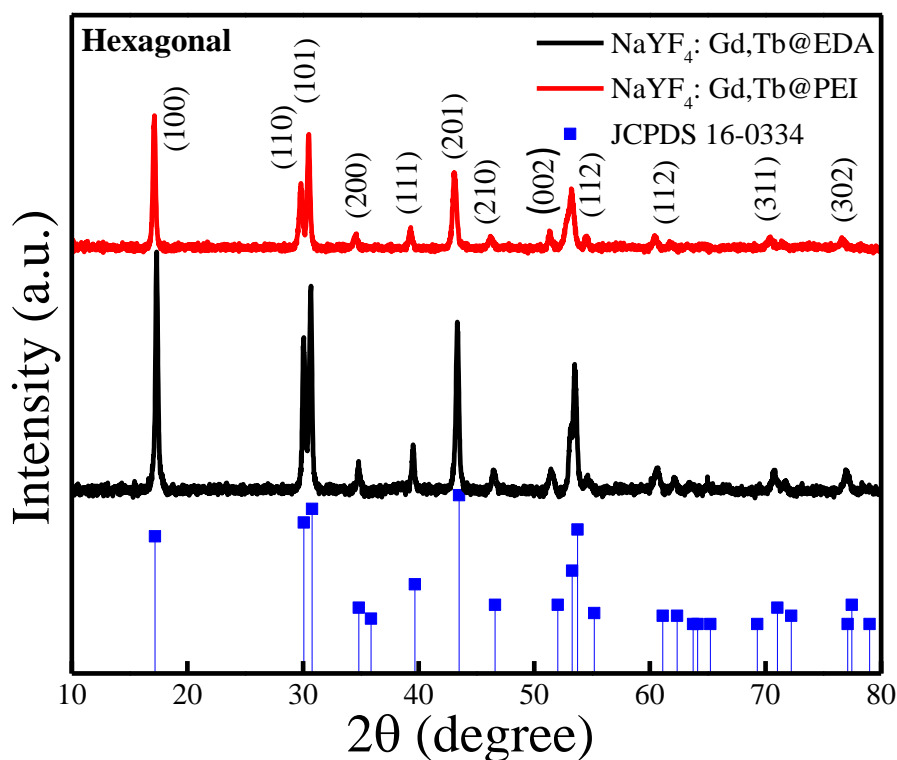


Figure 2.8 The XRD pattern of NaYF₄ capped with amine-functionalized ligands, EDA and PEI, synthesized at hydrothermally at 180 °C for 24 h.

temperature. From **Fig. 2.9**, it was observed that the hexagonal rods were formed in the presence of EDA and PEI with an average length/diameter of ~240 nm/115 nm and ~120 nm/60 nm, respectively. The plausible mechanism for the variation in phase and modulation in the morphology of NaYF₄ phosphors using different types of ligands is discussed next.

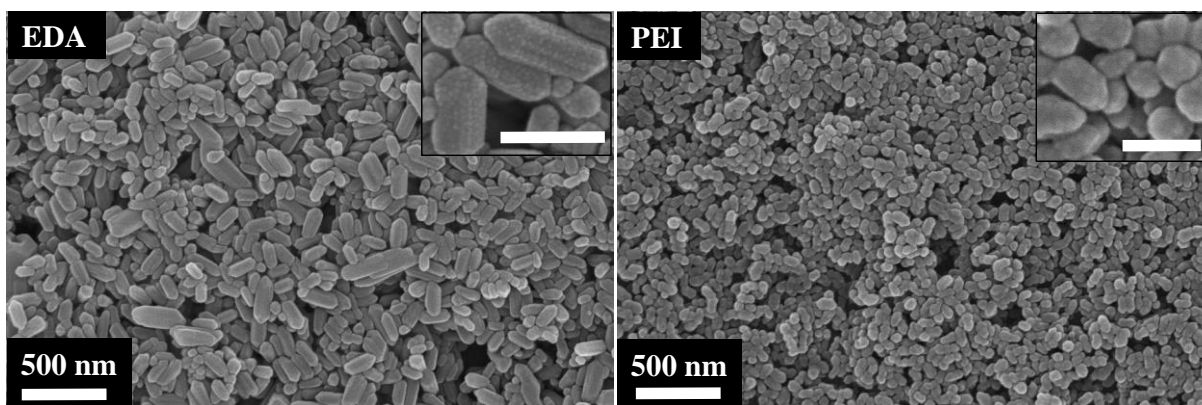


Figure 2.9 The FESEM images showing the morphology of the β -NaYF₄ phosphors capped with EDA and PEI, synthesized hydrothermally at 180 °C for 24 h. Insets show the zoomed image of the particles with a scale bar of 200 nm and 100 nm, respectively.

2.3.1 Growth mechanism and evolution of morphology

A possible growth mechanism for the formation of different phases of NaYF₄ in our system is described in this section.

Carboxylic-functionalized ligands: TSC and EDTA. It is worth mentioning here that for the formation of particles, the reaction has to go through two stages: nucleation and growth. The results that are summarized in the above sections have been acquired after the growth stage of the system since the nucleation stage is difficult to control and study. The crystals prepared with TSC and EDTA as ligands show a similar growth process at lower temperatures. Thus, the process is explained with TSC, taken as an example. With hydroxyl and three carboxylic groups (structure shown in **Fig. 2.1**), TSC is a known strong complexing agent and can form complex with Y³⁺ ions. During the reaction at ambient temperature, when TSC was added in the

lanthanide ions containing aqueous solution, Y³⁺ ions complexes with citrates through strong coordinative interactions. At this point of time, the pH of the solution is nearly 7, which is greater than the 3 pK_a values (pK_{a1} = 3.1, pK_{a2} = 4.8, and pK_{a3} = 6.4) of the citrate molecule. Thus, the molecule is in the form of cit³⁻ in the reaction system and is able to form complex effectively and strongly with Y³⁺ ions, which decreases the free Y³⁺ ions concentration in the solution. Usually, the Y³⁺-citrate complex is weakened or broken under the hydrothermal conditions of high temperature and pressure, so these Y³⁺ ions are released gradually in the solution.²⁷ But in our system, any extra energy is not given to break this complex apart from the thermal energy at room temperature as the reaction is carried out in laboratory conditions only. In this situation, only those Y³⁺ ions are used for the formation of the NaYF₄ phase, which have not been used in the complex formation. Hence, the nucleation and growth process of NaYF₄ would utilize the remaining free Y³⁺ ions in the solution and fluoride ions (F⁻) from the NaF source.

It should be noted here that enough F⁻ ions (ten times as compared to Y³⁺ ions) are available in the solution, which exceeds the solubility product of NaYF₄ to start the nucleation process. Thus, nuclei of cubic NaYF₄ were readily formed at low temperatures, which further grew to form quasi-spherical NPs as confirmed through FESEM and TEM images. During the growth process, TSC ligand, which also acts as a capping agent, interacted strongly with Y³⁺ ions onto different planes of cubic NaYF₄. It was observed that the pH changed to ~9 after the addition of F⁻ source. However, this pH change did not alter the binding affinity of the TSC to the crystal facets, as it was still greater than its pK_a values. Thus, the strong interaction of TSC controlled the growth of the cubic particles restricting their further growth in the system and hence their particle size. So, the cubic NPs of ~100 nm in size and high stability were formed with TSC. Furthermore, when the temperature was increased till 180 °C via hydrothermal route

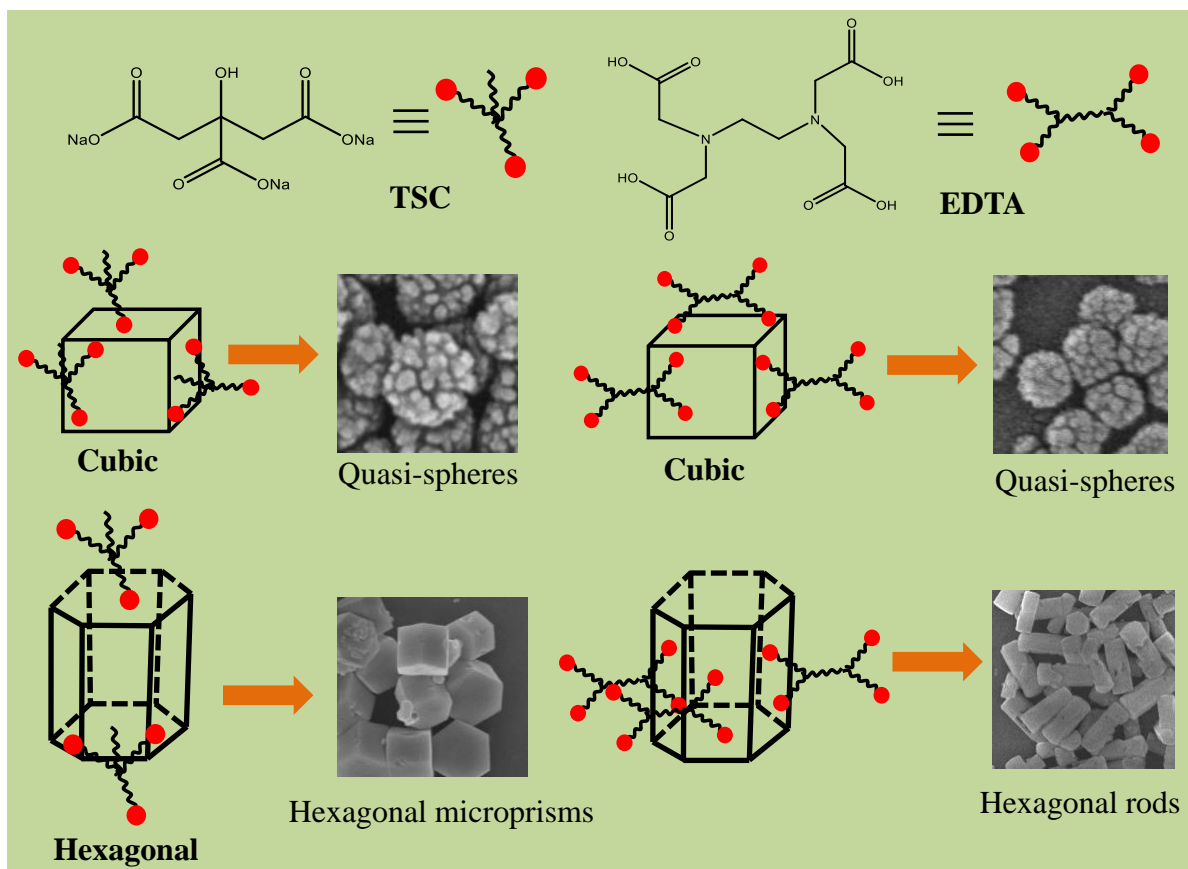
of synthesis, cubic to hexagonal phase transformation took place, and uniform hexagonal prismatic structures of NaYF₄ were formed. High temperature and prolonged time had provided enough energy for the conversion of cubic to thermodynamically stable hexagonal phase.

Similar to TSC, EDTA also formed a strong 1:1 complex with Y³⁺ ions, thereby leaving unbound Y³⁺ ions to bond with F⁻ to form NaYF₄ nuclei at ambient conditions. In this case also, the pH 7 was observed after adding EDTA into the lanthanide ion precursor solution, which is greater than the 3 pK_a values (pK_{a1} = 2, pK_{a2} = 2.7, pK_{a3} = 6.2, and pK_{a4} = 10.3) of EDTA molecule. Thus, the molecule had at least 3 carboxylic groups in the form of COO⁻ in the reaction system and is able to form complex effectively with Y³⁺ ions. Thus, with the availability of Y³⁺ ions, the nuclei of cubic NaYF₄ were readily formed at low temperatures, which further grew to form quasi-spherical NPs. Furthermore, during the growth process of cubic nuclei, the carboxylate group of EDTA strongly interacted with Y³⁺ on different planes, restricting their growth and particle size to ~90 nm. Similarly, when the temperature was increased to 180 °C, cubic to hexagonal phase transformation took place as in the case of TSC, and uniform hexagonal rods were formed with EDTA.

For variation in morphologies of NaYF₄ crystals prepared using the method as mentioned earlier at ambient and high temperature, the mechanism is proposed herewith and schematically shown in **Scheme 1**. Different types of ligands possess varying interactions with different facets and thus, lead to the distinct outlook of the final products. The ability of the ligands to absorb onto certain crystalline planes depends on the interactive force between them. In the case of a cubic crystal, all the sides are isotropic, i.e., the Y³⁺ ions density in all the planes are similar. Thus, the tendency of TSC and EDTA to bind to these planes are equal, giving equal opportunity to planes to grow in all directions; therefore, attaining quasi-spherical shapes in nature. For anisotropic hexagonal crystals, it is widely reported that TSC has the ability to bind

to (002) plane, i.e., the top plane of the hexagonal phase. Thence, it can be concluded that TSC inhibit the growth along the $\langle 0001 \rangle$ direction with a relative enhancement of the growth along $\langle 10\bar{1}0 \rangle$ direction and other parallel directions of hexagonal crystal, giving the outlook of a hexagonal prism.²⁸

In contrast to TSC, EDTA binds to the six symmetric facets of hexagonal crystal parallel to c -axis, thus inhibiting their growth and rendering growth along $\langle 0001 \rangle$ direction. Thus, carboxylate groups bind to the side planes where Ln³⁺ ions density is higher, forming the hexagonal rods.



Scheme 1. The schematic representation shows the evolution of shapes of NaYF₄: Gd³⁺, Tb³⁺ phosphors using carboxylic-functionalized ligands, TSC and EDTA.

Amine-functionalized ligands: EDA and PEI. Both of these ligands experience a similar growth process. The proposed plausible mechanism is discussed, taking EDA as an example. Similar to the above-mentioned cases, the pH of the reaction solution is nearly 7 after adding the amine-functionalized ligands. The pK_a values of EDA are 9.9 and 6.8, which keeps one of the amine groups protonated at pH 7. Thus, the amine-functionalized ligands act as weak ligands as compared to carboxylic-functionalized ligands and cannot effectively form complex and bind to the crystal facets.

Now, during the reaction at ambient temperature, when EDA was added in the precursor solution containing Y³⁺ ions, it formed a complex through amine groups that were not protonated. Therefore, the remaining Y³⁺ formed NaYF₄ nuclei when NaF was added as the F⁻ source, and hexagonal NaYF₄ particles were formed. Since it was mentioned earlier that it was after the growth process that the XRD and FESEM results were taken; so, at this point of time, it was not clear that whether the cubic-to-hexagonal transformation took place or the hexagonal phase was formed directly, which was very unlikely. It was found that the growth rate of formation of β-NaYF₄ was so fast that the NPs were formed within 2 min at ambient temperature. For this clarification, the samples for XRD were immediately taken after adding F⁻ source into the solution, which showed only hexagonal phase with no presence of cubic NaYF₄. It was assumed that if at all cubic phase was formed initially in the system, then due to the dynamic nature of amine ligands at this pH (9 after adding NaF), it did not effectively bind to the different planes of the cubic structure. Thus, the growth of the NPs was not controlled effectively, and the particles grew in size. This phenomenon was also observed in earlier studies in various NPs using different ligands.²⁹ In one of the studies,³⁰ different fatty acids-based ligands were selected to manipulate the growth process and morphology of NaYF₄ crystals. It was shown that fatty acids with different chain lengths such as decanoic acid, myristic acid,

hexanoic acid, lauric acid, and caprylic acid displayed different tendencies to leave the crystal facets, thereby changing the passivating activity of the ligands. This further changed the growth process of the particles with increment in particle size when the tendency of the ligand to leave the facet was high and controlled the particle size when the tendency was low. It was also demonstrated that their different tendencies dramatically influenced the phase transformation process. Short chain ligands with weak binding affinity to the facets did not stabilize the cubic NPs; hence they grew in size, making the phase transition process easier. The growth process in our system may be similar to this, where cubic NPs grew in size. Since the cubic NPs are metastable in nature beyond a certain particle size, thus, they are inevitably converted into hexagonal phase. It is demonstrated in numerous studies that the particle size of NaYF₄ crystal affect the phase transition process.¹⁶ Thus, the synthesis of hexagonal NaYF₄ even at such low temperatures was observed using amine-functionalized ligands, which otherwise take high temperature and prolonged time synthesis.

The same mechanism can be used to describe the growth process in the presence of PEI. The pK_a value of PEI is ~7.2; thus, some of the amine groups might be protonated at pH 7. This altered the complex formation capability of the ligand, changing the availability of the Y³⁺ ions for the nucleation and growth process. Further, after the addition of F⁻ source, pH changed to 9, which decreased the chances of protonation of -NH₂ groups. This might have slightly increased the interaction of PEI onto the crystal facets of the cubic phase, but not to a larger extent. Thus, cubic NPs transformed to hexagonal phase readily. The smaller size hexagonal phase NPs were formed with PEI as compared to EDA due to the stronger interaction of PEI because of its branched structure to control the size of the NPs.

For amine-functionalized NaYF₄ crystals, the mechanism of morphology variation is schematically shown in **Scheme 2**. At both temperatures, a hexagonal phase is formed, having

rods-like shapes. Thus, the growth process is same in all these cases, which is also explained earlier as in the case of EDTA. The amine-functionalized ligands also bind to the six symmetric planes parallel to *c*-axis, thus inhibiting their growth and rendering growth along <0001> direction giving rise to the formation of hexagonal rods. However, their binding affinity to the facets is not as strong as EDTA, which was confirmed by the FESEM images. The proper facets of the side planes were not observed in the case of EDA and PEI due to their dynamic nature in the facet binding.



Scheme 2. The schematic representation shows the evolution of shapes of NaYF₄: Gd³⁺, Tb³⁺ phosphors using amine-functionalized ligands, EDA and PEI.

2.3.2 Effect of ligands concentration on the phase and morphology

To elucidate the growth process of NaYF₄, which was affected by the ligand presence, systematic studies were conducted at laboratory temperature by increasing the concentration of the ligands. XRD and FESEM results revealed that the growth of NaYF₄ crystals was strongly affected by ligand concentrations. The mechanism of formation of NaYF₄ crystals is explained by taking TSC and EDA into consideration, which can be accordingly applied to other ligands

as well. In literature, the effect of temperature and time on phase, sizes, and shapes is well studied,²⁸ thus, the information have been gathered and utilized it to understand the mechanism in our system upon increasing the concentration of the ligands.

For *TSC* as a ligand, the growth process at different ligand concentrations was studied by XRD and SEM results, as shown in **Fig. 2.10**. The three different concentrations of TSC were taken with respect to Y³⁺ ions, Y³⁺:TSC viz. 1:1, 1:2, and 1:4. As already discussed in previous sections, at 1:1 concentration, the cubic phase of NaYF₄ was formed at laboratory temperature using carboxylic-functionalized ligands with quasi-spherical shapes having an average size of ~100 nm. When the Y³⁺:TSC concentration was increased to 1:2, a mixed-phase sample was formed with cubic phase in the majority, as mentioned in the table in **Fig. 2.10** based on XRD results. From the SEM image, it was concluded that quasi-spherical particles belonged to the cubic phase, while hexagonal-shaped plates belonged to the hexagonal phase of NaYF₄. The average sizes of cubic and hexagonal particles in this sample were ~90 nm and ~590 nm, respectively. Interestingly, with further increase in concentration to 1:4, the mixed-phase sample was formed with hexagonal phase in the majority this time with an average diameter of 540 nm of hexagonal plates. Overall, the particle size decreased when the ligand concentration was increased from 1:1 to 1:4. This was observed due to the increase in the capping ability of the TSC, restricting the growth of the particles in all directions, which led to smaller cubic phase particles and smaller and thinner hexagonal phase particles.

It was also demonstrated that in this case that hexagonal phase NPs were formed at ambient conditions with an increase in the concentration of carboxylic-functionalized ligands. With the increase in TSC concentrations, the amount of the complexation increased drastically, which decreased the free Y³⁺ ions in the solution at that temperature to form the NaYF₄ nuclei. Since the same amount of F⁻ source was added in these series of reactions, thus in comparison

to Y³⁺ ions, a large amount of F⁻ can break the bottleneck of the diffusion flux of F⁻ ions into the stagnant solution for the formation of the nuclei of β -phase even at low temperatures maintaining a suitable supersaturation for the nucleation and growth of the β -phase as well along with cubic phase. It has been well documented in the literature by various groups that a high ratio of F⁻ is crucial for synthesizing the hexagonal phase.³¹ However, when the high doses of ligands are used, particle size uniformity is lost, as can be seen in **Fig. 2.10**.

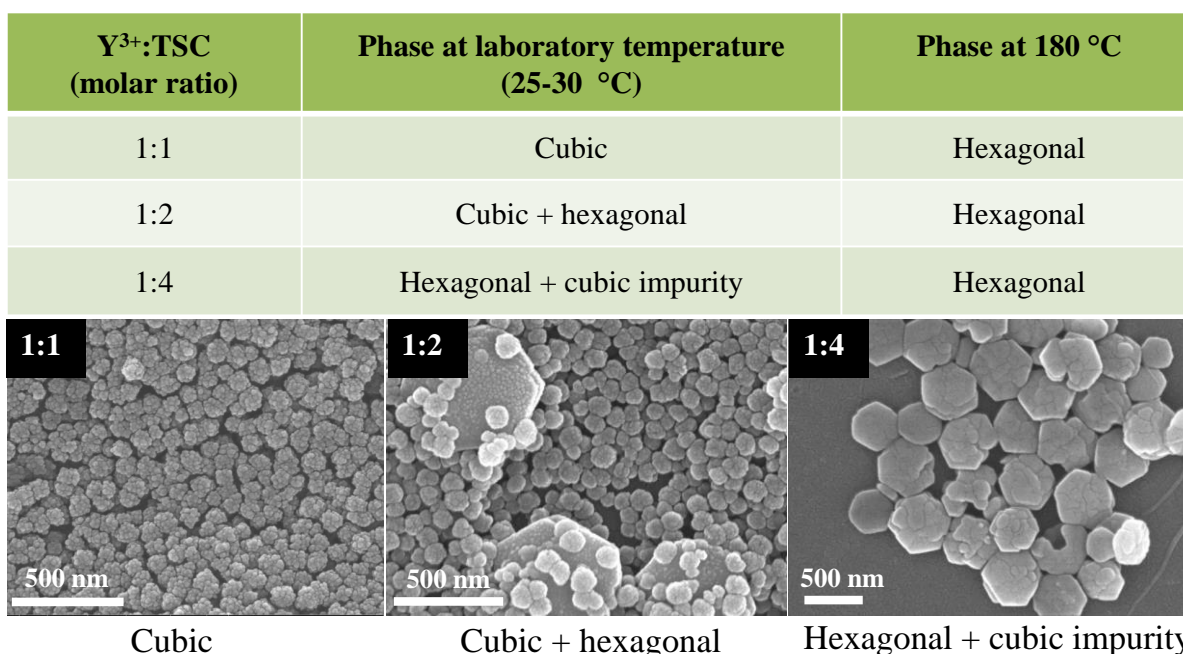
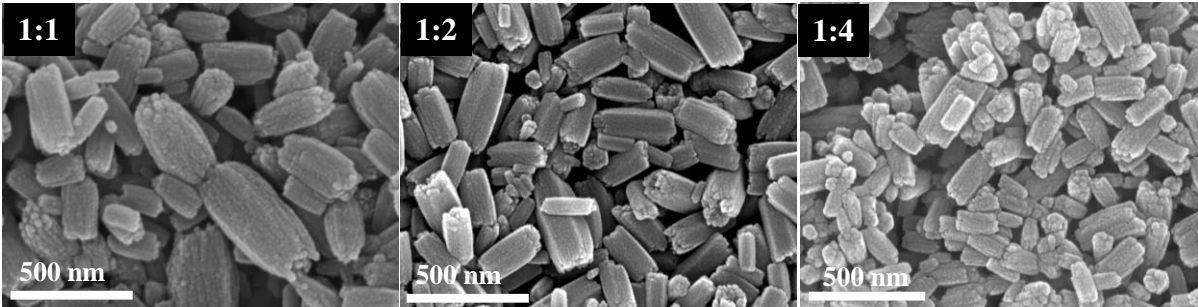


Figure 2.10 The top panel shows the table comprising the results of XRD with increasing concentration of TSC ligands, while the down panel shows the SEM images of the NaYF₄ particles formed with change in ligand concentrations.

Similarly, XRD and SEM analysis was performed for the experiments at ambient temperature with different *EDA* concentrations, as shown in **Fig. 2.11**. When the Y³⁺:EDA concentration was 1:1, the hexagonal phase of NaYF₄ crystals was formed with an average length/diameter of ~300 nm/110 nm. As it is clear from our above experiments, only a hexagonal phase was formed with the amine-functionalized ligands, as confirmed by XRD and FESEM results when the ligand concentrations were increased from 1:1 to 1:2 till 1:4. However,

there was a decrease in the particle sizes with an increase in the concentration of ligands. The average lengths/diameters of NaYF₄: Gd³⁺, Tb³⁺ NPs prepared at 1:2 and 1:4 EDA concentrations are ~280 nm/100 nm and ~230 nm/80 nm, respectively. The decrease in sizes was ascribed to the increase in the capping ability of the EDA and PEI due to their concentrations in the system, restricting the growth of the particles, which led to smaller hexagonal phase particles.

Y ³⁺ :EDA (molar ratio)	Phase at laboratory temperature (25-30 °C)	Phase at 180 °C
1:1	Hexagonal	Hexagonal
1:2	Hexagonal	Hexagonal
1:4	Hexagonal	Hexagonal



1:1

Hexagonal

1:2

Hexagonal

1:4

Hexagonal

Figure 2.11 The top panel shows the table comprising the results of XRD with increasing concentration of EDA ligands, while the down panel shows the SEM images of the NaYF₄ particles formed with change in ligands concentration.

2.3.3 Photoluminescent properties

The Y³⁺ ions do not have 4*d*-electrons ([Kr] 4*d*⁰); thus, the probability of emission in the visible range is negligible in undoped NaYF₄. However, when Ln³⁺ ions are doped in the host matrices, the emission occurs in UV, visible, and NIR range. The Ln³⁺ ion luminescence mainly originates from the electronic transitions within 4*f* configuration. The 4*f* electronic configuration consists of rich energy levels due to Coulombic repulsion between 4*f* electrons

and spin-orbit coupling. These $4f$ electrons are shielded by the filled $5s^2$ and $5p^6$ subshells, which results in the weak influence of the external environment giving the line-like emission spectra. Thus, the bands differ only in their relative intensities. In the present work, Gd^{3+} and Tb^{3+} ions are doped in the NaYF₄ matrix to study the luminescent properties. The molar concentration of Gd^{3+} and Tb^{3+} with respect to Y^{3+} ions in NaYF₄: Gd^{3+}, Tb^{3+} phosphors are 15% and 5%, respectively. This molar concentration was decided by performing experiments with different combinations of concentration of Ln^{3+} ions, which showed the highest luminescent intensity under the same measurement conditions. In this system, Gd^{3+} ion is used as a sensitizer to enhance the luminescence of Tb^{3+} ions. As Gd^{3+} ions exhibit a strong absorption band at 273 nm because of its $^8S_{7/2} \rightarrow ^6I_J$ transitions, as shown in **Fig. 2.12**, NPs containing Gd^{3+} and Ln^{3+} ions together exhibit a very intense excitation band at 273 nm because of this transition in Gd^{3+} ions followed by a nonradiative energy transfer to Ln^{3+} ions.³² Hence, Gd^{3+} ions enhance the emission of Tb^{3+} ions via nonradiative energy transfer.

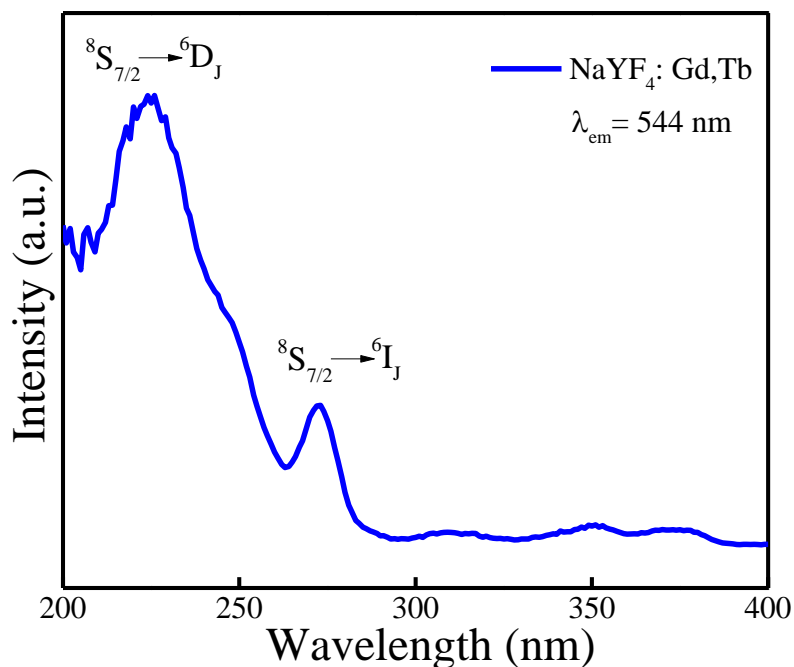


Figure 2.12 The excitation spectra of NaYF₄: Gd,Tb@TSC phosphors at $\lambda_{ex} = 544$ nm, showing the band at 273 nm due to $^8S_{7/2} \rightarrow ^6I_J$ transitions.

The emission spectra monitored at $\lambda_{\text{ex}} = 273$ nm yields emissions in the 480-680 nm region, centered at ~ 489 , ~ 544 , ~ 583 , and ~ 620 nm originating from the transitions of $^5\text{D}_4 \rightarrow ^7\text{F}_6$, $^5\text{D}_4 \rightarrow ^7\text{F}_5$, $^5\text{D}_4 \rightarrow ^7\text{F}_4$, and $^5\text{D}_4 \rightarrow ^7\text{F}_3$, respectively. Among these transitions, the green emission $^5\text{D}_4 \rightarrow ^7\text{F}_5$ at ~ 544 nm is the most intense emission, corresponding to a magnetic dipole transition.³³ **Fig. 2.13a** shows the comparative emission spectra of NaYF₄: Gd³⁺, Tb³⁺ phosphors capped with carboxylic-functionalized ligands. As it is mentioned earlier, the hexagonal phase has larger luminescence efficiency than the cubic phase; thus, it is evident from the spectra that cubic phases formed at laboratory temperature using TSC and EDTA ligands have low luminescence intensity as compared to the products formed at higher temperature hydrothermally. It was also noticed that among cubic-phased samples, the emission intensity is comparable to each other due to similarity in particle sizes. Also, it was believed that the change in the emission intensity between hexagonal-phased NaYF₄ NPs prepared hydrothermally at 180 °C is due to change in their particle size and, consequently, their surface area-to-volume ratio. TSC capped NaYF₄ crystals have an average size (length/diameter) of 1.5 $\mu\text{m}/1 \mu\text{m}$, which is larger than the sample prepared with EDTA as a ligand (1 $\mu\text{m}/200$ nm), which possess low surface area-to-volume ratio, subsequently, low surface defects giving rise to more emission intensity.

Comparing the emission spectra of the samples prepared using amine-functionalized ligands (**Fig. 2.13b**), it was found that all have comparable intensity with respect to each other as they all belong to the hexagonal phase of NaYF₄. However, there are still some differences in their relative emission intensity. EDA capped NPs prepared hydrothermally displayed the highest intensity under similar measurement conditions amongst all the samples. This is due to the difference in their particle size, which results in a change in their surface area-to-volume ratio. Generally, a high surface area allows more fractions of Ln³⁺ ions to be on the surface,

which causes the nonradiative transitions from the surrounding vibrations of molecules like hydroxyl, etc., and hence results in quenching or diminished emission intensity.³⁴ Also, since the NPs synthesized hydrothermally possess better crystallinity, they thus show higher luminescence intensity.

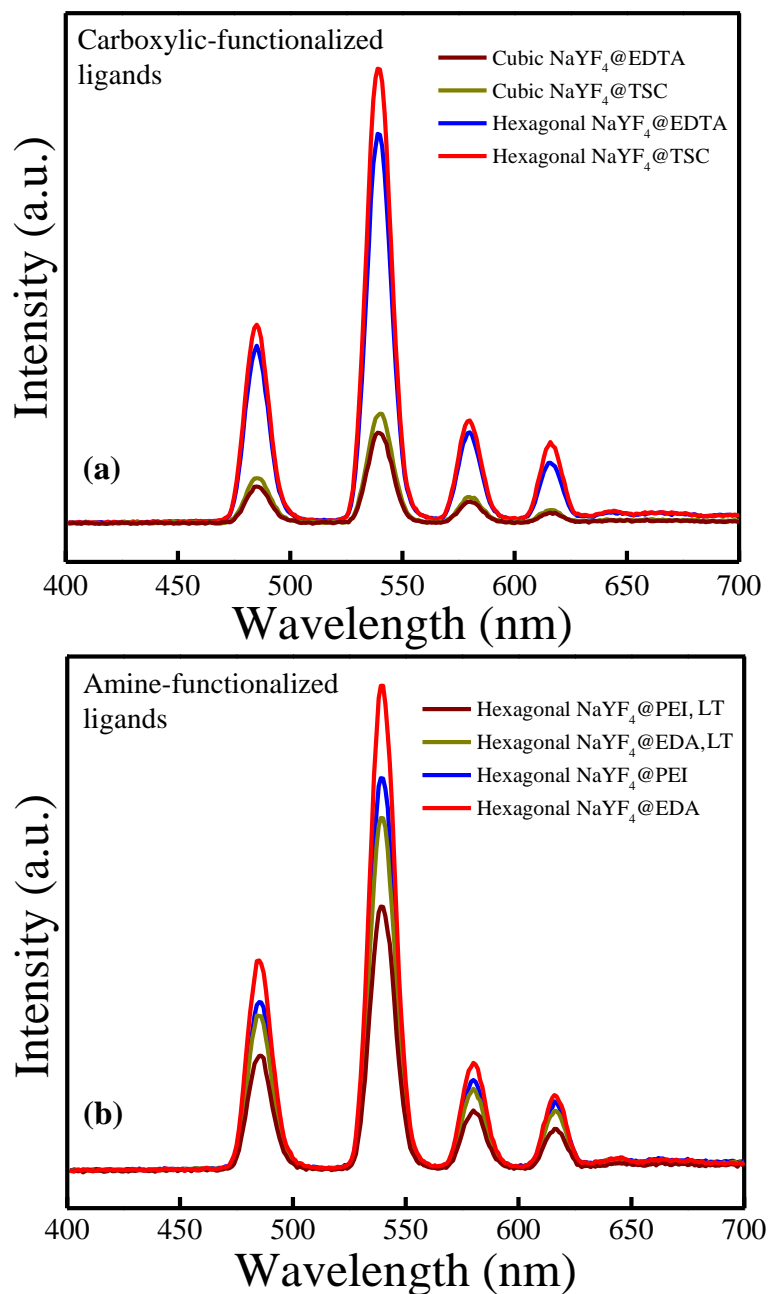


Figure 2.13 The comparison of emission spectra of NaYF₄: Gd³⁺, Tb³⁺ phosphors prepared using (a) carboxylic-functionalized ligands and (b) amine-functionalized ligands at different reaction conditions. All the samples were excited at 273 nm.

Nevertheless, NPs prepared at laboratory temperature have significant intensity so as to be utilized in various applications. The varying luminescence intensities of NaYF₄: Gd,Tb phosphors synthesized using various ligands are also represented by the CIE (Commission Internationale de l'Éclairage) chromaticity diagram, as shown in **Fig. 2.14**. The CIE coordinated values for the emission spectrum are determined to be $x = 0.2621$, $y = 0.5634$ (cubic NaYF₄: Gd,Tb@TSC, LT); $x = 0.2692$, $y = 0.6716$ (hexagonal NaYF₄: Gd,Tb@TSC); $x = 0.2883$, $y = 0.5891$ (hexagonal NaYF₄: Gd,Tb@EDA, LT); $x = 0.2895$, $y = 0.6416$ (hexagonal NaYF₄: Gd,Tb@EDA) located in the green region.

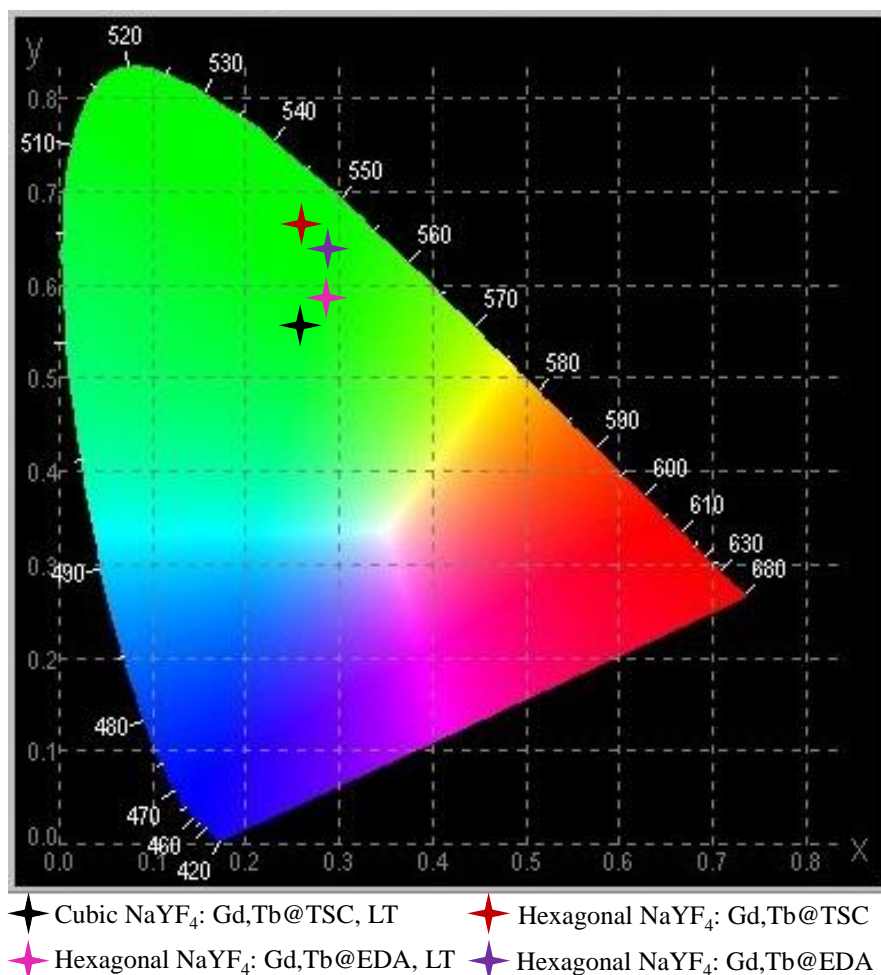


Figure 2.14 The CIE chromaticity diagram showing the emission colors for the as-synthesized phosphors at ambient conditions and high temperature using TSC and EDA as ligands.

Then, the emission intensity of the phosphors synthesized at laboratory temperature using TSC and EDA as ligands at various concentrations were compared. It can be seen in **Fig. 2.15**, the NaYF₄ phosphors synthesized using TSC at 1:1 concentration having a cubic phase and 1:2 concentration having mixed-phase displayed the lowest luminescence intensity among all the samples. This was due to the presence of the cubic phase, which usually displays lower emission intensity than the hexagonal phase. Although sample with 1:4 TSC concentration having hexagonal phase with cubic impurity showed better intensity than 1:1 EDA sample with only hexagonal phase. This was attributed to the difference in their particle size and morphology; hexagonal plates in the TSC sample with an average diameter of ~540 nm and rods in the EDA sample with an average length of ~300 nm was observed. Since the 1:4 TSC sample have larger particle size than 1:1 EDA sample, thus it shows higher emission intensity even with the presence of some cubic impurities in the sample.

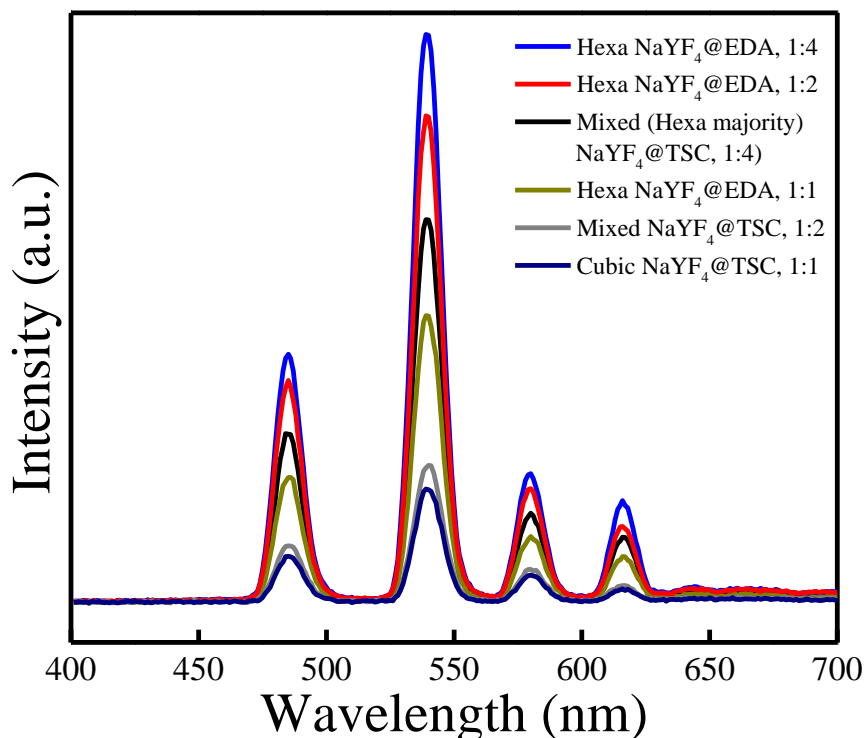


Figure 2.15 The comparison of emission spectra of NaYF₄: Gd³⁺, Tb³⁺ phosphors prepared using carboxylic- and amine-functionalized ligands at various concentrations.

Then, from our earlier knowledge, the emission intensity of 1:2 and 1:4 EDA samples being the highest could be predicted, as seen in the figure, due to their pure hexagonal phase and larger sizes. Based on the above results and analysis, it was reasonably believed that the change in luminescence intensities of the NaYF₄: Gd³⁺, Tb³⁺ crystals predominantly arise from their phase, sizes and morphologies. Accordingly, a suitable ligand and its concentration can be selected to prepare NPs with controlled phase and shape with better optical properties.

2.4 Conclusions

In conclusion, NaYF₄: Gd³⁺, Tb³⁺ phosphors were synthesized using different ligands at different temperatures. Utilizing the ligands during the reaction of NaYF₄ can induce phase and morphology control, crystal growth process, and phase transition. In this work, two different categories of ligands were chosen based on the functional groups it contained: carboxylic and amine group. It was observed that the cubic phase was formed using carboxylic-functionalized ligands at ambient conditions. In contrast, the hexagonal phase of NaYF₄ with high crystallinity was formed with amine-functionalized ligands at the same conditions. Since synthesizing the hexagonal phase directly at low temperatures is still a challenge, the synthesis using a simple approach was achieved even at room temperature. Moreover, the hexagonal phase of NaYF₄ was formed using both types of ligands when synthesized via hydrothermal route at 180 °C. The effect of the different functionalized ligands on the morphology of NaYF₄ was also observed. It can be seen in this work that not only morphology, as reported in various reports, phases can also be controlled using appropriate ligands. Thus, the possible mechanism of influence of ligands on the phase, morphology, and growth process of NaYF₄: Gd³⁺, Tb³⁺ was proposed. Furthermore, the effect of these parameters on optical properties was studied, which suggested that NPs prepared at laboratory temperature show comparable emission intensity with the samples prepared hydrothermally, thus can be utilized for further modification and

applications. Also, after achieving a better understanding of the complex phenomena of crystal growth, this approach can be extended further to synthesize different phases of NPs.

2.5 References

- 1 C. Li and J. Lin, *J. Mater. Chem.*, 2010, **20**, 6831.
- 2 R. K. Sharma, A.-V. Mudring and P. Ghosh, *J. Lumin.*, 2017, **189**, 44–63.
- 3 Y. Zhong and H. Dai, *Nano Res.*, 2020, **13**, 1281–1294.
- 4 J. Piella, N. G. Bastús and V. Puntes, *Chem. Mater.*, 2016, **28**, 1066–1075.
- 5 X. Zhou, K. H. L. Zhang, J. Xiong, J.-H. Park, J. H. Dickerson and W. He, *Nanotechnology*, 2016, **27**, 192001.
- 6 M. Ghalawat and P. Poddar, *J. Phys. Chem. C*, 2021, **125**, 7932–7943.
- 7 J. F. Suyver, J. Grimm, M. K. van Veen, D. Biner, K. W. Krämer and H. U. Güdel, *J. Lumin.*, 2006, **117**, 1–12.
- 8 C. Renero-Lecuna, R. Martín-Rodríguez, R. Valiente, J. González, F. Rodríguez, K. W. Krämer and H. U. Güdel, *Chem. Mater.*, 2011, **23**, 3442–3448.
- 9 C. Yan, H. Zhao, D. F. Perepichka and F. Rosei, *Small*, 2016, **12**, 3888–3907.
- 10 X. Zhu, J. Zhang, J. Liu and Y. Zhang, *Adv. Sci.*, 2019, **6**, 1901358.
- 11 B. X. Liang, X. Wang, J. Zhuang, Q. Peng and Y. Li, *Adv. Funct. Mater.*, 2007, 2757–2765.
- 12 F. Wang, Y. Han, C. S. Lim, Y. Lu, J. Wang, J. Xu, H. Chen, C. Zhang, M. Hong and X. Liu, *Nature*, 2010, **463**, 1061–1065.
- 13 K. Du, X. Xu, S. Yao, P. Lei, L. Dong, M. Zhang, J. Feng and H. Zhang, *CrystEngComm*, 2018, **20**, 1945–1953.
- 14 C. Sun, M. Schäferling, U. Resch-Genger and M. Gradzielski, *ChemNanoMat*, 2021, **7**, 174–183.

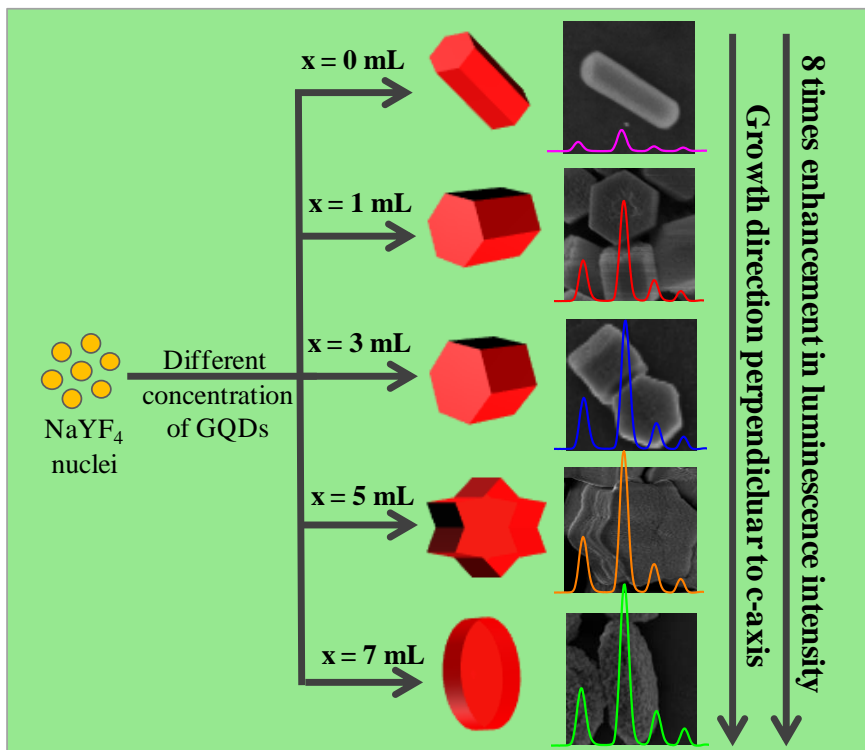
- 15 X. C. D. Tu, Y. Liu, H. Zhu, R. Li, L. Liu, *Angew. chem. Int. Ed*, 2013, **52**, 1128–1133.
- 16 H. Mai, Y. Zhang, R. Si, Z.-G. Yan, L. Sun, L. You and C. Yan, *J. Am. Chem. Soc.*, 2006, **128**, 6426–6436.
- 17 D. T. Klier and M. U. Kumke, *J. Mater. Chem. C*, 2015, **3**, 11228–11238.
- 18 Y. Sui, K. Tao, Q. Tian and K. Sun, *J. Phys. Chem. C*, 2012, **116**, 1732–1739.
- 19 L. Wang and Y. Li, *Chem. Mater.*, 2007, **19**, 727–734.
- 20 X. Zhai, Y. Wang, X. Liu, S. Liu, P. Lei, S. Yao, S. Song, L. Zhou, J. Feng and H. Zhang, *ChemPhotoChem*, 2017, **1**, 369–375.
- 21 C. Li, Z. Quan, J. Yang, P. Yang and J. Lin, *Inorg. Chem.*, 2007, **46**, 6329–6337.
- 22 J. Huang, X. Wang, A. Shao, G. Du and N. Chen, *Materials (Basel)*, 2019, **12**, 3711.
- 23 Z. Wang, F. Tao, L. Yao, W. Cai and X. Li, *J. Cryst. Growth*, 2006, **290**, 296–300.
- 24 H. Schäfer, P. Ptacek, H. Eickmeier and M. Haase, *Adv. Funct. Mater.*, 2009, **19**, 3091–3097.
- 25 C. Tang, Q. Wu, J. Zhuang, X. Yang, J. Wang, M. Wu and G. A. Ozin, *CrystEngComm*, 2014, **16**, 6526–6529.
- 26 P. Padhye, A. Alam, S. Ghorai, S. Chattopadhyay and P. Poddar, *Nanoscale*, 2015, **7**, 19501–19518.
- 27 T. Jiang, W. Qin, W. Di, R. Yang, D. Liu, X. Zhai and G. Qin, *CrystEngComm*, 2012, **14**, 2302–2307.
- 28 P. Padhye and P. Poddar, *J. Mater. Chem. A*, 2014, **2**, 19189–19200.
- 29 N. Pradhan, D. Reifsnnyder, R. Xie, J. Aldana and X. Peng, *J. Am. Chem. Soc.*, 2007, **129**, 9500–9509.
- 30 S. Wu, Y. Liu, J. Chang and S. Zhang, *CrystEngComm*, 2014, **16**, 4472–4477.
- 31 J. Zhao, Y. Sun, X. Kong, L. Tian, Y. Wang, L. Tu, J. Zhao and H. Zhang, *J. Phys. Chem.*

- B*, 2008, **112**, 15666–15672.
- 32 G. Seeta Rama Raju, E. Pavitra and J. S. Yu, *Phys. Chem. Chem. Phys.*, 2014, **16**, 18124.
- 33 S. Kundu, A. Kar and A. Patra, *J. Lumin.*, 2012, **132**, 1400–1406.
- 34 J. Shan, M. Uddi, R. Wei, N. Yao and Y. Ju, *J. Phys. Chem. C*, 2010, **114**, 2452–2461.

Chapter 3



Graphene Quantum Dots driven multiform morphologies of β -NaYF₄: Gd³⁺, Tb³⁺ phosphors: the underlying mechanism and their optical properties



Outline

Dimension and shape tunable architectures of inorganic crystals are of extreme interest due to morphology-dependent modulation of the properties of materials. This chapter presents the influence of *in situ* incorporation of graphene quantum dots (GQDs) on the growth of β -NaYF₄: Gd³⁺, Tb³⁺ phosphor crystals via hydrothermal route. The GQDs functioned as a nucleation site, and by changing the concentration of GQDs, the morphology of β -NaYF₄: Gd³⁺, Tb³⁺ phosphor was changed from rod to flower-like structure to disk-like structure, without any phase transformation. The influence of the size and functionalization of GQDs on the size and shape of phosphor crystals were also systematically studied and discussed. Plausible formation mechanisms of multiform morphologies were proposed based on heterogeneous nucleation and growth. Most interestingly, the experimental results indicated that the photoluminescence properties of β -NaYF₄: Gd³⁺, Tb³⁺ phosphor crystals were strongly dependent on the crystallite size and morphology. This study would be suggestive for the precisely controlled growth of inorganic crystals; consequently, it will open new avenues and thus may possess potential applications in the field of materials and biological sciences.

3.1 Introduction

Lanthanide ion-doped phosphors possess potential applications such as solid-state lasers,¹ high-resolution displays devices, security and brand protection, photodynamic therapy,² fluorescent labels for the detection of molecules,³ bioimaging,^{4,5} medical diagnostics, sensors,^{6,7} light-emitting devices,⁸ solar cells,^{9,10} and so forth, which are better substitutes of conventional fluorophores and organic dyes.¹¹ Although the molar absorption coefficient of organic dyes and quantum dots is comparatively higher than the lanthanide ion-doped phosphors, but high background noise, high blinking probability, poor photostability, potential long-term toxicity hamper the use of these materials.^{12,13} In contrast, the fascinating luminescence features of lanthanide ions arising from intra $4f$ transitions like— narrow bandwidth, long-lived emission, large Stokes and anti-Stokes shift, less blinking, photostability, and low autofluorescence offer excellent prospects for designing new luminescent materials with enhanced properties.^{14,15} As explained, β -NaYF₄ has been demonstrated as the most efficient host for UC and DC emissions because of its low phonon energy ($\sim 350 \text{ cm}^{-1}$), high chemical stability, good optical transparency, high radiative emission rates, and low nonradiative decay rates.¹⁶

In recent years, the research focused on the design and synthesis of inorganic nano/microcrystals with well-defined morphologies and accurately tunable sizes. The precise control over shape and size allows manipulation of the physical, chemical, and biological properties of the nanocrystals as desired. Therefore, developing efficient methods to fabricate multiform inorganic crystals was essential to enhance their performance in existing applications. In the last decades, various efforts have been dedicated to synthesize the lanthanide ion-doped phosphors in uniform but different sizes and shapes.¹⁷ In the kinetic control of the growth process of crystals, various external factors, such as concentration and type of precursors, pH of precursor solution, reaction time/temperature/pressure, type of

solvents, and organic additives, drastically influence the shape of the crystals.¹⁸ All of these factors have been studied quite intensively, and the influence of the organic additives or ligands have been studied in the last chapter. A large number of organic additives and shape directing agents such as OA,¹⁹ polyethylene glycol (PEG),^{5,20} TSC,²¹ CTAB,²² dodecyl trimethylammonium bromide (DTAB),²³ EDTA,²⁴ poly(4-styrenesulfonate),²⁵ etc., are extensively used to control the particle size and tune the crystallinity and morphology of the anisotropic crystals; few have been already mentioned in our previous work. These agents selectively bind to the different facets of the crystals and change their surface energy and chemical potential, which affects the orientation growth rate of different crystals facets, resulting in the formation of different architecture under various environments.¹⁷ Other ligands such as polyvinylpyrrolidone and PEI are also used to control the particle growth of the nanocrystals and endow them with surface functionality for further modification.²⁶ Adjusting the molar ratio of complexing agent/Ln³⁺ ion can also tune the crystal size and shape.²⁷ Various impurity dopant ions such as K⁺, Li⁺, Zn²⁺, Sc³⁺, Gd³⁺ have been used to study the change in phase and morphology.²⁸⁻³² Hitherto, numerous methods have been reported to fabricate the anisotropic nanoparticles such as rods, plates, prism, tubes, spheres, disks, and spindles, etc. These methods include solvothermal, co-precipitation, thermal decomposition, combustion and sol-gel process, among which hydro/solvothermal method is considered a relatively environment friendly method which renders high crystallinity, monodispersity to the material with diverse controllable morphologies and architectures.¹¹ Apart from the homogenous nucleation, the crystal growth strategies based on the heterogenous nucleation are quite popular. The choice of substrates provides an ideal nucleation site by lowering the activation energy barrier for the phase to form. In fact, the heterogenous nucleation makes it possible for some metastable crystalline states to form well below the supersaturation limit of the monomer

concentration.

In this work, the role of graphitic carbon materials with varying surface functionality, size, and shape as a nucleation site for the growth of NaYF₄ nanocrystals were investigated. The rationale behind using these materials was due to their versatile application as the co-components in optically active hybrid materials, as well as their role in defining the crystalline and optical properties of the crystals. Previously, our group reported the *in situ* insertion of graphene quantum dots (GQDs) during the growth of TiO₂ particles. Due to the presence of GQDs, irregular structures of TiO₂-GQDs hybrid were formed instead of regular rod-like TiO₂ particles.³³ The carbon-based nanomaterials such as graphene, carbon nanotubes (CNTs), GQDs, etc., have attracted significant attention owing to their advantageous properties such as high surface area, low density, high thermal stability, and minimal cost. Carbon-based materials possess excellent mechanical strength, electrical and thermal conductivity, and optical properties.³⁴ The GQDs have grabbed more attention due to their chemical inertness, solubility, tunable photoluminescence, long-term photobleaching resistance, biocompatibility, and low cytotoxicity.³⁵ The GQDs have carbon with sp² hybridization having one or a few layers of graphene sheets with lateral dimensions smaller than 100 nm³⁶ and oxygen-containing functional groups on their surfaces and at their edges. The GQDs are called zero-dimension graphene materials. The quantum confinement of electrons has been demonstrated in GQDs and led to applications in photovoltaics, light-emitting diodes and bioimaging.³⁷

Composites of carbon-based materials have become crucial for various applications due to their unique physical and chemical properties. Various composites with GQDs have been synthesized, such as GQD with polyaniline composite films, which have applications in photonic devices.³⁸ The GQDs have also been used as a co-sensitizer in the hybrid dye-sensitized solar cells architectures.^{39,40} In other studies, the amine-functionalized GQDs were

incorporated into the flexible and transparent clay host and cellulose nanofibers (CNF). The resultant GQD@CNF-clay films exhibited photoluminescence, therefore were used as a material for blue light-emitting diodes to achieve white light emission.⁴¹ The development of multifunctional hybrid materials of lanthanide ion-doped phosphors is gearing tremendous interest for a broad range of potential applications in biological and material sciences due to their unique tunable electronic and magnetic properties.⁴² It is worth mentioning that very few reports of the composites of carbon-based materials and lanthanide ion-doped phosphors are known to date for their sensing or photocatalytic applications. A new generation nanocomposites of NaYF₄: Yb,Er and graphene oxide (GO) was fabricated with superior optical limiting performance⁴³ followed by their mechanistic studies in the same year.⁴⁴ Composites of reduced GO and NaYF₄: Yb,Er were proposed to achieve good electrical conductivity, which increased solar cell efficiency by 10 %.⁴⁵ The fabrication of optical pH sensor based on flexible and biocompatible free-standing optical hybrid film composed of GO and NaYF₄:Yb³⁺/Er³⁺ nanoparticles was reported. In this work, the high surface area, mechanical stability, and luminescence quenching capability of GO were utilized as a sensing platform for pH sensing.⁴⁶ In another work, TiO₂-NaYF₄:Yb,Er-Graphene composite photoanode was prepared, which improved solar cell efficiency by increasing interfacial electron transport of FTO/TiO₂.⁴⁷ For biomedical application, multifunctional MWCNT-NaGdF₄: Yb,Er,Eu hybrid nanocomposite was developed for simultaneous magnetic and optical imaging by NaGdF₄: Yb,Er,Eu NPs and photothermal conversion property from MWCNT.⁴⁸ Later, a sensor based on GQDs and ssDNA-UCNP@SiO₂ was developed for the detection of microRNA sequence.⁴⁹ Although the composites of Ln³⁺-doped phosphors and carbon-based nanomaterials have been explored, but the *in situ* incorporation of carbon-based nanomaterials into the Ln³⁺-doped phosphors was not studied.

Thus, a novel strategy was reported to incorporate carbon-based nanomaterial GQDs as a foreign impurity into the β -NaYF₄: Gd³⁺,Tb³⁺ phosphors and their effect on the crystal phase, morphology, and optical properties of β -NaYF₄: Gd³⁺,Tb³⁺ was studied. Interestingly, it was observed that the *in situ* incorporation of GQDs into the β -NaYF₄: Gd³⁺,Tb³⁺ phosphors have significantly influenced the morphology and consequently the optical properties of β -NaYF₄: Gd³⁺,Tb³⁺ crystals. The effect of the concentration of GQDs, the type of surface chemical functionalization, and CNTs on the morphology and photoluminescence properties of the β -NaYF₄: Gd³⁺,Tb³⁺ phosphors were also discussed. For the first time, the morphology tuning of inorganic crystals via the incorporation of GQDs was reported to the best of our knowledge. This work will lead to new opportunities for extending the use of this system in the area of architectural manipulation.

3.2 Materials and methods

3.2.1 Materials: All the chemicals were of analytical grade and were used without further purification. Yttrium nitrate hexahydrate (Y(NO₃)₃.6H₂O, 99.89 %), gadolinium nitrate hexahydrate (Gd(NO₃)₃.6H₂O, 99.89 %), and terbium nitrate hexahydrate (Tb(NO₃)₃.6H₂O, 99.89 %) were purchased from Sigma Aldrich Inc. The sodium chloride (NaCl, 99.9 %) and potassium permanganate (KMnO₄, 99.0 %) were received from Thomas Baker. The ammonium fluoride (NH₄F, > 95 %), and sodium nitrate (NaNO₃, > 99 %) were received from Merck. The graphite powder was obtained from Loba Chemie. The polyethyleneimine (with Mw = 25000 and Mn = 10000), multiwalled carbon nanotubes (MWCNT) and carboxylic-functionalized multiwalled carbon nanotube (COOH-MWCNT) were received from Sigma Aldrich Inc. Deionized water (DI) was used throughout the experiments.

3.2.2 Synthesis

3.2.2.1 Synthesis of GO: The graphene oxide (GO) was prepared using the modified Hummers'

method from the graphite powder.⁵⁰ Briefly, graphite powder (2 g) and sodium nitrate (1 g) were added to a 250 mL round bottom flask at 0 °C. Then 50 mL of concentrated H₂SO₄ was added slowly with stirring below 5 °C. The solution was then stirred for 30 min. KMnO₄ (0.3 g) was then added to the solution below 10 °C. The solution was again stirred for 30 min. Then KMnO₄ (7 g) was added over 1 h below 20 °C. After this, the solution was warmed to 35 ± 3 °C and was stirred for 2 h. Water (90 mL) was then slowly dripped into the paste, causing an increase in temperature to 70 °C. This diluted suspension was stirred at this temperature for 15 min. The mixture was treated with 10 mL of H₂O₂ (30 %) and 55 mL of water to quench the reaction. The suspension turned bright yellow, and subsequently, the solution was filtered, resulting in a light brown precipitate. The precipitate was then washed with a warm solution of 3 % HCl (150 mL). It was dried at 40 °C for 24 h in a vacuum. The GO stock solution was obtained with a concentration of 4 mg/mL.

3.2.2.2 Synthesis of carboxylic and amine co-functionalized GQDs (GQDs): The synthesis of GQDs was done using the previously reported method.⁵¹ To the above-prepared stock solution of graphene oxide (15 mL), 40 mL of H₂O₂ (30 %), and 10 mL of ammonia (25-28 %) were added. This mixture was reacted at 80 °C for 24 h with vigorous stirring. The solution was evaporated at 65 °C to remove unreacted H₂O₂, ammonia, and water. Finally, ethanol was used to precipitate and wash the final GQD product. The GQDs obtained by this method had both the functional groups— carboxylic and amine and were highly stable and dispersible in water. These carboxylic and amine co-functionalized GQDs have been named as “GQDs” everywhere else in this chapter for the sake of convenience.

3.2.2.3 Synthesis of carboxylic-functionalized GQDs (COOH-GQDs): To the prepared graphene oxide (GO) stock solution (15 mL), 40 mL of H₂O₂ (30 %) was added. This mixture was reacted at 80 °C for 24 h with vigorous stirring. The solution was evaporated at 65 °C to

remove unreacted H₂O₂ and water. Finally, ethanol was used to precipitate and wash the final carboxylic-functionalized GQDs. These carboxylic-functionalized GQDs have been named as “COOH-GQDs” everywhere else in this work.

3.2.2.4 Synthesis of amine-functionalized GQDs (NH₂-GQDs): Amine-functionalized GQDs were prepared using the hydrothermal method reported elsewhere.⁵² For NH₂-GQDs, 15 mL of GO stock solution, 15 mL of DI water, and 10 mL ammonia were added together. The mixture was stirred for 30 min, followed by ultrasonication for another 30 min. The resultant solution was transferred into 50 mL Teflon-lined autoclave and heated at 150 °C for 6 h by hydrothermal treatment. Next, the solution was cooled down to room temperature, and NH₂-GQDs were filtered through 0.22 μm microporous membrane. The filtered solution was heated at 100 °C for another 1 h to remove excess ammonia in the mixture. The obtained solution was stored for further characterization. These amine-functionalized GQDs have been named as “NH₂-GQDs” everywhere else in this work.

3.2.2.5 Synthesis of reduced GQDs (rGQDs): Carboxylic-functionalized GQDs were reduced by using sodium borohydride, following a previously reported method.⁵³ Briefly, to the above-prepared (*Section 2.2.2.2*) carboxylic-functionalized GQDs (15 mL), 1 g of NaBH₄ were added. The mixture was allowed to stir at room temperature for 2 h. When the mixture color faded to light yellow, then HNO₃ was added to terminate the reaction. Finally, pH was tuned to 8. The resultant solution was filtered through a 0.22 μm microporous membrane and stored for further characterization. These as-synthesized reduced GQDs have been named as “rGQDs” everywhere.

3.2.2.6 Synthesis of amine-functionalized β -NaYF₄: Gd³⁺,Tb³⁺: In a typical procedure^{54,55} for the synthesis of β -NaYF₄: 15 % Gd³⁺, 5 % Tb³⁺, solutions of Y(NO₃)₃, Gd(NO₃)₃ and Tb(NO₃)₃ (0.2 M) were added in a 10 mL solution of NaCl (0.2 M). The solution was

continuously stirred for 30-40 min. Then 20 mL of ethanol was added, followed by PEI (5 wt %). Then, 0.5 M of NH₄F was added dropwise to the resultant solution. The whole mixture was stirred for 30 minutes. Finally, the mixture was poured in a Teflon container with 80 mL capacity, and the reaction was set for 24 h hydrothermally at 180 °C.

3.2.2.7 Synthesis of β -NaYF₄: Gd³⁺,Tb³⁺ incorporated with GQDs: Similar procedure was followed to synthesize GQDs incorporated β -NaYF₄: Gd³⁺,Tb³⁺ phosphors except for different concentrations of as-prepared xGQDs (x = 0, 1, 3, 5, and 7 mL) were incorporated *in situ* in the initial solution reaction system.

3.2.3 Characterization techniques

The instrumental details of PXRD, FESEM, TEM, and PL can be obtained from *Chapter 2*. UV-Vis spectroscopy measurements were performed on a Jasco UV-Vis-NIR (Model V570) dual-beam spectrometer operated at a resolution of 2 nm. Raman spectra were recorded on HR-800 Raman spectrophotometer (Jobin Yvon-Horiba, France) using monochromatic radiation emitted by a He-Ne laser (633 nm), operating at 20 mW and with an accuracy of $\pm 1 \text{ cm}^{-1}$ in the range (450-850) nm, equipped with thermoelectrically cooled, multi-channel, spectroscopic grade CCD detector (1024×256 pixels of 26 microns) with dark current lower than 0.002 electrons pixel⁻¹s⁻¹. An objective of 50 xLD magnification was used to focus and collect the signal from the powder sample dispersed on the glass slide. Thermogravimetric analysis (TGA) was done using SDT model Q600 of TA Instruments Inc. USA at a heating rate of 10 °C/min under nitrogen flow at 100 mL/min. A PALS Zeta Potential Analyzer Ver 3.54 (Brookhaven Instrument Corps.) was used to determine the electrophoretic mobilities. Mobilities were converted to zeta potentials (ζ) using the Smolochowski model. DI water was the dispersion medium.

3.3 Results and discussion

Intentional incorporation of foreign elements into the hosts has a significant influence on the nucleation and growth of nanocrystals (heterogeneous nucleation) by lowering the thermodynamic activation energy barrier for the nucleation events to occur. This is influenced by the several microscopic properties—the crystal structure of foreign element and the precipitate, the lattice mismatch between two species, surface roughness, surface wetting properties, etc., from microscopic to the atomistic details. Thus, it provides a unique approach to modify the crystallographic phase, size, morphology, and consequently the optical properties of nanomaterials. In this chapter, the varying concentrations of carboxylic and amine co-functionalized graphene quantum dots (mentioned as GQDs hereafter) were incorporated in β -NaYF₄: Gd³⁺,Tb³⁺ phosphor crystals in the reaction vessel during the synthesis itself. To investigate the effect of GQDs and other carbon-based materials on the morphology of β -NaYF₄: Gd³⁺,Tb³⁺ phosphor crystals, the as-prepared GQDs were first characterized, and then structural, morphological, and optical properties of GQD incorporated β -NaYF₄: Gd³⁺,Tb³⁺ phosphor crystals were studied.

3.3.1 Characterization of GQDs

The size and morphology of as-prepared GQDs were characterized by TEM. **Fig. 3.1a** showed the TEM images of the carboxylic and amine co-functionalized GQDs with a size of 3-5 nm. The concentration of the GQDs was calculated from the TGA analysis at a heating rate of 10 °C/min under nitrogen atmosphere (**Fig. 3.1b**), which was found to be 10 mg/mL. The UV-vis absorbance (**Fig 3.1c**) showed the presence of broad absorbance in the UV range with a knee around ~230 nm due to π - π^* transitions of sp² C=C bonds present in the GQDs, which is in good agreement with the previous studies.⁵⁶ Detailed PL studies were carried out at different excitation wavelengths ranging from 250 to 550 nm. It was found that the PL intensity

firstly increased till 330 nm excitation and then decreased remarkably. The GQDs fluorescence emission peak red-shifted from 440 nm to 570 nm when the excitation wavelength increased from 250 to 550 nm. The highest intensity of the PL was observed for the GQDs at 445 nm when excited at 330 nm. Raman spectroscopy was performed at an excitation wavelength of 633 nm. **Fig. 3.1d** showed the Raman spectrum where two well-resolved peaks corresponding to D and G bands at ~ 1340 and ~ 1600 cm^{-1} , respectively, were observed.

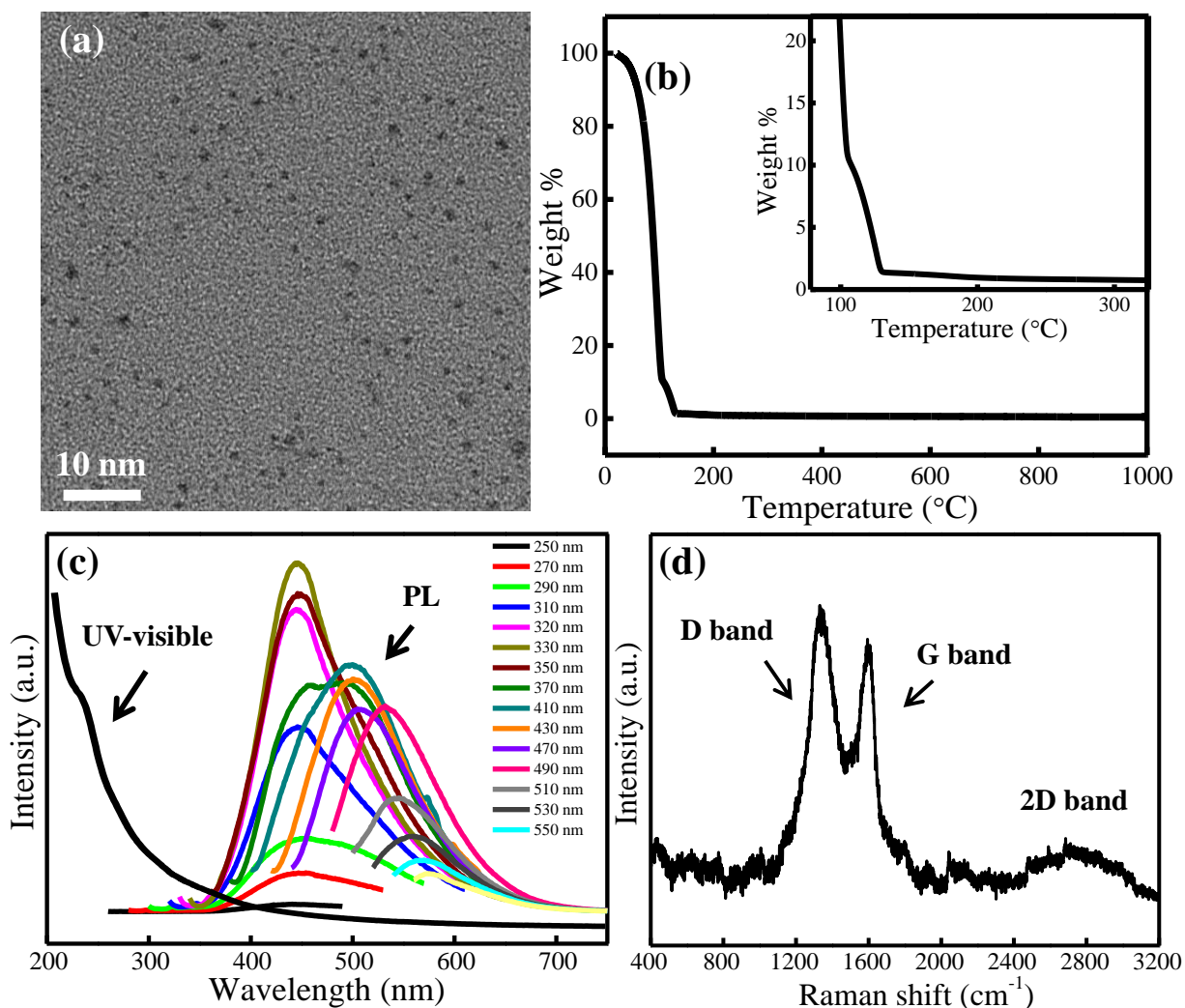


Figure 3.1 (a) TEM image of as-prepared carboxylic and amine co-functionalized GQDs showing particle size of 3-5 nm, (b) TGA curve shows the weight fraction of GQDs under inert atmosphere, (c) UV-visible absorbance spectra showing a broad UV absorption with a small knee at 230 nm and PL spectra at different excitation wavelengths from 250 to 550 nm and (d) Raman spectra of as-prepared GQDs using 633 nm laser as a source.

The G band corresponds to the E_{2g} phonon at the Brillouin zone center, while the disordered induced D band corresponds to the transverse optical phonons around the K-point of the Brillouin zone. The D band requires a defect for the momentum conservation. The intensity ratio I_D/I_G of D to G band is greater than 1, suggesting that the as-prepared GQDs have defects due to the dominant contributions from the edge states at the periphery. The 2D band is a second-order Raman process that originates from in-plane breathing-like modes of the carbon rings.⁵⁷ The broadening of the 2D band at ~2800 cm⁻¹ may be due to the relaxation of the double-resonance Raman selection rules associated with the random orientation of GQDs with respect to each other.⁵⁸ The broadness of this peak increased with an increase in the defect states in the system.

3.3.2 Structural and morphological investigations of β -NaYF₄: Gd³⁺,Tb³⁺-xGQDs

The composition, crystallinity, and phase purity of the β -NaYF₄: Gd³⁺,Tb³⁺-xGQDs phosphors were first examined by XRD. **Fig. 3.2** shows the XRD patterns of the as-synthesized PEI-capped NaYF₄: Gd³⁺,Tb³⁺, incorporated with different concentrations of GQDs (x = 0, 1, 3, 5, and 7 mL). The relative intensity of the peaks was changed compared with that of standard data, suggesting the probable anisotropic growth behavior of the particles. The sharp diffraction peaks in all the samples can be indexed to the pure hexagonal phase β -NaYF₄ (space group: *P*6₃/*m*) with calculated lattice parameters a = 5.9 Å and c = 3.5 Å, which was in good agreement with the reported data (JCPDS 16-0334). The absence of other peaks in XRD patterns indicated the high purity of as-prepared samples implying that no secondary phase was formed. The pure hexagonal phase of all the samples revealed that the incorporation of GQDs at all concentrations did not induce the transformation in the β -NaYF₄ crystal structure. It is worth mentioning that there was a difference in the relative intensities based on (100), (101), (110), (002), and (201) peaks, indicating the existence of different preferential orientation growth at different GQDs

concentrations. The size, shape, and structure of the as-prepared samples were characterized by the TEM and FESEM. As shown in **Fig. 3.3**, the TEM images showed that the as-prepared PEI-capped β -NaYF₄: Gd³⁺, Tb³⁺ crystals possess rod shape with an average length \sim 280 nm and diameter of \sim 96 nm. It can be seen that the β -NaYF₄: Gd³⁺, Tb³⁺-xGQDs (x = 0) rods were highly uniform and monodispersed in nature.

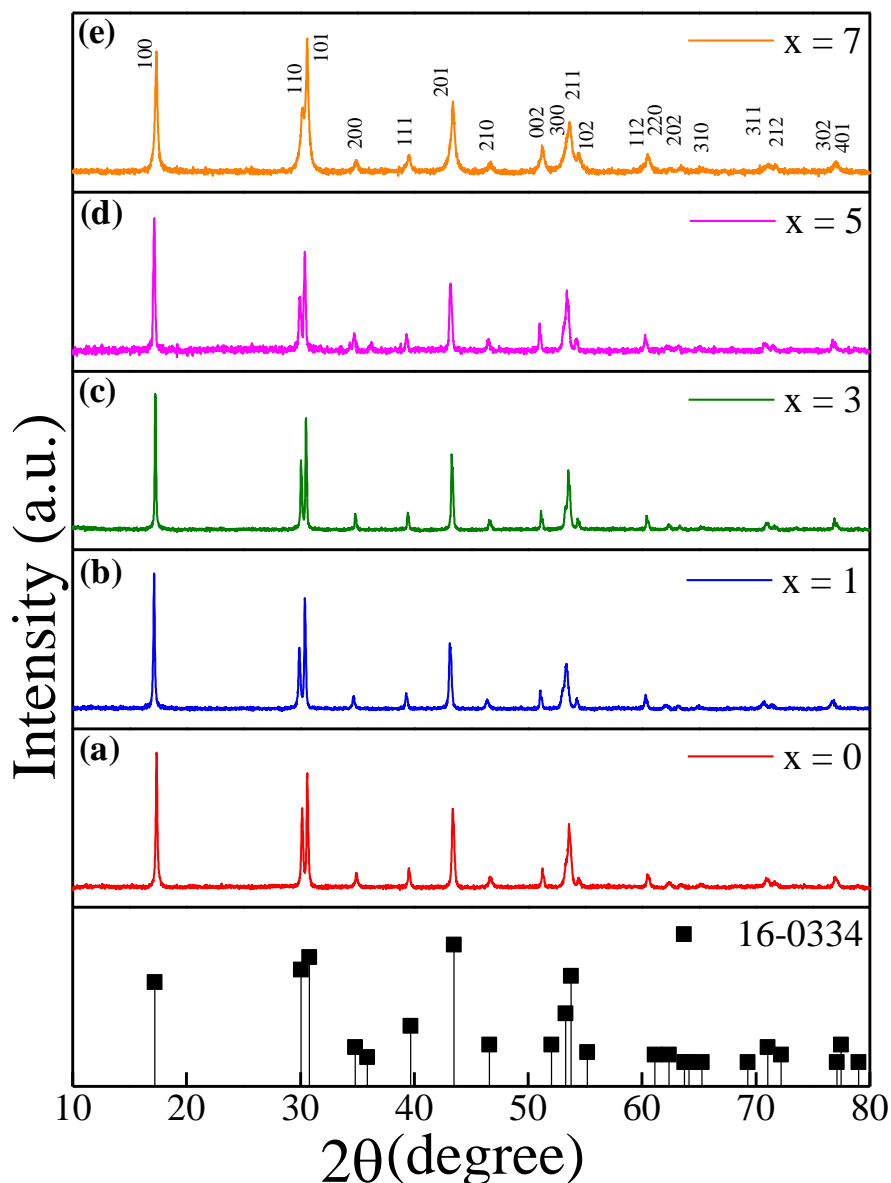


Figure 3.2 The comparison of XRD patterns of β -NaYF₄:Gd³⁺, Tb³⁺ and β -NaYF₄:Gd³⁺, Tb³⁺-xGQDs phosphor crystals where x = (a) 0 mL (b) 1 mL (c) 3 mL (d) 5 mL and (e) 7 mL. The standard data of β -NaYF₄ (JCPDS 16-0334) is also compared. The incorporation of GQDs did not induce any phase transformation in the β -NaYF₄ crystal structure.

Interestingly, upon *in situ* incorporation of the GQDs into the PEI-capped β -NaYF₄: Gd³⁺, Tb³⁺ phosphors during the synthesis, the variation in morphology was observed as a function of different concentrations of GQDs. As it can be seen from **Fig. 3.3b,c**, at the lower concentrations of GQDs, i.e., at $x = 1$ and $x = 3$, hexagonal prismatic structures were formed with average lengths/diameters of ~ 225 nm/ ~ 130 nm and ~ 280 nm/ ~ 250 nm, respectively. At $x = 5$, flower-shaped crystals were observed with an average length and diameter of ~ 325 nm and ~ 300 nm, respectively (**Fig. 3.3d**). While, the crystallites observed at $x = 7$ were composed of disk-like structures having an average length and diameter of ~ 260 nm and ~ 620 nm, as shown in **Fig. 3.3e**.

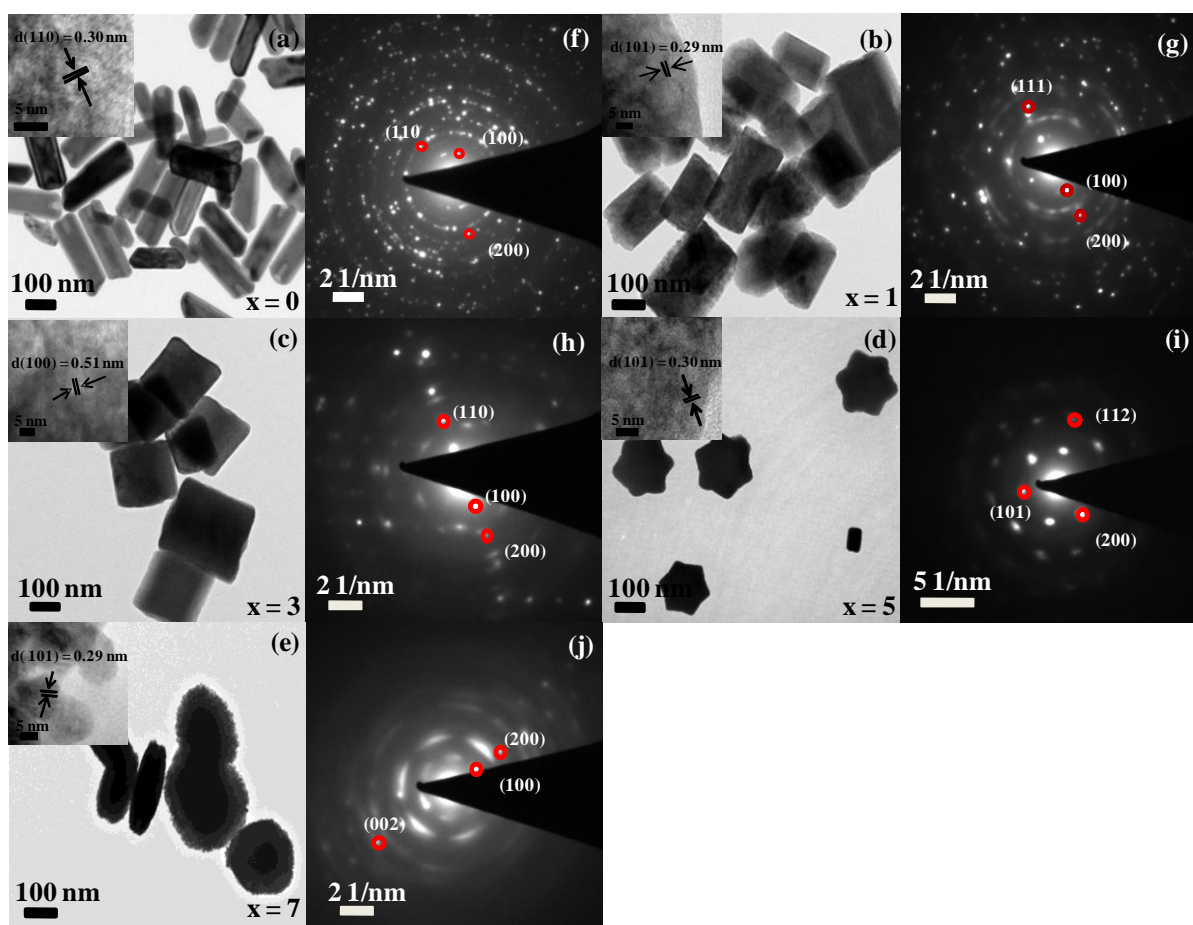


Figure 3.3 The TEM images of GQDs incorporated β -NaYF₄: Gd³⁺, Tb³⁺ particles showed the modification of nucleation and growth of these particles when the concentration of GQDs was varied from $x = 0$ to 7 mL (a-e). The figures (f-j) show their respective SAED patterns.

These results strongly suggested that the morphology of the β -NaYF₄:Gd³⁺,Tb³⁺-xGQDs crystals (x = 0, 1, 3, 5, 7 mL) exhibited striking dependence on the different concentrations of the GQDs, where the shape changed from rods (x = 0) to disk-like structures (x = 7). The corresponding selected area electron diffraction patterns (SAED) and high-resolution TEM images shown in **Fig. 3.3f,g,h,i,j** and insets, respectively, demonstrated that the as-synthesized β -NaYF₄: Gd³⁺,Tb³⁺-xGQDs crystals were highly crystalline in nature. Meanwhile, the lattice fringes with an interplanar spacing of respective planes of β -NaYF₄: Gd³⁺,Tb³⁺-xGQDs crystals were ascribed. The detailed observations with their proper facets at various concentrations of GQDs in the as-prepared samples can be clearly seen by the FESEM images (**Fig. 3.4**). The FESEM images laid more evidence that the incorporation of the GQDs had a huge effect on the morphology of the as-prepared crystals. It was noted that the pH of the solution was not changed due to the addition of GQDs in the precursor solution. Therefore, the effect of pH had not influenced any changes in the product. Hence, these results clearly indicated that the size and morphology control in these experiments is closely related to the incorporation of GQDs, since the concentration of GQDs was the only parameter changed in the system. The plausible mechanism for the modulation in the morphology of β -NaYF₄: Gd³⁺,Tb³⁺ phosphors due to the incorporation of GQDs is discussed in the next section.

3.3.3 Growth mechanism of GQDs incorporated NaYF₄: Gd³⁺,Tb³⁺ multiform morphologies

For a better understanding of the formation processes of multiform morphologies of β -NaYF₄: Gd³⁺,Tb³⁺ phosphor crystals via incorporation of GQDs during the synthesis, reaction samples were carefully investigated by taking the different concentrations of as-prepared GQDs. It was believed that GQDs particles of nearly 5 nm served as the nucleation sites for the nucleation and further growth of the crystals. Since the precursors used in the reaction were

ionic and GQDs contained functional groups at the edges and on the surface, therefore Ln³⁺ ions interacted with these functional groups, especially -COOH and -OH groups, and formed metal-GQD complex. Then after, nuclei were formed upon the addition of a fluoride source. Interaction of GQDs with the precursor ions played an important role, where the charge or the functional groups such as carboxylic acid, amine, hydroxyl, etc., present in the GQDs had a

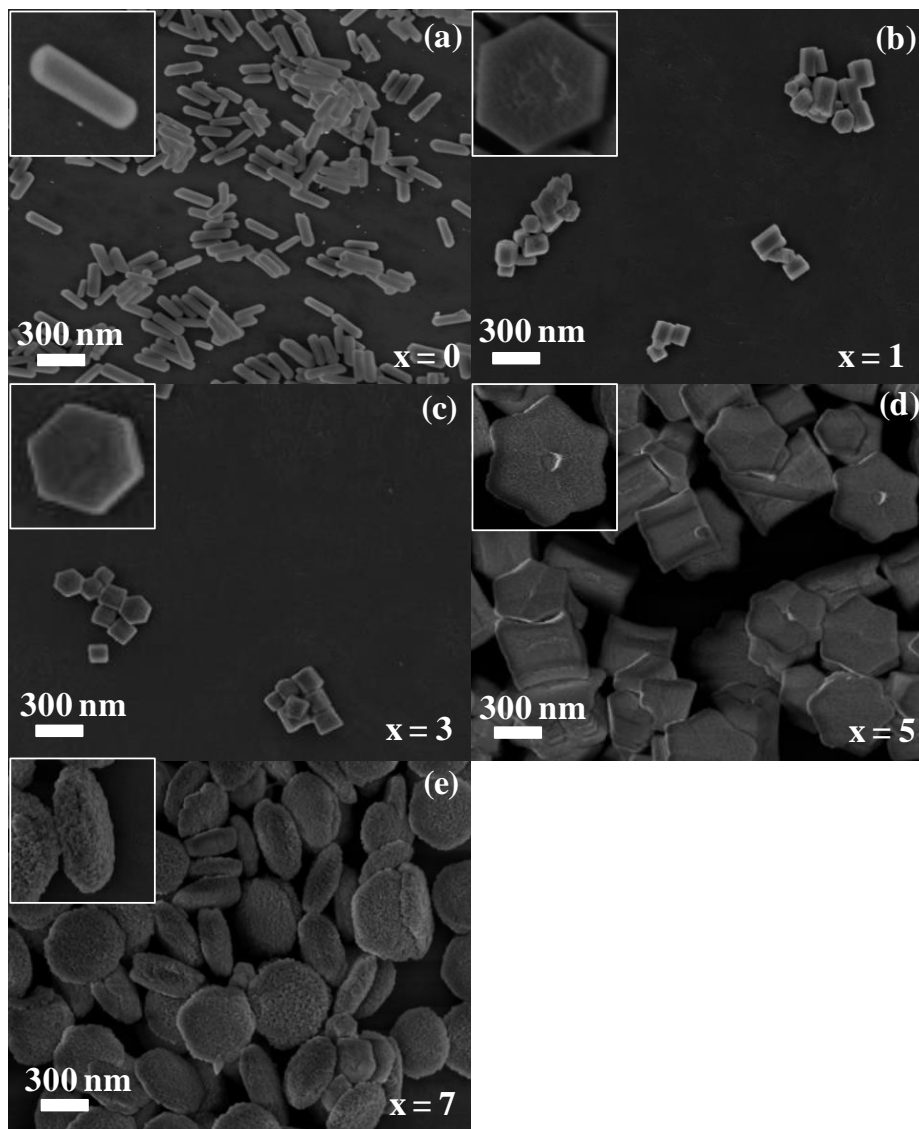


Figure 3.4 The FESEM images show the change in morphology of β -NaYF₄: Gd³⁺, Tb³⁺ after the incorporation of GQDs, where the concentration of GQDs was varied from $x = 0$ to 7 mL (a-e). With an increase in the concentration of GQDs, the aspect ratio (length/width) of the phosphors has decreased. NaYF₄ rods were formed at 0 mL with an aspect ratio of 2.6 and disk-like structures with an aspect ratio of 0.4 at 7 mL GQDs.

significant role by binding to the Ln³⁺ ions. As the seeds grow, the GQDs bound to the particular surface of the phosphor seeds, governing the shape and size of the particles. With an increase in the GQD concentration, their probability of binding to the surface increased, which rendered the growth of the crystals along the (100) plane, thereby giving rise to the lowest aspect ratio of the rods. Consequently, with a larger concentration of GQDs, disk-like structures were formed, having the lowest aspect ratio among all. The above results were formulated on the same hypothesis as given by Yang et al. for DEG molecule for the growth of KGdF₄ nanocrystals.⁵⁹ Here, GQDs may have different functions— firstly, it can form a metal-GQDs complex by which the growth rate of nanoparticles was slowed down, thereby decreasing the crystallite size. This was similar to the mechanism reported by Zeng's group, where the metal-oleic acid complex was formed when oleic acid was used as a ligand for the preparation of NaLnF₄ nanocrystals.⁶⁰ Secondly, this also slowed down the diffusing rate of the cations and anions, which may reduce the collisions probability of the ions in the system. Thirdly, it can also cap the external surfaces of the NPs, giving them directional growth. By virtue of this, the size control and shape evolution of the NPs can be easily realized by changing the GQDs' amount, which governs the growth of the crystal in a particular direction.

Further, growth directional analysis was done by measuring the XRD intensity. In general, facets perpendicular to the fast directions of growth have smaller surface areas; therefore, a slow-growing face dominates the morphology having a large surface area and thus is more exposed to the environment. Hence, the more exposed plane will show higher intensity in XRD having the slower growth. In **Fig. 3.5**, variation in the normalized XRD intensity of different planes was plotted with varying concentrations of GQDs used in the system. It can be seen that the intensity of the plane (100) was decreased with a higher concentration of co-functionalized GQDs, suggesting that the plane was less exposed, and growth took place along

this direction, giving rise to disk-like structures at 7 mL of GQDs. Similarly, when compared with other side planes in hexagonal structure (110) and (101), the normalized intensity was decreased, indicating the same. While in the case of the (002) plane (**Fig. 3.5d**), the intensity increased with increase in the concentration of GQDs, thus implying that the growth direction was perpendicular to this plane. Thence, it was concluded that carboxylic and amine co-functionalized GQDs has the function of inhibiting the longitudinal growth along $\langle 0001 \rangle$ direction with a relative enhancement of the growth along $\langle 10\bar{1}0 \rangle$ direction in the form of hexagonal prism first and then disk-like structures. Schematic showing the growth direction and proposed mechanism have been depicted in **Scheme 3.1 and 3.2**, respectively.

In order to validate the influence of the GQDs on the resultant morphology, the controlled experiments were then carried out by changing the dimension of foreign impurity and the functionality of the as-prepared GQDs.

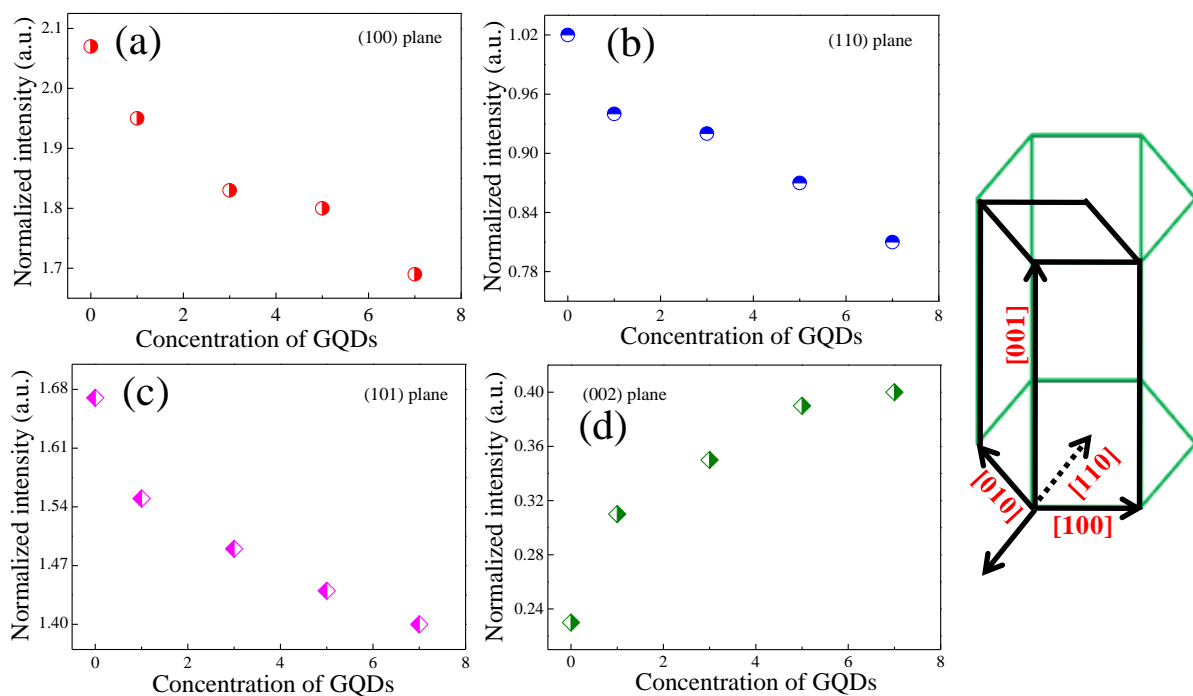
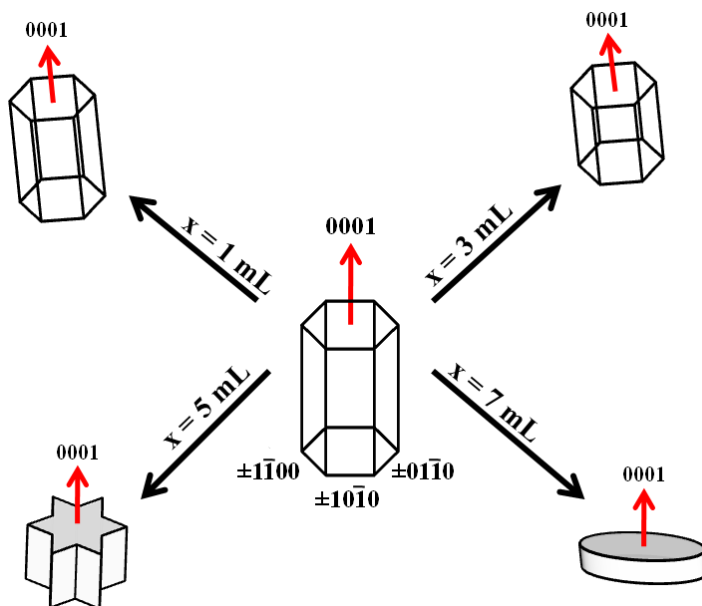
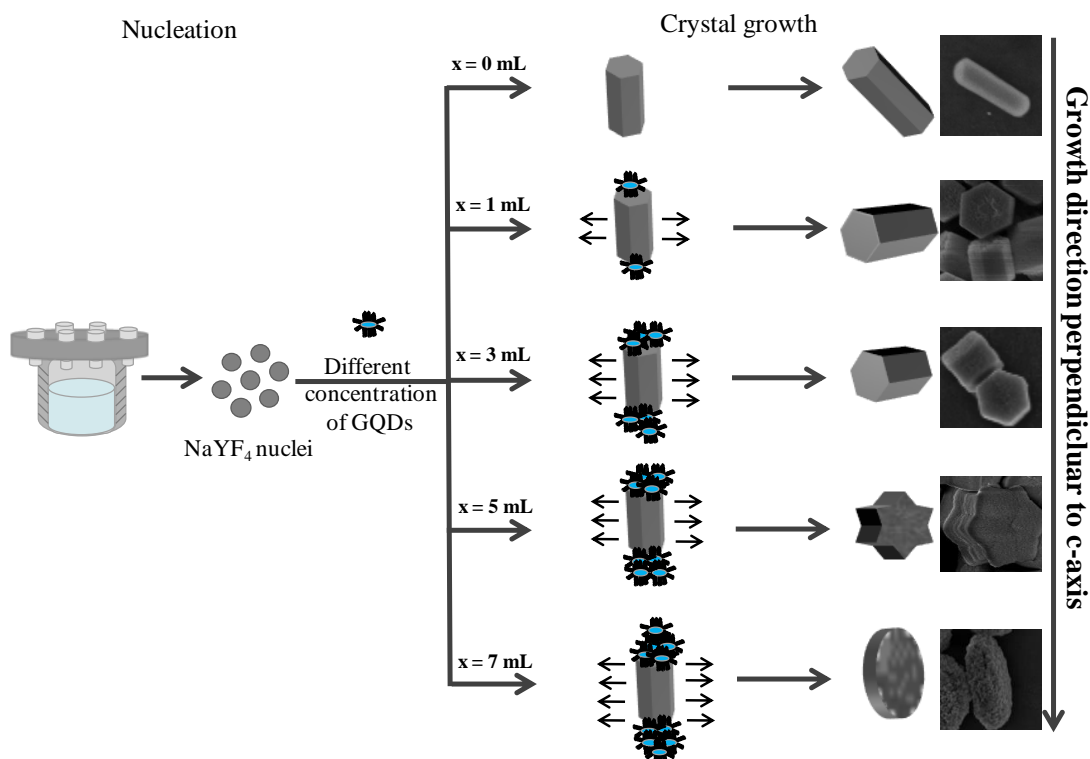


Figure 3.5 Variation of normalized XRD intensity of different planes (a) 100, (b) 110, (c) 101 and (d) 002 in β -NaYF₄: Gd³⁺, Tb³⁺ with the change in concentration of GQDs. Respective direction of planes is shown in the anisotropic hexagonal crystal structure.



Scheme 3.1 Schematic illustration of the directional growth of anisotropic structure of β -NaYF₄: Gd³⁺, Tb³⁺ -xGQDs shown with different planes with the change in concentration of GQDs where x is varied as x = 1 mL, x = 3 mL, x = 5 mL and x = 7 mL.



Scheme 3.2 Schematic illustration of nucleation and growth process and the effect of GQDs incorporation on the morphology of final β -NaYF₄: Gd³⁺, Tb³⁺ phosphors. Here, the GQDs provided nucleation sites for the nucleation as well as acted as a capping agent and manipulated the growth of β -NaYF₄: Gd³⁺, Tb³⁺ crystals.

3.3.3.1 Effect of size of the foreign particles introduced in the reaction (GO vs. CNT)

To study the effect of size of foreign particles incorporated during the synthesis of β -NaYF₄: Gd³⁺, Tb³⁺ crystals and to examine whether the change in the morphology of β -NaYF₄: Gd³⁺, Tb³⁺ phosphors was due to the incorporation of GQDs, a control experiment was performed. In two separate reactions of β -NaYF₄: Gd³⁺, Tb³⁺ phosphors, graphene oxide (GO), and multiwalled carbon nanotubes (MWCNT) were incorporated. The synthesis procedure was similar to the preparation of β -NaYF₄: Gd³⁺, Tb³⁺-xGQDs, except that GO and MWCNT were incorporated instead of GQDs. The as-obtained products were named as β -NaYF₄: Gd³⁺, Tb³⁺-xGO and β -NaYF₄: Gd³⁺, Tb³⁺-xMWCNT. The composition and phase purity of the products were examined by XRD as shown in **Fig. 3.6**, where the diffraction peaks of the samples were indexed to the pure hexagonal phase of NaYF₄ (JCPDS 16-0334).

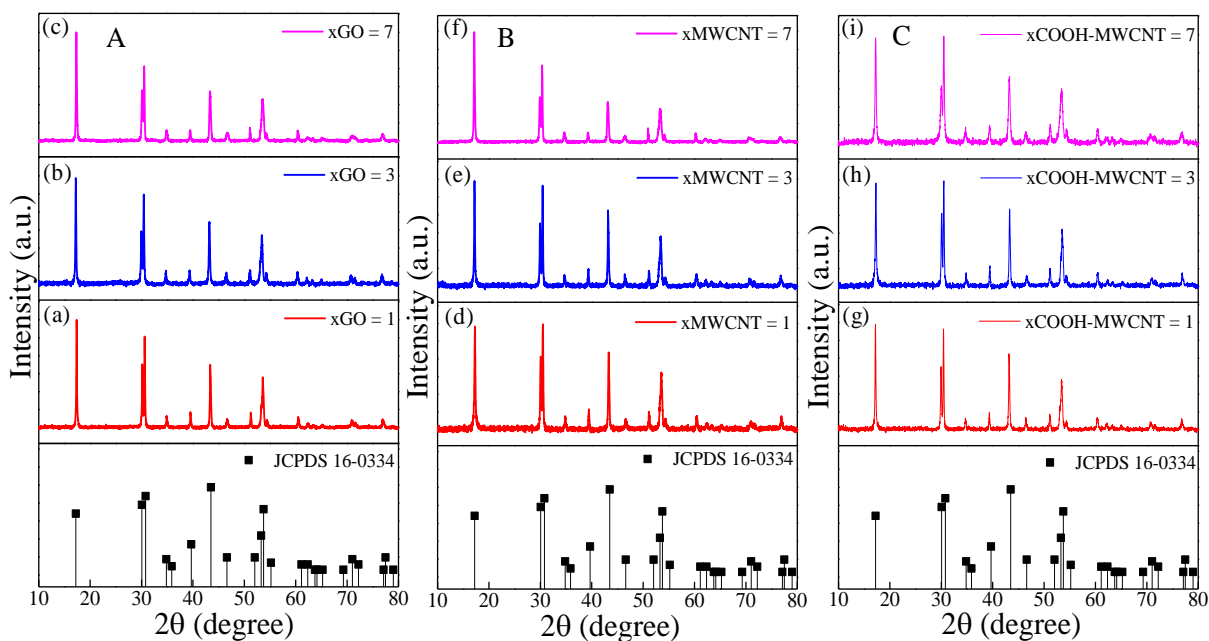


Figure 3.6 XRD patterns of β -NaYF₄:Gd³⁺/Tb³⁺ incorporated with different graphitic carbon-based materials were compared with the standard data of β -NaYF₄ (JCPDS -16-0334). Various columns show the following samples: β -NaYF₄: Gd³⁺/Tb³⁺-xGO (A), β -NaYF₄: Gd³⁺/Tb³⁺-xMWCNT (B), β -NaYF₄: Gd³⁺/Tb³⁺-xCOOH-MWCNT (C), where respective values of x are mentioned in the panels. The incorporation of these foreign impurities did not induce any phase change in the β -NaYF₄ structure.

As represented in **Fig. 3.7**, it was observed that due to the incorporation of GO sheets and MWCNT, the morphology of the β -NaYF₄: Gd³⁺,Tb³⁺ phosphors crystals remained unchanged. These results inferred that the size of the foreign particles introduced in the reaction played a role in the morphology tuning of β -NaYF₄: Gd³⁺,Tb³⁺ phosphors where only small GQDs particles could tune the morphology whereas large carbon materials; sheet or tube-like structures such as GO and MWCNT could not influence and alter the shape of β -NaYF₄: Gd³⁺,Tb³⁺ phosphors.

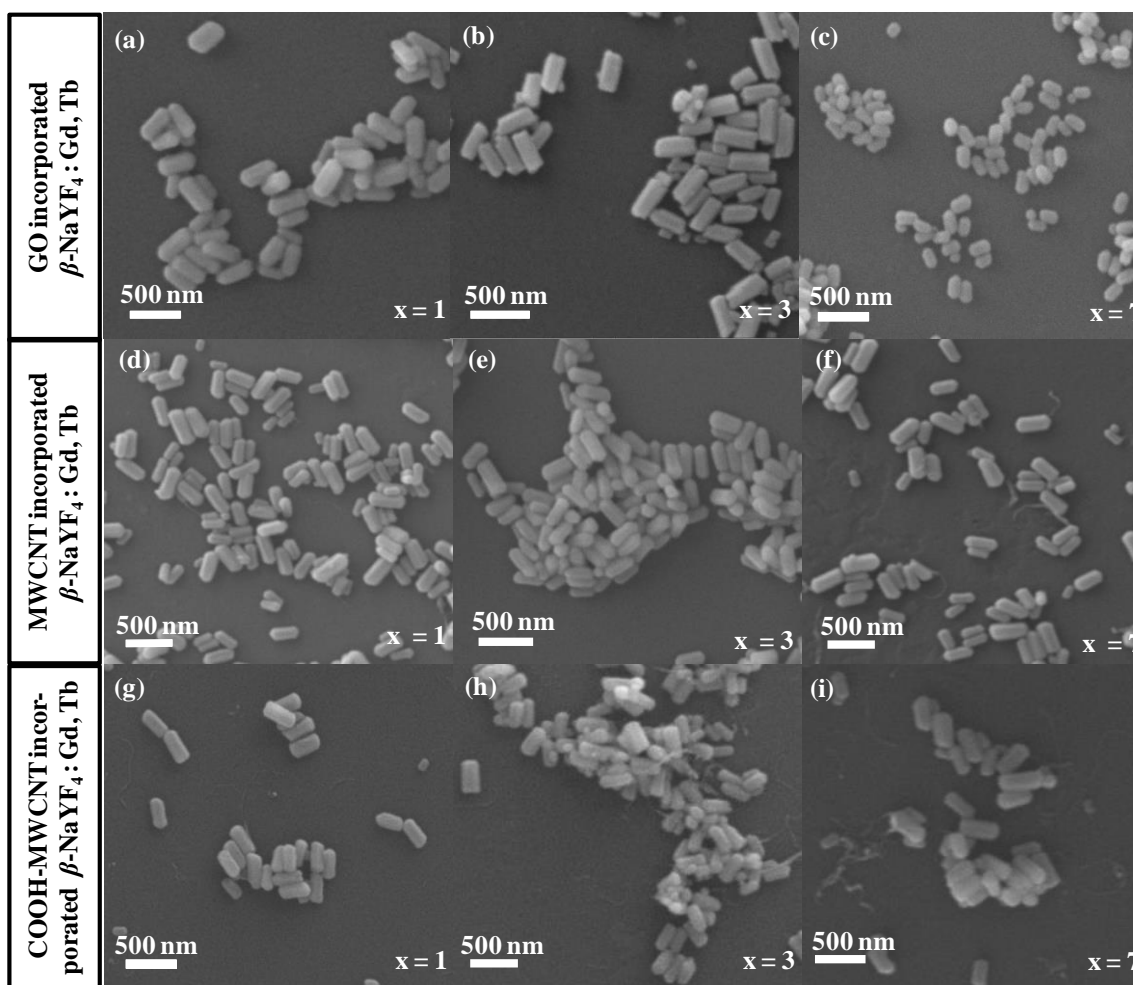


Figure 3.7 The SEM images show the effect of different concentrations of graphene oxide, GO (a-c), multiwalled carbon nanotube, MWCNT (d-f) and carboxylic-functionalized multiwalled carbon nanotube, COOH-MWCNT (g-i) on the growth morphology of β -NaYF₄: Gd³⁺,Tb³⁺ phosphors. There was no change in the morphology of β -NaYF₄: Gd³⁺,Tb³⁺ phosphors due to the incorporation of these materials as foreign impurities was observed.

3.3.3.2 Effect of functionalization of GQDs on the β -NaYF₄: Gd³⁺, Tb³⁺ phosphors growth

Furthermore, to analyze the effect of the functionalization of GQDs on the morphology of β -NaYF₄: Gd³⁺, Tb³⁺ phosphors, carboxylic-functionalized (COOH-GQDs), and amine-functionalized (NH₂-GQDs) were synthesized along with reduced GQDs (rGQDs). COOH-GQDs, NH₂-GQDs, and rGQDs were characterized by TEM to see the particle size and UV-vis to see their absorbance. **Fig. 3.8** compared the TEM images of COOH-GQDs, NH₂-GQDs, and reduced GQDs (rGQDs), showing a relatively narrow size distribution (~2-5 nm). To explore the optical properties, UV-vis spectra were recorded showing the main absorbance peak at around 230 nm, which was attributed to the π - π^* transitions of sp² C=C in as-synthesized

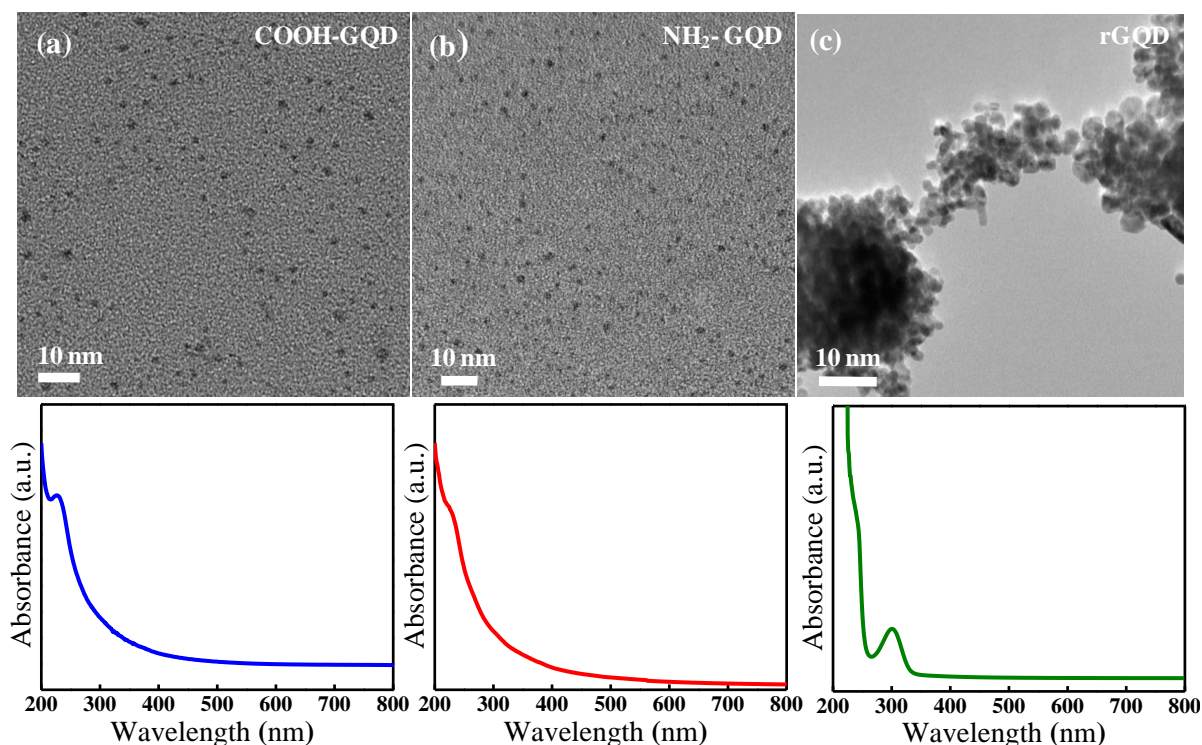


Figure 3.8 The TEM images of (a) COOH-functionalized GQDs, (b) NH₂-functionalized GQDs and (c) reduced GQDs showing the average particle size in the range of 2-5 nm. In case of reduced GQDs, particles were aggregated due to the less surface charge after the reduction reaction. Their respective UV-visible absorbance spectra are also shown below, showing the main absorbance peak at around 230 nm as-synthesized COOH-GQDs, NH₂-GQDs, and rGQDs, while a peak at around ~ 300 nm in rGQD.

COOH-GQDs, NH₂-GQDs and rGQDs, while a peak at around ~ 300 nm was attributed to n - π^* transitions of C=O in case of rGQDs.⁵³ The measured zeta potentials of COOH-GQDs, NH₂-GQDs, and rGQDs were -32.8 mV, -15.8 mV, and -20.5 mV, respectively. The positive shift of the zeta potential for the amine-functionalized GQDs and reduced GQDs indirectly indicated the introduction of amine groups. Since the introduced amine groups can counteract part of the electronegative effect and reduction in the hydroxyl group, respectively.⁵¹ The concentration of the functionalized GQDs was calculated from the TGA analysis at a heating rate of 10 °C/min under nitrogen atmosphere (**Fig. 3.9**), which was found to be 10 mg/mL for all the types of GQDs.

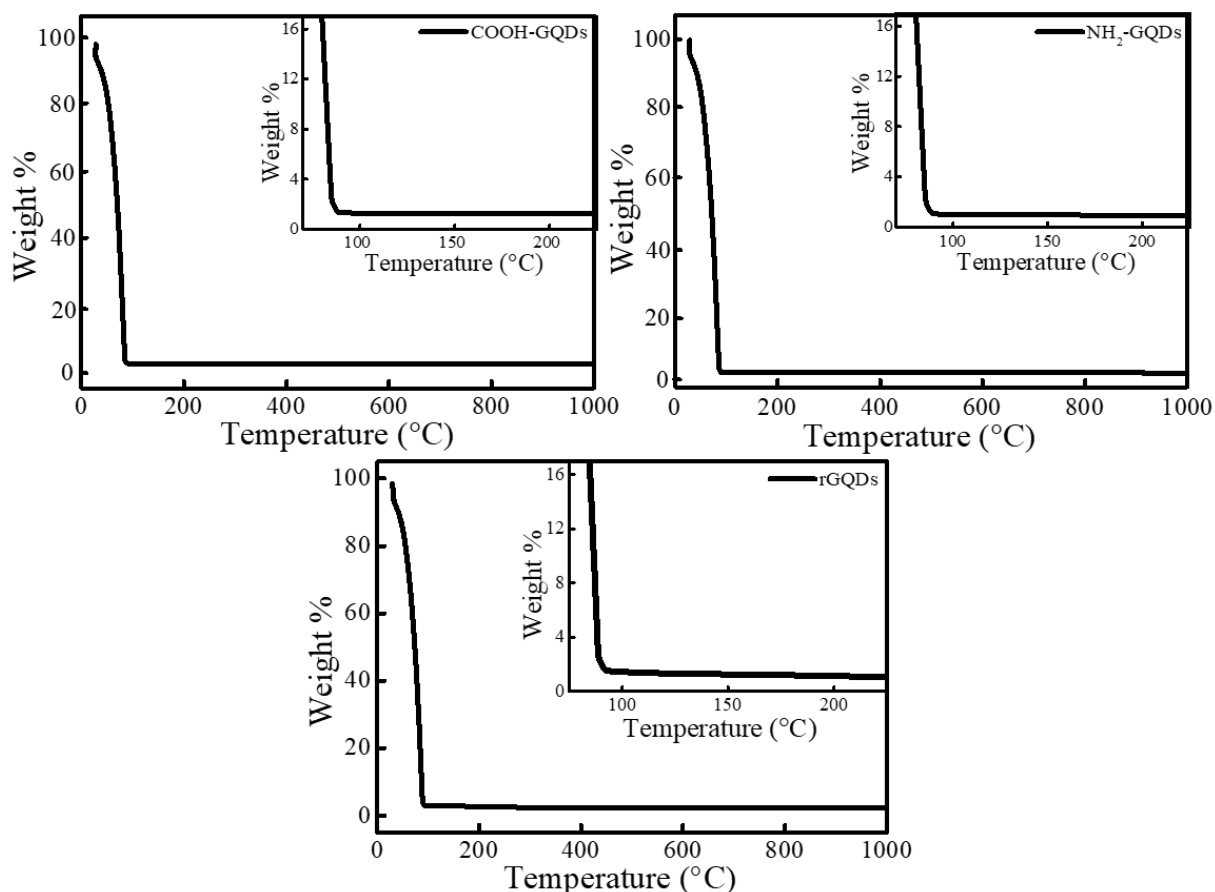


Figure 3.9 The TGA curves of (a) carboxylic-functionalized GQDs, COOH-GQDs, (b) amine-functionalized GQDs, NH₂-GQDs, and (c) reduced GQDs, rGQDs showing the weight fraction. In all the samples, 1 mL of suspension equals 10 mg of GQDs.

Furthermore, the synthesis of β -NaYF₄: Gd³⁺,Tb³⁺ by incorporating COOH-GQDs and NH₂-GQDs in the reaction vessel was performed. The phase purity and crystallinity of the as-prepared samples were monitored by XRD and compared in **Fig. 3.10A**, where the diffraction peaks matched very well with the standard JCPDS data of β -NaYF₄. No traces of impurity peaks were observed, indicating that all the samples crystallized in a single phase of β -NaYF₄. It can be seen in **Fig. 3.11** that functionalization had a notable effect on the morphology and size of the resultant products. Microrods with cracked ends were formed using COOH-GQDs having an average length of $\sim 15 \mu\text{m}$ at $x = 5 \text{ mL}$, while the average size of the microrods increased to $\sim 30 \mu\text{m}$ when the concentration of COOH-GQDs increased further to 7 mL. In a study in 2006, during the growth of NaYF₄ crystals, OA selectively bound to the surface, which was parallel

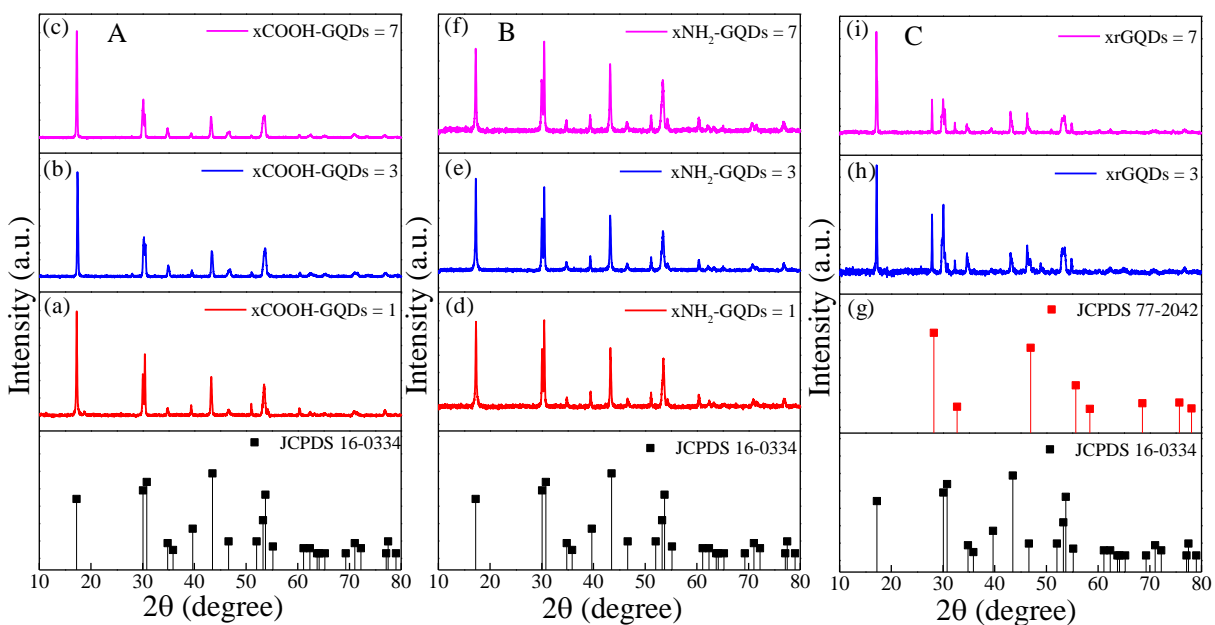


Figure 3.10 XRD patterns of β -NaYF₄: Gd³⁺,Tb³⁺ incorporated with different types of functionalized-GQDs: (A) β -NaYF₄: Gd³⁺,Tb³⁺-xCOOH-GQDs, (B) β -NaYF₄: Gd³⁺,Tb³⁺-xNH₂-GQDs, (C) β -NaYF₄: Gd³⁺,Tb³⁺-xrGQDs were compared with the standard data of β -NaYF₄ (JCPDS 16-0334) and α -NaYF₄ (JCPDS 77-2042) in case of rGQDs where values of x are mentioned in the panels. There was no phase change occurred in the case of the incorporation of COOH-GQDs and NH₂-GQDs, while the incorporation of rGQDs induced phase change in the β -NaYF₄ crystal structure.

to the *c*-axis rendering the growth along $\langle 0001 \rangle$ direction and hence resulted in the formation of nanorods.⁶¹ Supporting the above mechanism, in another study, it was concluded that the anionic form of oleic acid (OA⁻) preferentially binds to the Y³⁺ ions exposed more on the six symmetric facets of the hexagonal fluoride crystal rendering the formation of rods.¹⁹ Given the same hypothesis, it was concluded that the functional groups such as carboxylic and hydroxyl might bind to the side planes of the hexagonal prismatic structures where Y³⁺ ions were more exposed, giving rise to the formation of microrods; therefore, the preferential growth direction was along $\langle 0001 \rangle$. Additionally, growth direction was confirmed by normalized XRD intensity. As shown in **Fig. 3.12a**, the intensity of different planes in β -NaYF₄ was changed when the concentration of COOH-GQDs was increased. The increment in the intensity of (100), (110), and (101) planes suggested that the growth direction was perpendicular to these planes, thus rendering the growth in the (001) plane.

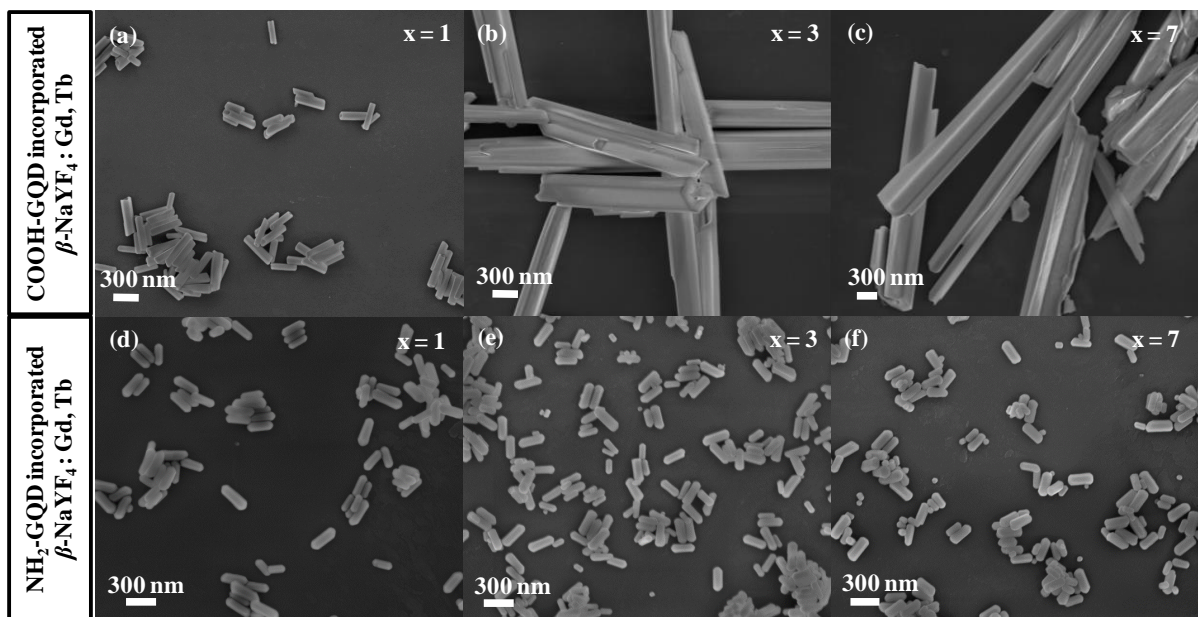


Figure 3.11 The FESEM images of β -NaYF₄: Gd³⁺, Tb³⁺ -xCOOH-GQDs (a-c), and β -NaYF₄: Gd³⁺, Tb³⁺ -xNH₂-GQDs (d-f) phosphors where concentration of respective GQDs was varied from x = 1 ml, x = 3 ml, and x = 7 ml. Microrods were formed when COOH-GQDs were incorporated while there was no change observed in the case of the incorporation of NH₂-GQDs during the synthesis of β -NaYF₄: Gd³⁺, Tb³⁺.

Further, the effect of amine-functionalized GQDs (NH₂-GQDs) on the growth process of β -NaYF₄ was studied. The crystallinity of the β -NaYF₄: Gd³⁺, Tb³⁺-xNH₂-GQDs was examined by XRD. The diffraction peaks in XRD pattern shown in **Fig. 3.10B** can be indexed to pure β -NaYF₄. The presence of NH₂-GQDs had no obvious impact on the morphology of the crystals, which can be seen in the FESEM images (**Fig. 3.11(d-f)**). Moreover, the XRD intensity of different planes, as shown in **Fig. 3.12b**, was not changed with the concentration of NH₂-GQDs, confirming the unaltered morphology of β -NaYF₄.

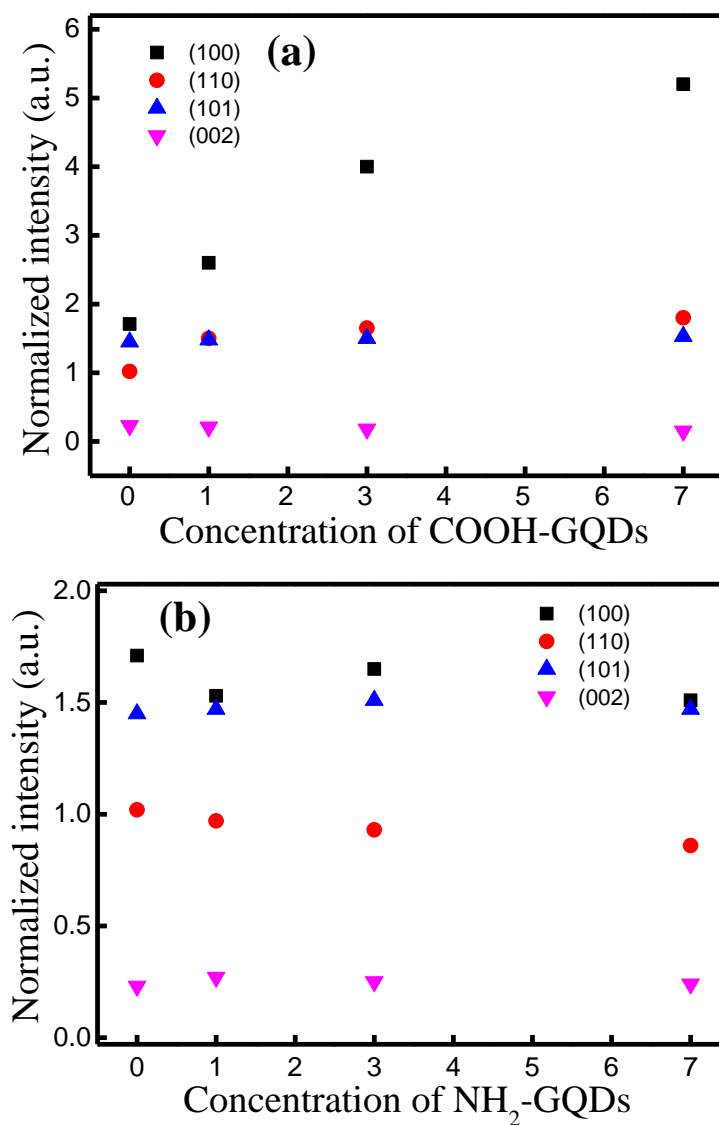


Figure 3.12 Variation of normalized XRD intensity of different planes in β -NaYF₄: Gd³⁺, Tb³⁺ with the change in the concentration of (a) carboxylic-functionalized GQDs and (b) amine-functionalized GQDs.

To study the effect of non-functionalized GQDs, the reduced GQDs were used during the synthesis of NaYF₄. Oxygen-rich functional groups such as carboxyl, hydroxyl, and epoxy groups are introduced to the edges and onto the basal plane during the top-down synthesis,^{62,63} which can be reduced using some of the reducing agents such as NaBH₄, hydrazine hydrate, etc. In this work, COOH-GQDs were reduced with NaBH₄, which reduced hydroxyl and epoxy groups on the basal plane of the GQDs while carboxyl moieties remained unreduced at the edges. As observed in the XRD pattern shown in **Fig. 3.10C** that some of the diffraction peaks belonged to the cubic phase of NaYF₄, which matched very well with the standard face-centered cubic structure data (JCPDS 77-2042), while other peaks were indexed to the pure hexagonal phase of NaYF₄ (JCPDS 16-0334). It can be seen in **Fig. 3.13** that similar microrods were formed when the reaction with rGQDs was performed, having few carboxylic acid groups at the edges. Hence, the proposed mechanism for the formation of microrods may be the same as that in the case of COOH-GQDs. Apart from microrods, small spherical particles were seen, which have been assigned as the cubic phase as indexed in the XRD pattern. Careful investigation revealed that the microrods were composed of solid interiors with small quasi-spheres attached to them. Together with the XRD pattern, it can be judged from SEM images

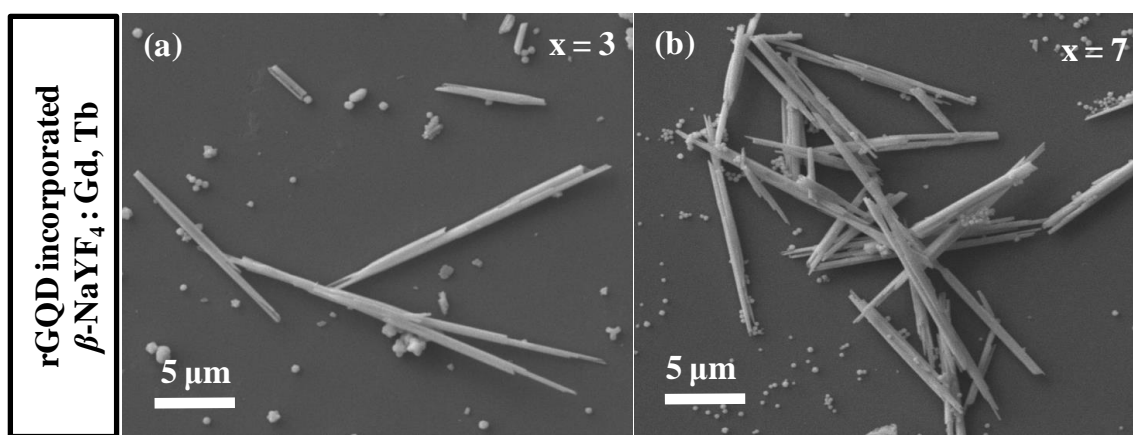
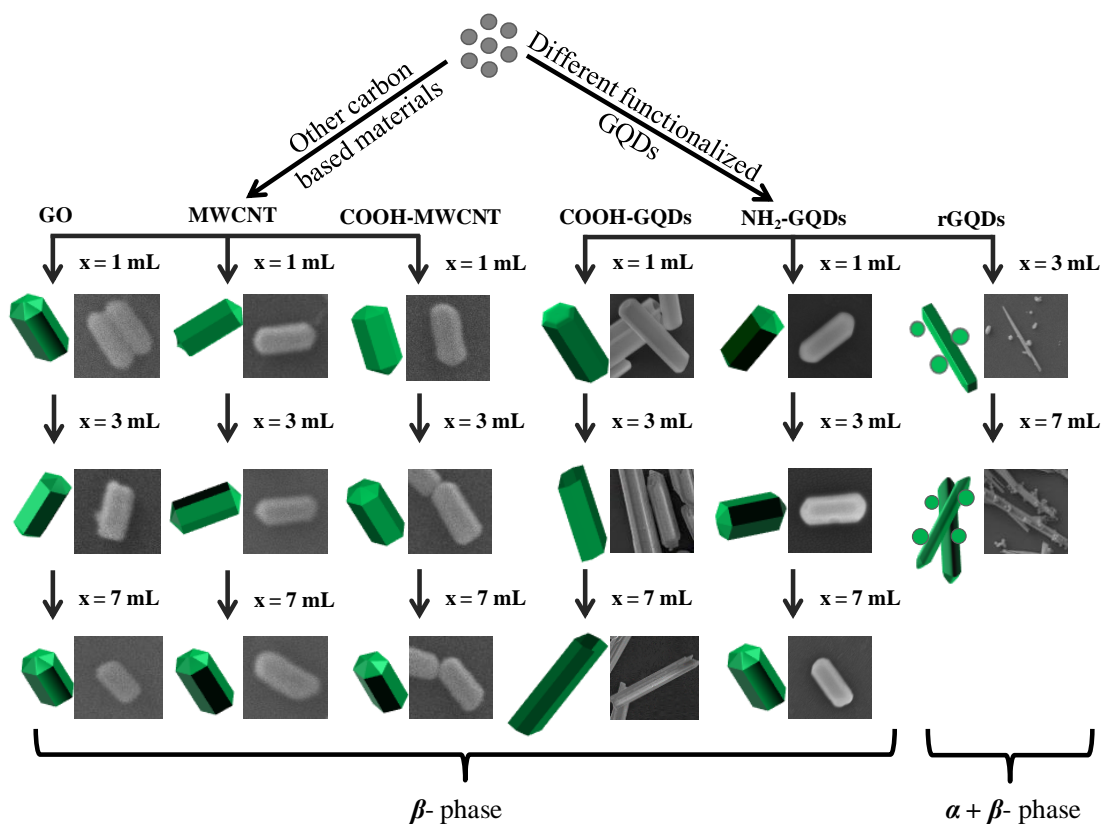


Figure 3.13 The SEM images of β -NaYF₄: Gd³⁺, Tb³⁺ phosphors with varied concentrations of rGQDs. Microrods were formed along with some small quasi-spherical particles with the *in situ* incorporation of rGQDs during the synthesis.

that the microrods were hexagonal phase and small quasi-spherical NPs were cubic. Although the formation of the cubic phase in the system is unclear at present, the following explanation for the existence of the cubic phase can be provided. Since the rGQDs contained a fewer number of functional groups, it would lead to the availability of more number of Ln³⁺ ions, which would bring on fast nucleation and growth of NaYF₄ crystals. So, there weren't enough monomers to supply the growth of small particles under the same circumstances. Thus, small NPs with cubic phase as well as microrods with hexagonal phase co-existed in the final products with rGQDs. The schematic and table showing corresponding morphologies obtained at different concentrations of GQDs, differently functionalized GQDs, and different foreign impurities are represented in **Scheme 3.3**, and details of aspect ratios are summarized in **Table 3.1**.



Scheme 3.3 Schematic illustration of the effect of other carbon-based materials and differently functionalized GQDs on the morphology of NaYF₄: Gd³⁺,Tb³⁺ phosphors. Only the incorporation of COOH-GQDs and rGQDs have made a significant change in the morphology of the NaYF₄: Gd³⁺,Tb³⁺ phosphor crystals.

Table 3.1 Summary of the effect of GQDs and other carbon-based materials on the morphology and aspect ratio of the final β -NaYF₄: Gd³⁺, Tb³⁺ phosphors where x was varied as x = 1 mL, x = 3 mL and x = 7 mL in the respective system.

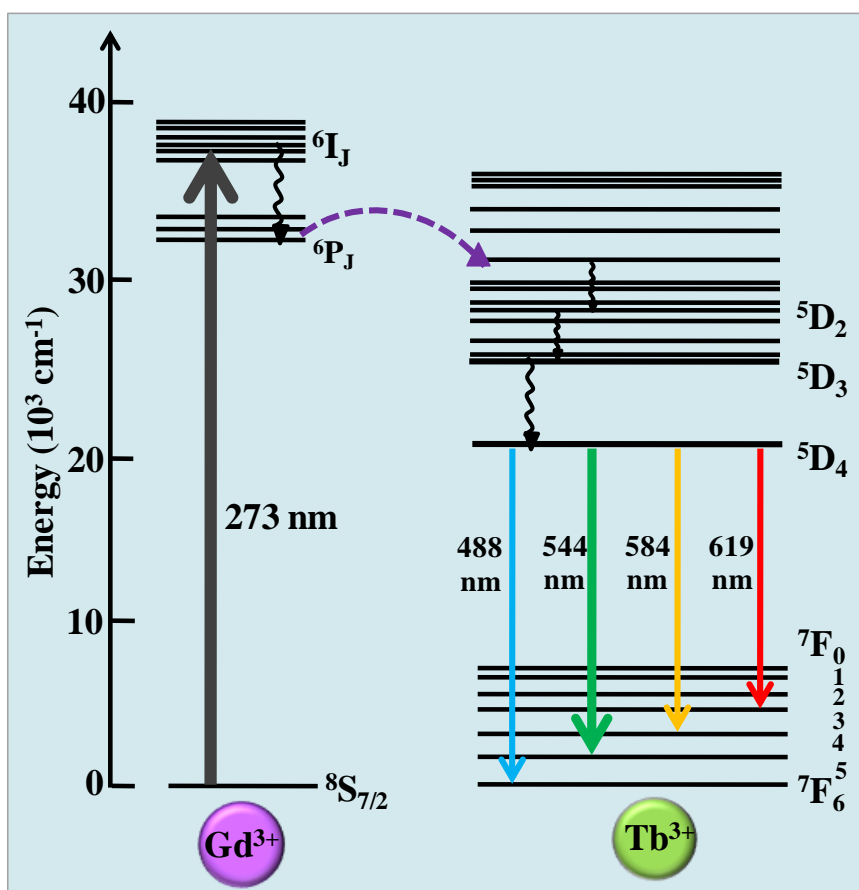
S. No.	Sample	Concentration (mL)	Morphology	Aspect ratio (L/W)
1.	β -Na YF ₄ :Gd,Tb-xGQD	0	rods	2.9
		1	hexagonal prism	1.7
		3	hexagonal prism	1.2
		5	flower-like structure	1.1
		7	disk-like structure	0.4
2.	β -Na YF ₄ :Gd,Tb-xGO	1	rods	3.1
		3	rods	2.6
		7	rods	2.1
3.	β -Na YF ₄ :Gd,Tb-xMWCNT	1	rods	2.9
		3	rods	2.7
		7	rods	2.8
4.	β -Na YF ₄ :Gd,Tb-xCOOH-MWCNT	1	rods	2.4
		3	rods	2.3
		7	rods	2.3
5.	β -Na YF ₄ :Gd,Tb-xCOOH-GQDs	1	microrods	4.1
		3	microrods	9.8
		7	microrods	23.3
6.	β -Na YF ₄ :Gd,Tb-xNH ₂ -GQDs	1	rods	3.1
		3	rods	2.8
		7	rods	2.4
7.	β -Na YF ₄ :Gd,Tb-xrGQDs	3	microrods	15.1
		7	microrods	20.5

3.3.4 Photoluminescence studies

Owing to the non-existence of *d*-electrons in Y³⁺ ([Kr] 4d⁰) in undoped NaYF₄, the probability of emission is negligible in the host matrix. As it is already mentioned, the emissive electronic transitions are characteristic features of dopant Ln³⁺ ions, so the incorporation of GQDs does not render any peak shift in the transition emission of Tb³⁺ ions, and bands differ only in their relative intensities. Here, Gd³⁺ ions acted as a sensitizer to enhance the emission of Tb³⁺ ions via nonradiative energy transfer. For the excitation spectra of Gd and Tb doped phosphor, **Fig. 2.12** in *Chapter 2* can be referred. The obtained emission spectra monitored at $\lambda_{\text{ex}} = 273$ nm, yielded intense green emissions in the region of 480-680 nm, which were due to the ⁵D₄ → ⁷F_{*J*} (*J* = 3, 4, 5, 6) transitions of Tb³⁺ ions. Four prominent emission peaks centered at ~488, ~544, ~584, and ~619 nm, originated from the transitions of ⁵D₄ → ⁷F₆, ⁵D₄ → ⁷F₅, ⁵D₄ → ⁷F₄, and ⁵D₄ → ⁷F₃ respectively.^{64,65,22} The mechanism for luminescence in Gd³⁺-Tb³⁺ pair under excitation of 273 nm has been demonstrated in **Scheme 3.4**. Among these transitions, the green emission ⁵D₄ → ⁷F₅ at ~ 544 nm was the most intense emission, which corresponded to a magnetic dipole transition. **Fig. 3.14** showed the comparative emission spectra of β -NaYF₄: Gd³⁺,Tb³⁺ phosphors incorporated with different concentrations of GQDs. It can be seen that with increasing concentration of GQDs, the PL intensity of the β -NaYF₄: Gd³⁺,Tb³⁺ phosphors showed a remarkable enhancement. It was believed that the change or increase in luminescence intensity was due to the change in morphology and size of the β -NaYF₄:Gd³⁺,Tb³⁺-xGQDs crystals. Different morphology of the host matrix greatly influences the emission intensity and the shape of the spectra^{65,66}. It was evident from the spectra that among all the samples, the disk-like structures obtained from β -NaYF₄:Gd³⁺,Tb³⁺-xGQDs (*x* = 7) displayed the strongest emission intensity under similar measurement conditions shown in **Fig. 3.14**. The β -NaYF₄: Gd³⁺,Tb³⁺-xGQDs (*x* = 0) rods possessed lowest emission intensity. While the relative

luminescence intensity of other β -NaYF₄: Gd³⁺,Tb³⁺-xGQDs crystals i.e., hexagonal microprisms obtained at x = 1 and x = 3, and flower-shaped crystals obtained at x = 5 lied in between the rods and disk-like structure.

The reason behind the difference in relative PL intensity might be due to the difference in surface area of different facets/shapes, defects, and crystallinity. Herein, the highest luminescence intensity of disk-like structures might be due to their low surface area-to-volume ratio and consequently possessed low surface defects when compared to other anisotropic structures.^{67,68} While the rods and other as-formed morphologies were predicted to have more surface defects owing to their high surface area.⁶⁹



Scheme 3.4 Partial energy level diagram showing the most probable energy transfer pathway, nonradiative decay, and emissive pathway in Gd³⁺-Tb³⁺ pair under excitation of 273 nm. The full, dotted, and curly arrows represent emission, energy transfer, and multiphonon relaxation processes, respectively.

The defects may have acted as the nonradiative recombination centers, which were thus responsible for luminescence quenching. Moreover, high surface area also rendered greater Gd³⁺ or Tb³⁺ ion fraction on the particle surface which again caused the enhanced nonradiative quenching and resulted in diminished emission intensity^{68,70}. In addition, to further understand the variation in PL performance, the PL spectra of β -NaYF₄: Gd³⁺/Tb³⁺-xGO, β -NaYF₄: Gd³⁺,Tb³⁺-xMWCNT, and β -NaYF₄: Gd³⁺,Tb³⁺-xCOOH-MWCNT (x = 7) crystals were also studied. **Fig. 3.15** showed the comparative PL spectra of β -NaYF₄: Gd³⁺,Tb³⁺-xGQDs (x = 0 and 7), β -NaYF₄:Gd³⁺,Tb³⁺-xGO, β -NaYF₄: Gd³⁺,Tb³⁺-xMWCNT, and β -NaYF₄: Gd³⁺,Tb³⁺-xCOOH-MWCNT (x = 7) crystals. As discussed above in *Section 3.3.3.1*, the incorporation of other carbon materials; as GO and MWCNTs had a very little influence on the morphology and size of the β -NaYF₄:Gd³⁺,Tb³⁺ crystals.

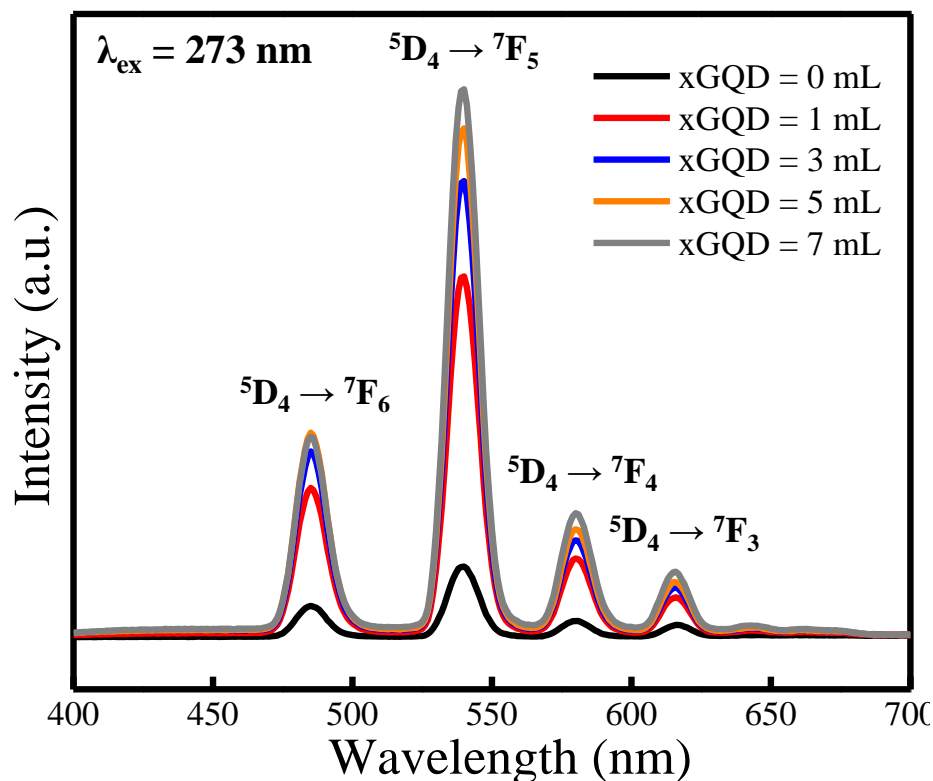


Figure 3.14 A comparison of static photoluminescence emission spectra at the excitation wavelength $\lambda_{\text{ex}} = 273$ nm of β -NaYF₄: Gd³⁺,Tb³⁺+xGQDs phosphors with different concentrations of GQDs.

As a consequence of a negligible change in the morphologies, it can be clearly seen that the relative luminescence intensities hardly changed with the incorporation of the above-mentioned foreign materials. However, when compared with the disk-like structures, PL intensity showed a remarkable change. The luminescence intensity of the disk-like structure was observed to be 8 times stronger than the β -NaYF₄: Gd³⁺, Tb³⁺ crystals incorporated with GO and MWCNT and β -NaYF₄: Gd³⁺, Tb³⁺ rods. In order to get further insight into the effect of incorporation of GQDs on luminescence intensity of β -NaYF₄:Gd³⁺, Tb³⁺ phosphor crystals, PL spectra of β -NaYF₄:Gd³⁺/Tb³⁺ crystals incorporated with different functionalized GQDs; β -NaYF₄: Gd³⁺, Tb³⁺-xCOOH-GQDs, and β -NaYF₄: Gd³⁺, Tb³⁺-xNH₂-GQDs were demonstrated (Fig. 3.16).

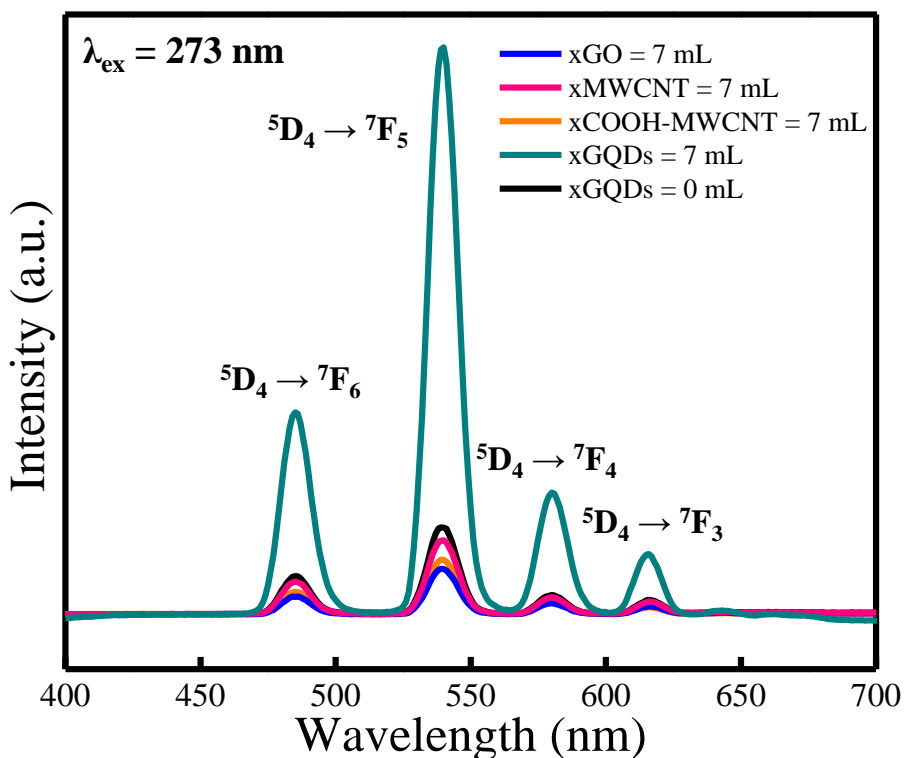


Figure 3.15 A static photoluminescence emission spectra at the excitation wavelength $\lambda_{\text{ex}} = 273$ nm of β -NaYF₄: Gd³⁺, Tb³⁺ phosphors with different concentration ($x = 7$ ml) of GO and multiwalled carbon nanotube, MWCNT. A comparison has been made with the β -NaYF₄: Gd³⁺, Tb³⁺ phosphors incorporated with carboxylic and amine co-functionalized GQDs.

As it is already discussed above, the functionalization of GQDs plays an important role in the morphology tuning of the crystals; consequently, it could be clearly reflected in the PL spectra. In the case of β -NaYF₄: Gd³⁺,Tb³⁺-xCOOH-GQDs (x = 1, 3 and 7) crystals, with increasing concentration of COOH-GQDs, the size of as-formed microrods increased, and thus the PL intensity also increased. Since the surface area-to-volume ratio increased with a decrease in the size of the material, thus a phosphor with the largest size would possess the lowest surface area and highest luminescence intensity.⁷¹ Therefore, the β -NaYF₄: Gd³⁺,Tb³⁺-xCOOH-GQD (x=7) microrod (~30 μ m) possessed highest luminescence intensity, while β -NaYF₄: Gd³⁺,Tb³⁺-xCOOH-GQD (x = 1) microrods (~15 μ m) and β -NaYF₄: Gd³⁺,Tb³⁺ rods have lower PL intensity.

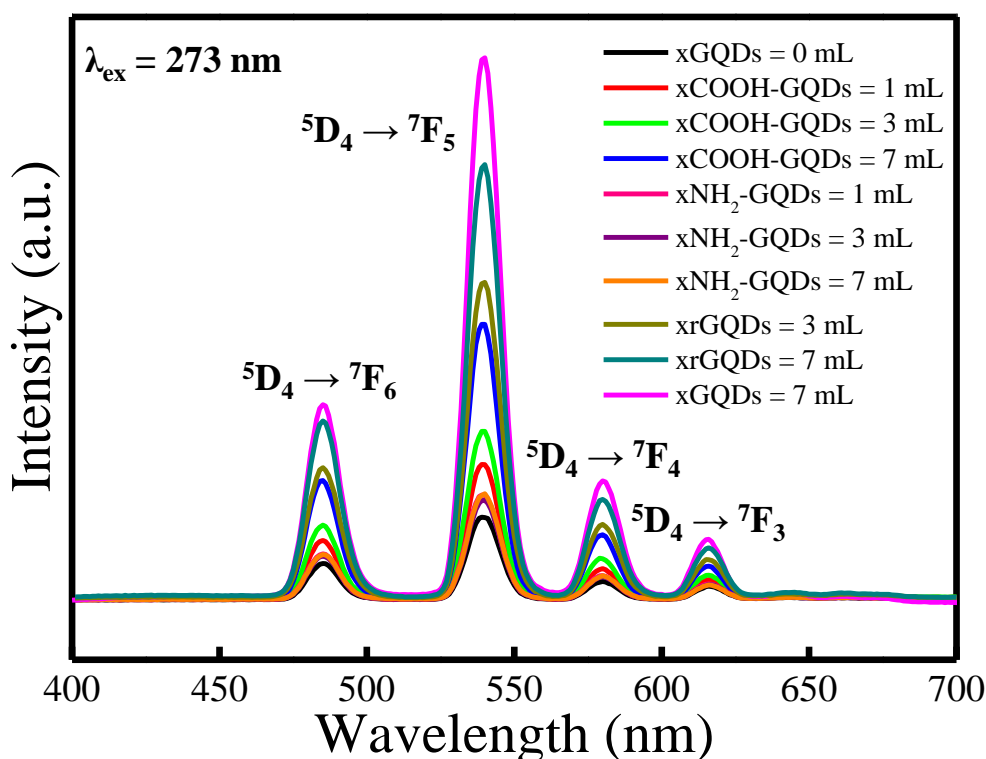


Figure 3.16 A comparative static photoluminescence emission spectra of β -NaYF₄: Gd³⁺,Tb³⁺ phosphors with different concentrations of carboxylic-, amine-functionalized GQDs, respectively, reduced GQDs and β -NaYF₄: Gd³⁺,Tb³⁺-xGQDs phosphors at $\lambda_{\text{ex}} = 273$ nm where x is varied as x = 1 mL, x = 3 mL and x = 7 mL.

Negligible change in PL intensity was observed owing to negligible change in size and morphology of β -NaYF₄:Gd³⁺,Tb³⁺-xNH₂-GQDs (x = 1, 3, and 7) rod-shaped crystals (**Fig. 3.16**). PL spectra of the NaYF₄: Gd³⁺,Tb³⁺ with rGQDs were also recorded and compared with disk-like structure. The emission intensity of NaYF₄: Gd³⁺,Tb³⁺-xrGQDs were obviously lower than disk-like structures, but higher than the β -NaYF₄: Gd³⁺,Tb³⁺-xCOOH-GQD microrods. Since, NaYF₄: Gd³⁺,Tb³⁺-xrGQDs attained cubic phase along with hexagonal phase, i.e., mixed-phase, its emission intensity was expected to be lower because the mixed-phase system is less luminescent than the pure hexagonal phase.^{72,73,25} But, the higher intensity of NaYF₄: Gd³⁺,Tb³⁺-xrGQDs microrods as compared to β -NaYF₄: Gd³⁺,Tb³⁺-xCOOH-GQD microrods was might be due to their larger size (~ 35 μ m). However, the overall spectra revealed that the PL intensity of disk-like structures remained the strongest emission intensity amongst all the samples. The luminescent properties of inorganic materials were dependent on several factors such as crystal structure around emitting ions, morphology, size, crystallinity, impurity doping, surface defects, surface adsorbed species, solvent molecules, ligands, etc.⁷⁴ In this study, although the incorporation of GQDs had a significant influence on the growth of β -NaYF₄: Gd³⁺,Tb³⁺ crystals, but on the basis of the above analysis, among all the factors, it was believed that the variation in photoluminescence properties of the samples are predominantly arise from their size and morphologies.

3.4 Conclusions

In summary, a novel impurity-driven strategy for morphology tuning of β -NaYF₄: Gd³⁺,Tb³⁺ phosphor crystals was presented, wherein GQDs were incorporated *in situ* into the β -NaYF₄: Gd³⁺,Tb³⁺ crystal system to manipulate the growth of phosphor crystals. Consequently, the morphology of the crystals was drastically changed upon the incorporation of GQDs at different concentrations. The results were also compared with differently

functionalized GQDs at varied concentrations. The plausible growth mechanism of β -NaYF₄: Gd³⁺,Tb³⁺-xGQDs crystals was proposed. The effect of two dimensional and one dimensional other carbon-based structures such as; GO and MWCNT were investigated and compared with the results obtained with the incorporation of GQDs. It was found that the PL properties of β -NaYF₄: Gd³⁺,Tb³⁺ phosphor crystals were strongly dependent on the particle size and morphology. To the best of our knowledge, for the first time, an approach to incorporate GQDs was implied to influence the growth of β -NaYF₄: Gd³⁺,Tb³⁺ phosphor crystals to attain their multiform morphologies. The results presented here underline the critical role that controlled morphological synthesis can play in optimizing key properties of advanced functional materials and could be extended to other lanthanide-doped nanocrystals. This unique approach paves the way to new opportunities for designing and tuning the phosphor crystals, and their unique luminescence properties may endow potential applications in the field of color displays, light-emitting diodes, solid-state lasers, and luminescent biological labels.

3.5 References

- 1 B. M. Walsh, N. P. Barnes, M. Petros, J. Yu and U. N. Singh, *J. Appl. Phys.*, 2004, **95**, 3255–3271.
- 2 Y. Zhang, B. Chen, S. Xu, X. Li, J. Zhang, J. Sun, H. Zheng, L. Tong, G. Sui, H. Zhong, H. Xia and R. Hua, *Sci. Rep.*, 2017, **7**, 11849.
- 3 H. Jia, K. Ren, X. Wang and L. Li, *Sensors Actuators B Chem.*, 2016, **228**, 308–316.
- 4 M. He, P. Huang, C. Zhang, H. Hu, C. Bao, G. Gao, R. He and D. Cui, *Adv. Funct. Mater.*, 2011, **21**, 4470–4477.
- 5 G. Tian, Z. Gu, L. Zhou, W. Yin, X. Liu, L. Yan, S. Jin, W. Ren, G. Xing, S. Li and Y. Zhao, *Adv. Mater.*, 2012, **24**, 1226–1231.
- 6 L. Tong, X. Li, J. Zhang, S. Xu, J. Sun, H. Zheng, Y. Zhang, X. Zhang, R. Hua, H. Xia and

- B. Chen, *Opt. Express*, 2017, **25**, 16047.
- 7 L. Tong, X. Li, J. Zhang, S. Xu, J. Sun, L. Cheng, H. Zheng, Y. Zhang, X. Zhang, R. Hua, H. Xia and B. Chen, *Sensors Actuators B Chem.*, 2017, **246**, 175–180.
- 8 K. Li, S. Liang, M. Shang, H. Lian and J. Lin, *Inorg. Chem.*, 2016, **55**, 7593–7604.
- 9 P. Padhye, S. Sadhu, M. Malik and P. Poddar, *RSC Adv.*, 2016, **6**, 53504–53518.
- 10 G.-B. Shan, H. Assaouidi and G. P. Demopoulos, *ACS Appl. Mater. Interfaces*, 2011, **3**, 3239–3243.
- 11 D. E. Achatz, R. Ali and O. S. Wolfbeis, in *Top Curr Chem*, 2010, vol. 300, pp. 29–50.
- 12 U. Resch-Genger, M. Grabolle, S. Cavaliere-Jaricot, R. Nitschke and T. Nann, *Nat. Methods*, 2008, **5**, 763–775.
- 13 Y. Liu, D. Tu, H. Zhu, E. Ma and X. Chen, *Nanoscale*, 2013, **5**, 1369–1384.
- 14 B. Zhou, B. Shi, D. Jin and X. Liu, *Nat. Nanotechnol.*, 2015, **10**, 924–936.
- 15 M. Haase and H. Schäfer, *Angew. Chemie Int. Ed.*, 2011, **50**, 5808–5829.
- 16 M. Ding, C. Lu, Y. Song, Y. Ni and Z. Xu, *CrystEngComm*, 2014, **16**, 1163.
- 17 C. Li and J. Lin, *J. Mater. Chem.*, 2010, **20**, 6831.
- 18 D. Gao, W. Gao, P. Shi and L. Li, *RSC Adv.*, 2013, **3**, 14757.
- 19 D. Liu, X. Xu, Y. Du, X. Qin, Y. Zhang, C. Ma, S. Wen, W. Ren, E. M. Goldys, J. A. Piper, S. Dou, X. Liu and D. Jin, *Nat. Commun.*, 2016, **7**, 10254.
- 20 C. Wang, H. Tao, L. Cheng and Z. Liu, *Biomaterials*, 2011, **32**, 6145–6154.
- 21 C. Li, J. Yang, P. Yang, H. Lian and J. Lin, *Chem. Mater.*, 2008, **20**, 4317–4326.
- 22 P. Padhye and P. Poddar, *J. Mater. Chem. A*, 2014, **2**, 19189–19200.
- 23 P. Qiu, N. Zhou, Y. Wang, C. Zhang, Q. Wang, R. Sun, G. Gao and D. Cui, *CrystEngComm*, 2014, **16**, 1859.
- 24 Y. Sun, Y. Chen, L. Tian, Y. Yu, X. Kong, J. Zhao and H. Zhang, *Nanotechnology*, 2007,

18, 275609.

- 25 Y. Wang, S. Gai, N. Niu, F. He and P. Yang, *Phys. Chem. Chem. Phys.*, 2013, **15**, 16795.
- 26 F. Wang and X. Liu, *Chem. Soc. Rev.*, 2009, **38**, 976.
- 27 P. Qiu, N. Zhou, H. Chen, C. Zhang, G. Gao and D. Cui, *Nanoscale*, 2013, **5**, 11512.
- 28 Q. Dou and Y. Zhang, *Langmuir*, 2011, **27**, 13236–13241.
- 29 M. Ding, D. Chen, S. Yin, Z. Ji, J. Zhong, Y. Ni, C. Lu and Z. Xu, *Sci. Rep.*, 2015, **5**, 12745.
- 30 Y. Wang, T. Wei, X. Cheng, H. Ma, Y. Pan, J. Xie, H. Su, X. Xie, L. Huang and W. Huang, *J. Mater. Chem. C*, 2017, **5**, 3503–3508.
- 31 X. Xue, L. Wang, L. Huang, D. Zhao and W. Qin, *CrystEngComm*, 2013, **15**, 2897.
- 32 S. Y. Wu, X. Lin, W. Shao, and K. Zhang, J. Xu, L. Yu and Chen, *RSC Adv.*, 2016, **6**, 102869–102874.
- 33 A. Biswas, G. Salunke, P. Khandelwal, R. Das and P. Poddar, *New J. Chem.*, 2017, **41**, 2642–2657.
- 34 C. Cha, S. R. Shin, N. Annabi, M. R. Dokmeci and A. Khademhosseini, *ACS Nano*, 2013, **7**, 2891–2897.
- 35 Y. Li, H. Shu, X. Niu and J. Wang, *J. Phys. Chem. C*, 2015, **119**, 24950–24957.
- 36 M. Roushani and Z. Abdi, *Sensors Actuators, B Chem.*, 2014, **201**, 503–510.
- 37 L. Li and X. Yan, *J. Phys. Chem. Lett.*, 2010, **1**, 2572–2576.
- 38 C. M. Luk, B. L. Chen, K. S. Teng, L. B. Tang and S. P. Lau, *J. Mater. Chem. C*, 2014, **2**, 4526–4532.
- 39 L. Chen, C. X. Guo, Q. Zhang, Y. Lei, J. Xie, S. Ee, G. Guai, Q. Song and C. M. Li, *ACS Appl. Mater. Interfaces*, 2013, **5**, 2047–2052.
- 40 I. Mihalache, A. Radoi, M. Mihaila, C. Munteanu, A. Marin, M. Danila, M. Kusko and C.

- Kusko, *Electrochim. Acta*, 2015, **153**, 306–315.
- 41 H. Tetsuka, a. Nagoya and R. Asahi, *J. Mater. Chem. C Mater. Opt. Electron. Devices*, 2015, **3**, 3536–3541.
- 42 K. Binnemans, *Chem. Rev.*, 2009, **109**, 4283–4374.
- 43 W. Wei, T. He, X. Teng, S. Wu, L. Ma, H. Zhang, J. Ma, Y. Yang, H. Chen, Y. Han, H. Sun and L. Huang, *Small*, 2012, **8**, 2271–2276.
- 44 T. He, W. Wei, L. Ma, R. Chen, S. Wu, H. Zhang, Y. Yang, J. Ma, L. Huang, G. G. Gurzadyan and H. Sun, *Small*, 2012, **8**, 2163–2168.
- 45 M. Luoshan, M. Li, X. Liu, K. Guo, L. Bai, Y. Zhu, B. Sun and X. Zhao, *J. Power Sources*, 2015, **287**, 231–236.
- 46 L. Yan, Y.-N. Chang, W. Yin, X. Liu, D. Xiao, G. Xing, L. Zhao, Z. Gu and Y. Zhao, *Phys. Chem. Chem. Phys.*, 2014, **16**, 1576–1582.
- 47 Y. Li, G. Wang, K. Pan, B. Jiang, C. Tian, W. Zhou and H. Fu, *J. Mater. Chem.*, 2012, **22**, 20381.
- 48 W. Liu, G. Liu, X. Dong, J. Wang and W. Yu, *Phys. Chem. Chem. Phys.*, 2015, **35**, 22659–67.
- 49 M. Laurenti, M. Paez-Perez, M. Algarra, P. Alonso-Cristobal, E. Lopez-Cabarcos, D. Mendez-Gonzalez and J. Rubio-Retama, *ACS Appl. Mater. Interfaces*, 2016, **8**, 12644–12651.
- 50 K. Wang, J. Ruan, H. Song, J. Zhang, Y. Wo, S. Guo and D. Cui, *Nanoscale Res. Lett.*, 2011, **6**, 1–8.
- 51 F. Jiang, D. Chen, R. Li, Y. Wang, G. Zhang, S. Li, J. Zheng, N. Huang, Y. Gu, C. Wang and C. Shu, *Nanoscale*, 2013, **5**, 1137.
- 52 G. Sandeep Kumar, R. Roy, D. Sen, U. K. Ghorai, R. Thapa, N. Mazumder, S. Saha and K. K. Chattopadhyay, *Nanoscale*, 2014, **6**, 3384.

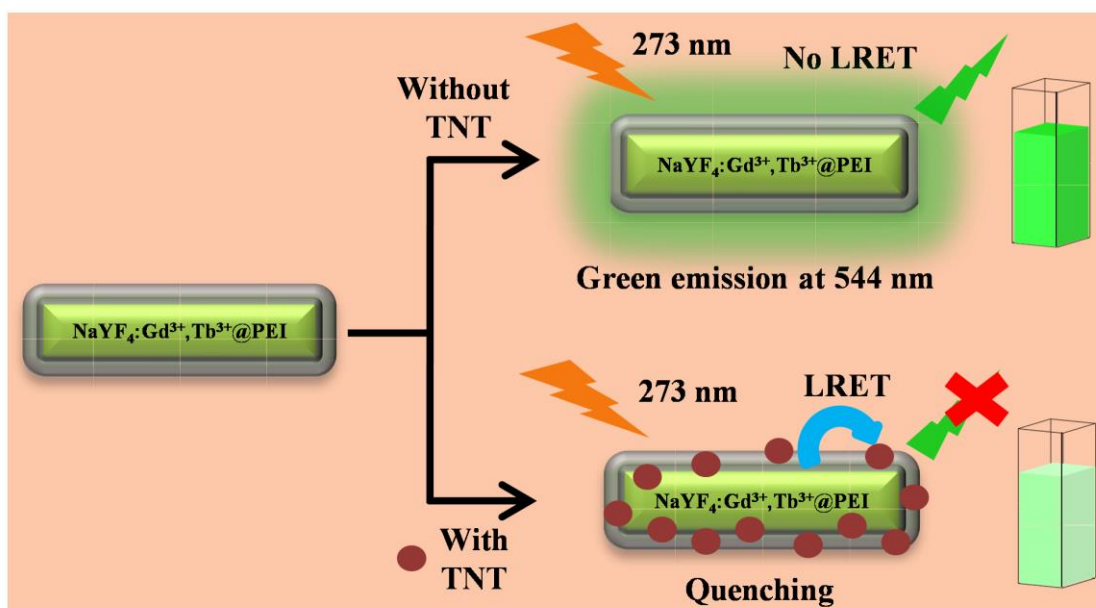
- 53 L.-L. Li, J. Ji, R. Fei, C.-Z. Wang, Q. Lu, J.-R. Zhang, L.-P. Jiang and J.-J. Zhu, *Adv. Funct. Mater.*, 2012, **22**, 2971–2979.
- 54 F. Wang, D. K. Chatterjee, Z. Li, Y. Zhang, X. Fan and M. Wang, *Nanotechnology*, 2006, **17**, 5786–5791.
- 55 P. Padhye, A. Alam, S. Ghorai, S. Chattopadhyay and P. Poddar, *Nanoscale*, 2015, **7**, 19501–19518.
- 56 L. Wang, Y. Wang, T. Xu, H. Liao, C. Yao, Y. Liu, Z. Li, Z. Chen, D. Pan, L. Sun and M. Wu, *Nat. Commun.*, 2014, **5**, 5357.
- 57 R. Beams, L. Gustavo Cançado and L. Novotny, *J. Phys. Condens. Matter*, 2015, **27**, 083002.
- 58 S. Kim, D. Hee Shin, C. Oh Kim, S. Seok Kang, S. Sin Joo, S.-H. Choi, S. Won Hwang and C. Sone, *Appl. Phys. Lett.*, 2013, **102**, 053108.
- 59 D. Yang, G. Li, X. Kang, Z. Cheng, P. Ma, C. Peng, H. Lian, C. Li and J. Lin, *Nanoscale*, 2012, **4**, 3450.
- 60 S. Zeng, G. Ren, C. Xu and Q. Yang, *CrystEngComm*, 2011, **13**, 1384–1390.
- 61 H. Mai, Y. Zhang, R. Si, Z.-G. Yan, L. Sun, L. You and C. Yan, *J. Am. Chem. Soc.*, 2006, **128**, 6426–6436.
- 62 A. Bagri, C. Mattevi, M. Acik, Y. J. Chabal, M. Chhowalla and V. B. Shenoy, *Nat. Chem.*, 2010, **2**, 581–587.
- 63 W. Zhang, Y. Liu, X. Meng, T. Ding, Y. Xu, H. Xu, Y. Ren, B. Liu, J. Huang, J. Yang and X. Fang, *Phys. Chem. Chem. Phys.*, 2015, **17**, 22361–22366.
- 64 P. C. Ricci, C. M. Carbonaro, R. Corpino, C. Cannas and M. Salis, *J. Phys. Chem. C*, 2011, **115**, 16630–16636.
- 65 S. Kundu, A. Kar and A. Patra, *J. Lumin.*, 2012, **132**, 1400–1406.

- 66 M. Zhang, H. Fan, B. Xi, X. Wang, C. Dong and Y. Qian, *J. Phys. Chem. C*, 2007, **111**, 6652.
- 67 L. Zhu, Q. Li, X. Liu, J. Li, Y. Zhang, J. Meng and X. Cao, *J. Phys. Chem. C*, 2007, **111**, 5898–5903.
- 68 J. Shan, M. Uddi, R. Wei, N. Yao and Y. Ju, *J. Phys. Chem. C*, 2010, **114**, 2452–2461.
- 69 P. R. Sajanlal, T. S. Sreepasad, A. K. Samal and T. Pradeep, *Nano Rev.*, 2011, **2**, 5883.
- 70 S. Zeng, G. Ren, C. Xu and Q. Yang, *CrystEngComm*, 2011, **13**, 4276.
- 71 J. Yang, C. Li, Z. Cheng, X. Zhang, Z. Quan, C. Zhang and J. Lin, *J. Phys. Chem. C*, 2007, **111**, 18148–18154.
- 72 D.-K. Ma, S.-M. Huang, Y.-Y. Yu, Y.-F. Xu and Y.-Q. Dong, *J. Phys. Chem. C*, 2009, **113**, 8136–8142.
- 73 Y. Wang, R. Cai and Z. Liu, *CrystEngComm*, 2011, **13**, 1772.
- 74 A. Nadort, J. Zhao and E. M. Goldys, *Nanoscale*, 2016, **8**, 13099–13130.

Chapter 4



A downconversion luminescence-based nanosensor for label-free detection of explosives



Outline

In this chapter, a selective and sensitive nanosensor probe based on the polyethylenimine (PEI) capped downconverting nanophosphors; β -NaYF₄: Gd³⁺, Tb³⁺@PEI was designed for the detection of 2,4,6-trinitrotoluene (TNT), both in water and buffer media. These downconverting phosphors were synthesized via a hydrothermal route and showed excellent chemical, thermal, and photostability. They emitted sharp emission peaks centered around ~488 nm, ~544 nm, ~584 nm, and ~619 nm, among which the peak around ~544 nm was remarkably quenched (~90%) by the addition of TNT without giving any new emission peak. The sensing mechanism was proposed based on the formation of Meisenheimer complex between the electron-rich amine-functionalized β -NaYF₄: Gd³⁺, Tb³⁺ nanophosphors, and electron-deficient TNT molecule, which was prominently visualized by the change in color of the solution from whitish to brownish-yellow, which also enabled visual detection, followed by luminescence resonance energy transfer (LRET) between the nanophosphors and the complex. A linear range for TNT detection was obtained from 0.1 to 300 μ M with a limit of detection as low as 119.9 nM. This method displayed excellent selectivity towards TNT over other nitroaromatic compounds, which had no influence on the detection. Moreover, various other classes of analytes, viz. amino acids, pesticides, and sugars, did not quench the luminescence intensity of the nanophosphors. This developed nanosensor probe possessed high, stable fluorescence brightness and capability for the selective and sensitive on-site recognition of TNT molecules in aqueous media, avoiding complicated strategies and instruments. Thus, this work promised to pave the way for many applications in detecting ultra-trace analytes.

4.1 Introduction

The riveting optical features of lanthanide ions such as narrow and sharp emission bandwidth, large Stokes and anti-Stokes shift, tunable emission spectra, long-lived emission usually in milliseconds, low autofluorescence, and reduced blinking arise from their electronic transitions within the $4f$ orbitals, hence giving them an edge over conventional fluorophores and quantum dots.¹ Having these advantages, recently, lanthanide-doped phosphors have emerged as a potential material in various applications such as solid-state lasers,² light-emitting devices,³ solar cells,⁴ sensing,⁵ cell imaging,⁶ drug delivery,^{7,8} and so forth. One of the most propitious applications of these luminescent phosphors is their use as the optical probes for the identification of molecules such as glutathione,⁹ glucose,¹⁰ avidin,¹¹ and ions like cyanide,¹² mercury,¹³ and so forth for the sensing applications. Profound efforts have been devoted to the development of novel, innovative, and implicit sensors. Thus, these lanthanide ion-doped phosphors can be applied to the highly selective and sensitive real-time and on-site detection of the explosives.

Identification and quantification of explosives have constituted an emerging and important topic of interest. Reliable detection of trace amounts of explosive substances is of importance concerning homeland security threats, military applications, mine-field analysis, forensic investigations, etc. Moreover, these compounds are known to have toxicity, carcinogenicity, mutagenicity, and their release into the environment from military sites and ammunition plants causes the contamination of water and soil.¹⁴ Because of the risk associated with the environment, humans, and wildlife, the detection has gained increasing attention. The detection could help in reducing the fatalities among the civilians and health risk hazards.

The chemical structures of the commonly used nitro compounds are shown in **Fig. 4.1**. In recent years, a variety of analytical techniques and detection methods of explosives

have been developed, including gas chromatography (GC),¹⁵ ion mobility spectrometry,¹⁶ surface-enhanced Raman spectroscopy,^{17,18} conductivity-based techniques,¹⁹ and so forth. However, these methods are usually limited by several intrinsic shortcomings; some require complicated instrumentation or synthetic processes while others require labeling procedures, which are typically time-consuming, expensive, and require specialized personnel. Thence, to meet this need, the fluorescence quenching approach has been explored for the analysis of nitro-based explosives. Fluorescence-based sensing methods have gained immense attention because of the relatively lower operational costs than the conventional methods, simplicity, higher sensitivities, portability, short response times, and its pertinence in both solution and the solid phase.

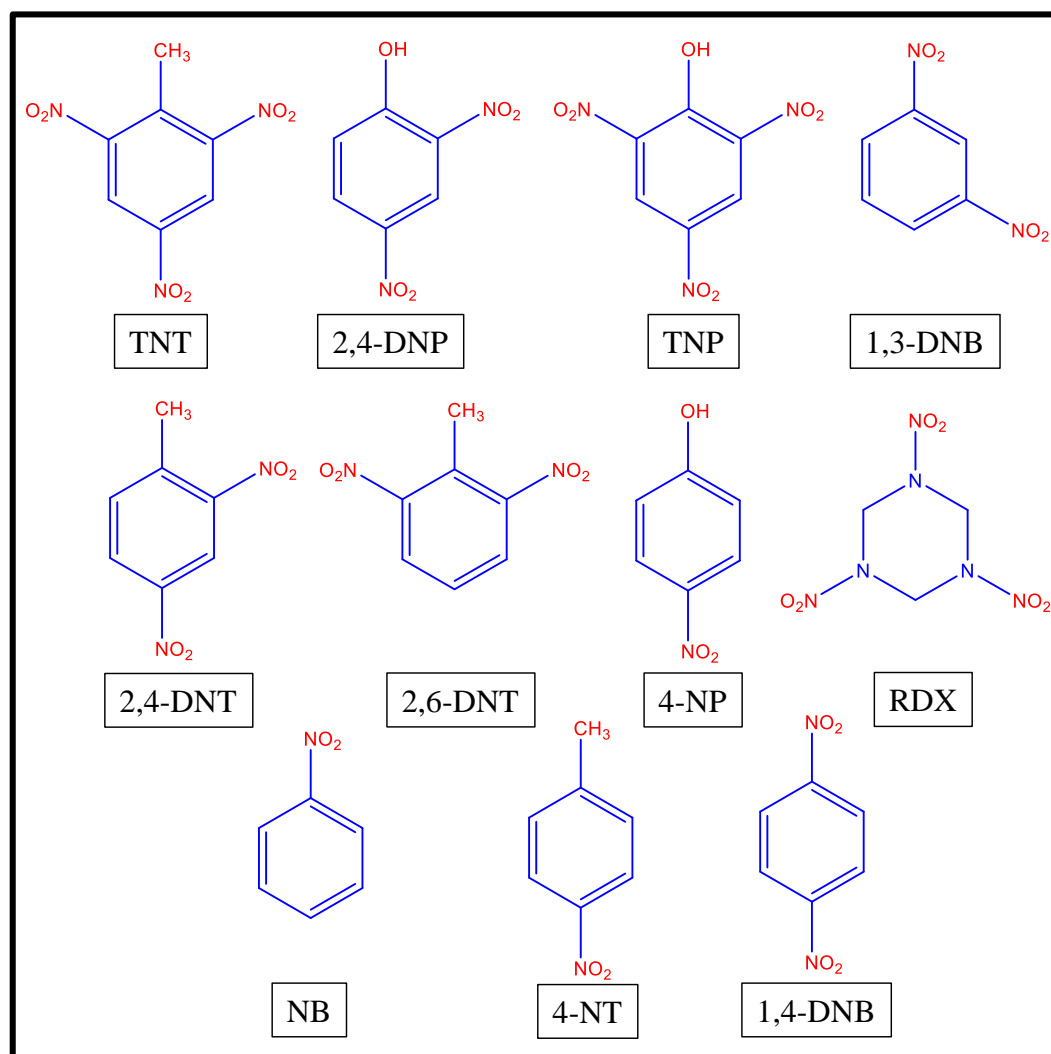


Figure 4.1 The chemical structures of the commonly used nitro compounds.

Various nanomaterials were used to develop a fluorescence sensing platform for explosive sensing.^{20–23} Although these various nanostructured materials reported to construct fluorescent probes for the selective detection of the explosives, there is still a challenge to utilize them as sensors because they possess low chemical and thermal stability, poor aqueous solubility, require time-consuming synthetic method, and are receptive towards photobleaching, thus are insufficient for the detection of analytes in aqueous samples. Therefore, other classes of compounds based on Ln^{3+} ions have garnered attention for sensing applications in the past few years.

Due to good chemical, thermal, and photostability, the Ln^{3+} ion-doped phosphors are highly desirable as sensors.²⁴ Moreover, long-lived luminescence of Ln^{3+} ions could allow them to be potentially used for analyte detection in strongly autofluorescent biological matrices. These have been used in sensing of various hazardous analytes of environmental and clinical importance.^{25–27} These phosphors have also been employed for sensing explosives via fluorescence-based detection up to a level of nM concentration. In 2014, Ma et al. reported label-free detection of TNT using upconverting nanoparticles $\text{NaYF}_4:\text{Yb,Er}$ at $\text{pH} = 12$ with a detection limit of 9.7 ng/mL.²⁸ In the same year, a miniaturized device was fabricated using $\text{NaYF}_4:\text{Yb,Er}@PEI$, which detected TNT explosives by the formation of the Meisenheimer complex and quenched the green luminescence.²⁹ Although the mentioned methods utilized the selectivity of these materials over other analogous analytes, but they involved multistep and time-consuming synthetic processes. Also, these sensors worked in the high pH range (12 and above), thus, limiting their applicability as sensors. Nevertheless, $\beta\text{-NaYF}_4:\text{Gd,Tb}$ downconverting nanophosphors being highly luminescent have rarely been explored as a fluorescent probe for the selective and sensitive detection of explosives.

In this contribution, a label-free method for the selective detection of TNT was developed, in the aqueous solution of nitro compounds, characteristics to explosives based

on the green-emitting phosphors. These Ln^{3+} ion-doped phosphors were functionalized with amine groups (NH_2) using PEI via a hydrothermal route. The detection was based on the photoluminescence method by observing the change in intensity at 544 nm of the green light, which was selectively and dramatically quenched *via* LRET-based energy transfer from nanophosphors to the Meisenheimer complex, the detailed mechanism of which is explained. Meanwhile, the intensity was not influenced by the addition of other nitro compounds in the aqueous solution. Furthermore, no drastic change in intensity was observed with other categories of analytes such as amino acids, pesticides, and sugars. The currently developed sensing probe was also applicable in a wide pH range from 7-13. Combined with good water and chemical stability, photostability and wide pH adaptability will facilitate the application of this system as a potential nanosensor probe.

4.2 Materials and methods

4.2.1 Materials: All the chemicals were of analytical grade and were used without further purification. $\text{Y}(\text{NO}_3)_3 \cdot 6\text{H}_2\text{O}$, $\text{Gd}(\text{NO}_3)_3 \cdot 6\text{H}_2\text{O}$, and $\text{Tb}(\text{NO}_3)_3 \cdot 6\text{H}_2\text{O}$, PEI (with $M_w = 25000$ and $M_n = 10000$). TNP, 2,4-DNT, 2,6-DNT, 2,4-DNP, RDX, phenylalanine, cysteine, isoleucine, tryptophan, glutamic acid, aspartic acid, lysine, histidine, and glutamine were purchased from Sigma Aldrich Inc. TNT and RDX were purchased from HEMRL, Pune. NaCl , Na_2HPO_4 , NaH_2PO_4 , Na_2CO_3 , NaHCO_3 and NaOH were received from Thomas Baker. NH_4F was received from Merck. Dextrose, glucose, sucrose, fructose, lactose, and maltose were received from Himedia Laboratories Pvt. Ltd. 1,3-DNB, 4-NP, 2,4-DNB, NM, 4-NT, NB, copper oxychloride, cypermethrin, malathion, fenvalerate, carbendazim, and chlorpyrifos were purchased from a local company and used as received. Ethanol was obtained from Hayman Ltd. Deionized water (DI) was used throughout the experiments.

4.2.2 Synthesis

4.2.2.1 Synthesis of amine-functionalized β -NaYF₄: 15%Gd³⁺,5%Tb³⁺ (β -NaYF₄:Gd³⁺, Tb³⁺@PEI): Downconverting NaYF₄ nanophosphors were prepared using the hydrothermal method reported earlier.^{7,30} Briefly, 10 mL of 0.2 M solutions of Y(NO₃)₃, Gd(NO₃)₃, and Tb(NO₃)₃ were added in a 10 mL solution of NaCl (0.2 M). The solution was continuously stirred for nearly 30 min. Thereafter, 10 mL of PEI (10 wt%) was added, followed by the addition of 20 mL of ethanol. In the resultant solution, 0.5 M of NH₄F was added dropwise. Finally, the mixture was poured in a Teflon container with 100 mL capacity and reaction was set for 24 h at 180 °C. The autoclave was cooled to room temperature; the green luminescent nanophosphors were obtained after washing with water and ethanol thrice. Then, the product was dried under vacuum at 70 °C overnight.

4.2.2.2 Preparation of stock solutions: For the photoluminescence study (PL), 300 μ M stock solution of the analytes were prepared in deionized water and added to the fixed amount of β -NaYF₄: Gd³⁺,Tb³⁺@PEI to the desired concentrations levels in 1 mL quartz cuvette (path length of 1 cm). The mixture was then incubated at room temperature for 10 min before the spectral measurements. The luminescence spectra of the solutions were measured at an excitation wavelength of 273 nm, and emission data were collected in the range of (400-700) nm. Each measurement was repeated at least thrice, and consistent results were recorded. The feasibility of the probe was also investigated in buffer solution with pH 7 to pH 13. For pH ranging from 7 to 8, NaH₂PO₄-Na₂HPO₄, pH ranging from 9 to 11 NaHCO₃-Na₂CO₃-NaOH, and pH ranging from 12 to 13 KCl-NaOH were used.

4.2.3 Characterization techniques

The instrumental details of PXRD, TEM and PL can be obtained from *Chapter 2*, while the details of TGA, and UV-vis spectrometer can be obtained from *Chapter 3*. To analyze the shape and size of the samples, FESEM was done using Hitachi S-4200. EDXA of the samples was performed during FESEM to obtain the elemental composition of the

samples. The XPS spectra were recorded on Thermo Fisher Scientific Instruments K Alpha+ with monochromatic Al K alpha as the X-ray source with 6 mA beam current and 12 kV voltage. A PALS Zeta Potential Analyzer Ver 3.54 (Brookhaven Instrument Corps.) was used to determine the zeta potentials (ζ). Deionized water was the dispersion medium. Fourier transform infrared spectrum (FTIR) was recorded by Perkin Elmer spectrum two FT-IR spectrophotometer with a resolution of 4 cm^{-1} and a scan speed of 32 scans/min.. PL spectra were acquired using a Cary Eclipse fluorescence spectrophotometer, equipped with a 400 W Xe lamp as an excitation source with an excitation and emission slit width of 10 nm and a Hamamatsu R928 photomultiplier tube as a detector. PL decay dynamics were carried out on FLS 980 (Edinburgh Instruments).

4.3 Results and discussion

The composition, crystallinity and phase purity of the NaYF₄ nanophosphors were first checked by powder XRD, as shown in **Fig. 4.2**. The sample diffraction peaks can be indexed to NaYF₄ with lattice parameters as $a = 5.9\text{ \AA}$, and $c = 3.5\text{ \AA}$, which is in good agreement with standard JCPDS data (JCPDS no. 16-0334), confirming the hexagonal phase of the as-synthesized product. The TEM and FESEM images (**Fig. 4.3a,b**) showed that the β -NaYF₄: Gd³⁺,Tb³⁺@PEI particles prepared at 180 °C are grown in rod-shaped particles and exhibit uniform shapes and are monodispersed with an average diameter of ~ 92 nm and length of ~ 280 nm. The contrast in the TEM image observed was due to the different orientations of the crystalline nanoparticles with respect to the electron beam, which changed the elastic scattering diffraction and thus appeared in different contrast. Further, the chemical composition of the β -NaYF₄: Gd³⁺,Tb³⁺ nanophosphors was characterized by EDXA analysis where all the elements in the nanophosphors could be detected, including doped Gd³⁺ and Tb³⁺ ions confirming the presence of the lanthanide ions (**Fig. 4.3c**). Furthermore, the detailed structure analysis was done through HRTEM analysis.

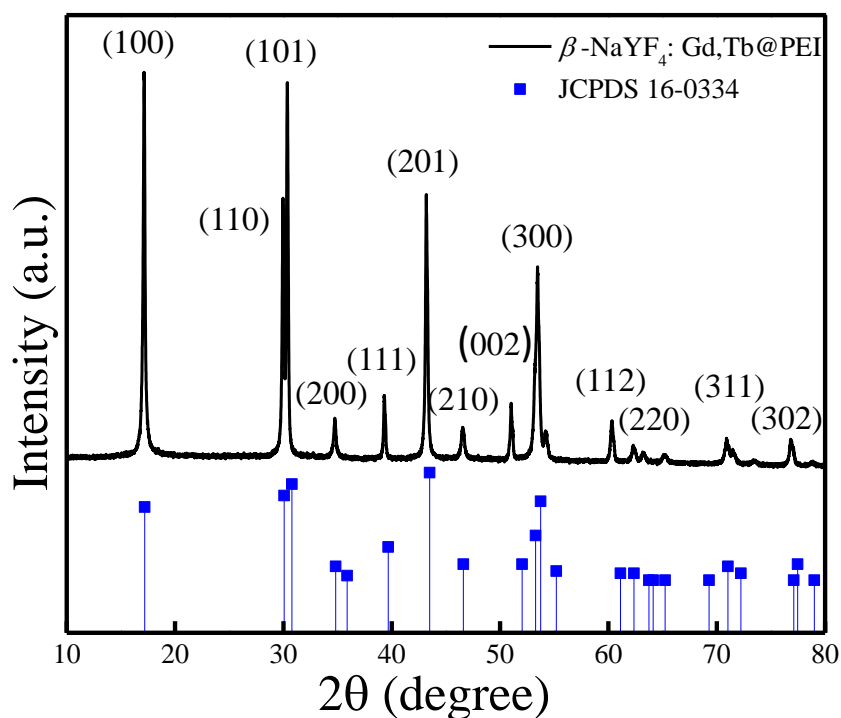


Figure 4.2 The XRD pattern of as-prepared β - NaYF_4 : Gd^{3+} , Tb^{3+} @PEI. The data has been compared with standard data of hexagonal NaYF_4 , JCPDS 16-0334 as the reference.

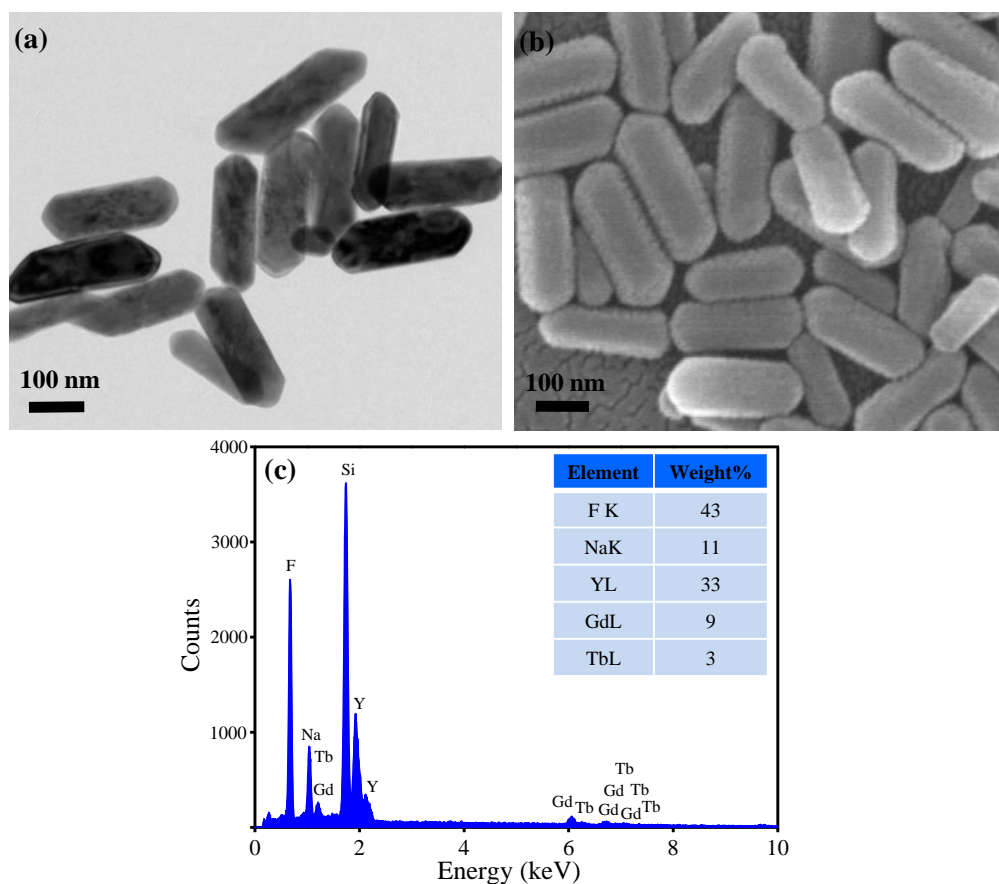


Figure 4.3 (a) TEM and (b) FESEM images showing the morphology of the β - NaYF_4 : Gd^{3+} , Tb^{3+} @PEI phosphors NPs, which were monodispersed in nature, (c) the EDXA pattern showing the elemental composition consisting of Na, F, Y, Gd, and Tb ions.

Fig. 4.4a showed the high-resolution TEM (HRTEM) image of the pristine sample, which was subsequently analyzed by a combination of fast Fourier transform (FFT) followed by inverse fast Fourier transform image (IFFT) to check crystal lattice periodicity. **Fig. 4.4b** showed the IFFT image of the selected region (marked as a red square) in the HRTEM image, which was constructed after the masking of (110) plane using the Digital MicrographTM software, as shown in the FFT image in the inset. The IFFT image clearly showed the presence of an array of ordered planes whose interplanar spacing was measured from the line profile and came out to be 0.30 nm corresponding to (110) plane of hexagonal NaYF₄ lattice.

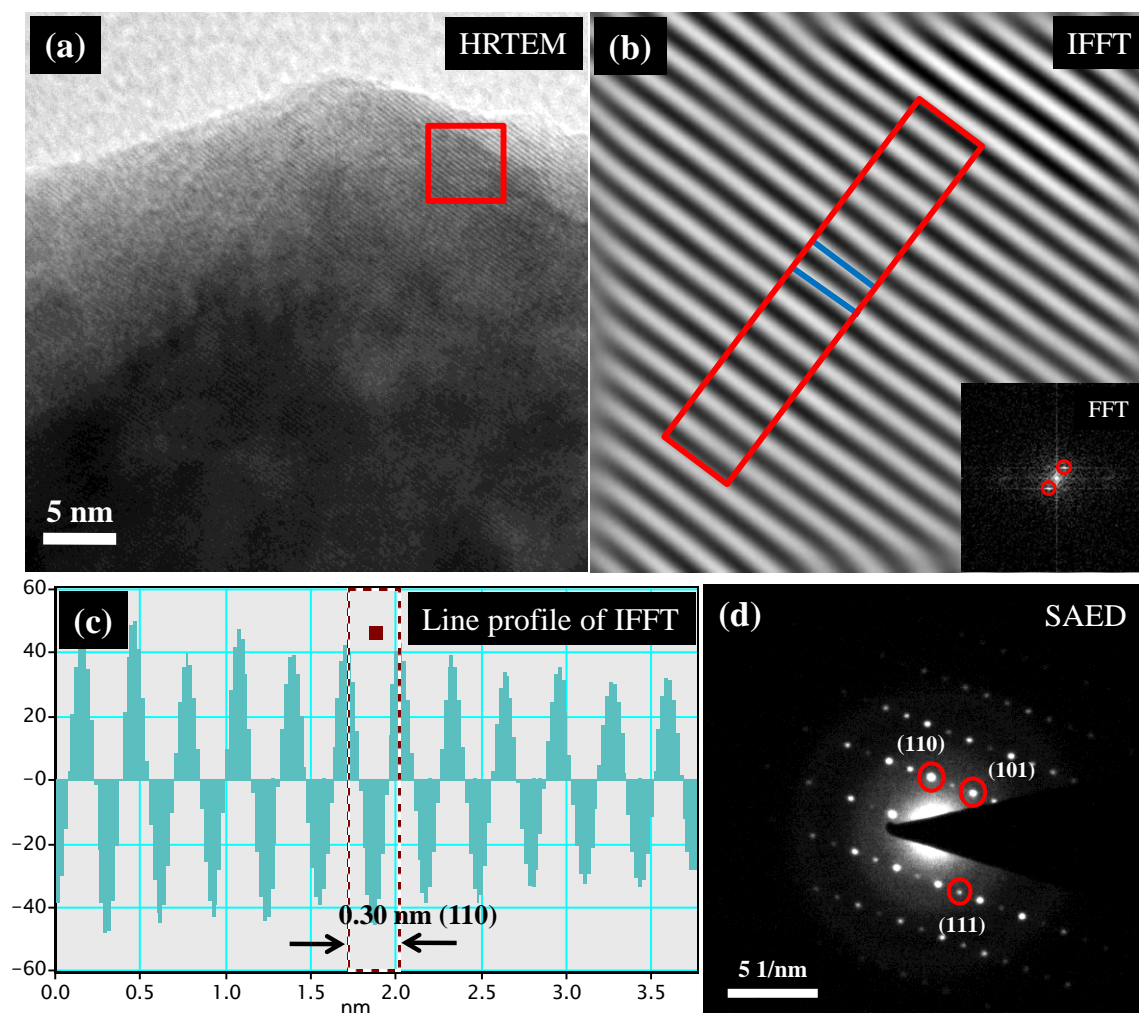


Figure 4.4 (a) The HRTEM image, (b) corresponding inverse fast Fourier transformation (IFFT) image of the square region marked red in figure (a), corresponding to (110) plane masked in the FFT pattern with red circles as shown in inset, (c) the line profile of the selected region in IFFT image for interplanar spacing of 0.30 nm, and (d) SAED pattern of β -NaYF₄: Gd³⁺, Tb³⁺@PEI.

The SAED pattern shown in **Fig. 4.4d** revealed the crystalline nature of β -NaYF₄: Gd³⁺,Tb³⁺@PEI NPs. The diffraction pattern obtained matched well with the crystal planes of hexagonal NaYF₄ and have been assigned to (110), (101), (111) planes. Thus, d-spacing calculated in HRTEM and SAED are in agreement with those given in the standard JCPDS data no. 16-0334, confirming the hexagonal phase of the as-prepared samples. The functionalization of PEI was investigated by zeta potential of β -NaYF₄: Gd³⁺,Tb³⁺@PEI NPs, which came out to be + 43 mV suggesting the successful capping of PEI on the surface rendering the rods to be positively charged. The presence of amino groups on the surface of rods was further verified by FT-IR spectroscopy (**Fig. 4.5a**). The β -NaYF₄: Gd³⁺,Tb³⁺@PEI nanophosphors exhibited absorption band at 3446 cm⁻¹ due to typical N-H stretching vibration of the amino groups, which overlaps with the O-H stretching band, and its presence was supported by the peak ascribed to bending mode of amino groups (-NH₂) at 1656 cm⁻¹, thus revealing the abundance of electron-rich amino groups on the terminal of the rods.⁷ Moreover, the absorption band at 1398 cm⁻¹ was attributed to the stretching vibrations of the C-N bond, while bands at 2857 cm⁻¹ and 2937 cm⁻¹ were attributed to the methylene symmetric and asymmetric C-H stretching vibrations as shown in the inset of **Fig. 4.5a**. The PEI capping was further confirmed by TGA results which were carried out in a nitrogen atmosphere at a heating rate of 10 °C/min. As shown in **Fig. 4.5b**, the initial weight loss of 5.5% occurred in the temperature range (300-550) °C due to the degradation of bound PEI present in the system, and no further loss was observed till 650 °C, confirming the stability of the fluorides. Inset shows the first derivative of the TGA curve confirming the presence of PEI in the system and degradation at 510 °C. The TGA spectra were recorded for bare β -NaYF₄: Gd³⁺,Tb³⁺ nanophosphors, which showed a slight weight loss of 2.1 wt% in the range of (300-550) °C. It is believed that the decomposition temperature of branched PEI is situated at around 400 °C in a nitrogen atmosphere,³¹ which was verified in the TGA results shown in **Fig. 4.5c**. The observed

increase in the decomposition temperature of PEI in the β -NaYF₄: Gd³⁺,Tb³⁺@PEI as compared to free PEI was attributed to the fact that the capping agent is protected from degradation due to its binding to the particles.³² This confirms that the PEI was indeed bound to the nanorods.

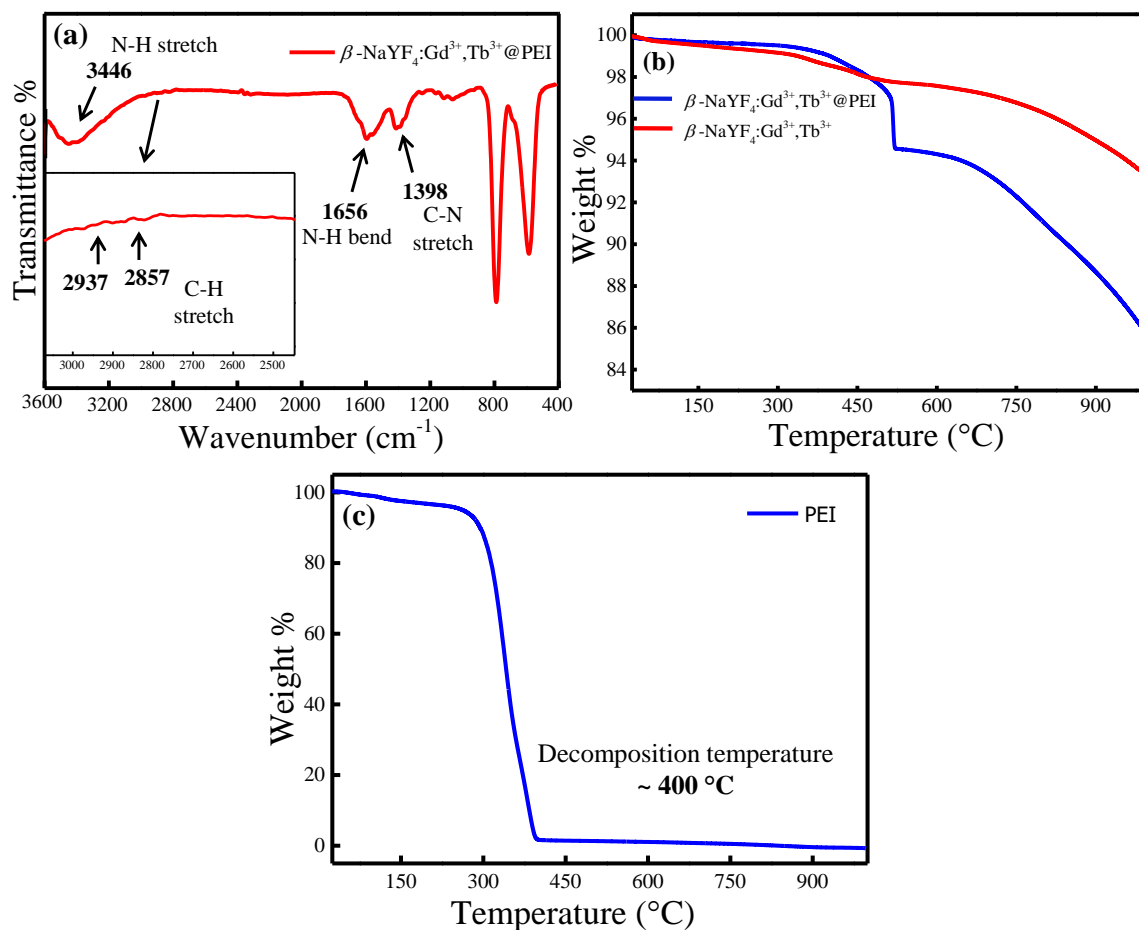


Figure 4.5 (a) The FT-IR spectra indicated the capping of PEI on the surface of the rods. Inset: Zoomed view in the range of 3000-2500 cm⁻¹, (b) the TGA results confirmed the presence of PEI on the terminus. The decomposition temperature obtained for branched PEI when coated on the surface is ~ 510 °C, as shown in the derivative curve of TGA in the inset. Bare β -NaYF₄: Gd³⁺,Tb³⁺ phosphors without the capping of PEI showed no weight loss at this temperature. (c) The TGA curve for branched PEI showed decomposition temperature at ~ 400 °C.

The composition and chemical state of the β -NaYF₄:Gd³⁺,Tb³⁺@PEI were ascertained by XPS measurements. As shown in **Fig. 4.6a**, the survey scan spectrum confirmed the presence of Na, Y, F, C, N, and lanthanides (Gd, Tb) in the material. It should be mentioned here that the presence of C 1s and N 1s in the spectrum was due to

the capping of the PEI on the surface. The high-resolution peak analyses of Gd 3d and 4d core-level spectra revealed that these energy levels were split into doublet due to spin-orbit coupling (**Fig. 4.6b,c**). The energy levels $3d_{5/2}$ and $3d_{3/2}$ appeared at 1189.2 eV and 1220.9 eV, respectively, with the spin-orbit splitting of 31.9 eV, while peaks at 144.8 eV and 150.4 eV can be assigned to the binding energy of levels $4d_{5/2}$ and $4d_{3/2}$, respectively. The presence of Gd 3d and 4d peaks showed that Gd ion existed as Gd^{3+} in the crystal lattice of hexagonal $NaYF_4$. As shown in **Fig. 4.6d**, the energy level of Tb 3d also split into doublet corresponding to $3d_{5/2}$ and $3d_{3/2}$ at 1243.7 eV and 1278.4 eV, respectively. Also, satellite appeared between the two main peaks. These results suggested that the Tb ion substituted Y^{3+} ion in $NaYF_4$ appeared in only one oxidation state, i.e., +3.

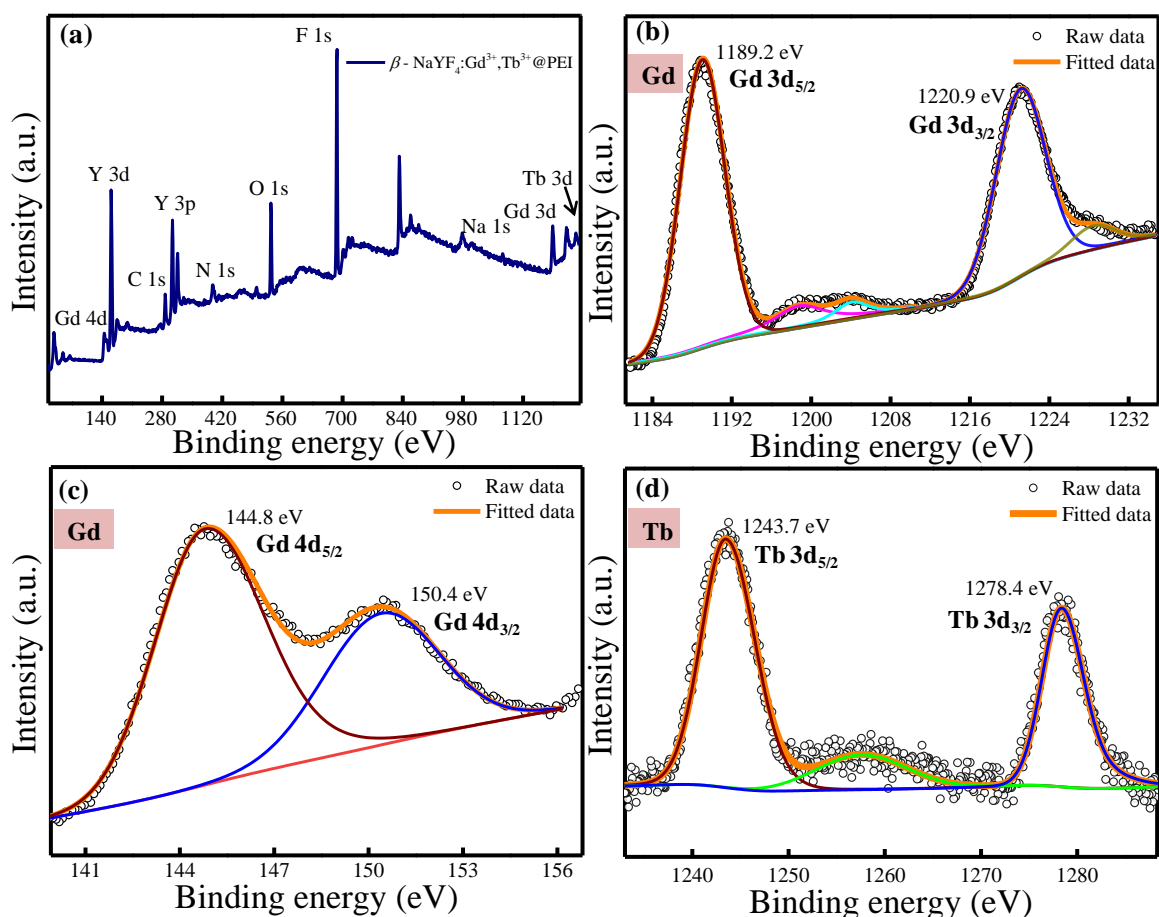


Figure 4.6 (a) The XPS survey spectra of as-synthesized $\beta-NaYF_4: Gd^{3+},Tb^{3+}@PEI$ and high-resolution spectra of (b) Gd 3d, (c) Gd 4d and (d) Tb 3d shows the binding energy of the core-levels.

The magnified XPS spectra of other elements such as Na, Y, and F in β -NaYF₄: Gd³⁺, Tb³⁺@PEI can be seen in **Fig. 4.7**, which displayed the energy levels; Na 1s, Y 3d, and F 1s core-levels. The surface functionalization of the downconverting nanorods conducted by XPS was in accordance with the FTIR results. The presence of these hydrophilic functional groups improved the water dispersibility and stability of the nanorods.

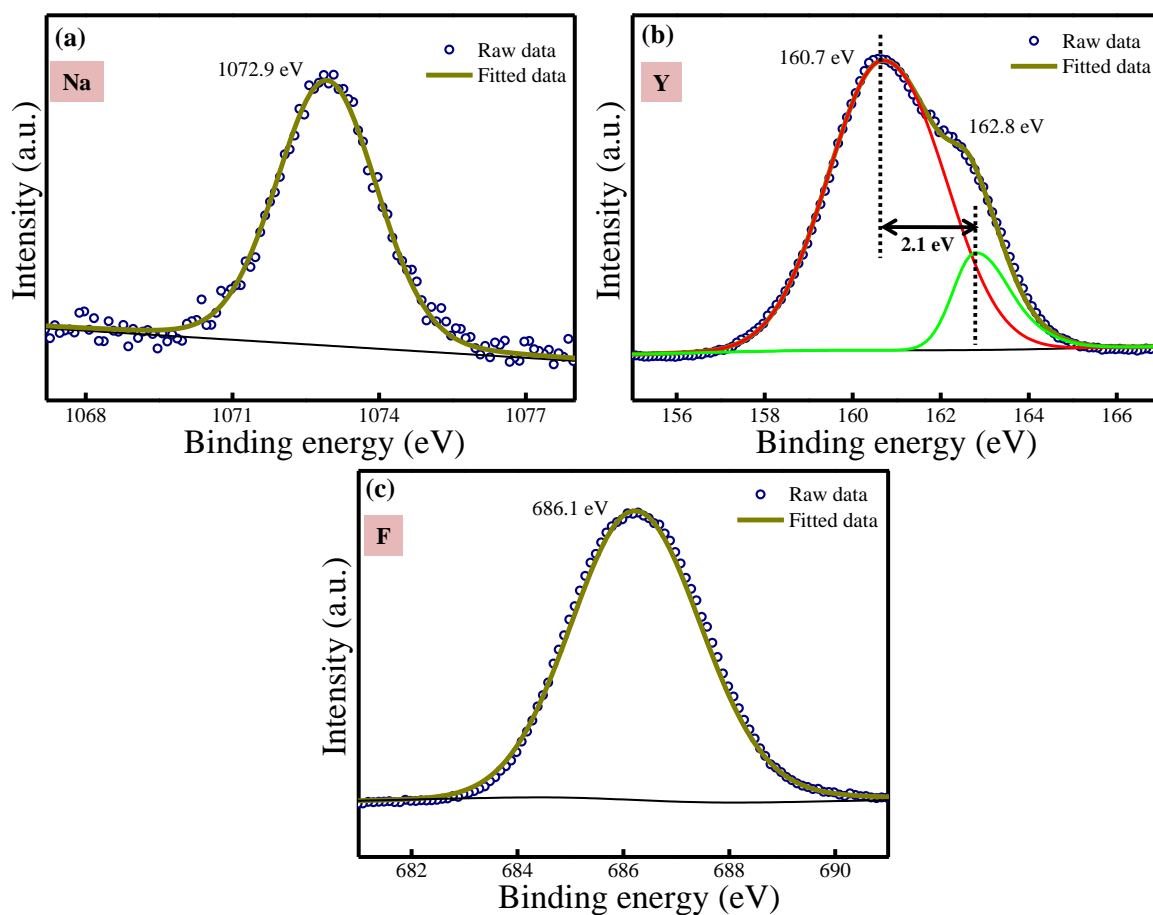


Figure 4.7 The high-resolution XPS spectra of the elements present in β -NaYF₄: Gd³⁺, Tb³⁺@PEI shows the binding energy of (a) Na 1s, (b) Y 3d, and (c) F 1s revealing the core energy levels.

The optical emission spectra of β -NaYF₄: Gd³⁺, Tb³⁺ are displayed in **Fig. 4.8a**, where the photon emission originates from the transition within the 4*f* electronic transitions of Tb³⁺ ions. The emission spectra of Tb³⁺ ions can be obtained at the excitation wavelength, $\lambda_{\text{ex}} = 375 \text{ nm}$.³³ The efficient emission is difficult to realize in the system containing Tb ions under direct excitation at 375 nm due to intraconfigurational parity-

forbidden transitions. Hence, Gd^{3+} ions acted as a sensitizer to enhance the luminescence of Tb^{3+} ions.⁷ The obtained emission spectra excited at $\lambda_{ex} = 273$ nm (**Fig. 4.8a**), yielded emissions from Tb^{3+} ions in the range of (480-680) nm. Four prominent emission peaks centered around ~ 488 nm, ~ 544 nm, ~ 584 nm, and ~ 619 nm, originates from the transitions of ${}^5D_4 \rightarrow {}^7F_6$, ${}^5D_4 \rightarrow {}^7F_5$, ${}^5D_4 \rightarrow {}^7F_4$, and ${}^5D_4 \rightarrow {}^7F_3$, respectively. It was clear that among the above-mentioned transitions, the green emission ${}^5D_4 \rightarrow {}^7F_5$ at ~ 544 nm was the most intense emission. **Fig. 4.8b** showed the PL decay curve for the luminescence of Tb^{3+} in β -NaYF₄: Gd^{3+}, Tb^{3+} @PEI nanorods. Here, the PL decay displayed the curve fitted over first 20 ms with biexponential decay functions due to the variation in decay rates of Tb^{3+} ions in the NPs. This emissive biexponential decay was ascribed due to the inhomogeneous distribution of Tb ions close to the surface giving the short lifetime and inside the NPs with a long lifetime.³⁵ The curve was well fitted by decay equation: $I = I_0 + A_1(e^{-x/\tau_1}) + A_2(e^{-x/\tau_2})$; where I and I_0 were the intensities at time x and 0, respectively, A_1 and A_2 are constants, τ_1 and τ_2 were the decay times for the two exponential components which came out to be 0.35 ms and 2.50 ms for ${}^5D_4 \rightarrow {}^7F_5$ electronic transition of Tb^{3+} under excitation at 375 nm.

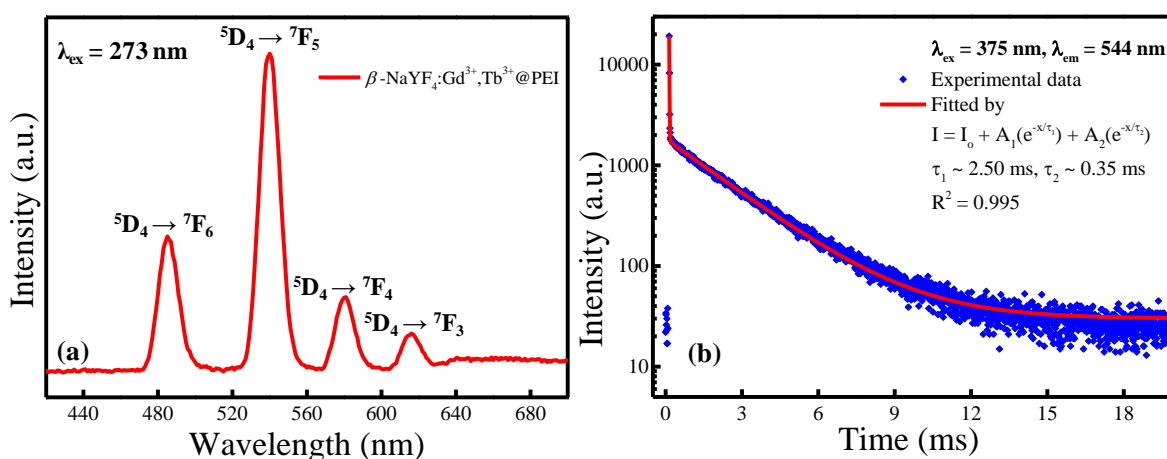


Figure 4.8 (a) The PL spectra of PEI capped β -NaYF₄: Gd^{3+}, Tb^{3+} at an excitation wavelength of 273 nm yielding emission in the visible region corresponding to the Tb^{3+} ion transitions. (b) The luminescence decay kinetics behavior for the emission of Tb^{3+} ion corresponding to transition ${}^5D_4 \rightarrow {}^7F_5$ at 544 nm in hexagonal NaYF₄ lattice under excitation of 375 nm.

The average lifetime of these nanophosphors was in milliseconds indicating the usability of these phosphors in biological applications also, where the autofluorescence and background fluorescence can be suppressed, offering high signal-to-noise ratio.³⁶

4.3.1 Detection of explosives

Nitro groups-based compounds, such as 1,3-dinitrobenzene (1,3-DNB), 2,4-dinitrophenol (2,4-DNP), 2,4,6-trinitrophenol (TNP), 2,4-dinitrotoluene (2,4-DNT), 2,6-dinitrotoluene (2,6-DNT), 2,4,6-trinitrotoluene (TNT), 1,3,5-Trinitro-1,3,5-triazinane (RDX), 4-nitrophenol (4-NP), 1,4-dinitrobenzene (1,4-DNB), nitromethane (NM), 4-nitrotoluene (4-NT) and nitrobenzene (NB) were used in this experiment. The designed principle of detection was based on the interaction of the amine groups on the surface of the NPs with the electron-deficient nitro compounds. For comparison, the PL intensity of nanophosphors was detected in deionized water at 544 nm. Equal amounts of analytes were taken in the cuvette for the measurements as discussed in the synthesis section and compared against the PL intensity in the deionized water. It was interesting to note that among these explosive samples (**Fig. 4.9a**), only TNT could quench the PL intensity of the nanophosphors. **Fig. 4.9b** presents the quenching profile for all the analytes for the emission at 544 nm. One can see in figure that the quenching efficiency for 300 μ M TNT was about 90% while all other analytes contributed little changes in the luminescence intensity. Based on the results mentioned, TNT was recognized as a detection target owing to its ability to quench the luminescence dramatically, suggesting the high sensitivity of the sensing probe. As a result of the significant quenching, the quenching phenomenon with varied concentrations of TNT was studied next (**Fig. 4.9c**). As shown in **Fig. 4.9d**, under the optimum conditions in our experimental procedure, the PL quenching was analyzed using the Stern-Volmer (SV) plot between the change in PL intensity at 544 nm and the concentration of TNT. A significant linear correlation ($R^2 = 0.998$) existed between the relative PL intensity (I_0/I) and the concentration of TNT in the range of 0.1-

300 μM . The quenching efficiency was investigated using the SV equation, $I_0/I - 1 = K_{sv}[Q]$, where I_0 is the PL intensity in the absence of analyte, I is the PL intensity in the presence of analyte with the molar concentration $[Q]$, and K_{sv} is the quenching constant in M^{-1} . The quenching constant was determined to be $3.32 \times 10^4 \text{ M}^{-1}$. The limit of detection (LOD) of TNT was found using the linear regression method and calculated using the formula: $3\sigma/m$; where 3 is the factor of 99% confidence level, σ is the standard deviation of the measured intensity for the blank $\beta\text{-NaYF}_4: \text{Gd}^{3+}, \text{Tb}^{3+} @ \text{PEI}$ nanophosphors ($n=5$) while m denotes the slope of the linear calibration curve.

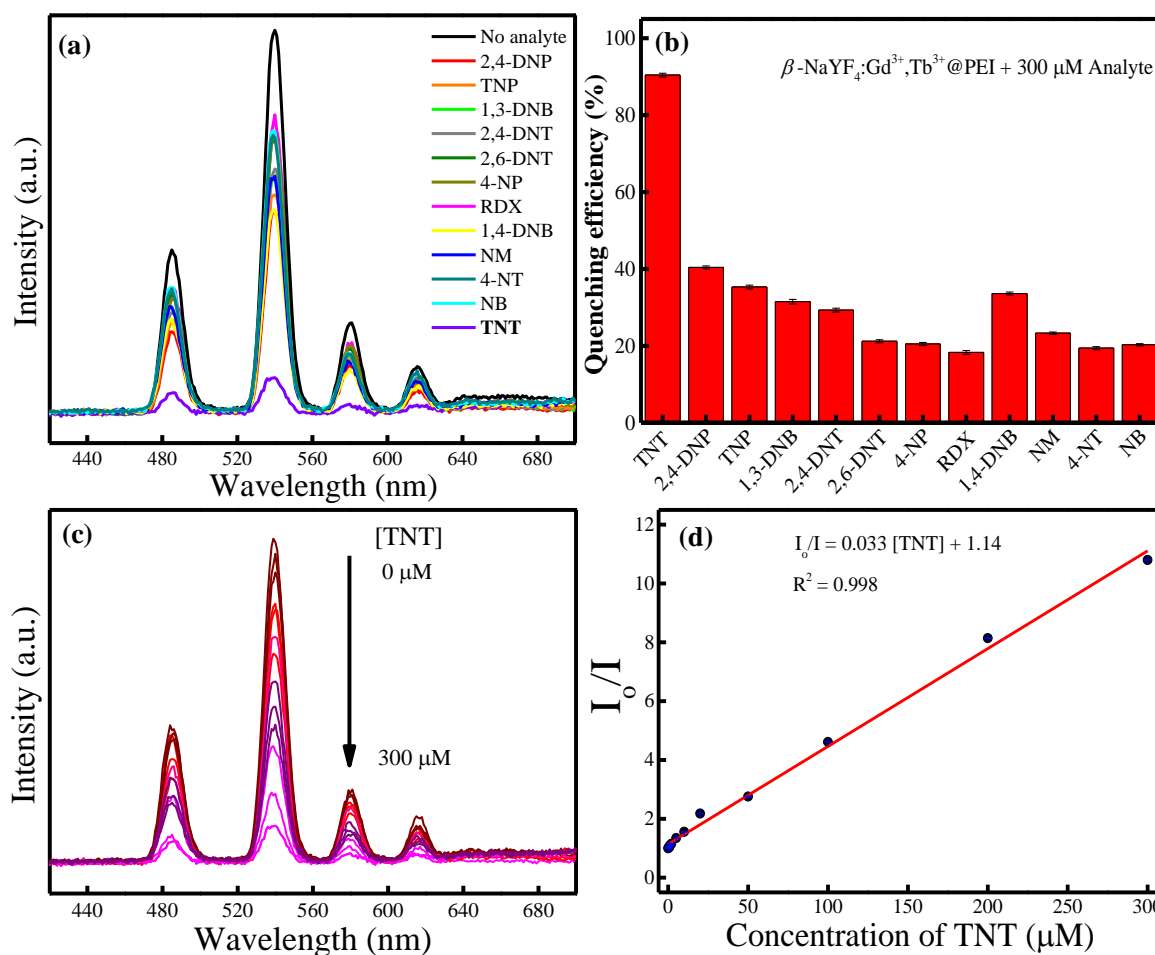


Figure 4.9 (a) The emission spectra and (b) the quenching efficiency of the samples containing $\beta\text{-NaYF}_4: \text{Gd}^{3+}, \text{Tb}^{3+} @ \text{PEI}$ and different nitro compounds (300 μM) in aqueous solution, (c) the emission spectra of $\beta\text{-NaYF}_4: \text{Gd}^{3+}, \text{Tb}^{3+} @ \text{PEI}$ containing different concentrations of TNT (0-300 μM) in aqueous solution, (d) fitting graph of the linear S-V plot for TNT by the equation; $I_0/I - 1 = K_{sv}[Q]$, where K_{sv} is quenching constant and found out to be $3.32 \times 10^4 \text{ M}^{-1}$. Error bar was calculated from three parallel samples.

It should be mentioned here that the LOD was found to be 119.9 nM (27.2 ppb), revealing higher sensitivity of the as-synthesized nanophosphors compared to the other earlier reported results (**Table 4.1**).

Table 4.1 The comparison of different methods and limit of detection for TNT (*NA= Not applicable).

Detection techniques	Probe	Detection range ^a / linear range ^b	LOD
Electrochemical method	Graphene nanoribbons	4.4-66 μM^{b}	4.4 μM^{37}
Surface-enhanced Raman spectroscopy	Molecularly imprinted polymers	NA	3 μM^{38}
Fluorescence method	Mesoporous silica nanoparticles	1-25 μM^{a}	0.6 μM^{39}
	Graphene quantum dots	2.2-800 μM^{b}	2.2 μM^{40}
	Polymer substrate and fibers	0.1-5.5 $\times 10^3 \mu\text{M}^{\text{a}}$	1 μM^{41}
	Pyrene derivative	1-14 μM^{a}	1 μM^{42}
	Carbon quantum dots	10 ⁻³ -1 μM^{a}	0.213 μM^{43}
	NaYF ₄ :Ce ³⁺ /Gd ³⁺ / Eu ³⁺ @NaGdF ₄ :Tb ³⁺	5-300 μM^{a}	7.2 μM^{44}
	NaCeF ₄ :Tb ³⁺ /Eu ³⁺	5-400 μM^{a}	5.8 μM^{45}
NaYF ₄ : Gd,Tb@PEI Downconverting phosphors (this work)	0.1-10 μM^{b}	0.119 μM	

4.3.2 Interference study

To assess the possibility of the analytical application of our phosphors based nanosensor in terms of the sensitivity, the effect of different mixed samples of analogous compounds of TNT such as 2,4-DNT, 2,6-DNT, 4-NP, 1,3-DNB, TNP, 2,4- DNP, RDX, 1,4-DNB, NM, 4-NT, and NB: 300 μM , on the quenching of PL intensity was also studied. In spite of the presence of other analytes, quenching of the PL intensity due to the TNT was observed, having no interference because of the other analytes. Therefore, they showed high sensitivity and selectivity for the specific nitro compounds detection. The TNT quenching was also observed in the buffer solution, NaH₂PO₄-Na₂HPO₄ (pH 7.0).

Furthermore, the effects of pH on the PL intensity before and after the addition of TNT were scrutinized. In the wide range of pH 7-13, it showed no variation in the luminescence intensity (**Fig. 4.10a**), suggesting the stability of the nanophosphors over the wide range of pH in the neutral and alkali environment. In addition, the influence of incubation time on the luminescence intensity was also studied to ensure the quenching solely because of TNT. As seen in **Fig. 4.10b**, the intensity at 544 nm was quenched with the addition of TNT after 10 min. Meanwhile, by prolonging the incubation time to 48 h, the PL intensity was almost unchanged. Moreover, the PL intensity remained unchanged for almost 8 months, when stored at room temperature.

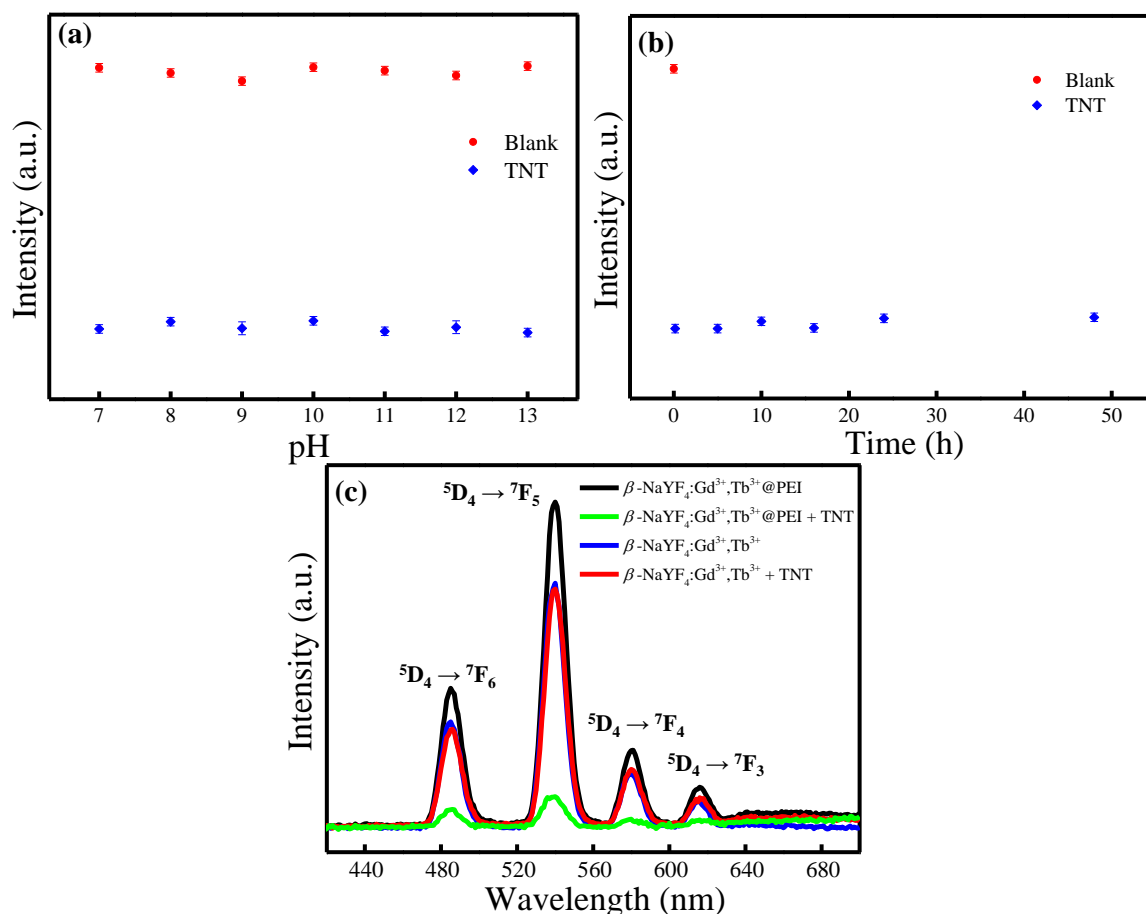
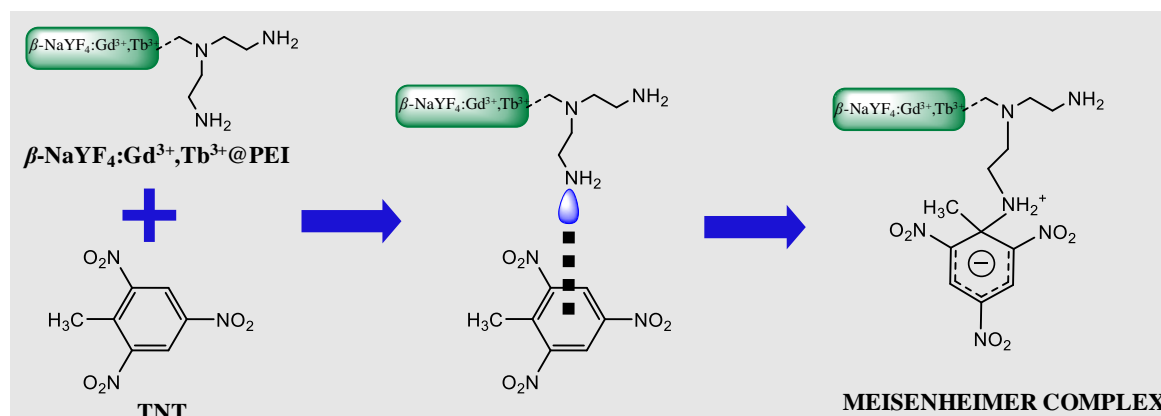


Figure 4.10 (a) Influence of pH on the luminescence intensity before and after the addition of TNT (300 μ M). For pH 7-8, NaH₂PO₄-Na₂HPO₄, pH 9-11 NaHCO₃-Na₂CO₃-NaOH, and pH 12-13 KCl-NaOH were used. (b) Effects on incubation time on the PL intensity at 544 nm due to the presence of TNT were studied at pH 7 in buffer solution at room temperature. (c) The comparison of static photoluminescence spectra of β -NaYF₄: Gd³⁺,Tb³⁺ nanophosphors with and without PEI in the presence and in the absence of TNT in an aqueous medium.

This demonstrated that these nanophosphors can detect analytes over a long period of time, thus are stable in nature. It should be mentioned here that no quenching was observed when only $\beta\text{-NaYF}_4:\text{Gd}^{3+},\text{Tb}^{3+}$ was used for the PL measurements without being capped by PEI (**Fig. 4.10c**). Hitherto, it was concluded that the interaction of the TNT molecule with amino groups played an important role.

4.3.3 Mechanism of highly selective detection

To unravel the origin of the high selectivity of $\beta\text{-NaYF}_4:\text{Gd}^{3+},\text{Tb}^{3+}@\text{PEI}$ nanophosphors towards TNT, the quenching mechanism was investigated. A plausible mechanism for the detection could be proposed to be based on the donor-acceptor interaction between amino groups of phosphor nanorods and TNT. Since TNT is an electron-deficient compound due to the presence of three electron-withdrawing nitro groups; therefore, it acted as an electron-acceptor while amino groups were electron donors. Thus, an electron transfer mechanism took place between TNT and amino groups of the PEI on the surface of NPs, which led to the formation of the Meisenheimer complex (**Scheme 4.1**). The three electron-withdrawing nitro groups present at ortho- and para-position in TNT enabled the nucleophile amino groups to attack at position 1 (where a methyl group is attached) in the molecule, which led to the formation of this stable anionic σ -complex where the negative charge was delocalized over the ring.⁴⁶



Scheme 4.1 A schematic representation of the formation of the Meisenheimer complex due to the interaction between amino groups present on the surface of the NPs and TNT through the charge-transfer mechanism in an aqueous medium.

The formation of such complex with amino groups is typical of nitro compounds, especially TNT. This complex formation can be confirmed by the change in the color of the solution of nanophosphors containing TNT to brownish-yellow (**Fig. 4.11e**). While there was no color change in the case of NM, 1,3-DNB, 4-NT, 1,4-DNB, 2,4-DNT, 2,6-DNT, and RDX. A pale yellow appeared in the case of 2,4-DNP, 4-NP, NB, and TNP, which was easily distinguished with the brownish-yellow color of TNT. The UV-vis spectra of the explosives in the presence of PEI capped nanophosphors were recorded and shown in **Fig. 4.11b**. As it can be seen, all other nitro compounds have a strong absorbance before 400 nm, hence did not interfere in the quenching. Meanwhile, it should be mentioned that the Meisenheimer complex formed with TNT and nanophosphors has a broad absorbance in the range (400-650) nm, which overlapped with the emission of the Tb^{3+} ions in the phosphors (**Fig. 4.11c**). Since the emission from the NPs overlapped with the absorbance of the complex formed, it gave the possibility of the LRET-based energy transfer and thereby, led to the quenching of the green emission. As mentioned above, when Ln^{3+} ion-based nanoparticles are used as the energy donor, the mechanism is named as LRET, whose principles are similar to fluorescence resonance energy transfer (FRET) and defined as a nonradiative optical energy transfer between a donor (D) in its excited state and proximal ground state acceptor (A) through long-range dipole-dipole interactions.

For the effective energy transfer, an acceptor absorption spectrum should overlap with a donor emission spectrum, and the donor and acceptor should be linked in proximity.⁴⁷ In **Fig. 4.11b**, it was observed that the absorption spectrum of β -NaYF₄: Gd³⁺, Tb³⁺@PEI + TNT largely overlaps with the emission spectra of the β -NaYF₄: Gd³⁺, Tb³⁺@PEI phosphors while there was no overlap with other analytes, thereby avoided the energy transfer. Although there was a suitable spectral overlap between the nanophosphors emission and the complex absorption in the UV-vis spectra, LRET cannot

occur unless the donor and acceptor are close enough. Due to the formation of the complex between TNT and amine groups, it was brought close enough for the energy transfer to take place.

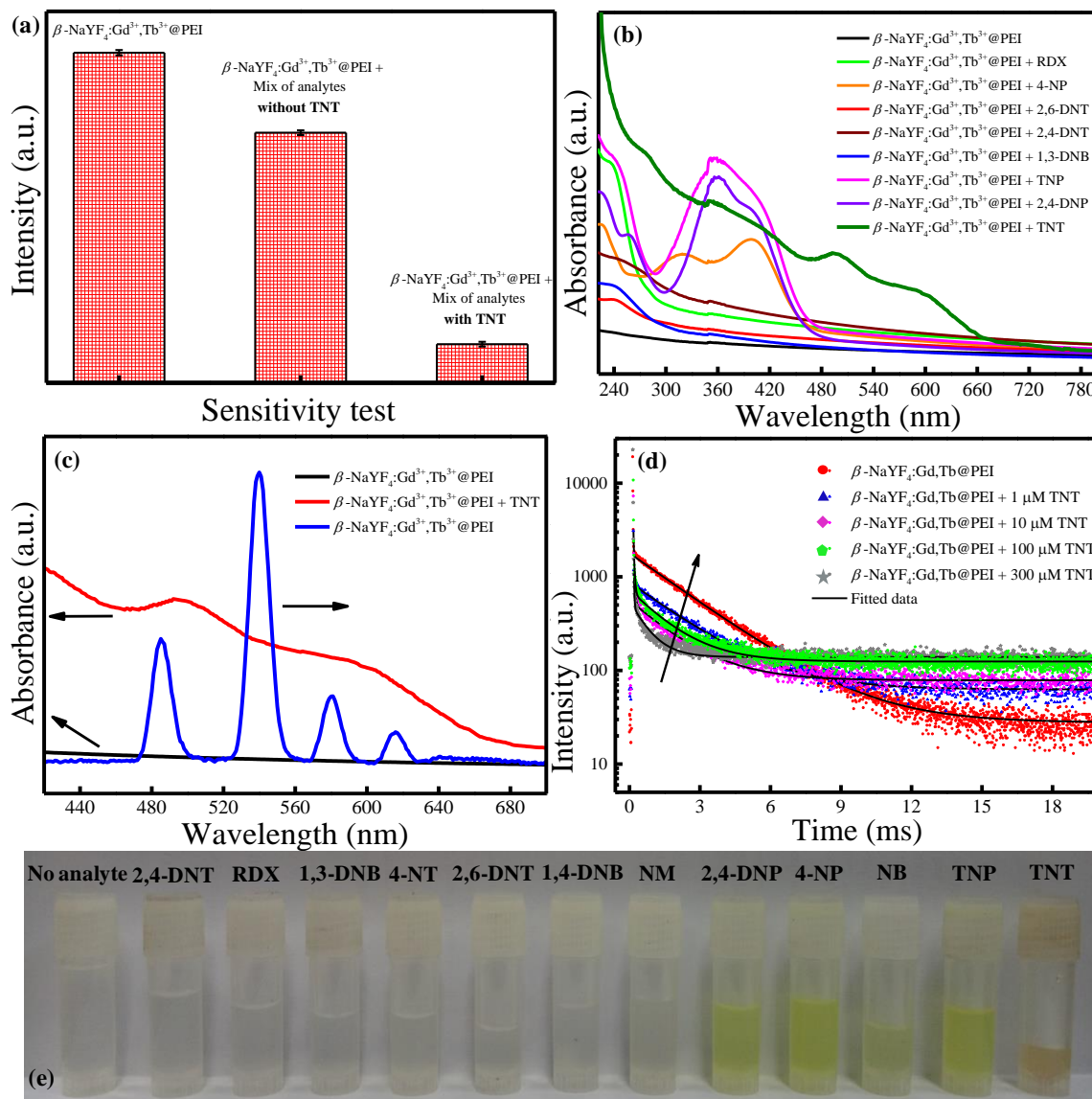


Figure 4.11 (a) The histogram demonstrating the sensitivity of the phosphors over other analogous compounds of TNT, (b) the UV-visible absorbance spectra of all the nitro compounds in presence of β -NaYF₄: Gd³⁺,Tb³⁺@PEI in aqueous medium. The Meisenheimer complex formed between TNT and PEI coated phosphors showed the broad absorbance in the visible range till 650 nm, (c) the spectral overlap of emission spectra of β -NaYF₄: Gd³⁺,Tb³⁺@PEI and absorbance spectra of β -NaYF₄: Gd³⁺,Tb³⁺@PEI before and after the addition of TNT, (d) the time-resolved decay dynamics of ⁵D₄ → ⁷F₅ transition of Tb³⁺ ions in β -NaYF₄: Gd³⁺,Tb³⁺@PEI after excitation at 375 nm in the presence of TNT (1, 10, 100, 300 μM), (e) photograph showing the complex formation which was confirmed by the change in the color of the solution to brownish-yellow containing TNT, while other samples looked white or pale yellow in color.

Thus, the spectral overlapping between DC emission of β -NaYF₄: Gd³⁺,Tb³⁺@PEI and absorbance of the Meisenheimer complex, and the close distance between the two manifests the LRET efficiency of the sensor. Meanwhile, in order to ascertain the above-mentioned reason, the lifetime of NPs with varied concentrations of TNT was explored. As displayed in **Fig. 4.11d**, the lifetime of the β -NaYF₄: Gd³⁺,Tb³⁺@PEI phosphors decreased with increasing concentrations of TNT, and average lifetimes were considered for consistency in results. The decay was fitted using a biexponential decay function to yield average lifetimes of 2.11, 1.91, 1.72, 1.49, and 0.98 ms under the TNT concentrations of 0, 1, 10, 100, and 300 μ M, respectively. **Table 4.2** shows the lifetime parameters viz. τ_i , rel % and an average lifetime of the samples. These results excluded the possibility of inner filter effect; thus the lifetime reduction indicated that LRET was the major process^{48,49} between nanophosphors and TNT complex as it offered the additional relaxation pathway. As mentioned above, the nanosensor exhibited high selectivity for the target TNT over other nitro compounds with similar structures such as TNP, DNT, DNP, NP, and DNB.

Other nitro compounds are much weaker electronic acceptors when compared with TNT due to lack of electron-withdrawing nitro groups, thus were not likely to form the effective Meisenheimer complex with the amine groups present on the surface of the nanoparticles.⁵⁰ Although weak interactions may lie between the amine groups and these compounds, no significant absorption peaks were detected in the UV-vis spectra in the spectral range of (400-700) nm; thus, they did not interfere with the emission of the downconverting nanophosphors. The proposed method demonstrated the feasibility of the PEI capped β -NaYF₄: Gd³⁺,Tb³⁺ phosphors nanoparticles application for preferentially detecting TNT as the analyte.

Table 4.2 The average lifetime of the β -NaYF₄: Gd³⁺,Tb³⁺@PEI with different concentrations of TNT.

S. No.	Sample	τ_1 (ms)	Rel %	τ_2 (ms)	Rel %	Average lifetime (ms)
1	β -NaYF ₄ :Gd ³⁺ ,Tb ³⁺ @PEI	0.35	18	2.50	82	2.11
2	β -NaYF ₄ :Gd ³⁺ ,Tb ³⁺ @PEI + 1 μ M TNT	0.42	22	2.34	78	1.91
3	β -NaYF ₄ :Gd ³⁺ ,Tb ³⁺ @PEI + 10 μ M TNT	0.21	27	2.17	73	1.72
4	β -NaYF ₄ :Gd ³⁺ ,Tb ³⁺ @PEI + 100 μ M TNT	0.24	24	1.89	76	1.49
5	β -NaYF ₄ :Gd ³⁺ ,Tb ³⁺ @PEI + 300 μ M TNT	0.23	30	1.32	70	0.98

4.3.4 Interference from other analytes

In order to illustrate the good selectivity, sensitivity, and feasibility of the developed nanosensor probe for the detection of TNT, the effects of other analytes such as pesticides, sugars, and amino acids were also checked on the luminescence quenching profile, and the results are shown in **Fig. 4.12**. The stock solution of 300 μ M of the following amino acids was prepared in water: phenylalanine, isoleucine, tryptophan, glutamine, glutamic acid, and histidine. Interestingly, among the amino acids, none of them showed any obvious quenching effects in the intensity of the nanophosphors. This is due to the groups present in the structure of the amino acids, which did not interact with the amine group in the PEI and thus were not able to form a complex with the nanorods. Similarly, the stock solution of some pesticides such as chlorpyrifos, malathion, cypermethrin, copper oxychloride, fenvalerate, carbendazim; and sugars such as glucose, fructose, sucrose, maltose, lactose, and sorbitol were also prepared. The samples were incubated for 10 min before the PL measurements. The findings in **Fig. 4.12** indicated that these analytes did not show any significant change in the intensity of the nanophosphors. Thence, it can be seen that this nanoprobe sensor promised to be an intriguing indicator for the existence of any risks and threats from the explosives, thus ensuring of our security.

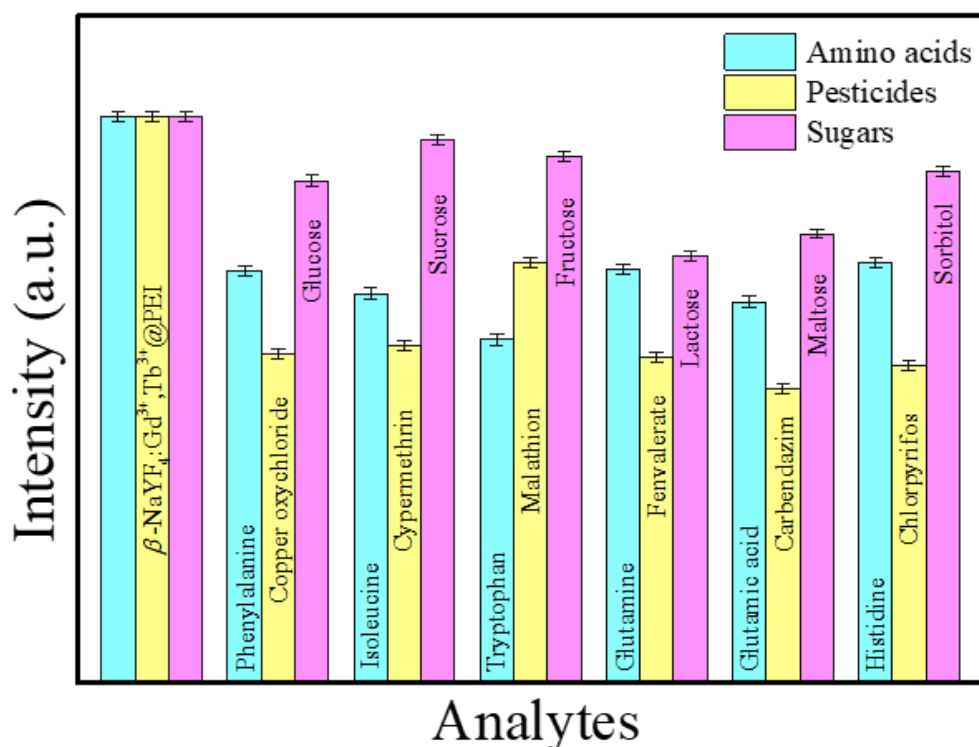


Figure 4.12 Histogram showing the selectivity of the phosphors over other analytes such as amino acids, pesticides, and sugars. There was no obvious change observed in the PL intensity, hence suggesting the selectivity towards TNT.

4.4 Conclusions

In summary, an approach has been reported for selectively detection of TNT over the number of other analogous nitro compounds using β -NaYF₄: Gd³⁺,Tb³⁺ nanophosphors based on fluorimetric sensing technique. The results from various characterization methods suggested the formation of β -NaYF₄: Gd³⁺,Tb³⁺ nanophosphors capped with PEI. The excellent selectivity towards TNT was ascribed due to the interactions of amine group present in PEI and nitro groups in TNT forming Meisenheimer complex, which have caused a decrease in the PL signal due to the LRET-based energy transfer mechanism between the nanophosphors and the complex formed. The PL intensity variations have displayed that the nanophosphors were sensitive and efficient for explosive detection with a limit of detection of 119.9 nM (27.2 ppb). To demonstrate the advantages of this work, the PL intensity of the nanophosphors with other analytes was also investigated, and no obvious effects were observed. Thus, the proposed method demonstrates the feasibility of

the PEI capped β -NaYF₄: Gd³⁺, Tb³⁺ phosphors NPs application for detecting TNT as the analyte independent of complicated instruments and immunoassays.

4.5 References

- 1 S. Gai, C. Li, P. Yang and J. Lin, *Chem. Rev.*, 2014, **114**, 2343–2389.
- 2 T. Sandrock, H. Scheife, E. Heumann and G. Huber, *Opt. Lett.*, 1997, **22**, 808–810.
- 3 K. Li, S. Liang, M. Shang, H. Lian and J. Lin, *Inorg. Chem.*, 2016, **55**, 7593–7604.
- 4 P. Padhye, S. Sadhu, M. Malik and P. Poddar, *RSC Adv.*, 2016, **6**, 53504–53518.
- 5 B. Gu and Q. Zhang, *Adv. Sci.*, 2018, **5**, 1700609.
- 6 H. L. Jo, Y. H. Song, J. Park, E.-J. Jo, Y. Goh, K. Shin, M.-G. Kim and K. T. Lee, *Nanoscale*, 2015, **7**, 19397–19402.
- 7 P. Padhye, A. Alam, S. Ghorai, S. Chattopadhyay and P. Poddar, *Nanoscale*, 2015, **7**, 19501–19518.
- 8 A. Bagheri, H. Arandiyani, C. Boyer and M. Lim, *Adv. Sci.*, 2016, **3**, 1500437.
- 9 Y. Zhang, Y. Tang, X. Liu, L. Zhang and Y. Lv, *Sensors Actuators B Chem.*, 2013, **185**, 363–369.
- 10 V. Muhr, M. Buchner, T. Hirsch, D. J. Jovanović, S. D. Dolić, M. D. Dramićanin and O. S. Wolfbeis, *Sensors Actuators B Chem.*, 2017, **241**, 349–356.
- 11 L. Wang, R. Yan, Z. Huo, L. Wang, J. Zeng, J. Bao, X. Wang, Q. Peng and Y. Li, *Angew. Chemie Int. Ed.*, 2005, **44**, 6054–6057.
- 12 L. Yao, J. Zhou, J. Liu, W. Feng and F. Li, *Adv. Funct. Mater.*, 2012, **22**, 2667–2672.
- 13 Q. Liu, J. Peng, L. Sun and F. Li, *ACS Nano*, 2011, **5**, 8040–8048.
- 14 K.-S. Ju and R. E. Parales, *Microbiol. Mol. Biol. Rev.*, 2010, **74**, 250–272.
- 15 R. Waddell, D. E. Dale, M. Monagle and S. A. Smith, *J. Chromatogr. A*, 2005, **1062**,

125–131.

16 L. Peng, L. Hua, W. Wang, Q. Zhou and H. Li, *Sci. Rep.*, 2015, **4**, 6631.

17 S. S. R. Dasary, A. K. Singh, D. Senapati, H. Yu and P. C. Ray, *J. Am. Chem. Soc.*, 2009, **131**, 13806–13812.

18 T. Liyanage, A. Rael, S. Shaffer, S. Zaidi, J. V. Goodpaster and R. Sardar, *Analyst*, 2018, **143**, 2012–2022.

19 A. Pal, M. P. Sk and A. Chattopadhyay, *ACS Appl. Mater. Interfaces*, 2016, **8**, 5758–5762.

20 S. S. Nagarkar, B. Joarder, A. K. Chaudhari, S. Mukherjee and S. K. Ghosh, *Angew. Chemie Int. Ed.*, 2013, **52**, 2881–2885.

21 S. Xu, H. Lu, J. Li, X. Song, A. Wang, L. Chen and S. Han, *ACS Appl. Mater. Interfaces*, 2013, **5**, 8146–8154.

22 X. Sun, J. He, Y. Meng, L. Zhang, S. Zhang, X. Ma, S. Dey, J. Zhao and Y. Lei, *J. Mater. Chem. A*, 2016, **4**, 4161–4171.

23 J. Yu, X. Wang, Q. Kang, J. Li, D. Shen and L. Chen, *Environ. Sci. Nano*, 2017, **4**, 493–502.

24 S. Hao, G. Chen and C. Yang, *Theranostics*, 2013, **3**, 331–345.

25 S. Xu, S. Xu, Y. Zhu, W. Xu, P. Zhou, C. Zhou, B. Dong and H. Song, *Nanoscale*, 2014, **6**, 12573–12579.

26 Y. Zhu, Y. Ni and E. Sheng, *Dalt. Trans.*, 2016, **45**, 8994–9000.

27 H. Wang, Y. Liu, Z. Wang, M. Yang and Y. Gu, *Nanoscale*, 2018, **10**, 10641–10649.

28 Y. Ma and L. Wang, *Talanta*, 2014, **120**, 100–105.

29 X. Hu, T. Wei, J. Wang, Z.-E. Liu, X. Li, B. Zhang, Z. Li, L. Li and Q. Yuan, *Anal.*

Chem., 2014, **86**, 10484–10491.

30 M. Malik, P. Padhye and P. Poddar, *ACS Omega*, 2018, **3**, 1834–1849.

31 R. Tutuianu, L. M. Popescu, M. B. Preda, A.-M. Rosca, R. M. Piticescu and A. Burlacu, *Nanomaterials*, 2017, **7**, 314.

32 H.-L. Chen and M.-S. Hsiao, *Macromolecules*, 1999, **32**, 2967–2973.

33 P. Padhye and P. Poddar, *J. Mater. Chem. A*, 2014, **2**, 19189–19200.

34 B. Szpikowska-Sroka, N. Pawlik, T. Goryczka and W. A. Pisarski, *RSC Adv.*, 2015, **5**, 98773–98782.

35 J. J. H. A. van Hest, G. A. Blab, H. C. Gerritsen, C. de Mello Donega and A. Meijerink, *J. Phys. Chem. C*, 2017, **121**, 19373–19382.

36 G. Chen, H. Qiu, P. N. Prasad and X. Chen, *Chem. Rev.*, 2014, **114**, 5161–5214.

37 M. S. Goh and M. Pumera, *Anal. Bioanal. Chem.*, 2011, **399**, 127–131.

38 E. L. Holthoff, D. N. Stratis-Cullum and M. E. Hankus, *Sensors*, 2011, **11**, 2700–2714.

39 L. Feng, H. Li, Y. Qu and C. Lü, *Chem. Commun.*, 2012, **48**, 4633.

40 L. Fan, Y. Hu, X. Wang, L. Zhang, F. Li, D. Han, Z. Li, Q. Zhang, Z. Wang and L. Niu, *Talanta*, 2012, **101**, 192–197.

41 J. L. Pablos, M. Trigo-López, F. Serna, F. C. García and J. M. García, *RSC Adv.*, 2014, **4**, 25562–25568.

42 I. S. Kovalev, O. S. Taniya, N. V. Slovesnova, G. a. Kim, S. Santra, G. V. Zyryanov, D. S. Kopchuk, A. Majee, V. N. Charushin and O. N. Chupakhin, *Chem. - An Asian J.*, 2016, **11**, 775–781.

43 X. Tian, H. Peng, Y. Li, C. Yang, Z. Zhou and Y. Wang, *Sensors Actuators B Chem.*,

2017, **243**, 1002–1009.

44 L. Tashi, R. Singhaal, M. Kumar and H. N. Sheikh, *New J. Chem.*, 2020, **44**, 19908–19923.

45 R. Singhaal, L. Tashi, Z. U. Nisa, N. A. Ashashi, C. Sen, S. Devi and H. N. Sheikh, *RSC Adv.*, 2021, **11**, 19333–19350.

46 D. Gao, Z. Wang, B. Liu, L. Ni, M. Wu and Z. Zhang, *Anal. Chem.*, 2008, **80**, 8545–8553.

47 L. Cheng, K. Yang, M. Shao, S.-T. Lee and Z. Liu, *J. Phys. Chem. C*, 2011, **115**, 2686–2692.

48 W. W. Ye, M.-K. Tsang, X. Liu, M. Yang and J. Hao, *Small*, 2014, **10**, 2390–2397.

49 V. Muhr, C. Würth, M. Kraft, M. Buchner, A. J. Baeumner, U. Resch-Genger and T. Hirsch, *Anal. Chem.*, 2017, **89**, 4868–4874.

50 S. Hughes, S. S. R. Dasary, S. Begum, N. Williams and H. Yu, *Sens. Bio-Sensing Res.*, 2015, **5**, 37–41.

Chapter 5



Summary and future scope

5.1 Summary

The field of lanthanide ion-doped phosphors-based research is continuing to grow as they become a better alternative to the conventional fluorophores in lighting and imaging applications. Before the advancement in nanotechnology, lanthanide ion-doped phosphors were mainly used in display applications. However, after the 1990s, this field, especially upconverting phosphors, increased its focus on synthesis, characterization and applications in biomedical and bioanalytical sciences as these phosphors helped in minimizing the autofluorescence from the molecules under NIR light excitation, which intrigued scientists at an academic stage to research for their bio applications. Apart from this, both up/downconverting phosphors offer multiple applications in a wide range of fields such as optoelectronics, light-emitting devices, security printing, solid-state lasers, sensing, catalysis, solar cells, and so forth. In this thesis, the optical properties of NaYF₄: Gd³⁺, Tb³⁺ phosphors and their applications in sensing were investigated. The effect of various ligands on the phase, sizes, and morphologies of NaYF₄ phosphors were understood and, consequently, their optical properties.

Firstly, the synthesis of NaYF₄: Gd³⁺, Tb³⁺ phosphors using different ligands at synthesis conditions were performed. It was observed that the ligands induced the formation of different phases, phase transition and morphology control during the synthesis of NaYF₄ crystals. Two different categories of ligands were chosen based on the functional groups it contained: carboxylic and amine group. It was noticed that the cubic phase was formed using carboxylic-functionalized ligands at laboratory temperature. In contrast, the hexagonal phase of NaYF₄ with high crystallinity was formed with amine-functionalized ligands at the same temperature. Since synthesizing the hexagonal phase directly at low temperatures is still a challenge, the successful synthesis of β -phase using a simple approach at room temperature was achieved. It was also noticed that the hexagonal phase of NaYF₄ was formed using both types of ligands when synthesized via

hydrothermal route at 180 °C. The effect of the different functionalized ligands on the morphology of NaYF₄ was also observed. Then, the possible mechanism of influence of ligands on the phase, morphology and growth process of NaYF₄: Gd³⁺, Tb³⁺ was proposed. Furthermore, the effect of these parameters on optical properties was studied, which suggested that NPs prepared at laboratory temperature show comparable emission intensity with the samples prepared hydrothermally, thus can be utilized for further modification and applications. Also, after achieving a better understanding of the complex phenomena of crystal growth, this approach can be extended further to synthesize different phases of NPs.

Then in the following work, a different strategy for morphology tuning of β -NaYF₄: Gd³⁺, Tb³⁺ phosphor crystals was selected by incorporating GQDs into the reaction system. This was an impurity-driven strategy to manipulate the growth of phosphor crystals. Consequently, the morphology of the crystals was drastically changed upon incorporating GQDs at different concentrations. The results were also compared with differently functionalized GQDs at varied concentrations. The plausible growth mechanism of β -NaYF₄: Gd³⁺, Tb³⁺-GQDs crystals was also proposed. The effects of two dimensional and one dimensional other carbon-based structures such as; GO and MWCNT were investigated and compared with the results obtained with the incorporation of only GQDs. It was found that the photoluminescence properties of β -NaYF₄: Gd³⁺, Tb³⁺ phosphor crystals were strongly dependent on the particle size and morphology. To the best of our knowledge, for the first time, an approach to incorporate GQDs was implied to influence the growth of β -NaYF₄: Gd³⁺, Tb³⁺ phosphor crystals to attain their multiform morphologies. The results presented underline the important role that controlled morphological synthesis can play in optimizing fundamental properties of advanced functional materials and could be extended to other nanocrystals. This unique approach paves the way to new opportunities for designing and tuning the lanthanide ion-doped

phosphor crystals. Moreover, their unique luminescence properties may endow potential applications in the field of light-emitting diodes, color displays, , solid-state lasers and luminescent biological labels and so forth.

Further, the lanthanide ion-doped phosphors were utilized for sensing applications. In this approach, the fluorimetric sensing technique presented the selective detection of TNT over the number of other analogous nitro compounds using β -NaYF₄: Gd³⁺,Tb³⁺ nanophosphors. The results from various characterization methods suggested the formation of β -NaYF₄: Gd³⁺,Tb³⁺ nanophosphors capped with PEI. The excellent selectivity towards TNT was ascribed due to the interactions of the amine groups present in PEI and nitro groups in TNT forming the Meisenheimer complex. The complex formation had caused a decrease in the luminescence intensity due to the LRET-based energy transfer mechanism between the nanophosphors and the complex formed. The emission intensity variations have displayed that the nanophosphors were sensitive and efficient for explosive detection with a limit of detection of 119.9 nM (27.2 ppb). To demonstrate the advantages of our work, the PL intensity of the nanophosphors with other analytes were investigated, and no apparent effects were observed. Thus, the proposed method demonstrated the feasibility of the PEI capped β -NaYF₄: Gd³⁺,Tb³⁺ phosphors NPs application for detecting TNT as the analyte independent of complicated instruments and immunoassays.

5.2 Future scope

Over the past decades, the research in lanthanide ion-based phosphors for upconversion and downconversion luminescence has been continuing to be interdisciplinary. The new arising dopant-host combinations are providing many opportunities for these optical materials. There have been significant progress and improvement over the years in the controlled synthesis for obtaining highly pure, crystalline, and monodispersed phosphors crystals. However, a challenge still remains to

synthesize high-quality NPs using a simple, low cost and low temperature synthetic approach. However, efforts in this aspect have been put forward in this thesis. Moreover, the nature of the surface of the capped NPs with ligands or surfactants is unknown; also, the modes of bonding of the ligands/capping agent at the surface is unexplored.

Apart from the NPs synthesis point of view, another major challenge is the low luminescence efficiency of lanthanide ion-based phosphors. Researchers worldwide adopted numerous strategies to enhance the luminescence of these phosphors. Still, there is a need to find an effective and robust method for efficiency enhancement. Another critical issue in this area is the specialized excitation source, which is primarily custom-built and generally unavailable in commercial instruments. This makes it difficult to reproduce the results and compare them from different research groups, making the development of commercial instruments crucial in this field. Thus, with the substantial improvement in the areas where it is lacking, the research in this field will then advance from the academic front into real-life applications.

ABSTRACT

Name of the Student: Monika Malik**Registration No.:** 10CC14A26020**Faculty of Study:** Chemical Sciences**Year of Submission:** 2021**CSIR Lab:** NCL, Pune**Name of the Supervisor:** Dr. Pankaj Poddar**Title of the Thesis:** Study of the effect of phase and morphology on the optical properties of lanthanide ion-doped phosphors and their applications

This thesis focuses on sodium yttrium fluoride (NaYF₄)-based phosphor as it possesses a wide bandgap, high chemical stability, and low phonon energy compared to other host materials, while Gd³⁺ and Tb³⁺ ions have been chosen as dopant ions. **Chapter 1** of this thesis gives an overview of the history and progress in the optical properties and applications of lanthanide ion-doped phosphors. **Chapter 2** investigates the phase transformation and growth mechanism of NaYF₄: Gd³⁺, Tb³⁺ nanophosphors prepared at ambient conditions and via hydrothermal route in the presence of various ligands. The plausible mechanisms of different phase formation and its transformation with the controlled morphologies of phosphors crystals are presented. It also deals with the effect of crystal structure, different surface capping, ligand functionalization, and different concentrations of ligands on the optical properties of as-prepared phosphors. Among the two phases of NaYF₄ identified, the hexagonal phase shows higher luminescence efficiency, which requires high temperature and a prolonged time for the synthesis; thus, a simple approach to prepare this phase at ambient conditions is also discussed. Keeping the same track in **chapter 3**, the mechanism of formation of multiform morphologies from rod to disk-like structures of NaYF₄: Gd³⁺, Tb³⁺ crystals where graphene quantum dots were *in situ* incorporated during the synthesis is probed. Then, the impact of phase, size, and morphology on the optical properties is presented. The effect of different functionalization and other carbon-based materials on the growth process and properties is also discussed. **Chapter 4** presents a simple synthetic approach developed to employ the Ln³⁺ ion-doped phosphors for the sensing of nitro-based explosives in a wide pH range with an acceptable detection limit. The potentiality of the probe for detecting trinitrotoluene (TNT) based on the fluorimetric sensing technique is explored in this chapter, with a detection limit of 119.9 nM. This work promises to pave the way for many applications in the detection of ultra-trace analytes. **Chapter 5** summarizes the overall work done in the present thesis and recommends the scope of the research for their applications in various fields.

List of Publication(s) in SCI Journal(s) Emanating from the Thesis Work

1. **Malik, M.**, Padhye, P., and Poddar, P. Graphene quantum dots-driven multiform morphologies of β -NaYF₄: Gd³⁺,Tb³⁺ phosphors: the underlying mechanism and their optical properties. *ACS Omega*, 2018, 3, 1834-1849. DOI: 10.1021/acsomega.7b01947
2. **Malik, M.**, Padhye, P., and Poddar, P. Downconversion luminescence-based nanosensor for label-free detection of explosives. *ACS Omega*, 2019, 4, 4259-4268. DOI: 10.1021/acsomega.8b03491

List of papers with abstract presented (oral or poster) at national or international conferences /seminars

1. *Electron microscopy society of India, EMSI, IIT-Bombay, 2015* (Presented poster titled "Lanthanide ion-doped rare earth fluoride crystals: controlled synthesis, morphology tuning and luminescence study")
2. *International Conference on Technologically Advanced Materials and Asian Meeting on Ferroelectricity, ICTAM-AMF10, University of Delhi, 2016* (Presented poster titled "GQDs mediated growth of multiform NaYF₄ phosphors")
3. *Physical and Materials Chemistry Divisional Day, CSIR-NCL, 2017* (Presented Oral talk titled "Graphene Quantum Dots-driven morphology of phosphors and their optical properties")
4. *Science Day Celebration*
CSIR-NCL, **2017** (Presented poster titled "Graphene quantum dots mediated morphology manipulation of NaYF₄: Gd³⁺,Tb³⁺ phosphors")
CSIR-NCL, **2018** (Presented poster titled "A downconversion luminescence-based turn-off nanosensors for label-free detection of explosives")

Graphene Quantum Dots-Driven Multiform Morphologies of β -NaYF₄:Gd³⁺/Tb³⁺ Phosphors: The Underlying Mechanism and Their Optical Properties

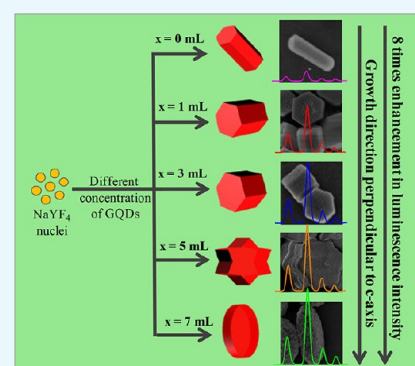
Monika Malik,^{†,‡} Preeti Padhye,^{†,‡} and Pankaj Poddar^{*,†,‡,§}

[†]Physical & Materials Chemistry Division, CSIR-National Chemical Laboratory, Pune 411 008, India

[‡]Academy of Scientific and Innovative Research (AcSIR), Anusandhan Bhawan, 2 Rafi Marg, New Delhi 110 001, India

Supporting Information

ABSTRACT: Dimension and shape tunable architectures of inorganic crystals are of extreme interest because of morphology-dependent modulation of the properties of the materials. Herein, for the first time, we present a novel impurity-driven strategy where we studied the influence of in situ incorporation of graphene quantum dots (GQDs) on the growth of β -NaYF₄:Gd³⁺/Tb³⁺ phosphor crystals via a hydrothermal route. The GQDs function as a nucleation site and by changing the concentration of GQDs, the morphology of β -NaYF₄:Gd³⁺/Tb³⁺ phosphors was changed from rod to flowerlike structure to disklike structure, without phase transformation. The influence of size and functionalization of GQDs on the size and shape of phosphor crystals were also systematically studied and discussed. Plausible mechanisms of formation of multiform morphologies are proposed based on the heterogeneous nucleation and growth. Most interestingly, the experimental results indicate that the photoluminescence properties of β -NaYF₄:Gd³⁺/Tb³⁺ phosphor crystals are strongly dependent on the crystallite size and morphology. This study would be suggestive for the precisely controlled growth of inorganic crystals; consequently, it will open new avenues and thus may possess potential applications in the field of materials and biological sciences.



1. INTRODUCTION

Rare earth ion-doped phosphors possess potential applications such as solid-state lasers;¹ high-resolution display devices, security and brand protection, photodynamic therapy,² fluorescent labels for the detection of molecules;³ in vivo imaging;^{4,5} medical diagnostics, fingerprint detection, and sensors;^{6,7} light-emitting devices;⁸ solar cells;^{9,10} and so forth which are better substitutes of conventional fluorophores and organic dyes.¹¹ Although the molar absorption coefficient of organic dyes and quantum dots is comparatively higher than that of the rare earth phosphors, high background noise, high blinking probability, poor photostability, and potential long-term toxicity hamper the use of these materials.^{12,13} In contrast, the fascinating luminescence features of lanthanide ions arising from intra 4f transitions such as narrow bandwidth, long-lived emission, large Stokes and antiStokes shift, less blinking, photostability, and low autofluorescence offer excellent prospects for designing new luminescent materials with enhanced properties.^{14,15} Among the phosphors, β -NaYF₄ has been demonstrated as the most efficient host for upconversion (UC) and downconversion (DC) emissions because of its low phonon energy (~ 350 cm⁻¹), high chemical stability, good optical transparency, high radiative emission rates, and low nonradiative decay rates.¹⁶

In recent years, the design and the synthesis of inorganic nano-/microcrystals with well-defined morphologies and

accurately tunable sizes remain the research focus as the precise control over shape and size allows manipulation of the physical, chemical, and biological properties of the nanocrystals as desired. Therefore, it is essential to develop efficient methods to fabricate multiform inorganic crystals to enhance their performance in existing applications. In the last decades, various efforts have been dedicated to synthesize the rare earth ion-doped phosphors in uniform but different sizes and shapes.¹⁷ In the kinetic control of the growth process of crystals, various external factors, such as concentration and types of precursors, reaction time/temperature/pressure, types of solvents, pH of precursor solution, and organic additives, drastically influence the shape of the crystals.¹⁸ All of these factors have been studied quite intensively. A large number of organic additives and shape-directing agents such as oleic acid,¹⁹ polyethylene glycol,^{5,20} trisodium citrate,²¹ cetyltrimethylammonium bromide,²² dodecyltrimethylammonium bromide,²³ ethylenediaminetetraacetic acid,²⁴ poly(4-styrenesulfonate),²⁵ and so forth are used to control the particle size and tune the crystallinity and morphology of the anisotropic crystals. These agents selectively bind to the different facets of the crystals and change their surface energy and chemical potential, which affects the

Received: December 6, 2017

Accepted: January 22, 2018

Published: February 13, 2018

orientation growth rate of different crystal facets, resulting in the formation of different architectures under various environments.¹⁷ Adjusting the molar ratio of a complexing agent/rare earth ion can also tune the crystal size and shape.²⁶ Commercially available ligands such as polyvinylpyrrolidone and polyethylenimine (PEI) are used to control the particle growth of the nanocrystals and endow them with surface functionality for further modification.²⁷ Various impurity dopant ions such as K^+ , Li^+ , Zn^{2+} , Sc^{3+} , and Gd^{3+} have been used intensively to study the change in phase and morphology. In a study by Dou and Zhang in 2011, Li^+ -ion doping in $NaYF_4:Yb^{3+}/Er^{3+}$ nanocrystals showed morphology change from nanorods to nanospheres along with the change in phase from hexagonal to cubic, when the doping percentage increased till 60%. While when K^+ ions were doped in the $NaYF_4:Yb^{3+}/Er^{3+}$ nanocrystals, morphology changed from elliptical shape to hexagonal prism and finally to nanorods as the K^+ content was increased in the system.²⁸ Similar to other studies, a mechanism was proposed for the influence of the molar ratio of K^+ to Y^{3+} on the anisotropic growth and morphology evolution of β - $NaYF_4$ nanocrystals.²⁹ In the same way, Li^+ ions were incorporated in the $KSc_2F_7:Yb^{3+}/Er^{3+}$ nanocrystals, which substituted K^+ or Sc^{3+} ions at lower doping concentration, whereas some of the Li^+ ions went into the interstitial site of the crystal lattice at higher doping concentration. An increase in size of the nanocrystals with 60 mol % of Li^+ -ion doping was observed.³⁰ In 2013, collective effect of different alkali metals onto the formation of multimorphologies of rare earth fluorides was also studied by Xue and co-workers.³¹ While Chen et al. studied the influence of Gd^{3+} ions on the phase transformation of $NaYF_4$ crystals from cubic to hexagonal phase and also observed decrease in luminescence intensity because of the decrease in the size of the nanorods with higher Gd^{3+} doping.³² Hitherto, numerous methods have been reported to fabricate the anisotropic nanoparticles such as rods, plates, prisms, tubes, spheres, disks, and spindles, and so forth. These methods include solvothermal, coprecipitation, thermal decomposition, combustion, and sol-gel process, among which hydro-/solvothermal method is considered a relatively environment-friendly method which provides high crystallinity and monodispersity to the material with diverse controllable morphologies and architectures.¹¹ Apart from the homogeneous nucleation, the crystal growth strategies based on the heterogeneous nucleation are quite popular. The choice of substrates provides an ideal nucleation site by lowering the activation energy barrier for the phase to form. In fact, the heterogeneous nucleation makes it possible for some metastable crystalline states to form well below the supersaturation limit of the monomer concentration.

In this article, we have investigated the role of graphitic carbon materials with varying surface functionality, size, and shape as a nucleation site for the growth of $NaYF_4$ nanocrystals. The rationale behind using these materials was due to their versatile application as the co-components in optically active hybrid materials as well as their role in defining the crystalline and optical properties of the crystals. Previously, our group reported the in situ insertion of graphene quantum dots (GQDs) during the growth of TiO_2 particles. Because of the presence of GQDs, irregular structures of the TiO_2 -GQD hybrid were formed instead of regular rodlike structure TiO_2 particles.³³ The carbon-based nanomaterials such as graphene, carbon nanotubes (CNTs), GQDs, and so forth have attracted significant attention owing to their advantageous properties

such as high surface area, low density, minimal cost, environment friendliness, and high thermal stability. Carbon-based materials possess excellent mechanical strength, electrical and thermal conductivity, and optical properties.³⁴ The GQDs have grabbed more attention because of their chemical inertness, solubility, tunable photoluminescence (PL), long-term photobleaching resistance, biocompatibility, and low cytotoxicity.³⁵ The GQDs have carbon with sp^2 hybridization having one or few layers of graphene sheets with lateral dimensions smaller than 100 nm³⁶ and oxygen-containing functional groups on their surfaces and at their edges. The GQDs are called zero-dimensional graphene materials. The quantum confinement of electrons has been demonstrated in GQDs and led to the practical applications in bioimaging, lasing, photovoltaics, and light-emitting diodes.³⁷

Composites of carbon-based materials have become important for various applications because of their unique physical and chemical properties. Various composites with GQDs have been synthesized such as GQD with polyaniline composite films, which have applications in photonic devices.³⁸ The GQDs have also been used as a co-sensitizer in the hybrid dye-sensitized solar-cell architectures.^{39,40} In other studies, the amine-functionalized GQDs (NH_2 -GQDs) were incorporated into the flexible and transparent clay host and cellulose nanofibers (CNFs). The resultant GQD@CNF-clay films exhibited PL; therefore, they were used as a material for blue light-emitting diodes to achieve white light emission.⁴¹

The development of multifunctional hybrid materials of lanthanide ion-doped phosphors is gearing tremendous interest for a broad range of potential applications in biological and material sciences because of their unique tunable electronic and magnetic properties.⁴² It is worth mentioning that a very few reports of the composites of carbon-based materials and lanthanide ion-doped phosphors are known till date for their sensing or photocatalytic applications. New-generation nanocomposites of $NaYF_4:Yb^{3+}/Er^{3+}$ and graphene oxide (GO) were fabricated with superior optical limiting performance,⁴³ followed by their mechanistic studies in the same year.⁴⁴ Composites of reduced GO and $NaYF_4:Yb^{3+}/Er^{3+}$ were proposed to achieve good electrical conductivity, which consequently increased the efficiency of the solar cell by 10%.⁴⁵ Fabrication of optical pH sensors based on the flexible and biocompatible freestanding optical hybrid film, which is composed of GO and $NaYF_4:Yb^{3+}/Er^{3+}$ nanoparticles (UCNPs), is reported. In this work, high surface area, mechanical stability, and luminescence quenching capability of GO are utilized as a sensing platform for pH sensing.⁴⁶ In another work, TiO_2 - $NaYF_4:Yb^{3+}/Er^{3+}$ -graphene composite photoanode was prepared, which improved the solar cell efficiency by increasing the interfacial electron transport of fluorine-doped tin oxide/ TiO_2 .⁴⁷ For biomedical applications, multifunctional multiwalled CNT (MWCNT)- $NaGdF_4:Yb^{3+}/Er^{3+}/Eu^{3+}$ hybrid nanocomposite was developed for simultaneous magnetic and optical imaging by $NaGdF_4:Yb^{3+}/Er^{3+}/Eu^{3+}$ NP and photothermal conversion property from MWCNT.⁴⁸ Recently, a sensor based on GQDs and ssDNA-UCNP@ SiO_2 is developed for the detection of microRNA sequence.⁴⁹ Although the composites of Ln^{3+} -doped phosphors and carbon-based nanomaterials have been explored, the in situ incorporation of carbon-based nanomaterials into the Ln^{3+} -doped phosphors is not studied yet.

Herein, we report a novel strategy to incorporate carbon-based nanomaterials; for example, we used GQDs as a foreign

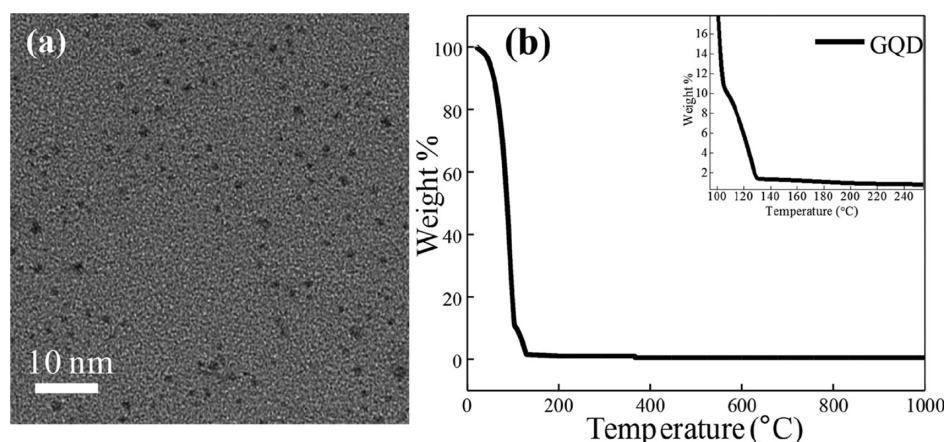


Figure 1. (a) TEM image of as-prepared GQDs showing a particle size of 3–5 nm and (b) TGA curve showing the weight fraction of GQDs under inert atmosphere.

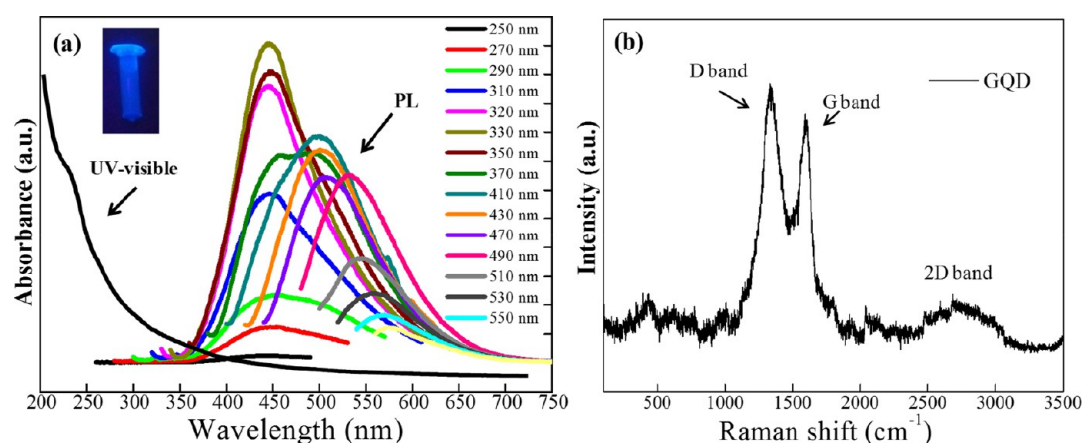


Figure 2. (a) UV–visible absorbance spectra showing a broad UV absorption with a small knee at 230 nm and PL spectra at different excitation wavelengths from 250 to 550 nm while the inset shows the photograph of the GQD aqueous suspension taken under 365 nm UV light exposure and (b) Raman spectra of the as-prepared GQDs using 633 nm laser as a source.

impurity into the β -NaYF₄:Gd³⁺/Tb³⁺ phosphor and studied their effect on the crystal phase, morphology, and optical properties of β -NaYF₄:Gd³⁺/Tb³⁺. Interestingly, we observed that the in situ incorporation of GQDs into the β -NaYF₄:Gd³⁺/Tb³⁺ phosphors has significantly influenced the morphology and consequently the optical properties of β -NaYF₄:Gd³⁺/Tb³⁺ crystals. We have studied the effect of the concentration of GQDs, the type of surface chemical functionalization, and CNTs on the morphology and PL properties of the β -NaYF₄:Gd³⁺/Tb³⁺ phosphors. To the best of our knowledge, for the first time, we are reporting the morphology tuning of inorganic crystals via incorporation of GQDs. This work has led to new opportunities of extending the use of this system in the area of architectural manipulation.

2. RESULTS AND DISCUSSION

Intentional incorporation of foreign elements into the hosts has a significant influence on the nucleation and growth of nanocrystals (heterogeneous nucleation) by lowering the thermodynamic activation energy barrier for the nucleation events to take place, which is influenced by the several microscopic properties such as the crystal structure of foreign elements and the precipitate, lattice mismatch between two species, surface roughness, surface wetting properties, and so forth from microscopic to the atomistic details. Thus, it

provides a unique approach to modify the crystallographic phase, size, morphology, and consequently the optical properties of nanomaterials. Here, we have incorporated varying concentrations of carboxylic and amine co-functionalized GQDs (mentioned as GQDs) in β -NaYF₄:Gd³⁺/Tb³⁺ phosphor crystals in the reaction vessel during the synthesis itself. To investigate the effect of GQDs and other carbon-based materials on the morphology of β -NaYF₄:Gd³⁺/Tb³⁺ phosphor crystals, we first characterized the as-prepared GQDs and then studied the structural, morphological, and optical properties of GQD-incorporated β -NaYF₄:Gd³⁺/Tb³⁺ phosphor crystals.

2.1. Characterization of GQDs. The size and morphology of the as-prepared GQDs were characterized by transmission electron microscopy (TEM). Figure 1a shows the TEM images of the GQDs having size in the range of 3–5 nm. The concentration of the GQDs was calculated from the thermogravimetric analysis (TGA) at a heating rate of 10 °C/min under nitrogen atmosphere (Figure 1b), which was found to be 10 mg/mL. The UV–visible absorbance (Figure 2a) showed the presence of broad absorbance in the UV range with a knee around ~230 nm because of π – π^* transitions of sp² C=C bonds present in the GQDs, which is in good agreement with the previous studies.⁵⁰ The inset of Figure 2a shows the photograph of the as-prepared GQDs aqueous solution taken under 365 nm UV light exposure. Detailed PL

studies were carried out at different excitation wavelengths ranging from 250 to 550 nm. It was found that the PL intensity first increased till 330 nm and then decreased remarkably. The fluorescence emission peak of GQDs red-shifted from 440 to 570 nm when the excitation wavelength increased from 250 to 550 nm. The highest intensity of the PL was observed for the GQDs at 445 nm when excited at 330 nm. Raman spectroscopy was performed at an excitation wavelength of 633 nm. Figure 2b shows the Raman spectrum where two well-resolved peaks corresponding to D and G bands at ~ 1340 and ~ 1600 cm^{-1} , respectively, were observed.

The G band corresponds to the E_{2g} phonon at the Brillouin zone center, whereas the disordered induced D band corresponds to the transverse optical phonons around the K-point of the Brillouin zone. The D band requires a defect for the momentum conservation. The intensity ratio I_D/I_G of D to G band is greater than 1, suggesting that the as-prepared GQDs have defects because of the dominant contributions from the edge states at the periphery. The 2D band is a second-order Raman process, which originates from in-plane breathing-like modes of the carbon rings.⁵¹ The broadening of the 2D band at ~ 2800 cm^{-1} may be due to the relaxation of the double-resonance Raman selection rules that are associated with the random orientation of GQDs with respect to each other.⁵² The broadness of this peak increases with increase in the defect states in the system.

2.2. Structural and Morphological Investigations of β -NaYF₄:Gd³⁺/Tb³⁺-xGQDs. The composition, crystallinity, and phase purity of the β -NaYF₄:Gd³⁺/Tb³⁺-xGQD phosphors were first examined by X-ray diffraction (XRD). Figure 3 shows the XRD patterns of the as-synthesized PEI-capped NaYF₄:Gd³⁺/Tb³⁺, incorporated with different concentrations of GQDs ($x = 0, 1, 3, 5,$ and 7 mL). The relative intensity of the peaks is changed compared with that of standard data, suggesting the probable anisotropic growth behavior of the particles. The rationale behind using PEI in the synthesis of NaYF₄ is not only to provide monodispersity to the particles but also to prevent particles from agglomeration. Here, we used GQDs, in which, as referred above, 1 mL of suspension is equal to 10 mg of GQDs. The sharp diffraction peaks in all the samples can be indexed to the pure hexagonal phase β -NaYF₄ (space group: $P6_3/m$) with calculated lattice parameters $a = 5.9$ Å and $c = 3.5$ Å, which are in good agreement with the reported data (JCPDS 16-0334). The absence of any other peak in XRD patterns indicates the high purity of as-prepared samples, implying that no secondary phase is formed. The pure hexagonal phase of all the samples reveals that the incorporation of GQDs at all concentrations does not induce the phase transformation in the β -NaYF₄ crystal structure. It is worth mentioning that on comparing the peak intensities of the prepared samples, we found that there is a difference in the relative intensities based on (100), (101), (110), (002), and (201) peaks, indicating the existence of different preferential orientation growths at different GQD concentrations. The size, shape, and structure of the as-prepared samples were characterized by TEM and field-emission scanning electron microscopy (FESEM) (Figures 4 and 5). The TEM images, as shown in Figure 4, show that the as-prepared PEI-capped β -NaYF₄:Gd³⁺/Tb³⁺ crystals possess a rod-shaped structure with an average length of ~ 280 nm and a diameter of ~ 96 nm. It can be seen that the β -NaYF₄:Gd³⁺/Tb³⁺-xGQD ($x = 0$) rods are highly uniform and monodispersed in nature. Interestingly, upon in situ incorporation of the GQDs into the PEI-capped β -

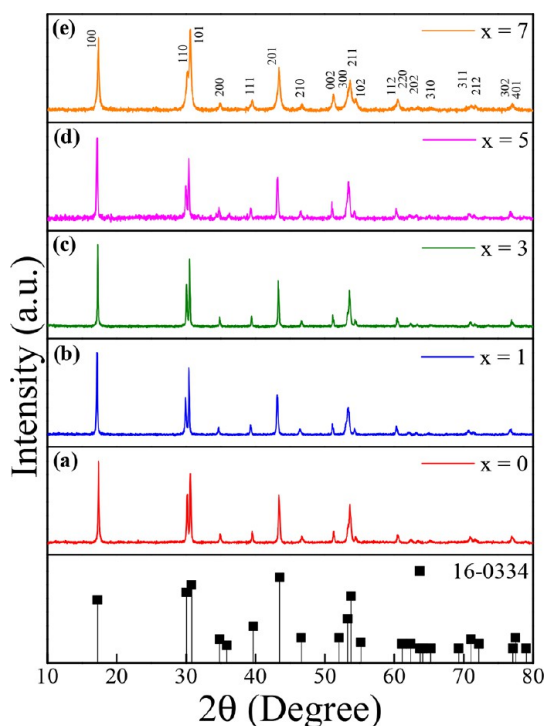


Figure 3. Comparison of XRD patterns of β -NaYF₄:Gd³⁺/Tb³⁺ and β -NaYF₄:Gd³⁺/Tb³⁺-xGQD phosphor crystals where $x =$ (a) 0, (b) 1, (c) 3, (d) 5, and (e) 7 mL. The standard data of β -NaYF₄ (JCPDS 16-0334) are also compared. Here, 1 mL of GQDs equals 10 mg by weight as calculated by the TGA curve. The incorporation of GQDs does not induce any phase transformation in the β -NaYF₄ crystal structure.

NaYF₄:Gd³⁺/Tb³⁺ phosphors during the synthesis, the variation in morphology was observed as a function of different concentrations of GQDs. As it can be seen from Figure 4b,c, at the lower concentrations of GQDs, that is, at $x = 1$ and $x = 3$, hexagonal prismatic structures were formed with average lengths/diameters of ~ 225 nm/ ~ 130 nm and ~ 280 nm/ ~ 250 nm, respectively. At $x = 5$, flower-shaped crystals were observed with a length and a diameter of ~ 325 and ~ 300 nm, respectively (Figure 4d). Whereas the crystallites observed at $x = 7$ are composed of disklike structures having an average length and a diameter of ~ 260 and ~ 620 nm, as shown in Figure 4e.

These results strongly suggest that the morphology of the β -NaYF₄:Gd³⁺/Tb³⁺-xGQD crystals ($x = 0, 1, 3, 5, 7$ mL) exhibited striking dependence on the different concentration of the GQDs, where the shape changed from rods ($x = 0$) to disklike structures ($x = 7$). The corresponding selected area electron diffraction patterns (SAEDs) and high-resolution TEM images shown in Figure 4f–j and insets, respectively, demonstrate that the as-synthesized β -NaYF₄:Gd³⁺/Tb³⁺-xGQD crystals are highly crystalline in nature. Meanwhile, the lattice fringes with an interplanar spacing of respective planes of β -NaYF₄:Gd³⁺/Tb³⁺-xGQD crystals are ascribed. The detailed observations with their proper facets at various concentrations of GQDs in the as-prepared samples can be clearly seen by the FESEM images (Figure 5). The FESEM images laid more evidence that the incorporation of the GQDs had huge effect on the morphology of the as-prepared crystals.

It should be noted that the pH of the solution has not changed because of the addition of GQDs in the precursor

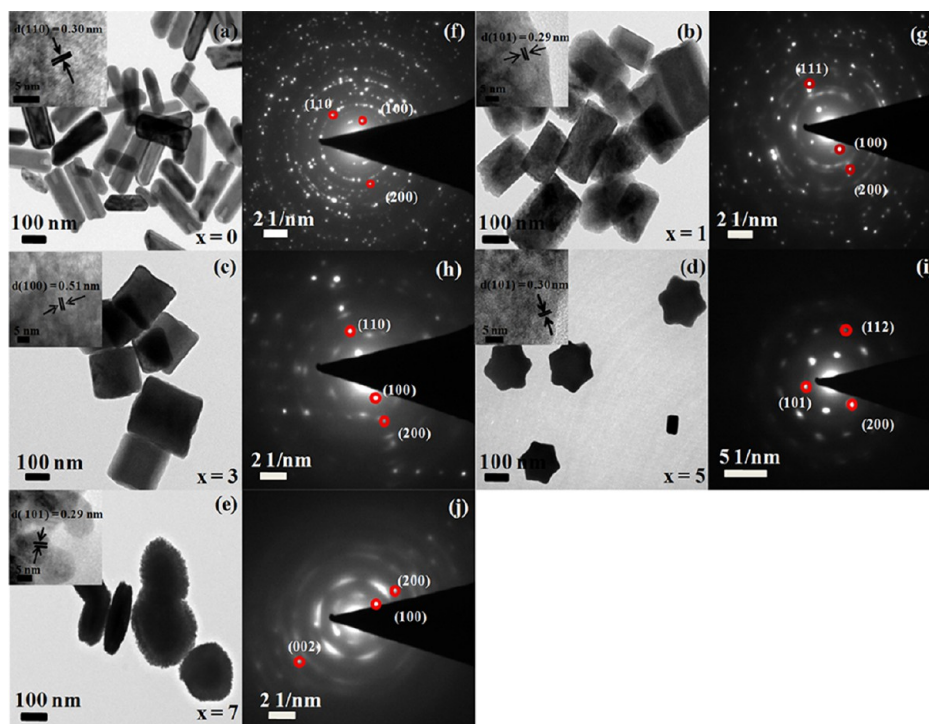


Figure 4. TEM images of GQDs-incorporated β - $\text{NaYF}_4:\text{Gd}^{3+}/\text{Tb}^{3+}$ particles show the modification of nucleation and growth of these particles when the concentration of GQDs was varied from $x = 0$ to 7 mL (a–e). The figures (f–j) show their respective SAED patterns. All samples were hydrothermally treated at 180 °C for 24 h.

solution. Therefore, the effect of pH has not influenced any changes of the product. Hence, these results clearly indicate that the size and morphology control in these experiments is closely related to the incorporation of GQDs because the concentration of GQDs was the only parameter changed in the system. The plausible mechanism for the modulation in the morphology of β - $\text{NaYF}_4:\text{Gd}^{3+}/\text{Tb}^{3+}$ phosphors because of the incorporation of GQDs is discussed in the next section.

2.3. Growth Mechanism of GQDs-Incorporated β - $\text{NaYF}_4:\text{Gd}^{3+}/\text{Tb}^{3+}$ Multiform Morphologies. For the better understanding of the formation processes of multiform morphologies of β - $\text{NaYF}_4:\text{Gd}^{3+}/\text{Tb}^{3+}$ phosphor crystals via incorporation of GQDs during the synthesis, reaction samples were carefully investigated by taking the different concentrations of as-prepared GQDs. Here, we believe that GQD particles of nearly 5 nm serve as the nucleation sites for the nucleation and further growth of the crystals. Because the precursors used in the reaction are ionic and GQDs contain functional groups at the edges and on the surface, lanthanide ions interact with functional group specially $-\text{COOH}$ and $-\text{OH}$ groups and form a metal–GQD complex. Then, nuclei are formed upon the addition of a fluoride source. Interaction of GQDs with the precursor ions plays an important role, where the charge or the functional groups such as carboxylic acid, amine, hydroxyl, etc. present in the GQDs have a significant role in binding to the lanthanide ions. As the seeds grow, the GQDs bind to the particular surface of the phosphor seeds, governing the shape and size of the particles. With an increase in the GQDs concentration, their probability to bind to the surface increases which increases the growth of the crystals along the (100) plane, thereby giving rise to the lowest aspect ratio of the rods. Consequently, with a larger concentration of GQDs, disklike structures were formed having the lowest aspect ratio among all. We have formulated the

above results on the same hypothesis as given by Yang et al. for the diethylene glycol molecule for the growth of KGdF_4 nanocrystals.⁵³ Here, GQDs may have different functions—first, it can form a metal–GQD complex by which the growth rate of the nanoparticles is slowed down, thereby decreasing the crystallite size. This is similar to the mechanism reported by Zeng’s group, where a metal–oleic acid complex was formed, when oleic acid was used as a ligand for the preparation of NaREF_4 nanocrystals.⁵⁴ Second, this may also slow down the diffusing rate of the cations and anions which may reduce the collisions’ probability of the ions in the system. Third, it can also cap the external surfaces of the nanoparticles, giving the nanoparticles a directional growth. By virtue of this, size control and shape evolution of the nanoparticles can be easily realized by changing the GQDs’ amount which governs the growth of the crystal in a particular direction.

Further, growth directional analysis was done by measuring the XRD intensity. In general, facets perpendicular to the fast direction of growth have smaller surface area; therefore, slow growing face will dominate the morphology having large surface area and thus will be more exposed to the environment. Hence, the more exposed plane will show higher intensity in XRD, which has slower growth. In Figure 6, variation in the normalized XRD intensity of different planes is plotted with varied concentration of GQDs used in the system. It can be seen that the intensity of the plane (100) decreases with higher concentration of co-functionalized GQDs, suggesting that the plane is less exposed and growth takes place along this direction, giving rise to disklike structures at 7 mL of GQDs. Similarly, when compared with other side planes in hexagonal structures (110) and (101), normalized intensity decreases, indicating the same. While in the case of the (002) plane (Figure 6d), the intensity increases with an increase in the

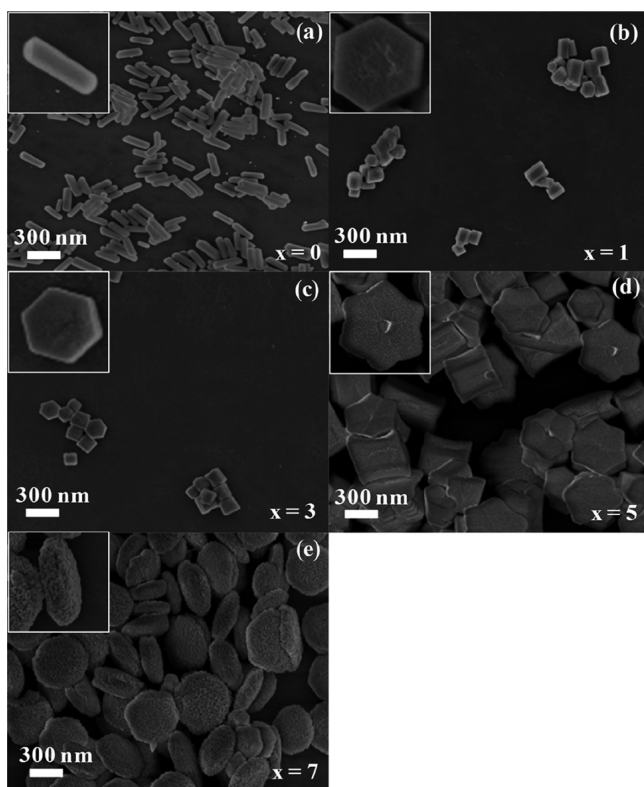


Figure 5. FESEM images show the change in the morphology of β - $\text{NaYF}_4:\text{Gd}^{3+}/\text{Tb}^{3+}$ after the incorporation of GQDs where the concentration of GQDs was varied from $x = 0$ to 7 mL (a–e). With increase in the concentration of GQDs, the aspect ratio (length/width) of the β - $\text{NaYF}_4:\text{Gd}^{3+}/\text{Tb}^{3+}$ phosphors decreased. NaYF_4 rods were formed at 0 mL of GQDs with an aspect ratio of 2.9 and disklike structures with an aspect ratio of 0.4 at 7 mL of GQDs.

concentration of GQDs, thus implying that growth direction is perpendicular to this plane.

Thence, it can be concluded that GQDs have the function of inhibiting the longitudinal growth along the $\langle 0001 \rangle$ direction with a relative enhancement of the growth along the $\langle 10\bar{1}0 \rangle$ direction in the form of hexagonal prism first and then disklike structures. Schematic showing the growth direction and proposed mechanism has been depicted in Schemes 1 and 2, respectively.

To validate the influence of the GQDs on the resultant morphology, we carried out the controlled experiments by changing the dimension of foreign impurity and the functionality of the as-prepared GQDs.

2.3.1. Effect of Size of the Foreign Particles Introduced in the Reaction (GO vs CNT). To study the effect of size of foreign particles incorporated during the synthesis of β - $\text{NaYF}_4:\text{Gd}^{3+}/\text{Tb}^{3+}$ crystals and to examine whether the change in the morphology of β - $\text{NaYF}_4:\text{Gd}^{3+}/\text{Tb}^{3+}$ phosphors is due to the incorporation of GQDs, a control experiment was performed. In three separate reactions of β - $\text{NaYF}_4:\text{Gd}^{3+}/\text{Tb}^{3+}$ phosphors, GO, MWCNTs and carboxylic-functionalized MWCNTs (COOH-MWCNT) were incorporated. The synthesis procedure is similar to the preparation of β - $\text{NaYF}_4:\text{Gd}^{3+}/\text{Tb}^{3+}$ - x GQDs, except that GO, MWCNTs and COOH-MWCNT were incorporated instead of GQDs. The as-obtained products were named as β - $\text{NaYF}_4:\text{Gd}^{3+}/\text{Tb}^{3+}$ - x GO and β - $\text{NaYF}_4:\text{Gd}^{3+}/\text{Tb}^{3+}$ - x MWCNT and β - $\text{NaYF}_4:\text{Gd}^{3+}/\text{Tb}^{3+}$ - x COOH-MWCNT. The composition and phase purity of the products were

examined by XRD as shown in Figure S1 given in the Supporting Information, where the diffraction peaks of the samples can be indexed to the pure hexagonal phase of NaYF_4 (JCPDS 16-0334). As represented in Figure 7, it was observed that due to the incorporation of GO sheets and MWCNT, the morphology of the β - $\text{NaYF}_4:\text{Gd}^{3+}/\text{Tb}^{3+}$ phosphor crystals remained unchanged. These results infer that the size of the foreign particles introduced in the reaction plays a role in the morphology tuning of β - $\text{NaYF}_4:\text{Gd}^{3+}/\text{Tb}^{3+}$ phosphors where only small GQD particles can tune the morphology, whereas large carbon materials: sheet or tubelike structures such as GO and MWCNT cannot influence and alter the shape of β - $\text{NaYF}_4:\text{Gd}^{3+}/\text{Tb}^{3+}$ phosphors.

2.3.2. Effect of Functionalization of GQDs on the β - $\text{NaYF}_4:\text{Gd}^{3+}/\text{Tb}^{3+}$ Phosphor Crystal Growth. Furthermore, to analyze the effect of the functionalization of GQDs on the morphology of β - $\text{NaYF}_4:\text{Gd}^{3+}/\text{Tb}^{3+}$ phosphors, we synthesized carboxylic-functionalized (COOH-GQDs) and amine-functionalized (NH_2 -GQDs) along with reduced GQDs (rGQDs). COOH-GQDs, NH_2 -GQDs, and rGQDs were characterized by TEM to see the particle size and UV–vis to see their absorbance. Figure 8 compares the TEM images of COOH-GQDs, NH_2 -GQDs, and rGQDs, showing a relatively narrow size distribution (~ 3 – 5 nm). To explore the optical properties, UV–vis spectra were recorded, showing the main absorbance peak at around 230 nm which is attributed to the π – π^* transitions of sp^2 C=C in as-synthesized COOH-GQDs, NH_2 -GQDs, and rGQDs, whereas a peak at around ~ 300 nm is attributed to the n – π^* transitions of C=O in the case of rGQDs.⁵⁵

The measured zeta potentials of COOH-GQDs, NH_2 -GQDs, and rGQDs were -32.8 , -15.8 , and -20.5 mV, respectively. The positive shift of the zeta potential for the NH_2 -GQDs and rGQDs indirectly indicates the introduction of amine groups because the introduced amine groups can counteract part of the electronegative effect and reduction in hydroxyl groups, respectively.⁵⁶ The concentration of the functionalized GQDs was calculated from the TGA at a heating rate of 10 °C/min under nitrogen atmosphere (Figure S2), which was found to be 10 mg/mL for all the types of GQDs. Furthermore, we performed the synthesis of β - $\text{NaYF}_4:\text{Gd}^{3+}/\text{Tb}^{3+}$ by incorporating COOH-GQDs and NH_2 -GQDs in the reaction vessel. The phase purity and crystallinity of the as-prepared samples were monitored by XRD and compared in Figure S3A, where the diffraction peaks matched very well with the standard JCPDS data of β - NaYF_4 . No traces of impurity peaks were observed, indicating that all the samples crystallized in a single phase of β - NaYF_4 . It can be seen in Figure 9 that functionalization has a notable effect on the morphology and size of the resultant products. Microrods with cracked ends were formed using COOH-GQDs having an average length of ~ 15 μm at $x = 5$ mL, whereas the average size of the microrods increased to ~ 30 μm when the concentration of COOH-GQDs increased further to 7 mL. In a study in 2006, during the growth of NaYF_4 crystals, oleic acid selectively bound to the surface which was parallel to the c -axis, rendering the growth along the (001) direction and hence resulting in the formation of nanorods.⁵⁷ Supporting the above mechanism, in another study, it was concluded that the anionic form of oleic acid (OA^-) preferentially binds to the RE^{3+} ions exposed more on the six symmetric facets of the hexagonal fluoride crystal, resulting in the formation of rods.¹⁹ Applying the same hypothesis, we can conclude that the functional groups such as carboxylic and

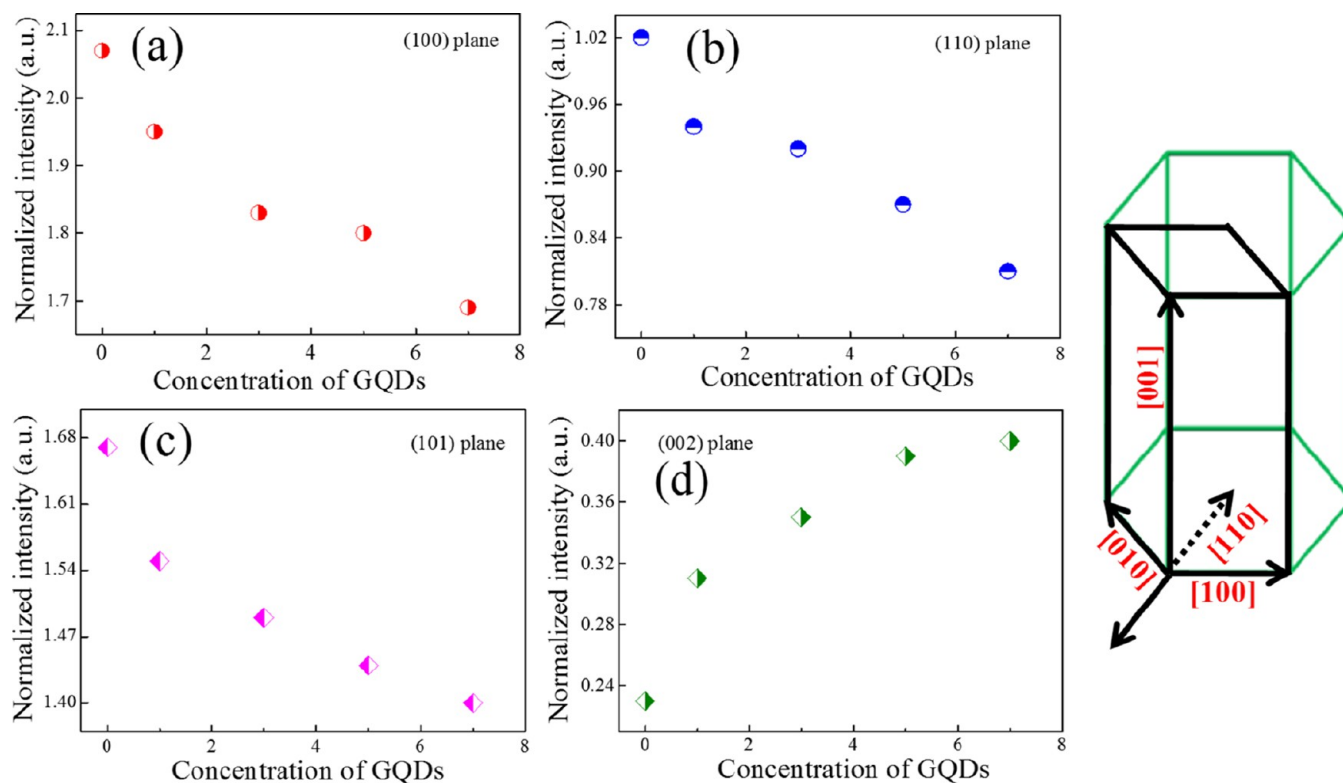
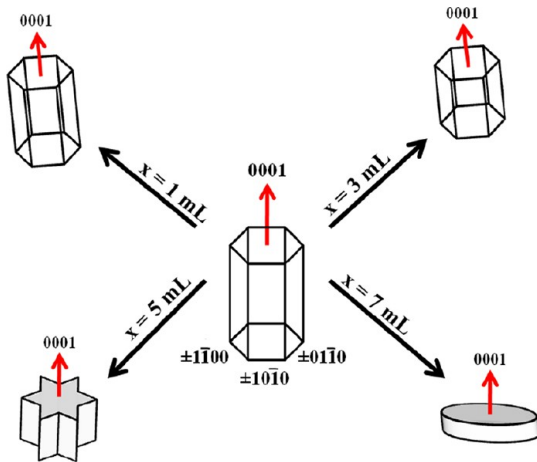


Figure 6. Variation of normalized XRD intensity of different planes (a) 100, (b) 110, (c) 101, and (d) 002 in β -NaYF₄:Gd³⁺/Tb³⁺ with the change in concentration of GQDs. Respective direction of planes is shown in the anisotropic hexagonal crystal structure.

Scheme 1. Schematic Illustration of the Directional Growth of Anisotropic Structure of β -NaYF₄:Gd³⁺/Tb³⁺-xGQDs Shown with Different Planes with the Change in Concentration of GQDs Where x Is Varied as $x = 1$ mL, $x = 3$ mL, $x = 5$ mL, and $x = 7$ mL



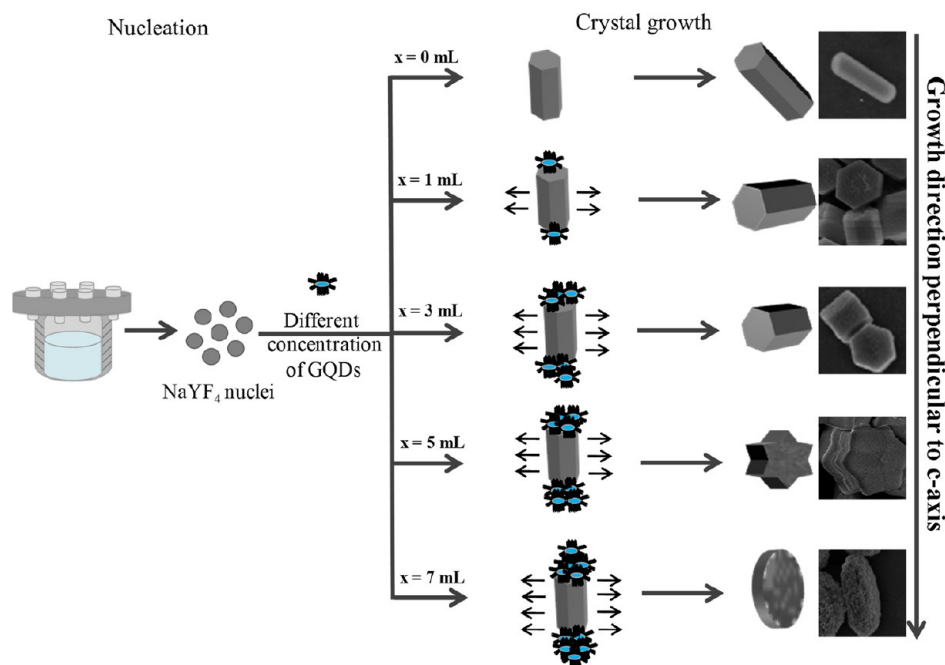
hydroxyl may bind to the side planes of the hexagonal prismatic structures where lanthanide ions are more exposed, giving rise to the formation of microrods; therefore, the preferential growth direction is along (0001). Additionally, growth direction was confirmed by normalized XRD intensity. As shown in Figure 10a, the intensity of different planes in β -NaYF₄ changes when we increase the concentration of COOH-GQDs. The increment in the intensity of the (100), (110), and (101) planes suggested that the growth direction was perpendicular to these planes, thus rendering the growth along the (001) plane.

Further, we have studied the effect of NH₂-GQDs on the growth process of β -NaYF₄. The crystallinity of the β -NaYF₄:Gd³⁺/Tb³⁺-xNH₂-GQDs was examined by XRD. The diffraction peaks in the XRD pattern shown in Figure S3B can be indexed to pure β -NaYF₄.

The presence of NH₂-GQDs has no obvious impact on the morphology of the crystals, which can be seen in the FESEM images (Figure 9d–f). Moreover, the XRD intensity of different planes as shown in Figure 10b has not changed with the concentration of NH₂-GQDs, confirming the unaltered morphology of β -NaYF₄.

To study the effect of non-functionalized GQDs, we have used rGQDs during the synthesis of NaYF₄. Oxygen-rich functional groups such as carboxyl, hydroxyl, and epoxy groups are introduced to the edges and onto the basal plane during the top-down synthesis,^{58,59} which can be reduced using some of the reducing agents such as NaBH₄, hydrazine hydrate, and so forth. Here, we have reduced COOH-GQDs with NaBH₄ which reduces hydroxyl and epoxy groups on the basal plane of the GQDs while carboxyl moieties remain unreduced at the edges. As observed in the XRD pattern shown in Figure S3C, some of the diffraction peaks belong to the cubic phase of NaYF₄ which matched very well with the standard face-centered cubic structure data (JCPDS 77-2042), whereas other peaks can be indexed to the pure hexagonal phase of NaYF₄ (JCPDS 16-0334). We can see in Figure 11 that similar microrods were formed when we performed the reaction with rGQDs having few carboxylic acid groups at the edges. Here, the proposed mechanism for the formation of microrods may be the same as that in the case of COOH-GQDs. Apart from microrods, small spherical particles were seen, which have been assigned as the cubic phase as indexed in the XRD pattern. Careful investigation revealed that the microrods were

Scheme 2. Schematic Illustration of Heterogeneous Nucleation and Growth Process and the Effect of GQD Incorporation on the Morphology of Final β -NaYF₄:Gd³⁺/Tb³⁺ Phosphors^a



^aHere, the GQDs provide nucleation sites for the heterogeneous nucleation as well as act as a capping agent and manipulate the growth of β -NaYF₄:Gd³⁺/Tb³⁺ crystals.

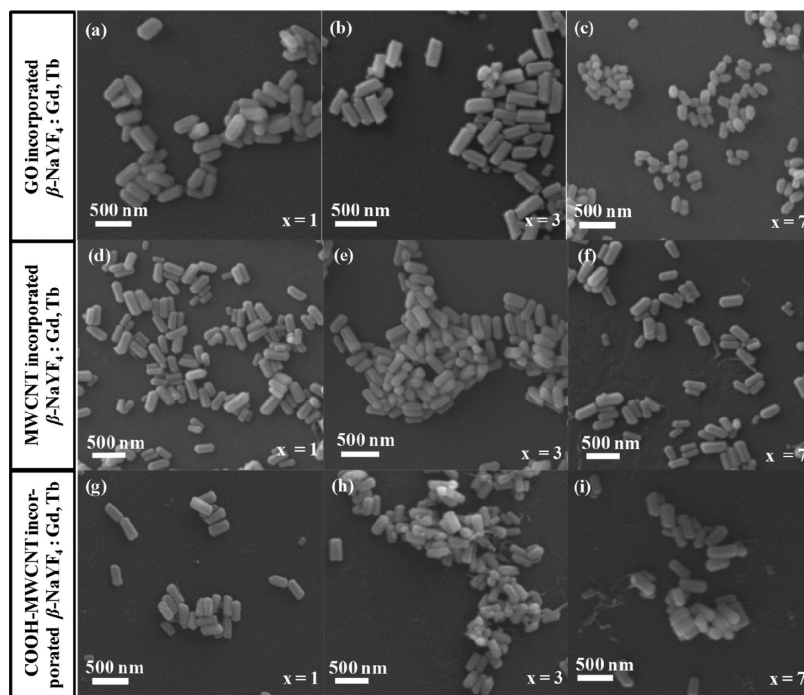


Figure 7. SEM images show the effect of different concentrations of GO (a–c), MWCNT (d–f), and COOH-MWCNT (g–i) on the growth morphology of β -NaYF₄:Gd³⁺/Tb³⁺ phosphors. We did not observe any change in the morphology of β -NaYF₄:Gd³⁺/Tb³⁺ phosphors because of the incorporation of these materials as foreign impurities.

composed of solid interiors with small quasi-spheres attached to them. Together with the XRD pattern, it can be judged from SEM images that the microrods were hexagonal phase and small quasi-spherical nanoparticles were cubic. Although the formation of cubic phase in the system is unclear at present, we can provide the following explanation for the existence of cubic

phase. Because the rGQDs contain less number of functional groups, it would lead to the availability of more number of lanthanide ions, which would provide fast nucleation and growth of NaYF₄ crystals. However, there were not enough monomers to supply the growth of small particles under the same circumstances. Thus, small nanoparticles with cubic phase

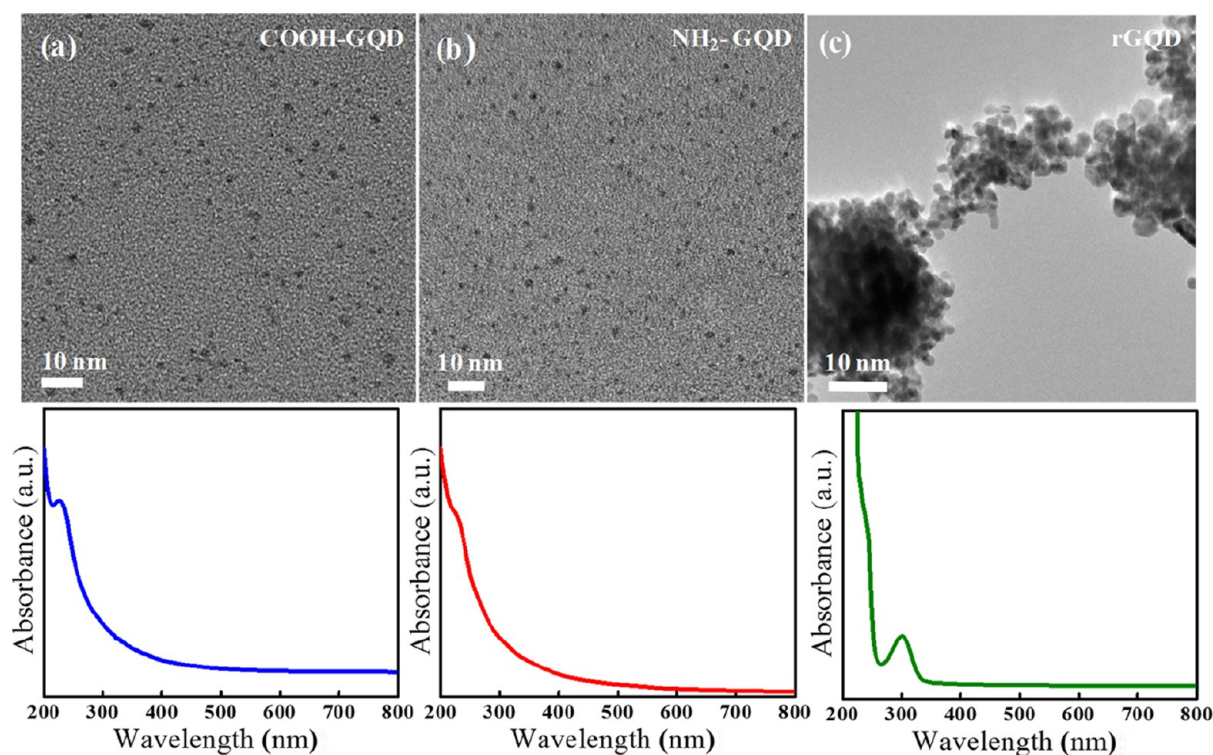


Figure 8. TEM images of (a) COOH-GQDs, (b) NH_2 -GQDs, and (c) rGQDs showing the average particle size in the range of 3–5 nm. In the case of rGQDs, particles are aggregated because of the less surface charge after the reduction reaction. Their respective UV–visible absorbance spectra are also shown below, showing the main absorbance peak at around 230 nm in as-synthesized COOH-GQDs, NH_2 -GQDs, and rGQDs, whereas a peak was observed at around ~ 300 nm in rGQD alone.

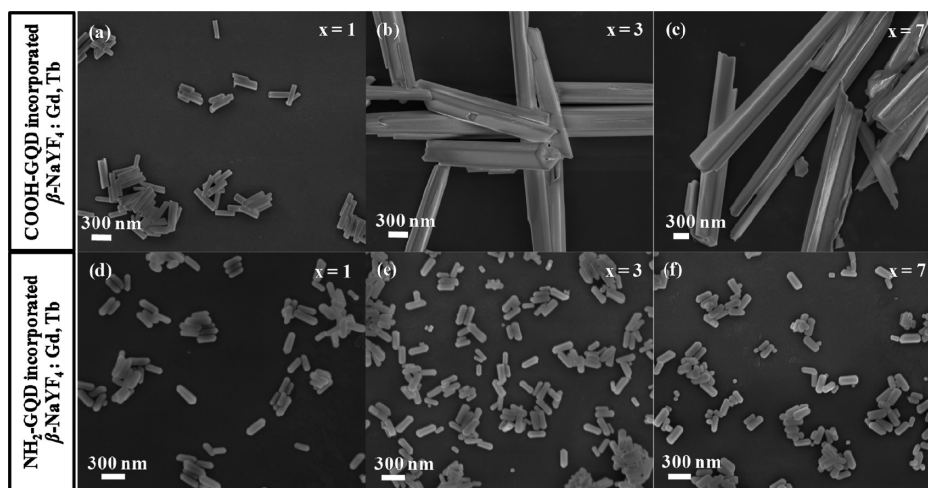


Figure 9. FESEM images of $\beta\text{-NaYF}_4\text{:Gd}^{3+}/\text{Tb}^{3+}\text{-}x\text{COOH-GQDs}$ (a–c) and $\beta\text{-NaYF}_4\text{:Gd}^{3+}/\text{Tb}^{3+}\text{-}x\text{NH}_2\text{-GQD}$ (d–f) phosphors where the concentration of respective GQDs was varied from $x = 1$ mL, $x = 3$ mL, and $x = 7$ mL. Microrods were formed when COOH-GQDs were incorporated, while there was no change observed in the case of the incorporation of NH_2 -GQDs during the synthesis of $\beta\text{-NaYF}_4\text{:Gd}^{3+}/\text{Tb}^{3+}$.

as well as microrods with hexagonal phase coexisted in the final products with rGQDs. The schematic and table showing corresponding morphologies obtained at different concentrations of GQDs, different functionalized GQDs, and different foreign impurities are represented in Scheme 3, and details of aspect ratios are summarized in Table 1.

2.4. PL Studies. Owing to the non-existence of d-electrons in Y^{3+} ($[\text{Kr}] 4d^0$) in undoped NaYF_4 , the probability of emission is negligible in the host matrix. Figure 12 compares the PL emission spectra of $\beta\text{-NaYF}_4\text{:Gd}^{3+}/\text{Tb}^{3+}$ and $\beta\text{-NaYF}_4\text{:Gd}^{3+}/\text{Tb}^{3+}\text{-}x\text{GQD}$ ($x = 1, 3, 5$, and 7 mL) phosphor

crystals. The luminescence of lanthanide ions mainly originates from the electron transition within 4f electronic configuration $[\text{Xe} 4f^N; N = 0\text{--}14]$, which consists of complex energy levels because of Coulombic repulsion and spin–orbit coupling. The shielding of the 4f electrons of Ln^{3+} by the filled $5s^2$ and $5p^6$ subshells results in weak influence of external environment, which is responsible for their sharp and narrow emission spectra. Thus, the emissive electronic transitions are a characteristic feature of lanthanide dopant ions, and so, the incorporation of GQDs does not render any peak shift in the transition emission of Tb^{3+} ions and bands differ only in their

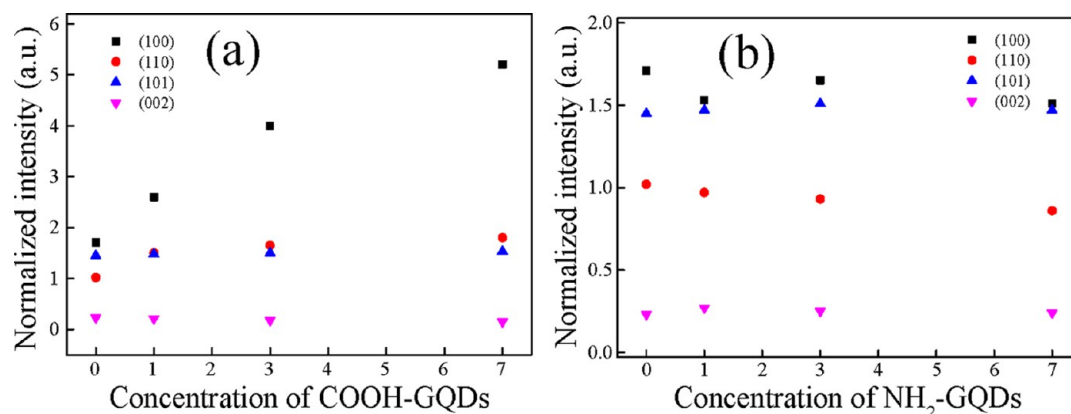


Figure 10. Variation of normalized XRD intensity of different planes in β - $\text{NaYF}_4\text{:Gd}^{3+}/\text{Tb}^{3+}$ with the change in the concentration of (a) COOH-GQDs and (b) NH_2 -GQDs.

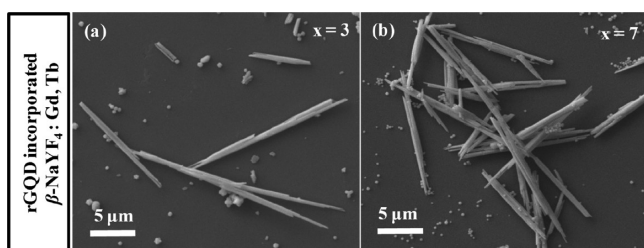
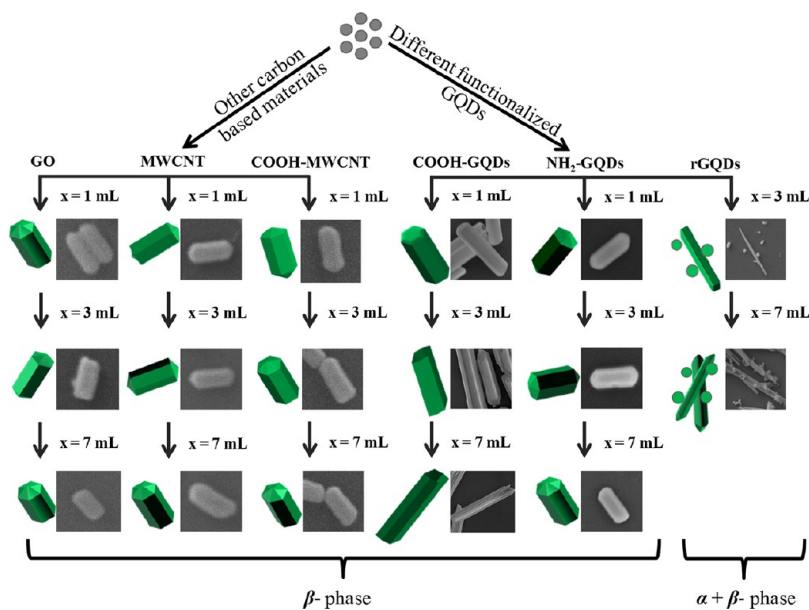


Figure 11. SEM images of β - $\text{NaYF}_4\text{:Gd}^{3+}/\text{Tb}^{3+}$ phosphors with varied concentration of rGQDs. Microrods were formed along with some small quasi-spherical particles with the in situ incorporation of rGQDs during the synthesis.

relative intensities. Here, Gd^{3+} ion is used as a sensitizer to enhance the luminescence of Tb^{3+} ions. As Gd^{3+} ions exhibit strong absorption band at 273 nm because of its $^8\text{S}_{7/2} \rightarrow ^6\text{I}_{11/2}$ transition, Gd^{3+} and Ln^{3+} together containing nanoparticles

exhibit a very intense Ln^{3+} excitation band at 273 nm because of the $^8\text{S}_{7/2} \rightarrow ^6\text{I}_J$ transition in Gd^{3+} ions followed by a nonradiative (nr) energy transfer to Ln^{3+} ions.^{60,61} Thus, Gd^{3+} ions act as a sensitizer to enhance the emission of Tb^{3+} ion via nr energy transfer. The obtained emission spectra monitored at $\lambda_{\text{ex}} = 273$ nm yielded intense green emissions in the region of 480–680 nm, which are due to the $^5\text{D}_4 \rightarrow ^7\text{F}_J$ ($J = 3, 4, 5, 6$) transitions of Tb^{3+} ions. Four prominent emission peaks centered at ~ 488 , ~ 544 , ~ 584 , and ~ 619 nm originate from the transitions of $^5\text{D}_4 \rightarrow ^7\text{F}_6$, $^5\text{D}_4 \rightarrow ^7\text{F}_5$, $^5\text{D}_4 \rightarrow ^7\text{F}_4$, and $^5\text{D}_4 \rightarrow ^7\text{F}_3$, respectively.^{22,62,63} The mechanism for DC in $\text{Gd}^{3+}-\text{Tb}^{3+}$ pair under excitation of 273 nm has been demonstrated in Figure S4 (Supporting Information). Among these transitions, the green emission $^5\text{D}_4 \rightarrow ^7\text{F}_5$ at ~ 544 nm is the most intense emission, which corresponds to a magnetic dipole transition. Figure 12 shows the comparative emission spectra of β - $\text{NaYF}_4\text{:Gd}^{3+}/\text{Tb}^{3+}$ phosphors incorporated with different concentrations of GQDs. It can be seen that with the increasing

Scheme 3. Schematic Illustration of the Effect of Other Carbon-Based Materials and Differently Functionalized GQDs on the Morphology of $\text{NaYF}_4\text{:Gd}^{3+}/\text{Tb}^{3+}$ Phosphors^a



^aOnly the incorporation of COOH-GQDs and rGQDs has made a significant change in the morphology of the β - $\text{NaYF}_4\text{:Gd}^{3+}/\text{Tb}^{3+}$ phosphor crystals.

Table 1. Summary of the Effect of GQDs and Other Carbon-Based Materials on the Morphology and Aspect Ratio of the Final β -NaYF₄:Gd³⁺/Tb³⁺ Phosphors Where x Is Varied as $x = 1$ mL, $x = 3$ mL, and $x = 7$ mL in the Respective System

S. no	sample	concentration (mL)	morphology	aspect ratio (L/W)
1	β -NaYF ₄ :Gd ³⁺ /Tb ³⁺ - x GQD	0	rods	2.9
		1	hexagonal prism	1.7
		3	hexagonal prism	1.2
		5	flowerlike structure	1.1
		7	disklike structure	0.4
2	β -NaYF ₄ :Gd ³⁺ /Tb ³⁺ - x GO	1	rods	3.1
		3	rods	2.6
		7	rods	2.1
3	β -NaYF ₄ :Gd ³⁺ /Tb ³⁺ - x MWCNT	1	rods	2.9
		3	rods	2.7
		7	rods	2.8
4	β -NaYF ₄ :Gd ³⁺ /Tb ³⁺ - x COOH-MWCNT	1	rods	2.4
		3	rods	2.3
		7	rods	2.3
5	β -NaYF ₄ :Gd ³⁺ /Tb ³⁺ - x COOH-GQDs	1	microrods	4.1
		3	microrods	9.8
		7	microrods	23.3
6	β -NaYF ₄ :Gd ³⁺ /Tb ³⁺ - x NH ₂ -GQDs	1	rods	3.1
		3	rods	2.8
		7	rods	2.4
7	β -NaYF ₄ :Gd ³⁺ /Tb ³⁺ - x rGQDs	3	microrods	15.1
		7	microrods	20.5

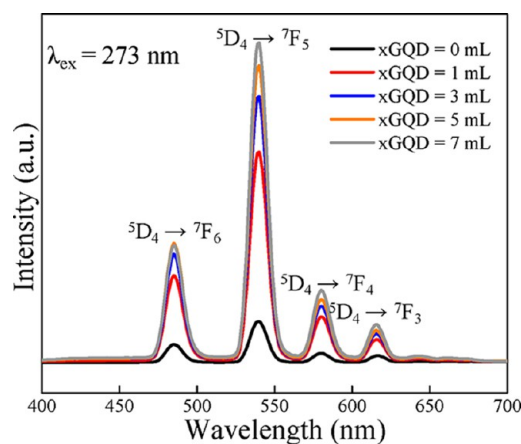


Figure 12. Comparison of static PL emission spectra at the excitation wavelength $\lambda_{\text{ex}} = 273$ nm of β -NaYF₄:Gd³⁺/Tb³⁺- x GQD phosphors with different concentrations of as-prepared GQDs.

concentration of GQDs, the PL intensity of the β -NaYF₄:Gd³⁺/Tb³⁺ phosphors showed a remarkable enhancement. We believe that the change or increase in luminescence intensity is due to change in morphology and size of the β -NaYF₄:Gd³⁺/Tb³⁺- x GQD crystals. Different morphologies of the host matrix greatly influence the emission intensity and the shape of the spectra.^{63,64} It is evident from the spectra that among all the samples, the disklike structure obtained from β -NaYF₄:Gd³⁺/Tb³⁺- x GQDs ($x = 7$) displayed the strongest emission intensity under similar measurement conditions shown in Figure 12. The β -NaYF₄:Gd³⁺/Tb³⁺- x GQD ($x = 0$) rods possess the lowest emission intensity. Whereas the relative luminescence intensity of other β -NaYF₄:Gd³⁺/Tb³⁺- x GQD crystals, that is, hexagonal micropillars obtained at $x = 1$ and $x = 3$ and flower-shaped crystals obtained at $x = 5$, lies in between the rods and the disklike structure. The reason behind the difference in relative PL intensity might be due to the difference in the surface area

of different facets, defects, and crystallinities. Herein, the highest luminescence intensity of disklike structures might be due to their low surface area to volume ratio and consequently possesses low surface defects when compared to that of other anisotropic structures.^{65,66} While the rods and other as-formed morphologies are predicted to have more surface defects owing to their high surface area.⁶⁷ The defects may act as the nonradiative recombination centers, which are thus responsible for luminescence quenching. Moreover, high surface area also renders greater Gd³⁺ or Tb³⁺ ion fraction on the particle surface, which again causes the enhanced nonradiative quenching and results in diminished emission intensity.^{66,68} In addition, to further understand the variation in PL performance, the PL spectra of β -NaYF₄:Gd³⁺/Tb³⁺- x GO, β -NaYF₄:Gd³⁺/Tb³⁺- x MWCNT, and β -NaYF₄:Gd³⁺/Tb³⁺- x COOH-MWCNT ($x = 7$) crystals were also studied. Figure 13 shows the comparative PL spectra of β -NaYF₄:Gd³⁺/Tb³⁺- x GQDs ($x = 0$ and 7), β -NaYF₄:Gd³⁺/Tb³⁺- x GO, β -NaYF₄:Gd³⁺/Tb³⁺- x MWCNT, and β -NaYF₄:Gd³⁺/Tb³⁺- x COOH-MWCNT ($x = 7$) crystals. As discussed in section 2.3.1, the incorporation of other carbon materials such as GO and MWCNTs had a very little influence on the morphology and size of the β -NaYF₄:Gd³⁺/Tb³⁺ crystals. As a consequence with negligible change in the morphologies, it can be clearly seen that the relative luminescence intensities hardly changed with the incorporation of the above-mentioned foreign impurities. However, when compared with that of the disklike structures, the PL intensity showed a remarkable change. The luminescence intensity of a disklike structure was observed to be eight times stronger than that of the β -NaYF₄:Gd³⁺/Tb³⁺ crystals incorporated with GO and MWCNT and β -NaYF₄:Gd³⁺/Tb³⁺ rods. To get further insights into the effect of the incorporation of GQDs on the luminescence intensity of β -NaYF₄:Gd³⁺/Tb³⁺ phosphor crystals, the PL spectra of β -NaYF₄:Gd³⁺/Tb³⁺ crystals incorporated with different functionalized GQDs, β -NaYF₄:Gd³⁺/Tb³⁺- x COOH-GQDs, and β -

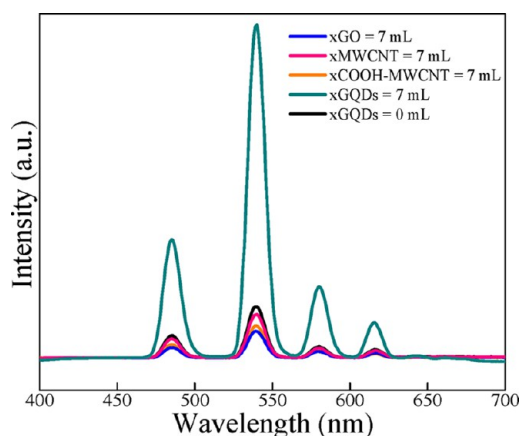


Figure 13. Static PL emission spectra at the excitation wavelength $\lambda_{\text{ex}} = 273$ nm of $\beta\text{-NaYF}_4\text{:Gd}^{3+}/\text{Tb}^{3+}$ phosphors with different concentrations ($x = 7$ mL) of GO, MWCNTs and COOH-MWCNT. A comparison has been made with the $\beta\text{-NaYF}_4\text{:Gd}^{3+}/\text{Tb}^{3+}$ phosphors incorporated with GQDs.

$\text{NaYF}_4\text{:Gd}^{3+}/\text{Tb}^{3+}\text{-xNH}_2\text{-GQDs}$ were demonstrated (Figure 14). As it is already discussed above that functionalization of

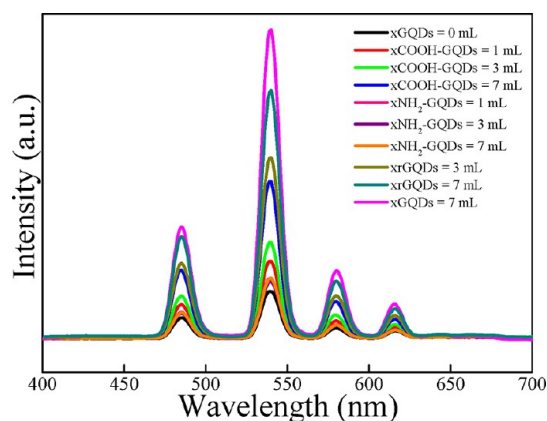


Figure 14. Comparative static PL emission spectra of $\beta\text{-NaYF}_4\text{:Gd}^{3+}/\text{Tb}^{3+}$ phosphors with different concentrations of COOH-GQDs, $\text{NH}_2\text{-GQDs}$, rGQDs, and $\beta\text{-NaYF}_4\text{:Gd}^{3+}/\text{Tb}^{3+}\text{-xGQD}$ phosphors at $\lambda_{\text{ex}} = 273$ nm where x is varied as $x = 1$ mL, $x = 3$ mL, and $x = 7$ mL.

GQDs plays an important role in the morphology tuning of the crystals, it could be clearly reflected in the PL spectra. In the case of $\beta\text{-NaYF}_4\text{:Gd}^{3+}/\text{Tb}^{3+}\text{-xCOOH-GQD}$ ($x = 1, 3,$ and 7) crystals, with increasing concentration of COOH-GQDs, the size of as-formed microrods increased and thus the PL intensity also increased. Because the surface area to volume ratio increases with decrease in the size of the material, a phosphor with the largest size would possess the lowest surface area and the highest luminescence intensity.⁶⁹ Therefore, the $\beta\text{-NaYF}_4\text{:Gd}^{3+}/\text{Tb}^{3+}\text{-xCOOH-GQD}$ ($x = 7$) microrod (~ 30 μm) possesses the highest luminescence intensity, while $\beta\text{-NaYF}_4\text{:Gd}^{3+}/\text{Tb}^{3+}\text{-xCOOH-GQD}$ ($x = 1$) microrods (~ 15 μm) and $\beta\text{-NaYF}_4\text{:Gd}^{3+}/\text{Tb}^{3+}$ rods have a lower PL intensity.

Negligible change in the PL intensity was observed owing to negligible change in size and morphology of $\beta\text{-NaYF}_4\text{:Gd}^{3+}/\text{Tb}^{3+}\text{-xNH}_2\text{-GQD}$ ($x = 1, 3,$ and 7) rod-shaped crystals (Figure 14). PL spectra of $\text{NaYF}_4\text{:Gd}^{3+}/\text{Tb}^{3+}$ with rGQDs were also recorded and compared with those of disklike structures. The emission intensity of $\text{NaYF}_4\text{:Gd}^{3+}/\text{Tb}^{3+}\text{-xrGQDs}$ was obviously

lower than that of disklike structures but higher than that of the $\beta\text{-NaYF}_4\text{:Gd}^{3+}/\text{Tb}^{3+}\text{-xCOOH-GQD}$ microrods. Because $\text{NaYF}_4\text{:Gd}^{3+}/\text{Tb}^{3+}\text{-xrGQDs}$ attained cubic phase along with the hexagonal phase, that is, mixed phase, their emission intensity is expected to be lower because the mixed phase system is less luminescent than the pure hexagonal phase.^{25,70,71}

However, the higher intensity of $\text{NaYF}_4\text{:Gd}^{3+}/\text{Tb}^{3+}\text{-xrGQD}$ microrods as compared with that of $\beta\text{-NaYF}_4\text{:Gd}^{3+}/\text{Tb}^{3+}\text{-xCOOH-GQD}$ microrods was due to their larger size (~ 35 μm). However, the overall spectra revealed that the PL intensity of disklike structures remained the strongest emission intensity among all the samples. The luminescent properties of inorganic materials are dependent on several factors such as crystal structure around emitting ions, morphology, size, crystallinity, impurity doping, surface defects, surface adsorbed species, solvent molecules, ligands, and so forth.⁷² In this study, although incorporation of GQDs had significant influence on the growth of $\beta\text{-NaYF}_4\text{:Gd}^{3+}/\text{Tb}^{3+}$ crystals, but on the basis of the above analysis, among all the factors we reasonably believe that the variation in PL properties of the samples predominantly arises from their size and morphologies.

3. CONCLUSIONS

In summary, a novel impurity-driven strategy for the morphology tuning of $\beta\text{-NaYF}_4\text{:Gd}^{3+}/\text{Tb}^{3+}$ phosphor crystals is presented, wherein GQDs were incorporated in situ into the $\beta\text{-NaYF}_4\text{:Gd}^{3+}/\text{Tb}^{3+}$ crystal system to manipulate the growth of phosphor crystals. Consequently, the morphology of the crystals was drastically changed upon the incorporation of GQDs at different concentrations. The results were also compared with differently functionalized GQDs at varied concentrations. The plausible growth mechanism of $\beta\text{-NaYF}_4\text{:Gd}^{3+}/\text{Tb}^{3+}\text{-xGQD}$ crystals is proposed. The effect of two-dimensional and one-dimensional other carbon-based structures such as GO and MWCNT was investigated and compared with the results obtained with the incorporation of GQDs. It was found that the PL properties of $\beta\text{-NaYF}_4\text{:Gd}^{3+}/\text{Tb}^{3+}$ phosphor crystals are strongly dependent on the crystallite size and morphology. To the best of our knowledge, for the first time, we have implied an approach to incorporate GQDs as an impurity to influence the growth of $\beta\text{-NaYF}_4\text{:Gd}^{3+}/\text{Tb}^{3+}$ phosphor crystals to attain their multiform morphologies. The results presented here underline the important role that controlled morphological synthesis can play in optimizing the key properties of advanced functional materials and could be extended to other lanthanide-doped nanocrystals. This unique approach paves way to new opportunities for designing and tuning the rare earth phosphor crystals and their unique luminescence properties may render potential applications in the field of color displays, light-emitting diodes, solid-state lasers, and luminescent biological labels.

4. METHODS

4.1. Materials. All the chemicals were of analytical grade and were used without further purification. Yttrium nitrate hexahydrate ($\text{Y}(\text{NO}_3)_3 \cdot 6\text{H}_2\text{O}$, 99.89%), gadolinium nitrate hexahydrate ($\text{Gd}(\text{NO}_3)_3 \cdot 6\text{H}_2\text{O}$, 99.89%), and terbium nitrate hexahydrate ($\text{Tb}(\text{NO}_3)_3 \cdot 6\text{H}_2\text{O}$, 99.89%) were purchased from Sigma-Aldrich Inc. Sodium chloride (NaCl , 99.9%) and potassium permanganate (KMnO_4 , 99.0%) were received from Thomas Baker. Ammonium fluoride (NH_4F , >95%) and sodium nitrate (NaNO_3 , >99%) were received from Merck.

The graphite powder was obtained from Loba Chemie. PEI (with $M_w = 25\,000$ and $M_n = 10\,000$), MWCNT, and COOH-MWCNT were received from Sigma-Aldrich Inc. Deionized (DI) water was used throughout the experiments.

4.2. Synthesis. **4.2.1. Synthesis of GO.** GO was prepared by using the modified Hummers method from the graphite powder.⁷³ Briefly, graphite powder (2 g) and sodium nitrate (1 g) were added to a 250 mL round-bottom flask at 0 °C. Then, 50 mL of concentrated H₂SO₄ was added slowly with stirring below 5 °C. The solution was then stirred for 30 min. KMnO₄ (0.3 g) was then added to the solution below 10 °C. The solution was again stirred for 30 min. Then KMnO₄ (7 g) was added over 1 h below 20 °C. After this, the solution was warmed to 35 ± 3 °C and was stirred for 2 h. Water (90 mL) was then slowly dripped into the paste, causing an increase in temperature to 70 °C. This diluted suspension was stirred at this temperature for 15 min. The mixture was treated with 10 mL of H₂O₂ (30%) and 55 mL of water to quench the reaction. The suspension turned bright yellow, and subsequently, the solution was filtered, resulting in light brown precipitate. The precipitate was then washed with warm solution of 3% HCl (150 mL). It was dried at 40 °C for 24 h in vacuum. The GO stock solution was obtained with a concentration of 4 mg/mL.

4.2.2. Synthesis of GQDs. **4.2.2.1. Synthesis of Carboxylic and Amine Co-Functionalized GQDs (GQDs).** We synthesized GQDs using the previously reported method elsewhere.⁵⁶ To the above prepared stock solution of GO (15 mL), 40 mL of H₂O₂ (30%) and 10 mL of ammonia (25–28%) were added. This mixture was reacted at 80 °C for 24 h with vigorous stirring. The solution was evaporated at 65 °C to remove unreacted H₂O₂, ammonia, and water. Finally, ethanol was used to precipitate and wash the final GQD product. The GQDs obtained by this method had both the functional groups such as carboxylic and amine and were highly stable and dispersible in water.

4.2.2.2. Synthesis of COOH-GQDs. To the prepared GO stock solution (15 mL), 40 mL of H₂O₂ (30%) was added. This mixture was reacted at 80 °C for 24 h with vigorous stirring. The solution was evaporated at 65 °C to remove unreacted H₂O₂ and water. Finally, ethanol was used to precipitate and wash the final COOH-GQDs.

4.2.2.3. Synthesis of NH₂-GQDs. NH₂-GQDs were prepared using the hydrothermal method reported elsewhere.⁷⁴ For NH₂-GQDs, 15 mL of GO stock solution, 15 mL of DI water, and 10 mL of ammonia were added together. The mixture was stirred for 30 min, followed by ultrasonication for another 30 min. The resultant solution was transferred into a 50 mL Teflon-lined autoclave and heated at 150 °C for 6 h by hydrothermal treatment. Next, the solution was cooled down to the room temperature, and NH₂-GQDs were filtered through a 0.22 μm microporous membrane. The filtered solution was heated at 100 °C for another 1 h to remove excess ammonia in the mixture. The obtained solution was stored for further characterization.

4.2.2.4. Synthesis of rGQDs. COOH-GQDs were reduced by using sodium borohydride, following a previously reported method.⁵⁵ Briefly, to the above-prepared (section 2.2.2.2) COOH-GQDs (15 mL), 1 g of NaBH₄ was added. The mixture was allowed to stir at room temperature for 2 h. When the color of the mixture changed from faded to light yellow, HNO₃ was added to terminate the reaction. Finally, pH was tuned to 8. The resultant solution was filtered through a 0.22 μm microporous membrane and stored for further characterization.

4.2.3. Synthesis of Amine-Functionalized β-NaYF₄:Gd³⁺/Tb³⁺. In a typical procedure^{60,75} for the synthesis of β-NaYF₄:15%Gd³⁺/5%Tb³⁺, solutions of Y(NO₃)₃, Gd(NO₃)₃, and Tb(NO₃)₃ (0.2 M) were added in a 10 mL solution of NaCl (0.2 M). The solution was continuously stirred for 30–40 min. Then 20 mL of ethanol was added, followed by the addition of PEI (5 wt %). Then, 0.5 M of NH₄F was added dropwise to the resultant solution. The whole mixture was stirred for 30 min. Finally, the mixture was poured in a Teflon container with 80 mL capacity, and the reaction was set for 24 h hydrothermally at 180 °C.

4.2.4. Synthesis of β-NaYF₄:Gd³⁺/Tb³⁺ Incorporated with GQDs. A similar procedure was followed to synthesize GQDs incorporated β-NaYF₄:Gd³⁺/Tb³⁺ phosphors except that different concentrations of the as-prepared xGQDs (x = 0, 1, 3, 5, and 7 mL) were incorporated in situ in the initial solution reaction system.

4.3. Characterization Techniques. The phase purity and crystallinity of the as-prepared samples were characterized by powder XRD using a PANalytical X'PERT PRO instrument and the iron-filtered Cu Kα radiation (λ = 1.54 Å) in the 2θ range of 10°–80° with a step size of 0.02°. To analyze the shape and size of the samples, FESEM (FESEM: Hitachi S-4200) was used. The specific structural details and morphology were obtained by using a FEI Tecnai T20 transmission electron microscope operated at 200 keV accelerating voltage with Schottky field emitter source with maximum beam current (>100 nA) and small energy spread (0.8 eV or less). The powder samples obtained were dispersed in ethanol and then drop-casted on carbon-coated copper TEM grids with 200 mesh and loaded to a single tilt sample holder. UV–vis spectroscopy measurements were performed on a Jasco UV–vis–NIR (model VS70) dual beam spectrometer operated at a resolution of 2 nm. PL spectra were acquired using a Cary eclipse fluorescence spectrophotometer, equipped with a 400 W Xe lamp as an excitation source and a Hamamatsu R928 photomultiplier tube as a detector. Raman spectra were recorded on an HR-800 Raman spectrophotometer (Jobin Yvon-HORIBA, France) using monochromatic radiation emitted by a He–Ne laser (633 nm), operating at 20 mW and with the accuracy of ±1 cm⁻¹ in the range between 450 and 850 nm, equipped with thermoelectrically cooled (with Peltier junctions), multichannel, spectroscopic grade CCD detector (1024 × 256 pixels of 26 μm) with dark current lower than 0.002 electrons pixel⁻¹ s⁻¹. An objective of 50 XLD magnification was used to both focus and collect the signal from the powder sample dispersed on a glass slide. TGA was done using the SDT model Q600 of TA Instruments Inc. USA at a heating rate of 10 °C/min under nitrogen flow at 100 mL/min. A PALS Zeta Potential Analyzer Ver 3.54 (Brookhaven Instrument Corps.) was used to determine the electrophoretic mobilities. Mobilities were converted to zeta potentials (ζ) using the Smoluchowski model. DI water was used as the dispersion medium.

■ ASSOCIATED CONTENT

Supporting Information

The Supporting Information is available free of charge on the ACS Publications website at DOI: 10.1021/acsomega.7b01947.

XRD and TGA of as-prepared products (PDF)

AUTHOR INFORMATION

Corresponding Author

*E-mail: p.poddar@ncl.res.in. Phone: +91-20-2590-2580. Fax: +91-20-2590-2636 (Pankaj Poddar).

ORCID

Pankaj Poddar: 0000-0002-2273-588X

Notes

The authors declare no competing financial interest.

ACKNOWLEDGMENTS

Pankaj Poddar acknowledges the Centre for Excellence in Surface Science at the CSIR-National Chemical Laboratory and network project Nano-Safety, Health & Environment (SHE) funded by the Council of Scientific and Industrial Research (CSIR), India. M.M. acknowledges the support from the Council of Industrial and Scientific Research (CSIR), India, for providing the Senior Research Fellowship (SRF).

REFERENCES

- Walsh, B. M.; Barnes, N. P.; Petros, M.; Yu, J.; Singh, U. N. Spectroscopy and Modeling of Solid State Lanthanide Lasers: Application to Trivalent Tm^{3+} and Ho^{3+} in $YLiF_4$ and $LuLiF_4$. *J. Appl. Phys.* **2004**, *95*, 3255–3271.
- Zhang, Y.; Chen, B.; Xu, S.; Li, X.; Zhang, J.; Sun, J.; Zheng, H.; Tong, L.; Sui, G.; Zhong, H.; Xia, H.; Hua, R. Dually Functioned Core-Shell $NaYF_4:Er^{3+}/Yb^{3+}@NaYF_4:Tm^{3+}/Yb^{3+}$ Nanoparticles as Nano-Calorifiers and Nano-Thermometers for Advanced Photothermal Therapy. *Sci. Rep.* **2017**, *7*, 11849.
- Jia, H.; Ren, K.; Wang, X.; Li, L. Study on Optical Sensing Composites for Cysteine Detection Using an up-Conversion Excitation Host and Two Rhodamine Derived Chemosensors. *Sens. Actuators, B* **2016**, *228*, 308–316.
- He, M.; Huang, P.; Zhang, C.; Hu, H.; Bao, C.; Gao, G.; He, R.; Cui, D. Dual Phase-Controlled Synthesis of Uniform Lanthanide-Doped $NaGdF_4$ Upconversion Nanocrystals Via an OA/Ionic Liquid Two-Phase System for In Vivo Dual-Modality Imaging. *Adv. Funct. Mater.* **2011**, *21*, 4470–4477.
- Tian, G.; Gu, Z.; Zhou, L.; Yin, W.; Liu, X.; Yan, L.; Jin, S.; Ren, W.; Xing, G.; Li, S.; Zhao, Y. Mn^{2+} Dopant-Controlled Synthesis of $NaYF_4:Yb/Er$ Upconversion Nanoparticles for in Vivo Imaging and Drug Delivery. *Adv. Mater.* **2012**, *24*, 1226–1231.
- Tong, L.; Li, X.; Zhang, J.; Xu, S.; Sun, J.; Zheng, H.; Zhang, Y.; Zhang, X.; Hua, R.; Xia, H.; Chen, B. $NaYF_4:Sm^{3+}/Yb^{3+}@NaYF_4:Er^{3+}/Yb^{3+}$ Core-Shell Structured Nanocalorifier with Optical Temperature Probe. *Opt. Express* **2017**, *25*, 16047.
- Tong, L.; Li, X.; Zhang, J.; Xu, S.; Sun, J.; Cheng, L.; Zheng, H.; Zhang, Y.; Zhang, X.; Hua, R.; Xia, H.; Chen, B. Microwave-Assisted Hydrothermal Synthesis, Temperature Quenching and Laser-Induced Heating Effect of Hexagonal Microplate $\beta-NaYF_4:Er^{3+}/Yb^{3+}$ Microcrystals under 1550 Nm Laser Irradiation. *Sens. Actuators, B* **2017**, *246*, 175–180.
- Li, K.; Liang, S.; Shang, M.; Lian, H.; Lin, J. Photoluminescence and Energy Transfer Properties with $Y+SiO_4$ Substituting $Ba+PO_4$ in $Ba_3Y(PO_4)_3:Ce^{3+}/Tb^{3+}, Tb^{3+}/Eu^{3+}$ Phosphors for W-LEDs. *Inorg. Chem.* **2016**, *55*, 7593–7604.
- Padhye, P.; Sadhu, S.; Malik, M.; Poddar, P. A Broad Spectrum Photon Responsive, Paramagnetic: $\beta-NaGdF_4:Yb^{3+}, Er^{3+}$. Mesoporous Anatase Titania Nanocomposite. *RSC Adv.* **2016**, *6*, 53504–53518.
- Shan, G.-B.; Assaoudi, H.; Demopoulos, G. P. Enhanced Performance of Dye-Sensitized Solar Cells by Utilization of an External, Bifunctional Layer Consisting of Uniform $\beta-NaYF_4:Er^{3+}/Yb^{3+}$ Nanoplatelets. *ACS Appl. Mater. Interfaces* **2011**, *3*, 3239–3243.
- Achatz, D. E.; Ali, R.; Wolfbeis, O. S. Luminescent Chemical Sensing, Biosensing, and Screening Using Upconverting Nanoparticles. *Top. Curr. Chem.* **2010**, *300*, 29–50.
- Resch-Genger, U.; Grabolle, M.; Cavaliere-Jaricot, S.; Nitschke, R.; Nann, T. Quantum Dots versus Organic Dyes as Fluorescent Labels. *Nat. Methods* **2008**, *5*, 763–775.
- Liu, Y.; Tu, D.; Zhu, H.; Ma, E.; Chen, X. Lanthanide-Doped Luminescent Nano-Bioprobes: From Fundamentals to Biodetection. *Nanoscale* **2013**, *5*, 1369–1384.
- Zhou, B.; Shi, B.; Jin, D.; Liu, X. Controlling Upconversion Nanocrystals for Emerging Applications. *Nat. Nanotechnol.* **2015**, *10*, 924–936.
- Haase, M.; Schäfer, H. Upconverting Nanoparticles. *Angew. Chem., Int. Ed.* **2011**, *50*, 5808–5829.
- Ding, M.; Lu, C.; Song, Y.; Ni, Y.; Xu, Z. Hydrothermal Synthesis of Ordered $\beta-NaYF_4$ Nanorod Self-Assemblies with Multicolor up- and down-Conversions. *CrystEngComm* **2014**, *16*, 1163–1173.
- Li, C.; Lin, J. Rare Earth Fluoride Nano-/microcrystals: Synthesis, Surface Modification and Application. *J. Mater. Chem.* **2010**, *20*, 6831.
- Gao, D.; Gao, W.; Shi, P.; Li, L. pH- and Surfactant-Mediated Tunable Morphology and Upconversion of Rare-Earth Doped Fluoride Microcrystals. *RSC Adv.* **2013**, *3*, 14757–14765.
- Liu, D.; Xu, X.; Du, Y.; Qin, X.; Zhang, Y.; Ma, C.; Wen, S.; Ren, W.; Goldys, E. M.; Piper, J. A.; Dou, S.; Liu, X.; Jin, D. Three-Dimensional Controlled Growth of Monodisperse Sub-50 Nm Heterogeneous Nanocrystals. *Nat. Commun.* **2016**, *7*, 10254.
- Wang, C.; Tao, H.; Cheng, L.; Liu, Z. Near-Infrared Light Induced in Vivo Photodynamic Therapy of Cancer Based on Upconversion Nanoparticles. *Biomaterials* **2011**, *32*, 6145–6154.
- Li, C.; Yang, J.; Yang, P.; Lian, H.; Lin, J. Hydrothermal Synthesis of Lanthanide Fluorides LnF_3 ($Ln = La$ to Lu) Nano-/Microcrystals with Multifunctional Structures and Morphologies. *Chem. Mater.* **2008**, *20*, 4317–4326.
- Padhye, P.; Poddar, P. Static and Dynamic Photoluminescence and Photocatalytic Properties of Uniform, Monodispersed Up/down-Converting, Highly Luminescent, Lanthanide-Ion-Doped $\beta-NaYF_4$ Phosphor Microcrystals with Controlled Multifunctional Morphologies. *J. Mater. Chem. A* **2014**, *2*, 19189–19200.
- Qiu, P.; Zhou, N.; Wang, Y.; Zhang, C.; Wang, Q.; Sun, R.; Gao, G.; Cui, D. Tuning Lanthanide Ion-Doped Upconversion Nanocrystals with Different Shapes via a One-Pot Cationic Surfactant-Assisted Hydrothermal Strategy. *CrystEngComm* **2014**, *16*, 1859.
- Sun, Y.; Chen, Y.; Tian, L.; Yu, Y.; Kong, X.; Zhao, J.; Zhang, H. Controlled Synthesis and Morphology Dependent Upconversion Luminescence of $NaYF_4:Yb,Er$ Nanocrystals. *Nanotechnology* **2007**, *18*, 275609.
- Wang, Y.; Gai, S.; Niu, N.; He, F.; Yang, P. Synthesis of $NaYF_4$ Microcrystals with Different Morphologies and Enhanced up-Conversion Luminescence Properties. *Phys. Chem. Chem. Phys.* **2013**, *15*, 16795–16805.
- Qiu, P.; Zhou, N.; Chen, H.; Zhang, C.; Gao, G.; Cui, D. Recent Advances in Lanthanide-Doped Upconversion Nanomaterials: Synthesis, Nanostructures and Surface Modification. *Nanoscale* **2013**, *5*, 11512.
- Wang, F.; Liu, X. Recent Advances in the Chemistry of Lanthanide-Doped Upconversion Nanocrystals. *Chem. Soc. Rev.* **2009**, *38*, 976.
- Dou, Q.; Zhang, Y. Tuning of the Structure and Emission Spectra of Upconversion Nanocrystals by Alkali Ion Doping. *Langmuir* **2011**, *27*, 13236–13241.
- Ding, M.; Chen, D.; Yin, S.; Ji, Z.; Zhong, J.; Ni, Y.; Lu, C.; Xu, Z. Simultaneous Morphology Manipulation and Upconversion Luminescence Enhancement of $\beta-NaYF_4:Yb^{3+}/Er^{3+}$ Microcrystals by Simply Tuning the KF Dosage. *Sci. Rep.* **2015**, *5*, 12745.
- Wang, Y.; Wei, T.; Cheng, X.; Ma, H.; Pan, Y.; Xie, J.; Su, H.; Xie, X.; Huang, L.; Huang, W. Insights into Li^+ -Induced Morphology Evolution and Upconversion Luminescence Enhancement of $KSc_2F_7:Yb/Er$ Nanocrystals. *J. Mater. Chem. C* **2017**, *5*, 3503–3508.
- Xue, X.; Wang, L.; Huang, L.; Zhao, D.; Qin, W. Effect of Alkali Ions on the Formation of Rare Earth Fluoride by Hydrothermal

Synthesis: Structure Tuning and Size Controlling. *CrystEngComm* **2013**, *15*, 2897.

(32) Wu, Y.; Lin, S.; Shao, W.; Zhang, X.; Xu, J.; Yu, L.; Chen, K. Enhanced up-Conversion Luminescence from NaYF₄:Yb,Er Nanocrystals by Gd³⁺ Ions Induced Phase Transformation and Plasmonic Au Nanosphere Arrays. *RSC Adv.* **2016**, *6*, 102869–102874.

(33) Biswas, A.; Salunke, G.; Khandelwal, P.; Das, R.; Poddar, P. Surface Disordered Rutile TiO₂-graphene Quantum Dot Hybrids: A New Multifunctional Material with Superior Photocatalytic and Biofilm Eradication Properties. *New J. Chem.* **2017**, *41*, 2642–2657.

(34) Cha, C.; Shin, S. R.; Annabi, N.; Dokmeci, M. R.; Khademhosseini, A. Carbon-Based Nanomaterials: Multi-Functional Materials for Biomedical Engineering. *ACS Nano* **2013**, *7*, 2891–2897.

(35) Li, Y.; Shu, H.; Niu, X.; Wang, J. Electronic and Optical Properties of Edge-Functionalized Graphene Quantum Dots and the Underlying Mechanism. *J. Phys. Chem. C* **2015**, *119*, 24950–24957.

(36) Roushani, M.; Abdi, Z. Novel Electrochemical Sensor Based on Graphene Quantum Dots/riboflavin Nanocomposite for the Detection of Persulfate. *Sens. Actuators, B* **2014**, *201*, 503–510.

(37) Li, L.-S.; Yan, X. Colloidal Graphene Quantum Dots. *J. Phys. Chem. Lett.* **2010**, *1*, 2572–2576.

(38) Luk, C. M.; Chen, B. L.; Teng, K. S.; Tang, L. B.; Lau, S. P. Optically and Electrically Tunable Graphene Quantum Dot-Polyaniline Composite Films. *J. Mater. Chem. C* **2014**, *2*, 4526–4532.

(39) Chen, L.; Guo, C. X.; Zhang, Q.; Lei, Y.; Xie, J.; Ee, S.; Guai, G.; Song, Q.; Li, C. M. Graphene Quantum-Dot-Doped Polypyrrole Counter Electrode for High-Performance Dye-Sensitized Solar Cells. *ACS Appl. Mater. Interfaces* **2013**, *5*, 2047–2052.

(40) Mihalache, I.; Radoi, A.; Mihaila, M.; Munteanu, C.; Marin, A.; Danila, M.; Kusko, M.; Kusko, C. Charge and Energy Transfer Interplay in Hybrid Sensitized Solar Cells Mediated by Graphene Quantum Dots. *Electrochim. Acta* **2015**, *153*, 306–315.

(41) Tetsuka, H.; Nagoya, A.; Asahi, R. Highly Luminescent Flexible Amino-Functionalized Graphene Quantum Dots@cellulose Nanofiber-Clay Hybrids for White-Light Emitting Diodes. *J. Mater. Chem. C* **2015**, *3*, 3536–3541.

(42) Binnemans, K. Lanthanide-Based Luminescent Hybrid Materials. *Chem. Rev.* **2009**, *109*, 4283–4374.

(43) Wei, W.; He, T.; Teng, X.; Wu, S.; Ma, L.; Zhang, H.; Ma, J.; Yang, Y.; Chen, H.; Han, Y.; Sun, H.; Huang, L. Nanocomposites of Graphene Oxide and Upconversion Rare-Earth Nanocrystals with Superior Optical Limiting Performance. *Small* **2012**, *8*, 2271–2276.

(44) He, T.; Wei, W.; Ma, L.; Chen, R.; Wu, S.; Zhang, H.; Yang, Y.; Ma, J.; Huang, L.; Gurzadyan, G. G.; Sun, H. Mechanism Studies on the Superior Optical Limiting Observed in Graphene Oxide Covalently Functionalized with Upconversion NaYF₄:Yb³⁺/Er³⁺ Nanoparticles. *Small* **2012**, *8*, 2163–2168.

(45) Luoshan, M.; Li, M.; Liu, X.; Guo, K.; Bai, L.; Zhu, Y.; Sun, B.; Zhao, X. Performance Optimization in Dye-Sensitized Solar Cells with β -NaYF₄:Er³⁺/Yb³⁺ and Graphene Multi-Functional Layer Hybrid Composite Photoanodes. *J. Power Sources* **2015**, *287*, 231–236.

(46) Yan, L.; Chang, Y.-N.; Yin, W.; Liu, X.; Xiao, D.; Xing, G.; Zhao, L.; Gu, Z.; Zhao, Y. Biocompatible and Flexible Graphene Oxide/upconversion Nanoparticle Hybrid Film for Optical pH Sensing. *Phys. Chem. Chem. Phys.* **2014**, *16*, 1576–1582.

(47) Li, Y.; Wang, G.; Pan, K.; Jiang, B.; Tian, C.; Zhou, W.; Fu, H. NaYF₄:Er³⁺/Yb³⁺-graphene Composites: Preparation, Upconversion Luminescence, and Application in Dye-Sensitized Solar Cells. *J. Mater. Chem.* **2012**, *22*, 20381.

(48) Liu, W.; Liu, G.; Dong, X.; Wang, J.; Yu, W. Multifunctional MWCNTs-NaGdF₄:Yb³⁺,Er³⁺,Eu³⁺ Hybrid Nanocomposites with Potential Dual-Mode Luminescence, Magnetism and Photothermal Properties. *Phys. Chem. Chem. Phys.* **2015**, *17*, 22659–22667.

(49) Laurenti, M.; Paez-Perez, M.; Algarra, M.; Alonso-Cristobal, P.; Lopez-Cabarcos, E.; Mendez-Gonzalez, D.; Rubio-Retama, J. Enhancement of the Upconversion Emission by Visible-to-Near-Infrared Fluorescent Graphene Quantum Dots for miRNA Detection. *ACS Appl. Mater. Interfaces* **2016**, *8*, 12644–12651.

(50) Wang, L.; Wang, Y.; Xu, T.; Liao, H.; Yao, C.; Liu, Y.; Li, Z.; Chen, Z.; Pan, D.; Sun, L.; Wu, M. Gram-Scale Synthesis of Single-Crystalline Graphene Quantum Dots with Superior Optical Properties. *Nat. Commun.* **2014**, *5*, 5357.

(51) Beams, R.; Cançado, L. G.; Novotny, L. Raman Characterization of Defects and Dopants in Graphene. *J. Phys.: Condens. Matter* **2015**, *27*, 083002.

(52) Kim, S.; Shin, D. H.; Kim, C. O.; Kang, S. S.; Joo, S. S.; Choi, S.-H.; Hwang, S. W.; Sone, C. Size-Dependence of Raman Scattering from Graphene Quantum Dots: Interplay between Shape and Thickness. *Appl. Phys. Lett.* **2013**, *102*, 053108.

(53) Yang, D.; Li, G.; Kang, X.; Cheng, Z.; Ma, P.; Peng, C.; Lian, H.; Li, C.; Lin, J. Room Temperature Synthesis of Hydrophilic Ln³⁺-Doped KGdF₄ (Ln = Ce, Eu, Tb, Dy) Nanoparticles with Controllable Size: Energy Transfer, Size-Dependent and Color-Tunable Luminescence Properties. *Nanoscale* **2012**, *4*, 3450.

(54) Zeng, S.; Ren, G.; Xu, C.; Yang, Q. High Uniformity and Monodispersity of Sodium Rare-Earth Fluoride Nanocrystals: Controllable Synthesis, Shape Evolution and Optical Properties. *CrystEngComm* **2011**, *13*, 1384–1390.

(55) Li, L.-L.; Ji, J.; Fei, R.; Wang, C.-Z.; Lu, Q.; Zhang, J.-R.; Jiang, L.-P.; Zhu, J.-J. A Facile Microwave Avenue to Electrochemiluminescent Two-Color Graphene Quantum Dots. *Adv. Funct. Mater.* **2012**, *22*, 2971–2979.

(56) Jiang, F.; Chen, D.; Li, R.; Wang, Y.; Zhang, G.; Li, S.; Zheng, J.; Huang, N.; Gu, Y.; Wang, C.; Shu, C. Eco-Friendly Synthesis of Size-Controllable Amine-Functionalized Graphene Quantum Dots with Antimycoplasma Properties. *Nanoscale* **2013**, *5*, 1137.

(57) Mai, H.-X.; Zhang, Y.-W.; Si, R.; Yan, Z.-G.; Sun, L.-d.; You, L.-P.; Yan, C.-H. High-Quality Sodium Rare-Earth Fluoride Nanocrystals: Controlled Synthesis and Optical Properties. *J. Am. Chem. Soc.* **2006**, *128*, 6426–6436.

(58) Bagri, A.; Mattevi, C.; Acik, M.; Chabal, Y. J.; Chhowalla, M.; Shenoy, V. B. Structural Evolution during the Reduction of Chemically Derived Graphene Oxide. *Nat. Chem.* **2010**, *2*, 581–587.

(59) Zhang, W.; Liu, Y.; Meng, X.; Ding, T.; Xu, Y.; Xu, H.; Ren, Y.; Liu, B.; Huang, J.; Yang, J.; Fang, X. Graphene Defects Induced Blue Emission Enhancement in Chemically Reduced Graphene Quantum Dots. *Phys. Chem. Chem. Phys.* **2015**, *17*, 22361–22366.

(60) Padhye, P.; Alam, A.; Ghorai, S.; Chattopadhyay, S.; Poddar, P. Doxorubicin-Conjugated β -NaYF₄:Gd³⁺/Tb³⁺ Multifunctional, Phosphor Nanorods: A Multi-Modal, Luminescent, Magnetic Probe for Simultaneous Optical and Magnetic Resonance Imaging and an Excellent pH-Triggered Anti-Cancer Drug Delivery Nanovehicle. *Nanoscale* **2015**, *7*, 19501–19518.

(61) Raju, G. S. R.; Pavitra, E.; Yu, J. S. Pechini Synthesis of Lanthanide (Eu³⁺/Tb³⁺ or Dy³⁺) Ions Activated BaGd₂O₄ Nanostructured Phosphors: An Approach for Tunable Emissions. *Phys. Chem. Chem. Phys.* **2014**, *16*, 18124.

(62) Ricci, P. C.; Carbonaro, C. M.; Corpino, R.; Cannas, C.; Salis, M. Optical and Structural Characterization of Terbium-Doped Y₂SiO₅ Phosphor Particles. *J. Phys. Chem. C* **2011**, *115*, 16630–16636.

(63) Kundu, S.; Kar, A.; Patra, A. Morphology Dependent Luminescence Properties of Rare-Earth Doped Lanthanum Fluoride Hierarchical Microstructures. *J. Lumin.* **2012**, *132*, 1400–1406.

(64) Zhang, M.; Fan, H.; Xi, B.; Wang, X.; Dong, C.; Qian, Y. Synthesis, Characterization, and Luminescence Properties of Uniform Ln³⁺-Doped YF₃ Nanospindles. *J. Phys. Chem. C* **2007**, *111*, 6652.

(65) Zhu, L.; Li, Q.; Liu, X.; Li, J.; Zhang, Y.; Meng, J.; Cao, X. Morphological Control and Luminescent Properties of CeF₃ Nanocrystals. *J. Phys. Chem. C* **2007**, *111*, 5898–5903.

(66) Shan, J.; Uddi, M.; Wei, R.; Yao, N.; Ju, Y. The Hidden Effects of Particle Shape and Criteria for Evaluating the Upconversion Luminescence of the Lanthanides Doped Nanophosphors. *J. Phys. Chem. C* **2010**, *114*, 2452–2461.

(67) Sajanlal, P. R.; Sreeprasad, T. S.; Samal, A. K.; Pradeep, T. Anisotropic Nanomaterials: Structure, Growth, Assembly, and Functions. *Nano Rev.* **2011**, *2*, 5883.

(68) Zeng, S.; Ren, G.; Xu, C.; Yang, Q. Modifying Crystal Phase, Shape, Size, Optical and Magnetic Properties of Monodispersed Multifunctional NaYbF₄ Nanocrystals through Lanthanide Doping. *CrystEngComm* **2011**, *13*, 4276–4281.

(69) Yang, J.; Li, C.; Cheng, Z.; Zhang, X.; Quan, Z.; Zhang, C.; Lin, J. Size-Tailored Synthesis and Luminescent Properties of One-Dimensional Gd₂O₃:Eu³⁺ Nanorods and Microrods. *J. Phys. Chem. C* **2007**, *111*, 18148–18154.

(70) Ma, D.-K.; Huang, S.-M.; Yu, Y.-Y.; Xu, Y.-F.; Dong, Y.-Q. Rare-Earth-Ion-Doped Hexagonal-Phase NaYF₄ Nanowires: Controlled Synthesis and Luminescent Properties. *J. Phys. Chem. C* **2009**, *113*, 8136.

(71) Wang, Y.; Cai, R.; Liu, Z. Controlled Synthesis of NaYF₄:Yb, Er Nanocrystals with Upconversion Fluorescence via a Facile Hydrothermal Procedure in Aqueous Solution. *CrystEngComm* **2011**, *13*, 1772.

(72) Nadort, A.; Zhao, J.; Goldys, E. M. Lanthanide Upconversion Luminescence at the Nanoscale: Fundamentals and Optical Properties. *Nanoscale* **2016**, *8*, 13099–13130.

(73) Wang, K.; Ruan, J.; Song, H.; Zhang, J.; Wo, Y.; Guo, S.; Cui, D. Biocompatibility of Graphene Oxide. *Nanoscale Res. Lett.* **2011**, *6*, 8.

(74) Kumar, G. S.; Roy, R.; Sen, D.; Ghorai, U. K.; Thapa, R.; Mazumder, N.; Saha, S.; Chattopadhyay, K. K. Amino-Functionalized Graphene Quantum Dots: Origin of Tunable Heterogeneous Photoluminescence. *Nanoscale* **2014**, *6*, 3384.

(75) Wang, F.; Chatterjee, D. K.; Li, Z.; Zhang, Y.; Fan, X.; Wang, M. Synthesis of polyethylenimine/NaYF₄ Nanoparticles with Upconversion Fluorescence. *Nanotechnology* **2006**, *17*, 5786–5791.

Downconversion Luminescence-Based Nanosensor for Label-Free Detection of Explosives

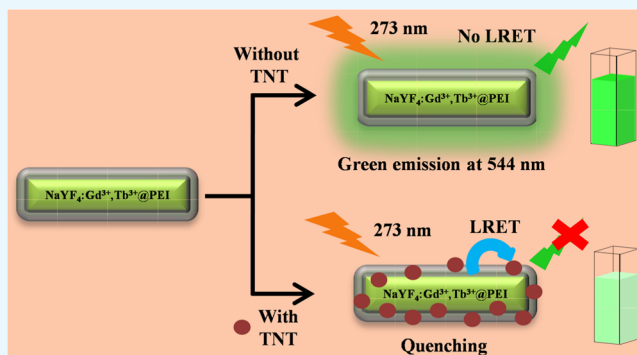
Monika Malik,^{†,‡} Preeti Padhye,^{†,‡} and Pankaj Poddar^{*,†,‡,§}

[†]Physical & Materials Chemistry Division, CSIR-National Chemical Laboratory, Pune 411008, India

[‡]Academy of Scientific and Innovative Research (AcSIR), Anusandhan Bhawan, 2, Rafi Marg, New Delhi 110001, India

Supporting Information

ABSTRACT: We report a selective and sensitive nanosensor probe based on polyethylenimine (PEI)-capped downconverting nanophosphors $\beta\text{-NaYF}_4\text{:Gd}^{3+},\text{Tb}^{3+}\text{@PEI}$ for the detection of 2,4,6-trinitrotoluene (TNT), both in water and buffer media. These downconverting phosphors were synthesized via a hydrothermal route and are known to show excellent chemical, thermal, and photostability. They emit sharp emission peaks centered at ~ 488 , 544, 584, and 619 nm, among which the peak at ~ 544 nm was remarkably quenched ($\sim 90\%$) by the addition of TNT without giving any new emission peak. The sensing mechanism is based on the formation of a Meisenheimer complex between the electron-rich amine-functionalized $\beta\text{-NaYF}_4\text{:Gd}^{3+},\text{Tb}^{3+}$ nanophosphors and electron-deficient TNT molecule, which was prominently visualized by the change in the color of the solution from whitish to brownish yellow, enabling visual detection, followed by luminescence resonance energy transfer between the nanophosphors and the complex. A linear range for TNT detection was obtained from 0.1 to 300 μM with a limit of detection as low as 119.9 nM. This method displayed excellent selectivity toward TNT over other nitroaromatic compounds, which had no influence on the detection. Moreover, various other classes of analytes, viz., amino acids, pesticides, and sugars, did not quench the luminescence intensity of the nanophosphors. This developed nanosensor probe possesses high, stable fluorescence brightness and capability for the selective and sensitive on-site recognition of TNT molecules in aqueous media, avoiding complicated strategies and instruments. Thus, this work promises to pave ways to many applications in the detection of ultratrace analytes.



1. INTRODUCTION

The riveting optical features of lanthanide ions such as narrow and sharp emission bandwidth, large Stokes and anti-Stokes shift, tunable emission spectra, long-lived emission generally in milliseconds, low autofluorescence, and reduced blinking arise from their electronic transitions within the 4f orbitals, hence giving them an edge over conventional fluorophores and quantum dots.¹ Having these advantages, recently, rare earth ion-doped phosphors have been emerging as a potential material in various applications such as solid-state lasers,² light-emitting devices,³ solar cells,⁴ sensing,⁵ cell imaging,⁶ drug delivery,^{7,8} and so forth. One of the most propitious applications of these luminescent phosphors is their use as the optical probes for the identification of molecules such as glutathione,⁹ glucose,¹⁰ avidin,¹¹ and ions such as cyanide,¹² mercury,¹³ and so forth for the sensing applications. Profound efforts have been devoted to the development of novel, innovative, and implicit sensors. Thus, these lanthanide ion-doped phosphors can be applied to the highly selective and sensitive real-time and on-site detection of the explosives.

Identification and quantification of explosives has constituted an emerging and important topic of interest. Reliable detection of trace amount of explosive substances is of critical

importance concerning homeland security threats, military applications, mine-field analysis, forensic investigations, and so forth. Moreover, these compounds are known to have toxicity, carcinogenicity, mutagenicity, and their release into the environment from military sites and ammunition plants causes the contamination of water and soil.¹⁴ Because of the risk associated with the environment, human and wildlife, the detection has gained increasing attention. The detection could help in reducing the fatalities among the civilians and health risk hazards.

The chemical structures of the commonly used nitro-compounds are shown in the Supporting Information in Figure S1. In recent years, a variety of analytical techniques and detection methods of explosives have been developed including gas chromatography,¹⁵ ion mobility spectrometry,¹⁶ surface-enhanced Raman spectroscopy,^{17,18} conductivity-based techniques,¹⁹ and so forth. However, these methods are usually limited by several intrinsic shortcomings; some require complicated instrumentation or synthetic processes, whereas

Received: December 13, 2018

Accepted: February 12, 2019

Published: February 26, 2019

others require labeling procedures, which are typically time-consuming, expensive, and require specialized personnel. Thence, to meet this need, the fluorescence quenching approach has been explored for the analysis of nitro-based explosives. Fluorescence-based sensing methods have gained immense attention because of the relatively lower operational costs than the conventional methods, simplicity, higher sensitivities, portability, short response times, and its pertinence in both solution and the solid phase. Various nanomaterials were used to develop a fluorescence-sensing platform for explosive sensing.^{20–23} Although these various nanostructured materials are reported to construct a fluorescent probe for the selective detection of the explosives, there is still a challenge to utilize them as sensors because they possess low chemical and thermal stability, poor aqueous solubility, require time-consuming synthetic methods, are receptive toward photobleaching, and thus are insufficient for the detection of analytes in aqueous samples. Therefore, other classes of compounds based on the lanthanide ions have garnered attention for sensing applications in the past few years.

Because of good chemical, thermal, and photostability, the lanthanide ion-doped phosphors are highly desirable as sensors.²⁴ Moreover, long-lived luminescence of lanthanide ions could allow them to be potentially used for analyte detection in strongly autofluorescent biological matrices. These have been used in sensing of various hazardous analytes of environmental and clinical importance.^{25–27} These phosphors have also been employed for sensing explosives via fluorescence-based detection up to a level of nanomolar concentration. In 2014, Ma and Wang reported label-free detection of 2,4,6-trinitrotoluene (TNT) using upconverting nanoparticles (NPs) $\text{NaYF}_4:\text{Yb}^{3+},\text{Er}^{3+}$ at pH = 12 with a detection limit of 9.7 ng/mL.²⁸ In the same year, a miniaturized device was fabricated using $\text{NaYF}_4:\text{Yb}^{3+},\text{Er}^{3+}@$ PEI, which detected the TNT explosive by the formation of the Meisenheimer complex and quenched the green luminescence.²⁹ Although the mentioned methods utilize the selectivity of these materials over other analogous analytes, they involved multistep and time-consuming synthetic processes. Also, these sensors worked in the high pH range (12 and above), thus limiting their applicability as sensors. Nevertheless, $\beta\text{-NaYF}_4:\text{Gd}^{3+},\text{Tb}^{3+}$ downconverting nanophosphors, being highly luminescent, have rarely been explored for their potentiality as a fluorescent probe for the selective and sensitive detection of explosives.

In this contribution, we have developed a label-free method for the selective detection of TNT, in the aqueous solution of nitrocompounds, characteristic to explosives based on the green-emitting phosphors. These lanthanide ion-doped phosphors are functionalized with amine groups (NH_2) using PEI via a hydrothermal route. The detection is based on photoluminescence (PL) method by observing the change in intensity at 544 nm of the green light which was selectively and dramatically quenched via luminescence resonance energy transfer (LRET)-based energy transfer from nanophosphors to the Meisenheimer complex, detailed mechanism of which is explained. Meanwhile, the intensity was not influenced by the addition of other nitrocompounds in the aqueous solution. Furthermore, no drastic change in intensity was observed with other category of analytes such as amino acids, pesticides, and sugars. The current developed sensing probe is also applicable in a wide pH range from 7 to 13. Combined with good water

and chemical stability, photostability and wide pH adaptability will facilitate the application of this system as a potential nanosensor probe.

2. RESULTS AND DISCUSSION

The composition, crystallinity, and phase purity of the NaYF_4 nanophosphors were first checked by powder XRD as shown in Figure 1. The sample diffraction peaks can be indexed to

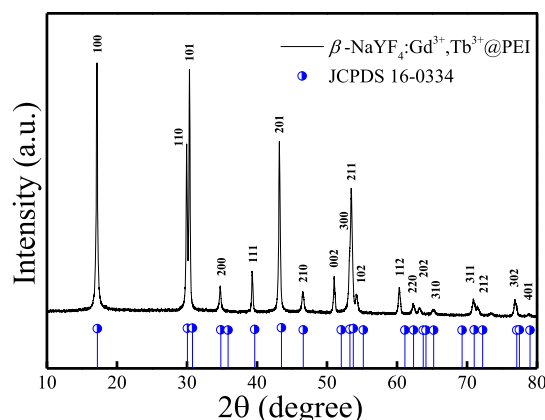


Figure 1. XRD pattern of as-prepared $\beta\text{-NaYF}_4:\text{Gd}^{3+},\text{Tb}^{3+}@$ PEI. The data have been compared with standard data of hexagonal NaYF_4 , JCPDS 16-0334 as the reference.

NaYF_4 with lattice parameters as $a = 5.9 \text{ \AA}$, and $c = 3.5 \text{ \AA}$, that is in good agreement with standard JCPDS data (JCPDS no. 16-0334), confirming the hexagonal phase of the as-synthesized product. The detailed structure analysis was carried out with the Rietveld refinement method using the general structure analysis system, GSAS–EXPGUI suit of programs.³⁰ The refinement proceeded smoothly with the Na1.SY1.5F6 model (ICSD collection code no. 51917) and the corresponding profile is displayed in the Supporting Information in Figure S2. The lattice parameters and reliability factors are summarized in Table S1. The background was fitted well with a shifted Chebyshev function and all the parameters including unit cell parameters, occupancy, Gaussian–Lorentzian factors were refined. The transmission electron microscopy (TEM) and field emission scanning electron microscopy (FESEM) images (Figure 2a,b) show that the $\beta\text{-NaYF}_4:\text{Gd}^{3+},\text{Tb}^{3+}@$ PEI particles prepared at 180 °C are grown in rod-shaped particles and exhibit uniform shapes and are monodispersed with an average diameter of $\sim 92 \text{ nm}$ and length of $\sim 280 \text{ nm}$. The contrast in the TEM image observed was due to the different orientation of the crystalline nanoparticles with respect to the electron beam, which changed the elastic scattering diffraction and thus appeared in different contrast. Further, the chemical composition of the $\beta\text{-NaYF}_4:\text{Gd}^{3+},\text{Tb}^{3+}$ nanophosphors was characterized by energy-dispersive X-ray analysis (EDXA) where all the elements in the nanophosphors could be detected including doped Gd^{3+} and Tb^{3+} ions, confirming the presence of the lanthanide ions (Figure S3). Furthermore, the detailed structure analysis was done through high-resolution TEM (HRTEM) analysis explained in Figure S4a, which shows the HRTEM image of the pristine sample, which was subsequently analyzed by a combination of fast Fourier transform (FFT) followed by inverse FFT (IFFT) image to check crystal lattice periodicity. Figure S4b shows the IFFT image of the selected

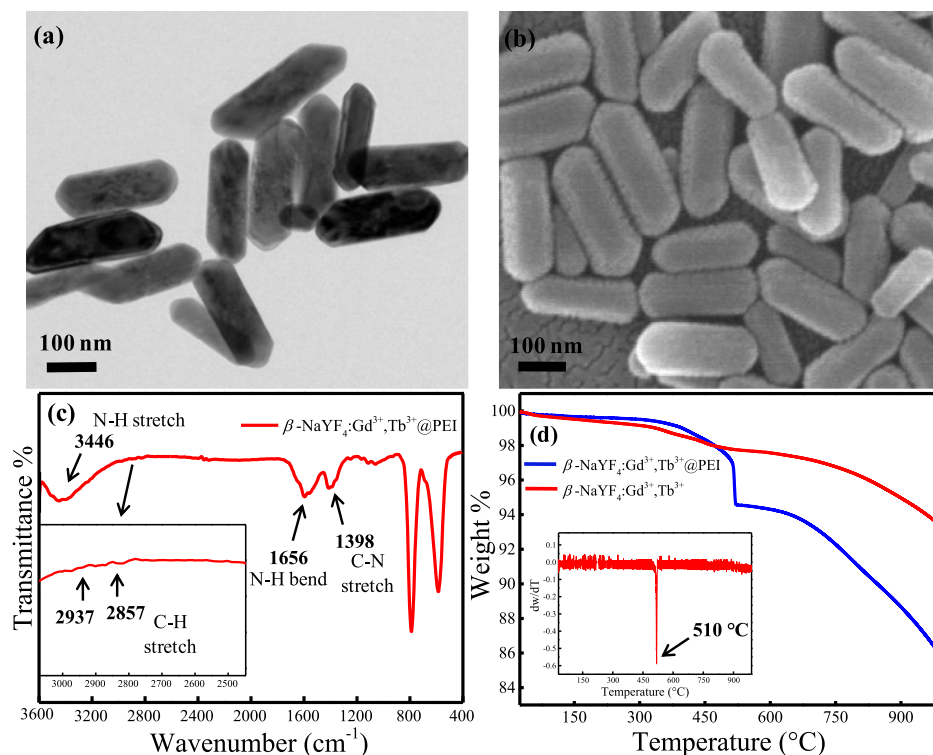


Figure 2. (a) TEM and (b) FESEM images showing the morphology of the β - $\text{NaYF}_4:\text{Gd}^{3+}, \text{Tb}^{3+}@\text{PEI}$ phosphor nanoparticles, which are monodispersed in nature, (c) FTIR spectra indicating the capping of PEI on the surface of the rods. Inset: Zoomed view in the range of $3000\text{--}2500\text{ cm}^{-1}$, (d) TGA results confirming the presence of PEI on the terminus. The decomposition temperature obtained for branched PEI when coated on the surface is $\sim 510\text{ }^\circ\text{C}$, as shown in the derivative curve of TGA in the inset. Bare β - $\text{NaYF}_4:\text{Gd}^{3+}, \text{Tb}^{3+}$ phosphors without the capping of PEI, showed no weight loss at this temperature.

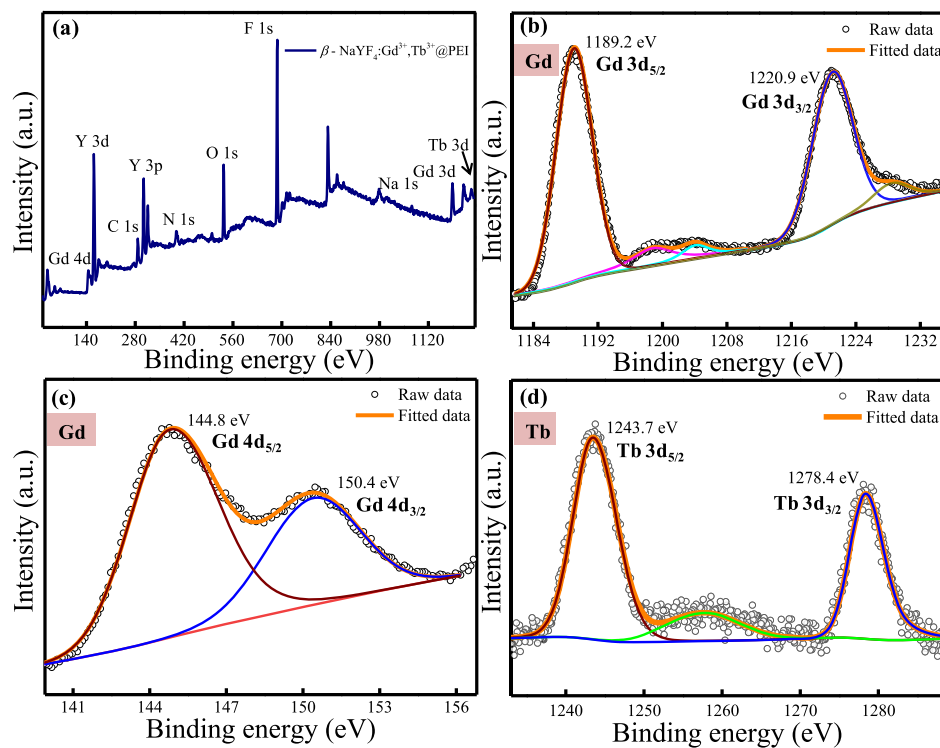


Figure 3. (a) XPS survey spectra of as-synthesized β - $\text{NaYF}_4:\text{Gd}^{3+}, \text{Tb}^{3+}@\text{PEI}$ and high-resolution spectra of (b) Gd 3d, (c) Gd 4d, and (d) Tb 3d showing the binding energy of the core levels.

region (marked as the red square) in the HRTEM image, which was constructed after the masking of the (110) plane

using the Digital Micrograph software as shown in the FFT image in the inset. The IFFT image clearly shows the presence

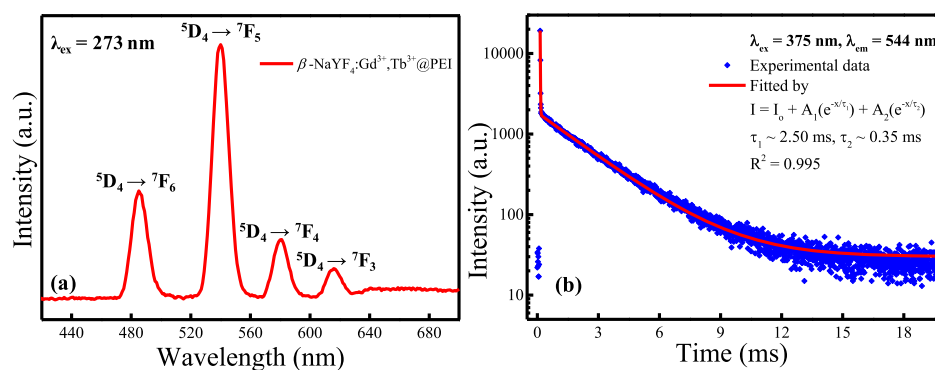


Figure 4. (a) PL emission spectra of PEI-capped β - $\text{NaYF}_4:\text{Gd}^{3+}, \text{Tb}^{3+}$ at an excitation wavelength of 273 nm yielding emission in the visible region corresponding to the Tb^{3+} ion transitions, (b) luminescence decay kinetics behavior for the emission of the 5% Tb^{3+} ion corresponding to transition ${}^5\text{D}_4 \rightarrow {}^7\text{F}_5$ at 544 nm in the hexagonal NaYF_4 lattice under excitation of 375 nm.

of an array of ordered planes whose interplanar spacing was measured from the line profile and was 0.30 nm, corresponding to the (110) plane of the hexagonal NaYF_4 lattice. The SAED pattern shown in Figure S4d revealed the crystalline nature of β - $\text{NaYF}_4:\text{Gd}^{3+}, \text{Tb}^{3+}@\text{PEI}$ NPs. The diffraction pattern obtained matched well with the crystal planes of hexagonal NaYF_4 and have been assigned to the (110), (101), and (111) planes. Thus, d -spacing calculated in HRTEM and SAED are in agreement with those given in the standard JCPDS data no. 16-0334, confirming the hexagonal phase of the as-prepared samples.

The functionalization of PEI was investigated by zeta potential of β - $\text{NaYF}_4:\text{Gd}^{3+}, \text{Tb}^{3+}@\text{PEI}$ NPs, which was +43 mV, suggesting the successful capping of PEI on the surface, rendering the rods to be positively charged. The presence of amino groups on the surface of rods was further verified by Fourier transform infrared (FTIR) spectroscopy (Figure 2c). The β - $\text{NaYF}_4:\text{Gd}^{3+}, \text{Tb}^{3+}@\text{PEI}$ nanophosphors exhibited an absorption band at 3446 cm^{-1} because of typical N–H stretching vibration of the amino groups, which overlaps with the O–H stretching band and its presence is supported by the peak ascribed to the bending mode of amino groups ($-\text{NH}_2$) at 1656 cm^{-1} , thus revealing the abundance of electron-rich amino groups on the terminal of the rods.⁷ Moreover, the absorption band at 1398 cm^{-1} is attributed to the stretching vibrations of the C–N bond, whereas the bands at 2857 and 2937 cm^{-1} are attributed to the methylene symmetric and asymmetric C–H stretching vibrations as shown in inset of Figure 2c. The PEI capping is further confirmed by thermo gravimetric analysis (TGA) results, which were carried out in nitrogen atmosphere at a heating rate of $10 \text{ }^\circ\text{C}/\text{min}$. As shown in Figure 2d, the initial weight loss of 5.5% occurred in the temperature range $300\text{--}550 \text{ }^\circ\text{C}$ due to the degradation of bound PEI present in the system and no further loss was observed till $650 \text{ }^\circ\text{C}$, confirming the stability of the fluorides. The inset shows the first derivative of the TGA curve, confirming the presence of PEI in the system and degradation at $510 \text{ }^\circ\text{C}$. The TGA spectra were recorded for bare β - $\text{NaYF}_4:\text{Gd}^{3+}, \text{Tb}^{3+}$ nanophosphors, which showed a slight weight loss of 2.1 wt % in the $300\text{--}550 \text{ }^\circ\text{C}$ temperature range. It is believed that the decomposition temperature of branched PEI is situated at around $400 \text{ }^\circ\text{C}$ in nitrogen atmosphere,³¹ which can be verified in the TGA results shown in Figure S5. The observed increase in the decomposition temperature of PEI in the β - $\text{NaYF}_4:\text{Gd}^{3+}, \text{Tb}^{3+}@\text{PEI}$ as compared to free PEI is attributed to the fact that the capping

agent is protected from degradation because of its binding to the rods.³² This confirms that the PEI is indeed bound to the nanorods.

The composition and chemical state of the β - $\text{NaYF}_4:\text{Gd}^{3+}, \text{Tb}^{3+}@\text{PEI}$ were ascertained by X-ray photoelectron spectroscopy (XPS) measurements. As shown in Figure 3a, the survey scan spectrum confirmed the presence of Na, Y, F, C, N, and lanthanides (Gd, Tb) in the material. It should be mentioned here that the presence of C 1s and N 1s in the spectrum was due to the capping of the PEI on the surface. The high-resolution peak analyses of Gd 3d and 4d core level spectra revealed that these energy levels are split into doublet because of spin-orbit coupling (Figure 3b,c). The energy levels $3d_{5/2}$ and $3d_{3/2}$ appeared at 1189.2 and 1220.9 eV, respectively, with spin-orbit splitting of 31.9 eV, whereas the peaks at 144.8 and 150.4 eV can be assigned to the binding energy of levels $4d_{5/2}$ and $4d_{3/2}$, respectively. The presence of Gd 3d and 4d peaks showed that the Gd ion exists as Gd^{3+} in the crystal lattice of hexagonal NaYF_4 . As shown in Figure 3d, the energy level of Tb 3d also split into doublet corresponding to $3d_{5/2}$ and $3d_{3/2}$ at 1243.7 and 1278.4 eV, respectively. Also, a satellite appeared between the two main peaks. These results suggested that the Tb ion substituted Y ion in NaYF_4 appeared in only one oxidation state, i.e., +3. The magnified XPS spectra of other elements such as Na, Y, and F in β - $\text{NaYF}_4:\text{Gd}^{3+}, \text{Tb}^{3+}@\text{PEI}$ is shown in Figure S6, displaying the energy levels; Na 1s, Y 3d, and F 1s core levels. The surface functionalization of the downconverting nanorods conducted by XPS was in accordance with the FTIR results. The presence of these functional hydrophilic groups improved the water dispersibility and stability of the nanorods. To explore the local structure of β - $\text{NaYF}_4:\text{Gd}^{3+}, \text{Tb}^{3+}$ crystals, Raman spectroscopy was recorded to analyze the vibrational properties of the sample under the laser 325 nm (Figure S7). The Raman spectra of β - $\text{NaYF}_4:\text{Gd}^{3+}, \text{Tb}^{3+}$ crystals revealed the strongest phonon bands at 308, 367, 416 cm^{-1} , which are in fair agreement with reported data of the NaYF_4 lattice.³³ These bands are attributed to the host lattice vibrations of Y–F and Na–F distances and bond strength features.

The optical emission spectra of β - $\text{NaYF}_4:\text{Gd}^{3+}, \text{Tb}^{3+}@\text{PEI}$ are displayed in Figure 4a, where the photon emission originates from the transition within the 4f electronic transitions of Tb^{3+} ions. The emission spectra of Tb^{3+} ions can be obtained at the excitation wavelength, $\lambda_{\text{ex}} = 375 \text{ nm}$.³⁴ The efficient emission is difficult to realize in the system containing Tb ions under direct excitation at 375 nm due to

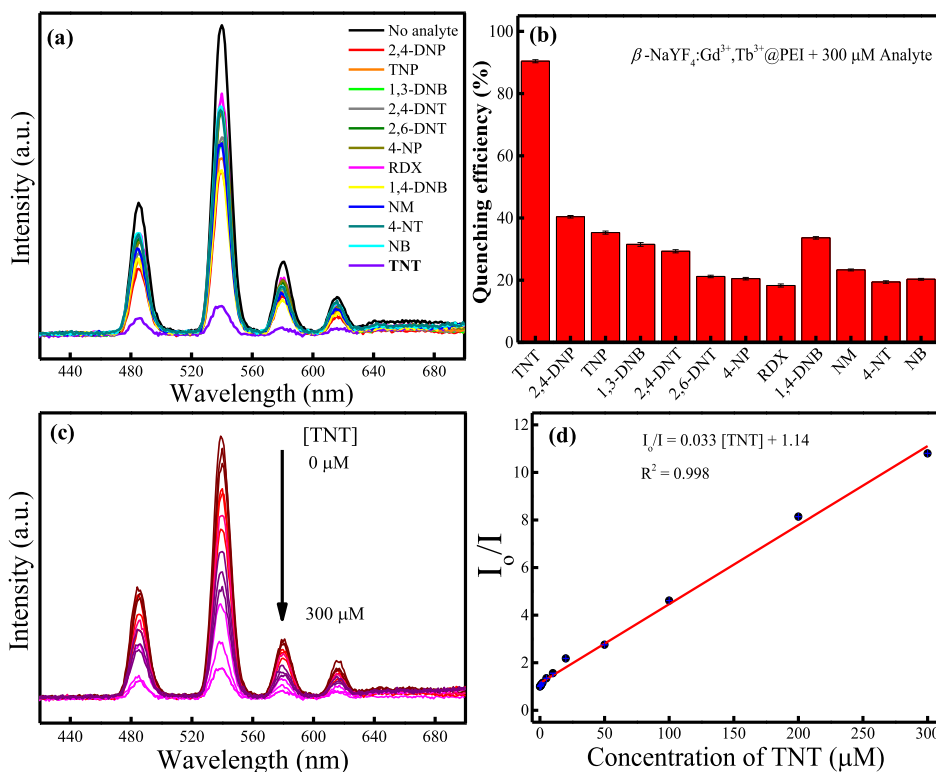


Figure 5. (a) Emission spectra and (b) quenching efficiency of the samples containing β -NaYF₄:Gd³⁺,Tb³⁺@PEI and different nitrocompounds (300 μ M) in aqueous solution, (c) emission spectra of β -NaYF₄:Gd³⁺,Tb³⁺@PEI containing different concentrations of TNT (0–300 μ M) in aqueous solution, (d) fitting graph of the linear S–V plot for TNT by equation; $I_0/I - 1 = K_{sv}[Q]$, where K_{sv} is quenching constant and found out to be $3.32 \times 10^4 \text{ M}^{-1}$. The error bar is calculated from three parallel samples.

intraconfigurational parity-forbidden transitions. Hence, Gd³⁺ ions act as a sensitizer (i.e., light-harvesting antenna) to enhance the luminescence of Tb³⁺ ions.⁷ As Gd³⁺ ions exhibit a strong absorption band at 273 nm because of their $^8S_{7/2} \rightarrow ^6I_{11/2}$ transition corresponding to f–f transitions, nanophosphors containing Gd³⁺, Tb³⁺ ions together exhibit a very intense excitation band at 273 nm followed by a nonradiative (nr) energy transfer to Tb³⁺ ions. The emission peak of Gd³⁺ is observed at 311 nm in the UV region, which is assigned to the $^6P_{7/2} \rightarrow ^8S_{7/2}$ transition under 273 nm irradiation.³⁵ Additionally, the obtained emission spectra excited at $\lambda_{ex} = 273 \text{ nm}$ (Figure 4a) yielded emissions from Tb³⁺ ions in the range of 480–680 nm. Four prominent emission peaks centered at ~488, ~544, ~584, and ~619 nm originate from the transitions of $^5D_4 \rightarrow ^7F_6$, $^5D_4 \rightarrow ^7F_5$, $^5D_4 \rightarrow ^7F_4$, and $^5D_4 \rightarrow ^7F_3$, respectively. It is clear that among the above mentioned transitions, the green emission $^5D_4 \rightarrow ^7F_5$ at ~544 nm is the most intense emission. The PL decay curve for the luminescence of Tb³⁺ in β -NaYF₄:Gd³⁺,Tb³⁺@PEI nanorods is shown in Figure 4b. Here, we displayed the PL decay curve fitted over first 20 ms with biexponential decay functions because of the variation in decay rates of Tb³⁺ ions in the nanoparticles. This emissive biexponential decay is ascribed to the inhomogeneous distribution of Tb ions close to the surface, giving the short lifetime, and inside the nanoparticles with a long lifetime.³⁶ The curve was well fitted by decay equation: $I = I_0 + A_1(e^{-x/\tau_1}) + A_2(e^{-x/\tau_2})$, where I and I_0 are the intensities at times x and 0, respectively, A_1 and A_2 are constants, τ_1 and τ_2 are the decay times for the two exponential components, which were 0.35 and 2.50 ms for $^5D_4 \rightarrow ^7F_5$ electronic transition of Tb³⁺ under excitation at 375 nm. The

average lifetime of these nanophosphors is in milliseconds, indicating the usability of these phosphors in biological applications also where the autofluorescence and background fluorescence can be suppressed offering high signal to noise ratio.³⁷

2.1. Detection of Explosives. Nitro group-based compounds, 1,3-dinitrobenzene (1,3-DNB), 2,4-dinitrophenol (2,4-DNP), 2,4,6-trinitrophenol (TNP), 2,4-dinitrotoluene (2,4-DNT), 2,6-dinitrotoluene (2,6-DNT), TNT, 1,3,5-trinitro-1,3,5-triazinane (RDX), 4-nitrophenol (4-NP), 1,4-dinitrobenzene (1,4-DNB), nitromethane (NM), 4-nitrotoluene (4-NT), and nitrobenzene (NB) were used in this experiment. The designed principle of detection is based on the interaction of the amine groups on the surface of the nanoparticles with the electron-deficient nitrocompounds. For comparison, the PL intensity of nanophosphors was detected in deionized water at ~544 nm. Equal amounts of analytes were taken in a cuvette for the measurements as discussed in the synthesis section and compared against the PL intensity in the deionized water. It is interesting to note that among these explosive samples (Figure 5a), only TNT could quench the PL intensity of the nanophosphors. Figure 5b presents the quenching profile for all the analytes for the emission at 544 nm. One can see in the figure that the quenching efficiency for 300 μ M TNT is about 90%, whereas all other analytes contributed little changes in the luminescence intensity. On the basis of the results mentioned, TNT was recognized as a detection target owing to its ability to quench the luminescence dramatically, suggesting the high sensitivity of the sensing probe. As a result of the significant quenching, we next studied the quenching phenomenon with varied concentrations of TNT

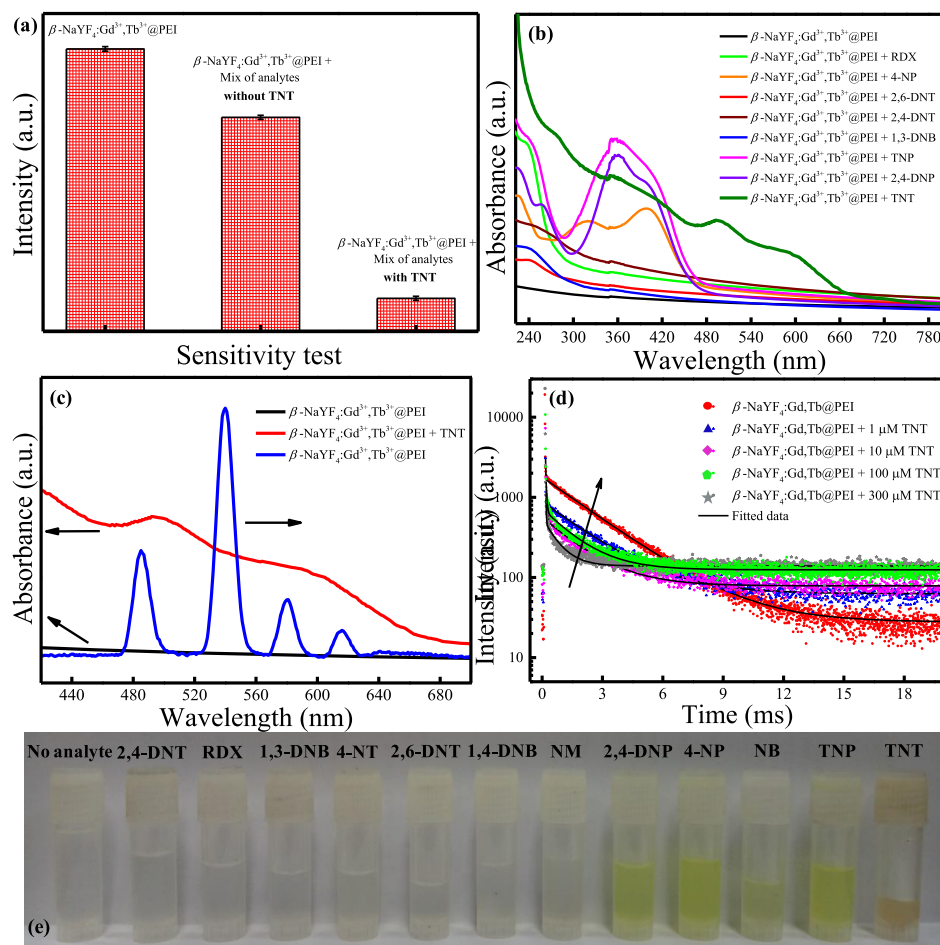
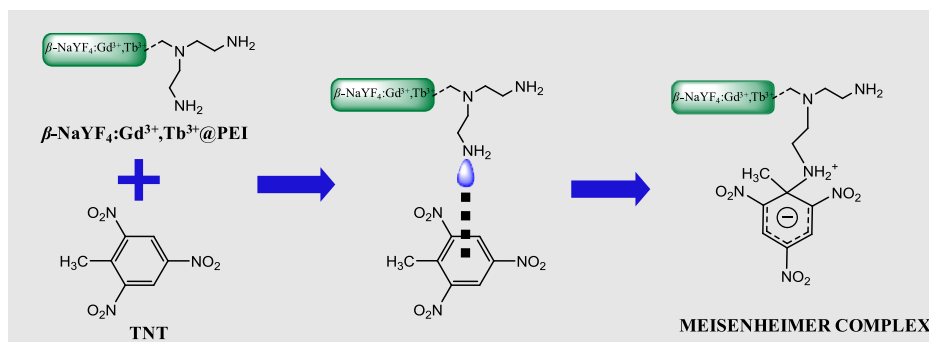


Figure 6. (a) Histogram demonstrating the sensitivity of the phosphors over other analogous compounds of TNT, (b) UV–visible absorbance spectra of all the nitrocompounds in the presence of β -NaYF₄:Gd³⁺,Tb³⁺@PEI in aqueous medium. The Meisenheimer complex formed between TNT- and PEI-capped phosphors shows the broad absorbance in the visible range till 650 nm, (c) spectral overlap of emission spectra of β -NaYF₄:Gd³⁺,Tb³⁺@PEI and absorbance spectra of β -NaYF₄:Gd³⁺,Tb³⁺@PEI before and after the addition of TNT, (d) time-resolved decay dynamics of ⁵D₄ → ⁷F₅ transition of Tb³⁺ ions in β -NaYF₄:Gd³⁺,Tb³⁺@PEI after excitation at 375 nm in the presence of TNT (1, 10, 100, 300 μ M), (e) photograph showing the complex formation, which is confirmed by the change in the color of the solution to brownish yellow containing TNT, whereas other samples look white or pale yellow.

(Figure 5c). As shown in Figure 5d, under the optimum conditions in our experimental procedure, the PL quenching was analyzed using the Stern–Volmer (SV) plot between the change in PL intensity at 544 nm and the concentration of TNT. A significant linear correlation ($R^2 = 0.998$) existed between the relative PL intensity (I_0/I) and the concentration of TNT in the range of 0.1–300 μ M. The quenching efficiency was investigated using S–V equation, $I_0/I - 1 = K_{sv} [Q]$, where I_0 is the PL intensity in the absence of analyte, I is the PL intensity in the presence of analyte with the molar concentration $[Q]$, and K_{sv} is the quenching constant in M^{-1} . The quenching constant was determined to be $3.32 \times 10^4 M^{-1}$. The limit of detection (LOD) of TNT can be found using the linear regression method and calculated using the formula $3\sigma/m$, where 3 is the factor of 99% confidence level, σ is the standard deviation of the measured intensity for the blank β -NaYF₄:Gd³⁺,Tb³⁺@PEI nanophosphors ($n = 5$), whereas m denotes the slope of the linear calibration curve. It should be mentioned here that the LOD was found to be 119.9 nM (27.2 ppb), revealing higher sensitivity of the as-synthesized nanophosphors compared to the other earlier reported results (Table S2).

2.2. Interference Study. To assess the possibility of the analytical application of our phosphor-based nanosensor in terms of the sensitivity, the effect of different mixed samples of analogous compounds of TNT such as 2,4-DNT, 2,6-DNT, 4-NP, 1,3-DNB, TNP, 2,4-DNP, RDX, 1,4-DNB, NM, 4-NT, and NB: 300 μ M on the quenching of PL intensity was also studied and the results are shown in Figure 6a. In spite of the presence of other analytes, quenching of the PL intensity owing to the TNT was observed, having no interference because of the other analytes. Therefore, they show high sensitivity and selectivity for the detection of specific nitrocompounds. The TNT quenching was also observed in the buffer solution, NaH₂PO₄–Na₂HPO₄ (pH 7.0). Furthermore, we scrutinized the effects of pH on the PL intensity before and after the addition of TNT. In the wide range of pH 7–13, it showed no variation in the luminescence intensity (Figure S8a), suggesting the stability of the nanophosphors over the wide range of pH in the neutral and alkali environments. In addition, the influence of incubation time on the luminescence intensity was also studied to ensure the quenching solely because of TNT. As seen in Figure S8b, the intensity at 544 nm was quenched with the addition of TNT after 10 min. Meanwhile, by prolonging the incubation time to

Scheme 1. Schematic Representation of the Formation of the Meisenheimer Complex Due to the Interaction between the Amino Group Present on the Surface of the Phosphor Nanoparticles and TNT through the Charge-Transfer Mechanism in Aqueous Medium



48 h, the PL intensity was almost unchanged. Moreover, the PL intensity remained unchanged for almost 8 months, when stored at room temperature. This demonstrates that these nanophosphors can detect analytes over a long period of time, and thus are stable in nature. It should be mentioned here that no quenching was observed when only $\beta\text{-NaYF}_4\text{:Gd}^{3+},\text{Tb}^{3+}$ was used for the PL measurements without being capped by PEI (Figure S9). Therefore, we can say that the interaction of the TNT molecule with amino groups plays an important role.

2.3. Mechanism of Highly Selective Detection. To unravel the origin of the high selectivity of $\beta\text{-NaYF}_4\text{:Gd}^{3+},\text{Tb}^{3+}\text{@PEI}$ nanophosphors toward TNT, the quenching mechanism was investigated. A plausible mechanism for the detection could be proposed to be based on the donor–acceptor interaction between amino groups of phosphor nanorods and TNT. As TNT is an electron-deficient compound because of the presence of three electron-withdrawing nitro groups, it acts as an electron–acceptor, whereas amino groups are electron donors. Thus, an electron transfer mechanism takes place between TNT and amino groups of the PEI on the surface of nanoparticles, which leads to the formation of the Meisenheimer complex (Scheme 1). The three electron-withdrawing nitro groups present at the ortho- and para-position in TNT enables the nucleophile amino groups to attack at position 1 (where the methyl group is attached) in the molecule, which leads to the formation of this stable anionic σ -complex where the negative charge is delocalized over the ring.³⁸ The formation of such a complex with amino groups is typical of nitrocompounds, especially TNT. This complex formation can be confirmed by the change in the color of the solution of nanophosphors containing TNT to brownish yellow (Figure 6e), whereas there was no color change in the case of 2,4-DNT, 2,6-DNT, 4-NT, 1,3-DNB, 1,4-DNB, NM, and RDX. A pale yellow color appeared in the case of 2,4-DNP, 4-NP, NB, and TNP, which can be easily distinguished from the brownish yellow color of TNT. The UV–vis spectra of the explosives in the presence of PEI-capped nanophosphors were recorded and are shown in Figure 6b. As it can be seen, all other nitrocompounds have a strong absorbance before 400 nm, and hence do not interfere in the quenching. Meanwhile, it should be mentioned that the Meisenheimer complex formed with the TNT and nanophosphors has a broad absorbance in the range 400–650 nm, which overlaps with the emission of the Tb^{3+} ions in the phosphors (Figure 6c). As the emission from the nanoparticles overlaps with the absorbance of the complex formed, it gives

the possibility of LRET-based energy transfer, thereby leading to the quenching of the green emission. As mentioned above, when lanthanide ion-based nanoparticles are used as the energy donor, the mechanism is named as LRET, whose principles are similar to fluorescence resonance energy transfer and defined as an nr optical energy transfer between a donor D in its excited state and proximal ground state acceptor A through long-range dipole–dipole interactions.

For effective energy transfer, an acceptor absorption spectrum should overlap with a donor emission spectrum and the donor and acceptor should be linked in close proximity.³⁹ In Figure 6b, it is observed that the absorption spectrum of $\beta\text{-NaYF}_4\text{:Gd}^{3+},\text{Tb}^{3+}\text{@PEI}$ + TNT largely overlaps with the emission spectra of the $\beta\text{-NaYF}_4\text{:Gd}^{3+},\text{Tb}^{3+}\text{@PEI}$ phosphors, whereas there is no overlap with other analytes, thereby avoiding energy transfer. Although there is a suitable spectral overlap between the nanophosphor emission and the complex absorption in the UV–vis spectra, LRET cannot occur unless the donor and acceptor are close enough. Because of the formation of the complex between TNT and amine groups, it is brought close enough for the energy transfer to take place. Thus, the spectral overlapping between down-conversion emission of $\beta\text{-NaYF}_4\text{:Gd}^{3+},\text{Tb}^{3+}\text{@PEI}$ and absorbance of the Meisenheimer complex, and the close distance between the two manifests the LRET efficiency of the sensor. Meanwhile, in order to ascertain the above mentioned reason, we explored the lifetime of nanophosphors with varied concentrations of TNT. As displayed in Figure 6d, the lifetime of the $\beta\text{-NaYF}_4\text{:Gd}^{3+},\text{Tb}^{3+}\text{@PEI}$ phosphors decreased with increasing concentrations of TNT, and average lifetimes were considered for consistency in results. The decay was fitted using a biexponential decay function to yield average lifetimes of 2.11, 1.91, 1.72, 1.49, and 0.98 ms under the TNT concentrations of 0, 1, 10, 100, and 300 μM , respectively. Table S3 shows the lifetime parameters, viz. τ_i , rel %, and average lifetime of the samples. These results excluded the possibility of inner filter effect; thus, the lifetime reduction indicated that LRET is the major process^{40,41} between nanophosphors and the TNT complex as it offers the additional relaxation pathway. As mentioned above, the nanosensor exhibited high selectivity for the target TNT over other nitrocompounds with similar structures such as TNP, DNT, DNP, NP, and DNB. Other nitrocompounds are much weaker electronic acceptors when compared with TNT because of lack of electron-withdrawing nitro groups, and thus are not likely to form an effective Meisenheimer complex with

the amine groups present on the surface of the nanoparticles.⁴² Although weak interactions may lie between the amine groups and these compounds, no significant absorption peaks are detected in the UV–vis spectra in the spectral range of 400–700 nm; thus, they do not interfere with the emission of the downconverting nanophosphors. The proposed method demonstrates the feasibility of the PEI-capped β -NaYF₄:Gd³⁺,Tb³⁺ phosphor nanoparticles' application for preferentially detecting TNT as the analyte.

2.4. Interference from Other Analytes. In order to illustrate the good selectivity, sensitivity, and feasibility of the developed nanosensor probe for the detection of TNT, the effects of other analytes such as pesticides, sugars, and amino acids were also checked on the luminescence quenching profile and the results are shown in Figure 7. The stock solution of

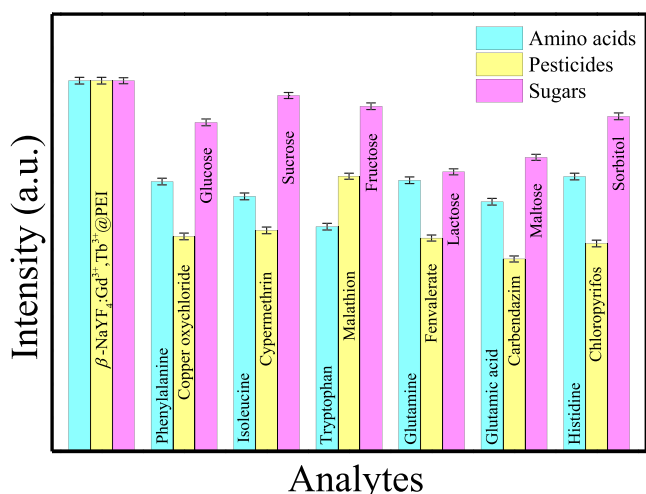


Figure 7. Histogram showing the selectivity of the phosphors over other analytes such as amino acids, pesticides, and sugars. There was no obvious change observed in the PL intensity, suggesting the selectivity toward TNT.

300 μ M of the following amino acids was prepared in water: phenylalanine, isoleucine, tryptophan, glutamine, glutamic acid, and histidine. The structures of all the analytes are given in Figure S10. Interestingly, among the amino acids, none of them showed any obvious quenching effects in the intensity of the nanophosphors. This is due to the groups present in the structure of the amino acids, which did not interact with the amine group in the PEI and thus are not able to form a complex with the nanorods. Similarly, stock solutions of some pesticides such as chloropyrifos, malathion, cypermethrin, copper oxychloride, fenvalerate, and carbendazim, and sugars such as glucose, fructose, sucrose, maltose, lactose, and sorbitol (Figure S10) were also prepared and incubated for 10 min before the PL measurements. The findings in Figure 7 indicate that these analytes did not show any significant change in the intensity of the nanophosphors. Thence, it can be seen that this nanoprobe sensor promised to be an intriguing indicator for the existence of any risks and threats from the explosives, thus assuring us of our security.

3. CONCLUSIONS

In summary, an approach has been reported for selective detection of TNT over a number of other analogous nitrocompounds using β -NaYF₄:Gd³⁺,Tb³⁺@PEI nanophosphors

based on fluorimetric sensing technique. The results from various characterization methods suggested the formation of β -NaYF₄:Gd³⁺,Tb³⁺ nanophosphors capped with PEI. The excellent selectivity toward TNT is ascribed to the interactions of the amine group present in PEI and nitro groups in TNT forming the Meisenheimer complex, which has caused a decrease in the PL signal because of the LRET-based energy-transfer mechanism between the nanophosphors and the complex formed. The PL intensity variations have displayed that the nanophosphors were sensitive and efficient for the explosive detection with a LOD of 119.9 nM (27.2 ppb). To further note the advantages of our work, we investigated the PL intensity of the nanophosphors with other analytes and no obvious effects were observed. Thus, the proposed method demonstrates the feasibility of the PEI-capped β -NaYF₄:Gd³⁺,Tb³⁺ phosphor nanoparticles' application for detecting TNT as the analyte independent of complicated instruments and immunoassays.

4. METHODS

Warning! Nitrocompounds, viz., TNT, TNP, and RDX, are highly explosive and therefore should be handled carefully in small amounts with proper safety precautions. In Figure S1, we have shown the chemical structure of some of the nitro explosives.

4.1. Chemicals and Reagents. All the chemicals were of analytical grade and were used without further purification; yttrium nitrate hexahydrate (Y(NO₃)₃·6H₂O, 99.89%), gadolinium nitrate hexahydrate (Gd(NO₃)₃·6H₂O, 99.89%), and terbium nitrate hexahydrate (Tb(NO₃)₃·6H₂O, 99.89%), PEI (with $M_w = 25\,000$ and $M_n = 10\,000$), TNP, 2,4-DNT, 2,6-DNT, 2,4-DNP, RDX, phenylalanine, cysteine, isoleucine, tryptophan, glutamic acid, aspartic acid, lysine, histidine, and glutamine were purchased from Sigma-Aldrich Inc. TNT and RDX were purchased from HEMRL, Pune. NaCl, Na₂HPO₄, NaH₂PO₄, Na₂CO₃, NaHCO₃, and NaOH were received from Thomas Baker. NH₄F was received from Merck. Dextrose, glucose, sucrose, fructose, lactose, and maltose were received from Himedia laboratories Pvt. Ltd. 1,3-DNB, 4-NP, 2,4-DNB, NM, 4-NT, NB, copper oxychloride, cypermethrin, malathion, fenvalerate, carbendazim, and chloropyrifos were purchased from a local company and used as received. Ethanol was obtained from Hayman Ltd. Deionized water was used throughout the experiments.

4.2. Synthesis. **4.2.1. Synthesis of Amine-Functionalized β -NaYF₄:15%Gd³⁺, 5%Tb³⁺ (β -NaYF₄:Gd³⁺,Tb³⁺@PEI).** Downconverting NaYF₄ nanophosphors were prepared using the hydrothermal method reported earlier.^{7,43} Briefly, 10 mL of 0.2 M solutions of Y(NO₃)₃, Gd(NO₃)₃, and Tb(NO₃)₃ were added in a 10 mL solution of NaCl (0.2 M). The solution was continuously stirred for nearly 30 min. Thereafter, 10 mL of PEI (10 wt %) was added followed by the addition of 20 mL of ethanol. In the resultant solution, 0.5 M of NH₄F was added dropwise. Finally, the mixture was poured in a Teflon container with 100 mL capacity and reaction was set for 24 h at 180 °C. The autoclave was cooled to room temperature, and the green luminescent nanophosphors were obtained after washing with water and ethanol thrice. Then, the product was dried under vacuum at 70 °C overnight.

4.2.2. Preparation of Stock Solutions. For the PL study, 300 μ M stock solution of the analytes was prepared in deionized water and a fixed amount of β -NaYF₄:Gd³⁺,Tb³⁺@PEI was added to the desired concentrations levels in a 1 mL

quartz cuvette (path length of 1 cm). The mixture was then incubated at room temperature for 10 min before the spectral measurements. The luminescence spectra of the solutions were measured at an excitation wavelength of 273 nm and emission data were collected in the range of 400–700 nm. Each measurement was repeated at least thrice and consistent results were recorded. The feasibility of the probe was also investigated in buffer solution with pH 7 to pH 13. For pH ranging from 7 to 8, NaH_2PO_4 – Na_2HPO_4 , pH ranging from 9 to 11 NaHCO_3 – Na_2CO_3 – NaOH and pH ranging from 12 to 13 KCl – NaOH were used.

4.3. Characterization Techniques. The phase purity and crystallinity of the as-synthesized samples were characterized by powder X-ray diffraction using a PANalytical X'PERT PRO instrument and the iron-filtered $\text{Cu-K}\alpha$ radiation ($\lambda = 1.54 \text{ \AA}$) in the 2θ range of 10° – 80° covered in a step size of 0.08° with a count time of 2s. The operating voltage and current were kept at 30 kV and 40 mA, respectively. The specific structural details and morphology were obtained by using an FEI Tecnai T20 transmission electron microscope equipped with a super-twin lens (s-twin) operated at 200 keV voltage. To analyze the shape and size of the samples, FESEM (Hitachi S-4200) was done. EDXA of the samples was performed during FESEM measurements to obtain the elemental composition of the samples. The XPS spectra were recorded on Thermo Fisher Scientific Instruments K Alpha + with monochromatic Al $\text{K}\alpha$ as the X-ray source with 6 mA beam current and 12 kV voltage. A PALS Zeta Potential Analyzer Ver 3.54 (Brookhaven Instrument Corps.) was used to determine the zeta potentials (ζ). Deionized water was the dispersion medium. The FTIR spectrum was recorded by a PerkinElmer spectrum two FTIR spectrophotometer with a resolution of 4 cm^{-1} and scan speed of 32 scans/min. TGA was done using SDT model Q600 of TA Instruments Inc., USA, at a heating rate of $10^\circ\text{C}/\text{min}$ under continuous flux of nitrogen at 100 mL/min. Raman spectroscopy measurements were recorded at room temperature on an HR 800 Raman spectrophotometer (Jobin Yvon, HORIBA, France) equipped with an achromatic Czerny–Turner type monochromator (800 mm focal-length) with silver-treated mirrors. Monochromatic radiation emitted by a 325 nm laser, operating at 20 mW, was used. PL spectra were acquired using a Cary eclipse fluorescence spectrophotometer, equipped with a 400 W Xe lamp as an excitation source with excitation and emission slit width of 10 nm and a Hamamatsu R928 photomultiplier tube as a detector. The UV–visible spectra were taken on a Cary 300 absorbance spectrometer. PL decay dynamics were carried out on FLS 980 (Edinburgh Instruments).

■ ASSOCIATED CONTENT

🔗 Supporting Information

The Supporting Information is available free of charge on the ACS Publications website at DOI: 10.1021/acsomega.8b03491.

Chemical structures of commonly used nitrocompounds; Rietveld refinement profile and parameters of NaYF_4 ; EDXA pattern showing the elemental composition consisting of Na, F, Y, Gd, and Tb ions; HRTEM, IFFT, and SAED pattern of $\beta\text{-NaYF}_4\text{:Gd}^{3+},\text{Tb}^{3+}$ @PEI nanophosphors; TGA curve for branched PEI; high-resolution XPS spectra of the elements present in $\beta\text{-NaYF}_4\text{:Gd}^{3+},\text{Tb}^{3+}$ @PEI; and Raman spectra of the as-

synthesized $\beta\text{-NaYF}_4\text{:Gd}^{3+},\text{Tb}^{3+}$ @PEI; comparison of different methods of detection and LODs for TNT; influence of pH and incubation time on luminescence intensity; comparison of PL spectra of $\beta\text{-NaYF}_4\text{:Gd}^{3+},\text{Tb}^{3+}$ @PEI nanophosphors with and without PEI and in presence and absence of TNT; average lifetime of the $\beta\text{-NaYF}_4\text{:Gd}^{3+},\text{Tb}^{3+}$ @PEI with different concentration of TNT; and chemical structures of commonly used amino acids, pesticides, and sugars (PDF)

■ AUTHOR INFORMATION

Corresponding Author

*E-mail: p.poddar@ncl.res.in. Phone: +91-20-25902580. Fax: +91-20-2590-2636.

ORCID

Pankaj Poddar: 0000-0002-2273-588X

Notes

The authors declare no competing financial interest.

■ ACKNOWLEDGMENTS

M.M. acknowledges the support from the Council of Industrial and Scientific Research (CSIR), India, for providing the Senior Research Fellowship (SRF). The authors also acknowledge the support from Dr. Sujit K. Ghosh, Department of Chemistry, Indian Institute of Science Education and Research, Pune, for providing the explosives.

■ REFERENCES

- (1) Gai, S.; Li, C.; Yang, P.; Lin, J. Recent Progress in Rare Earth Micro/Nanocrystals: Soft Chemical Synthesis, Luminescent Properties, and Biomedical Applications. *Chem. Rev.* **2014**, *114*, 2343–2389.
- (2) Sandrock, T.; Scheife, H.; Heumann, E.; Huber, G. High-Power Continuous-Wave Upconversion Fiber Laser at Room Temperature. *Opt. Lett.* **1997**, *22*, 808–810.
- (3) Li, K.; Liang, S.; Shang, M.; Lian, H.; Lin, J. Photoluminescence and Energy Transfer Properties with Y+SiO_4 Substituting Ba+PO_4 in $\text{Ba}_3\text{Y}(\text{PO}_4)_3\text{:Ce}^{3+}/\text{Tb}^{3+}$, $\text{Tb}^{3+}/\text{Eu}^{3+}$ Phosphors for w-LEDs. *Inorg. Chem.* **2016**, *55*, 7593–7604.
- (4) Padhye, P.; Sadhu, S.; Malik, M.; Poddar, P. A Broad Spectrum Photon Responsive, Paramagnetic $\beta\text{-NaGdF}_4\text{:Yb}^{3+},\text{Er}^{3+}$ –Mesoporous Anatase Titania Nanocomposite. *RSC Adv.* **2016**, *6*, 53504–53518.
- (5) Gu, B.; Zhang, Q. Recent Advances on Functionalized Upconversion Nanoparticles for Detection of Small Molecules and Ions in Biosystems. *Adv. Sci.* **2018**, *5*, 1700609.
- (6) Jo, H. L.; Song, Y. H.; Park, J.; Jo, E.-J.; Goh, Y.; Shin, K.; Kim, M.-G.; Lee, K. T. Fast and Background-Free Three-Dimensional (3D) Live-Cell Imaging with Lanthanide-Doped Upconverting Nanoparticles. *Nanoscale* **2015**, *7*, 19397–19402.
- (7) Padhye, P.; Alam, A.; Ghorai, S.; Chattopadhyay, S.; Poddar, P. Doxorubicin-Conjugated $\beta\text{-NaYF}_4\text{:Gd}^{3+}/\text{Tb}^{3+}$ Multifunctional, Phosphor Nanorods: A Multi-Modal, Luminescent, Magnetic Probe for Simultaneous Optical and Magnetic Resonance Imaging and an Excellent pH-Triggered Anti-Cancer Drug Delivery Nanovehicle. *Nanoscale* **2015**, *7*, 19501–19518.
- (8) Bagheri, A.; Arandiyani, H.; Boyer, C.; Lim, M. Lanthanide-Doped Upconversion Nanoparticles: Emerging Intelligent Light-Activated Drug Delivery Systems. *Adv. Sci.* **2016**, *3*, 1500437.
- (9) Zhang, Y.; Tang, Y.; Liu, X.; Zhang, L.; Lv, Y. A Highly Sensitive Upconverting Phosphors-Based Off–on Probe for the Detection of Glutathione. *Sens. Actuators, B* **2013**, *185*, 363–369.
- (10) Muhr, V.; Buchner, M.; Hirsch, T.; Jovanović, D. J.; Dolić, S. D.; Dramićanin, M. D.; Wolfbeis, O. S. Europium-Doped GdVO_4 Nanocrystals as a Luminescent Probe for Hydrogen Peroxide and for Enzymatic Sensing of Glucose. *Sens. Actuators, B* **2017**, *241*, 349–356.

- (11) Wang, L.; Yan, R.; Huo, Z.; Wang, L.; Zeng, J.; Bao, J.; Wang, X.; Peng, Q.; Li, Y. Fluorescence Resonance Energy Transfer Biosensor Based on Upconversion-Luminescent Nanoparticles. *Angew. Chem., Int. Ed.* **2005**, *44*, 6054–6057.
- (12) Yao, L.; Zhou, J.; Liu, J.; Feng, W.; Li, F. Iridium-Complex-Modified Upconversion Nanophosphors for Effective LRET Detection of Cyanide Anions in Pure Water. *Adv. Funct. Mater.* **2012**, *22*, 2667–2672.
- (13) Liu, Q.; Peng, J.; Sun, L.; Li, F. High-Efficiency Upconversion Luminescent Sensing and Bioimaging of Hg(II) by Chromophoric Ruthenium Complex-Assembled Nanophosphors. *ACS Nano* **2011**, *5*, 8040–8048.
- (14) Ju, K.-S.; Parales, R. E. Nitroaromatic Compounds, from Synthesis to Biodegradation. *Microbiol. Mol. Biol. Rev.* **2010**, *74*, 250–272.
- (15) Waddell, R.; Dale, D. E.; Monagle, M.; Smith, S. A. Determination of Nitroaromatic and Nitramine Explosives from a PTFE Wipe Using Thermal Desorption-Gas Chromatography with Electron-Capture Detection. *J. Chromatogr. A* **2005**, *1062*, 125–131.
- (16) Peng, L.; Hua, L.; Wang, W.; Zhou, Q.; Li, H. On-Site Rapid Detection of Trace Non-Volatile Inorganic Explosives by Stand-Alone Ion Mobility Spectrometry via Acid-Enhanced Evaporization. *Sci. Rep.* **2015**, *4*, 6631.
- (17) Dasary, S. S. R.; Singh, A. K.; Senapati, D.; Yu, H.; Ray, P. C. Gold Nanoparticle Based Label-Free SERS Probe for Ultrasensitive and Selective Detection of Trinitrotoluene. *J. Am. Chem. Soc.* **2009**, *131*, 13806–13812.
- (18) Liyanage, T.; Rael, A.; Shaffer, S.; Zaidi, S.; Goodpaster, J. V.; Sardar, R. Fabrication of a Self-Assembled and Flexible SERS Nanosensor for Explosive Detection at Parts-per-Quadrillion Levels from Fingerprint. *Analyst* **2018**, *143*, 2012–2022.
- (19) Pal, A.; Sk, M. P.; Chattopadhyay, A. Conducting Carbon Dot–Polypyrrole Nanocomposite for Sensitive Detection of Picric Acid. *ACS Appl. Mater. Interfaces* **2016**, *8*, 5758–5762.
- (20) Nagarkar, S. S.; Joarder, B.; Chaudhari, A. K.; Mukherjee, S.; Ghosh, S. K. Highly Selective Detection of Nitro Explosives by a Luminescent Metal-Organic Framework. *Angew. Chem., Int. Ed.* **2013**, *52*, 2881–2885.
- (21) Xu, S.; Lu, H.; Li, J.; Song, X.; Wang, A.; Chen, L.; Han, S. Dummy Molecularly Imprinted Polymers-Capped CdTe Quantum Dots for the Fluorescent Sensing of 2,4,6-Trinitrotoluene. *ACS Appl. Mater. Interfaces* **2013**, *5*, 8146–8154.
- (22) Sun, X.; He, J.; Meng, Y.; Zhang, L.; Zhang, S.; Ma, X.; Dey, S.; Zhao, J.; Lei, Y. Microwave-Assisted Ultrafast and Facile Synthesis of Fluorescent Carbon Nanoparticles from a Single Precursor: Preparation, Characterization and Their Application for the Highly Selective Detection of Explosive Picric Acid. *J. Mater. Chem. A* **2016**, *4*, 4161–4171.
- (23) Yu, J.; Wang, X.; Kang, Q.; Li, J.; Shen, D.; Chen, L. One-Pot Synthesis of a Quantum Dot-Based Molecular Imprinting Nanosensor for Highly Selective and Sensitive Fluorescence Detection of 4-Nitrophenol in Environmental Waters. *Environ. Sci.: Nano* **2017**, *4*, 493–502.
- (24) Hao, S.; Chen, G.; Yang, C. Sensing Using Rare-Earth-Doped Upconversion Nanoparticles. *Theranostics* **2013**, *3*, 331–345.
- (25) Xu, S.; Xu, S.; Zhu, Y.; Xu, W.; Zhou, P.; Zhou, C.; Dong, B.; Song, H. A Novel Upconversion, Fluorescence Resonance Energy Transfer Biosensor (FRET) for Sensitive Detection of Lead Ions in Human Serum. *Nanoscale* **2014**, *6*, 12573–12579.
- (26) Zhu, Y.; Ni, Y.; Sheng, E. Fluorescent LaVO₄:Eu³⁺ Micro/nanocrystals: pH-Tuned Shape and Phase Evolution and Investigation of the Mechanism of Detection of Fe³⁺ Ions. *Dalton Trans.* **2016**, *45*, 8994–9000.
- (27) Wang, H.; Liu, Y.; Wang, Z.; Yang, M.; Gu, Y. 808 nm-light-excited upconversion nanoprobe based on LRET for the ratiometric detection of nitric oxide in living cancer cells. *Nanoscale* **2018**, *10*, 10641–10649.
- (28) Ma, Y.; Wang, L. Upconversion Luminescence Nanosensor for TNT Selective and Label-Free Quantification in the Mixture of Nitroaromatic Explosives. *Talanta* **2014**, *120*, 100–105.
- (29) Hu, X.; Wei, T.; Wang, J.; Liu, Z.-E.; Li, X.; Zhang, B.; Li, Z.; Li, L.; Yuan, Q. Near-Infrared-Light Mediated Ratiometric Luminescent Sensor for Multimode Visualized Assays of Explosives. *Anal. Chem.* **2014**, *86*, 10484–10491.
- (30) Toby, B. H. EXPGUI, a Graphical User Interface for GSAS. *J. Appl. Crystallogr.* **2001**, *34*, 210–213.
- (31) Tutuianu, R.; Popescu, L.; Preda, M.; Rosca, A.-M.; Piticescu, R.; Burlacu, A. Evaluation of the Ability of Nanostructured PEI-Coated Iron Oxide Nanoparticles to Incorporate Cisplatin during Synthesis. *Nanomaterials* **2017**, *7*, 314.
- (32) Chen, H.-L.; Hsiao, M.-S. Self-Assembled Mesomorphic Complexes of Branched Poly(ethylenimine) and Dodecylbenzenesulfonic Acid. *Macromolecules* **1999**, *32*, 2967–2973.
- (33) Shan, J.; Uddi, M.; Yao, N.; Ju, Y. Anomalous Raman Scattering of Colloidal Yb³⁺,Er³⁺ Codoped NaYF₄ Nanophosphors and Dynamic Probing of the Upconversion Luminescence. *Adv. Funct. Mater.* **2010**, *20*, 3530–3537.
- (34) Padhye, P.; Poddar, P. Static and Dynamic Photoluminescence and Photocatalytic Properties of Uniform, Monodispersed Up/down-Converting, Highly Luminescent, Lanthanide-Ion-Doped β -NaYF₄ Phosphor Microcrystals with Controlled Multiform Morphologies. *J. Mater. Chem. A* **2014**, *2*, 19189–19200.
- (35) Szpikowska-Sroka, B.; Pawlik, N.; Goryczka, T.; Pisarski, W. A. Influence of Silicate Sol–gel Host Matrices and Catalyst Agents on the Luminescent Properties of Eu³⁺/Gd³⁺ under Different Excitation Wavelengths. *RSC Adv.* **2015**, *5*, 98773–98782.
- (36) van Hest, J. J. H. A.; Blab, G. A.; Gerritsen, H. C.; de Mello Donega, C.; Meijerink, A. Probing the Influence of Disorder on Lanthanide Luminescence Using Eu-Doped LaPO₄ Nanoparticles. *J. Phys. Chem. C* **2017**, *121*, 19373–19382.
- (37) Chen, G.; Qiu, H.; Prasad, P. N.; Chen, X. Upconversion Nanoparticles: Design, Nanochemistry, and Applications in Theranostics. *Chem. Rev.* **2014**, *114*, 5161–5214.
- (38) Gao, D.; Wang, Z.; Liu, B.; Ni, L.; Wu, M.; Zhang, Z. Resonance Energy Transfer-Amplifying Fluorescence Quenching at the Surface of Silica Nanoparticles toward Ultrasensitive Detection of TNT. *Anal. Chem.* **2008**, *80*, 8545–8553.
- (39) Cheng, L.; Yang, K.; Shao, M.; Lee, S.-T.; Liu, Z. Multicolor In Vivo Imaging of Upconversion Nanoparticles with Emissions Tuned by Luminescence Resonance Energy Transfer. *J. Phys. Chem. C* **2011**, *115*, 2686–2692.
- (40) Ye, W. W.; Tsang, M.-K.; Liu, X.; Yang, M.; Hao, J. Upconversion Luminescence Resonance Energy Transfer (LRET)-Based Biosensor for Rapid and Ultrasensitive Detection of Avian Influenza Virus H7 Subtype. *Small* **2014**, *10*, 2390–2397.
- (41) Muhr, V.; Würth, C.; Kraft, M.; Buchner, M.; Baeumner, A. J.; Resch-Genger, U.; Hirsch, T. Particle-Size-Dependent Förster Resonance Energy Transfer from Upconversion Nanoparticles to Organic Dyes. *Anal. Chem.* **2017**, *89*, 4868–4874.
- (42) Hughes, S.; Dasary, S. S. R.; Begum, S.; Williams, N.; Yu, H. Meisenheimer Complex between 2,4,6-Trinitrotoluene and 3-Aminopropyltriethoxysilane and Its Use for a Paper-Based Sensor. *Sens. Bio-Sensing Res.* **2015**, *5*, 37–41.
- (43) Malik, M.; Padhye, P.; Poddar, P. Graphene Quantum Dots-Driven Multiform Morphologies of β -NaYF₄: Gd³⁺/Tb³⁺ Phosphors: The Underlying Mechanism and Their Optical Properties. *ACS Omega* **2018**, *3*, 1834–1849.